A Novel Low-Dose Approach to Active Detection of Shielded High-Z Materials

by

Buckley E. O'Day III

M.S. Nuclear Engineering, Air Force Institute of Technology, 2009
M.I.M. International Management, University of Maryland University College, 2005
B.S. Civil Engineering, United States Military Academy, 1996

SUBMITTED TO THE DEPARTMENT OF NUCLEAR SCIENCE AND ENGINEERING IN PARTIAL FULFUILLMENT OF THE REQUIREMENTS FOR THE DEGREE OF

DOCTOR OF PHILOSOPHY IN NUCLEAR SCIENCE AND ENGINEERING
AT THE
MASSACHUSETTS INSTITUTE OF TECHNOLOGY

JUNE 2015

© 2015 Massachusetts Institute of Technology. All rights reserved.

Signature of Author: Signature redacted
Department of Nuclear Science and Engineering
17 April 2015

Certified by: Signature redacted
Areg Danagoulian
Assistant Professor of Nuclear Science and Engineering
Thesis Co-Supervisor

Certified by: Signature redacted
Richard C. Lanza
Senior Research Scientist
Thesis Co-Supervisor

Certified by: Signature redacted
R. Scott Kemp
Assistant Professor of Nuclear Science and Engineering

Certified by: Signature redacted
Gordon Kohse
NRL Principal Research Engineer

Certified by: Signature redacted
Zachary S. Hartwig
Postdoctoral Fellow

Accepted by: Signature redacted
Mujid S. Kazimi
TEPCO Professor of Nuclear Engineering
Chair, Department Committee on Graduate Students

MASSACHUSETTS INSTITUTE OF TECHNOLOGY
MAY 11 2016
LIBRARIES
ARCHIVES

-Blank Page-

A Novel Low-Dose Approach to Active Detection of Shielded High-Z Materials

by

Buckley E. O'Day III

Submitted to the Department of Nuclear Science and Engineering
on April 17, 2015 in Partial Fulfillment of the Requirements for the Degree of Doctor
of Philosophy in Nuclear Science and Engineering

ABSTRACT

This research demonstrates that multiple mono-energetic gamma lines produced from low threshold, high-Q nuclear reactions can be used to detect the presence of high-Z material shielded in low- and medium-Z cargo. Specifically, this work establishes a research foundation to inform the eventual development and optimization of a new type of low-dose, rapid-scan, transmission radiography imaging system designed to detect the presence of special nuclear material in cargo. This thesis explores the processes, reactions, and detection methods that may be used to develop a transmission imaging system significantly different from existing interrogation methods and major systems currently deployed in the field.

This thesis introduces the nuclear smuggling issue, provides relevant background information, and defines the high-Z material detection problem. It also provides a brief overview of SNM detection efforts, to include both passive and active detection, and shows why active detection methods are needed to detect shielded SNM. The thesis then explains the underlying physics important to multiple-monoenergetic gamma line imaging and defines key concepts to the characterization of cargo. An overview of the experimental concept and setup, to include development of a theoretical model to predict imaging counts, simulations conducted in support of the experiment, the presence and mitigation of neutrons in the beam line, major equipment and materials used, and the data acquisition and analysis software programs employed is then provided. This work considers and explains the difficulties of scanning of homogeneous and non-homogeneous cargoes, potential scanning system vulnerabilities to high-Z material smuggling, and suggests future efforts to address these vulnerabilities. The purpose, conduct, and results of 161 individual tests are provided. Finally, this thesis provides conclusions and recommendations for future work that could lead to development of a better cargo scanning system.

Key achievements of this thesis included development of a simple attenuation model to predict the theoretical ratio of two monoenergetic gamma lines transmitted through complex cargo, exploration of the ability to discriminate between medium- and high-Z materials both as pure cargo and when embedded in Fe, and the behavior of combinations of various materials. This thesis also considers the accuracy to which the areal density and effective atomic number of an arbitrary cargo might be determined.

This work establishes two distinct sets of data that can be used as a future basis to develop models to address these and other challenges. The first set of 126 experiments establishes how different Z materials embedded in Fe impacts the ratio of transmitted 15.11 MeV to 4.44 MeV gammas. The second set of 35 experiments explores how the ratio changes when U is shielded with combinations of various Z materials. Experimentally acquired data was compared to theoretical calculations to determine under what conditions and to what sensitivity the method may be used to determine the presence or absence of high-Z materials.

Results indicate the method may be used with confidence to detect the presence of 50 g/cm^2 of high-Z material within a material of total areal density of 125-235 g/cm^2.

Thesis Co-Supervisor: Richard C. Lanza
Title: Senior Research Scientist

Thesis Co-Supervisor: Areg Danagoulian
Title: Assistant Professor of Nuclear Science and Engineering

Thesis Reader: R. Scott Kemp
Title: Assistant Professor of Nuclear Science and Engineering

Thesis Reader: Gordon Kohse
Title: NRL Principal Research Engineer

Thesis Reader: Zachary S. Hartwig
Title: Postdoctoral Fellow

Acknowledgments

My MIT adventure has been both challenging and rewarding. I am fortunate to have had the opportunity to spend time with so many driven, talented, and intelligent people. I would like to thank the NSE faculty & staff and my thesis committee for providing me with so many great opportunities to learn. And I would like to thank my classmates and peers for helping me to capitalize on each opportunity and making my three years at MIT a great experience.

Dr. Dick Lanza, thank you for the mentorship, allowing me to serve as your Teaching Assistant and Research Assistant, and learning how you attack complex issues and turn them into manageable problems we can actually solve. Professor Areg Danagoulian, thank you for investing the time and effort into making me a better scientist and researcher. No one could have done a better job balancing the amount of guidance provided and allowing me the flexibility to find my own path. Dr. Zach Hartwig, thank you for getting in the trenches with me. Every time I hear your phrase—"there is something really interesting going on with the physics here"—I will think about the *gedankenexperiments* and white board work that allowed us to figure so many things out. Dr. Gordon Kohse and Professor Scott Kemp, thank you for serving on my committee, providing valuable insights, and asking the thought-provoking questions that led to many of the ideas in this work.

I would like to thank my peers at MIT for supporting and working with me throughout the process. A special thanks goes to Mareena Robinson-Snowden and Chad Schools for sidebar conversations that helped maintain my sanity, answering a plethora of questions about coursework, and helping me to prepare for the doctoral qualifying exam. To the entire qualifying exam study group—Daniel Curtis, Carl Haugen, Leigh Ann Kesler, Uuganbayar Otgonbaatar, Jude Safo, Brandon Sorbom, Lixin Sun, Aditi Verma, and the rest—thanks for helping to make my qualifying exam experience quite the adventure. It was incredible that as a team we were able to turn pages of hieroglyphics into material we actually understood. A special thanks to Brandon for being my go-to qualifying exam study partner, half-marathon running partner, and for being a great friend. Lixin, a special thanks to you for working with me on the most challenging problems in many of our classes and having the patience to explain things a second (or even a third) time. Having you down the hall was like having my very own professor on call.

Any success I have enjoyed is truly not mine alone. Many along the way have helped me to get where I am today. More than anyone else, I want to thank my family. To my incredible wife, Elen, I could not have done (and did not do) this without you. You have provided the most support and made the greatest sacrifices. You are truly my better half. To my wonderful kids—Helena, Buckley IV, Sascha, and Elettra—thank you for all the love and support, and for your patience and understanding. Thanks to Dad, Mom, Hilda, Anna, and Julie for always being in my corner. A special thanks to Mike and Geraldine O'Day for being a second set of parents for me and making me a part of their family.

And a very special thanks to Mr. Kroculick for kick-starting my interest in science almost three decades ago. *Pay it forward.*

I dedicate this work to the smartest man I ever met, my father. His example and encouragement set me on a lifelong journey of learning that I thoroughly enjoy.

Yesterday

I see a dim, familiar star
That sets my mood, diverts my mind
To long ago and far away
With things I've left behind;
A dusty road that wound its way
Across a dried and hoof-worn field
Where little boys', in scuffled shoes,
Resounding laughter pealed;
To moonless nights and greying dawns
And meadow larks with joyous sounds;
The shuffling trot of little men
A waking up the town;
And days beneath a turquoise sky;
A sun, whose golden eye admired
The clearest streams, the greenest trees
That e'er a boy desired.
I muse upon this paradise
That recently I knew as mine,
Which disappeared without a trace
As if by time's design.

--Buckley E. O'Day, Jr.
15 Dec 1942-29 Dec 2013

TABLE OF CONTENTS

LIST OF TABLES

LIST OF FIGURES

Figure Page

THESIS STRUCTURE AND PURPOSE

This thesis is divided into eight chapters. Chapter 1 provides an introduction to the nuclear smuggling issues, relevant background information, and defines the high-Z material detection problem. Chapter 2 provides a brief overview of SNM detection efforts, including descriptions of both passive and active detection efforts. Chapter 3 presents the underlying physics important to the multiple-monoenergetic gamma line imaging and defines critical concepts key to characterization of cargo. Chapter 4 provides an overview of the experimental concept and setup, to include development of a theoretical model to predict imaging counts, simulations conducted in support of the experiment, the presence and mitigation of neutrons in the beam line, major equipment and materials used, and the data acquisition and analysis software programs employed. Chapter 5 addresses scanning of homogeneous and non-homogeneous cargoes, and potential scanning system vulnerabilities to high-Z material smuggling and future efforts to address these vulnerabilities. Chapter 6 provides a brief overview of the thesis scope and experiments. Chapter 7 reports experimental results and analysis. Finally, Chapter 8 reports conclusions and provides recommendations for future work that could lead to development of a better cargo scanning system.

The purpose of this thesis is to provide a proof of principle and lay a firm research foundation for the eventual development of a new type of low-dose, rapid-scan, radiography imaging system using mono-energetic gamma lines from low-threshold, high-Q nuclear interactions. This thesis explores how transmission of 1-20 MeV gammas through cargo provides information about the areal density and effective atomic number of the cargo. Specifically, it seeks to show that multiple mono-energetic gamma lines can be used to detect the presence of high-Z material shielded in low- and medium-Z cargo. This thesis seeks to lay a firm research foundation to be used to inform the eventual development and optimization of a cargo imaging system that would provide a significant break from existing interrogation methods and major systems currently deployed in the field.

CHAPTER 1

INTRODUCTION

This chapter provides an introduction to the nuclear smuggling issues, relevant background information, and defines the high-Z material detection problem. Specifically, it provides a background of the nuclear smuggling issue, prominent examples of nuclear smuggling impacts, and explains how the 9/11 terrorist attacks had a global impact that has led to international cooperation on non- and counter-proliferation efforts. It also provides an overview of the scope and scale of the US border security as an example of the difficult problems countries face in securing their borders, and provides insights into the holistic approach to border security. An effort to clear cargo containers, known as the Container Security Initiative, is discussed. A brief overview of border special nuclear material (SNM) detection systems and the detectors used at ports of energy (POEs) is also provided. An informative characterization of cargo passing through US ports, which ultimately guides much of this research, is then discussed. An explanation of why the detection of a nuclear weapons, and especially a U-based weapon, is so difficult is provided. Finally, a brief discussion on how nuclear smuggling, border security, and the difficulty in detecting a nuclear weapon converge to create the very serious challenge this proposed cargo scanning system seeks to address is presented.

1.1 The Nuclear Smuggling Issue

With the end of the Cold War, the trafficking of nuclear materials emerged as a serious issue. Several private and international organizations began tracking reporting on unauthorized possession and illicit activities involving nuclear and radiological sources. Once such example, the International Atomic Energy Agency (IAEA) Incident and Trafficking Database (ITDB) tracks and disseminates among members information on "incidents of nuclear and other radioactive material out of regulatory control" [**1**]. While the details of the events are not open to the public, the ITDB 2014 Fact Sheet reports that from 1993-2013 there were 2,477 confirmed incidents of which sixteen were confirmed to involve unauthorized possession of special nuclear material[1] (SNM). The SNM incidents frequently involved grams of materials but some incidents involved kilogram quantities.

A second organization, the Nuclear Threat Initiative maintained from 2005-2012 a database on incidents involving nations of the former Soviet Union, and reported on over a dozen incidents involving or allegedly involving U [**2**]. Schmid and Spencer-Smith offer a summary of radiological and nuclear smuggling incidents and alleged incidents in the Black Sea region from 1990-2011 based on open source [**3**]. It should be noted that while all of the incidents have not been authenticated, it underscores that nuclear and radiological smuggling are very real issues. The James Martin Center for Nonproliferation Studies maintains a downloadable database of global incidents and trafficking that tracks more recent events [**4**]. A quick glance at the current databases shows the illicit trafficking problem continues. Two prominent recent examples include Iraq's July 2014 notification to the United Nations that Sunni militants seized nearly 90 lbs. of U compounds from Mosul University [**5**] and INTERPOL's December 2014 report on the capture of seven

---

[1] For purposes of this paper, SNM refers to U, Np, and Pu.

[2] It should be noted that as of January 1, 2015 the Russian Federation no longer permits U.S.

members of organized crime in possession of 200 g of ^{238}U and 1 kg of another unidentified radioactive material [**6**]. The identification of members or organized crime as possessors of SNM is particularly alarming since these organizations have extensive trafficking networks and experience.

The seriousness of the nuclear smuggling problem and the threat of nuclear terrorism make nuclear terrorism an issue frequently discussed by world leaders. According to the United Nations Secretary General, Ban Ki-moon, "Nuclear terrorism is one of the most serious threats of our time. Even one such attack could inflict mass casualties and create immense suffering and unwanted change in the world forever. This prospect should compel all of us to act to prevent such a catastrophe" [**7**]. His opinion is one shared by numerous world leaders, including American President Barack Obama [**8**].

1.2 Examples of Nuclear Smuggling Incidents

While many instances of radioactive material smuggling do not involve weapons grade material or material that can be used in a weapons, several instances have been of concern because of the quantity or enrichment of the material or both. Some historical instances of concern include [**9**]:

- In 1992, a Russian engineer smuggled 1.5 kg of weapons grade U (WGU) from a research institute.
- Russian naval officer and another individual stole 4.34 kg of HEU in fuel rods from a naval fuel storage facility in 1993.
- Three men from a Moscow flight were arrested at the Munich airport with 560 g of mixed Pu- and U-oxides in 1994.
- A joint US-Georgian operation led to the arrest of a Russian man with 100 g of weapons grade U and Georgian accomplices in Tbilisi in 2006.
- In 2008 two Ukrainians were arrested with U and Cs valued at $4.1M.
- Moldovan police arrested six people attempting to sell a kg of ^{235}U.

A November 2007 incident at the Pelindaba nuclear facility in South Africa is also a sobering case study [**10**]. Armed men penetrated a 10,000V fence, disabled alarms without detection, shot a worker, and spent 45 minutes in the facility where hundreds of kg of WGU was stored. If the perpetrators had been successful, they could have obtained sufficient material for several nuclear weapons.

1.3 The 9/11 Terrorist Attacks had a Global Impact

The September 11, 2001 (9/11) terrorist attacks fundamentally changed the United States' (US) perception of its own security and raised the asymmetrical foreign threat to the fore of the American psyche [**11**]. Nineteen Al Qaeda terrorists hijacked four commercial airplanes and used them to kill nearly 3,000 people, destroy a symbol of American economic power, the World Trade Center in New York, and to attack a symbol of American military power, the Pentagon [**12**]. Were it not for the heroics of the United Airlines Flight 93 passengers, an attack on a symbol of US political power—such as the US Capitol—would also have been executed.

While 9/11 did not mark the beginning of terrorism, nor was it the first terrorist attack in the United States, it refocused the US government's and the public's awareness on the asymmetric terrorist threat. America acknowledged the new reality that a non-state actor based anywhere could use a small number of people and a meager budget to inflict massive damage on the U.S. homeland.

In light of the devastation of the 9/11 attacks, policy makers began to question what damage a nuclear-armed terrorist organization could inflict on the United States. A US Department of Defense study determined a terrorist or clandestine nuclear attack on the homeland should be protected against because [**13**]:

- Proliferation of knowledge necessary to build a weapon.
- US enemies and adversaries have or are seeking weapons.
- Limits to nuclear forensics / attribution capabilities make clandestine (terrorist or Special Operations) delivery attractive options.
- A successful attack could upset nuclear stability among nuclear-armed States and make future nuclear use more probable.

As part of the effort to counter this newly acknowledged threat, the government placed additional emphasis and resources on securing the nation's borders to prevent smuggling a nuclear weapon or improvised nuclear device into the homeland. Many of the activities undertaken or expanded were a result of the 9/11 Commission report which recommended the U.S. increase non-proliferation and counter-proliferation efforts, integrate U.S. border security systems into a comprehensive screening network with the larger transportation system, increase coordination with trusted allies, and through international cooperation increase security standards for travel and border crossing throughout the world [**14**].

The effects of the 9/11 attacks did not stop at the U.S. borders; it had a global impact. The attacks cost the U.S. thousands of lives, billions of dollars to recover and rebuild, changed the public's perception of the terrorist threat, and changed the US counter-terrorism efforts from law-enforcement and limited military action to the Global War on Terror. The world annual economic growth dropped from 4.1 in 2000 to 1.4 % in 2001 [**15**]. At the same time, the peace dividend many countries had enjoyed after the end of the Cold War was canceled out by increased economic costs to include the costs of tighter border controls, increased public and private sector spending on security, and increased security measures for air and sea transportation [**16**].

1.4 Global Cooperation to Face a Global Threat

The global impact of the 9/11 attacks and widespread nuclear proliferation issue brought much attention to the potential far-reaching effects of a terrorist nuclear attack. The seriousness of the threat of nuclear terrorism brought many nations together in a spirit of cooperation. Even countries with serious disagreements on other matters, e.g. the U.S. and Russia, have extensive cooperation on matters of nuclear security [**17**].[2]

Two of the major initiatives include the 85 partner nations of the Global Initiative to Combat Nuclear Terrorism (GICNT) [**18**] and over 100 endorsee nations of the Proliferation Security Initiative (PSI) [**19**]. GICNT participants work through multilateral activities to strengthen global capacity to counter the threat of nuclear terrorism. The PSI members agree to take steps to counter the spread of WMD. When, how, and to what extent countries cooperate is not uniform among all members. Countries and groups of countries cooperate in ways tailored to meet their needs, capabilities, and relationships. Many other nonproliferation [**20**] and counterterrorism related organizations [**21**] exist with varied governmental, educational, and private participation.

---

[2] It should be noted that as of January 1, 2015 the Russian Federation no longer permits U.S. personnel to help protect their nuclear facilities but the two countries still work together on other matters of non-proliferation [**52**].

Each of these efforts requires time, manpower, and potentially significant resources. The United States alone budgeted $1.6 billion for nuclear non-proliferation programs, with $325 million (M) for the Global Threat Reduction Initiative, $393M for research and development, $271M for International Material Protection and Cooperation, $430M for Fissile Material Disposition, and $141M for Nonproliferation and International Security activities [**22**]. From 2002-2005, in the framework of the G8 Global Partnership, the European Union spent 311M € on improving nuclear installations, 98M € retraining scientists from nuclear installations, 40M € on nuclear submarine dismantlement, and tens of million more Euro on non-proliferation and nuclear security related projects in the Former Soviet Union [**23**]. For the years 2008-2013, the EU budgeted 72-79M € for instruments for Nuclear Security Cooperation to assist non-EU countries and from 2009-2012 33-46M € for nonproliferation of WMD activities [**24**]. The IAEA budget for 2015 is just over half a billion euros [**25**].

1.5 Scope and Scale of U.S. Border Security

The scope and scale of global border security issues is far too complex to describe in this thesis. The national and regional differences and commonalities of views on political, economic, social, and security matters and geographical, infrastructure, and transportation environments lead to a very complex situation.

A more reasonable task is to consider the scope and scale of the U.S. border security issue. Each year, the US imports trillions of dollars in foreign goods and services. In 2013, the United States imported $2,293B in goods [**26**]. Each day, more than 300,000 vehicles, 2,500 aircraft, 600 ships, and 57,000 containers cross US borders [**27**]. And on a typical day, the roughly 60,000 U.S. Customs and Border Protection (CBP) employees responsible for the country's borders screen for admittance nearly one million people, refuse admittance to about one thousand persons, identify over one-hundred people of suspected national security concern, discover 66 fraudulent documents, seize more than 10,000 pounds of drugs, confiscate over $250,000 in undeclared or illicit currency, and seize $3.5 million in products violating Intellectual Property Rights laws [**28**]. The manpower and resources necessary to complete these tasks greatly reduces the amount of effort the CBP can allocate to search for SNM.

Maintaining adequate focus on countering SNM smuggling requires vigilance on the part of CBP personnel. This task falls to the uniformed law enforcement arm of the CBP, the United States Border Patrol (BP), which maintains primary responsibility for "detection, apprehension, and/or deterrence of terrorists and terrorist weapons" [**29**]. BP's priority mission "is preventing terrorists and terrorists' weapons, including weapons of mass destruction, from entering the United States [**30**].

Smuggling of SNM is a low-probability, high-consequence event. This presents several unique challenges for CBP and BP personnel. First, the effort expended in detections can be significant and competes directly with other tasks such as the detection of persons of security concern, illicit drugs, currency, and illegal products. On a daily basis, these competing activities will appear to produce a visible return on investment, since these types of activities are interdicted on a daily basis while the chances of detecting SNM are very small.

While the large volume of traffic through established access points contributes to the difficulty of securing borders, the expanse of the US maritime and land borders makes securing them an impractical task. The US has over 7,000 miles of land, 12,000 miles of sea, and nearly 5,000 miles of freshwater borders [**31**]. As such, much of the effort to secure American borders focuses on official ports of entry (POEs) and border crossings. Securing such a large number of geographically dispersed points of entry requires a substantial effort. Figure 1 shows the locations of the more than 300 official POEs and 600 crossings into the United States. If one assumes that each border crossing were manned and secure up to one-half mile on either side, then roughly 2.5% of U.S. land, fresh water, and sea borders are secure.

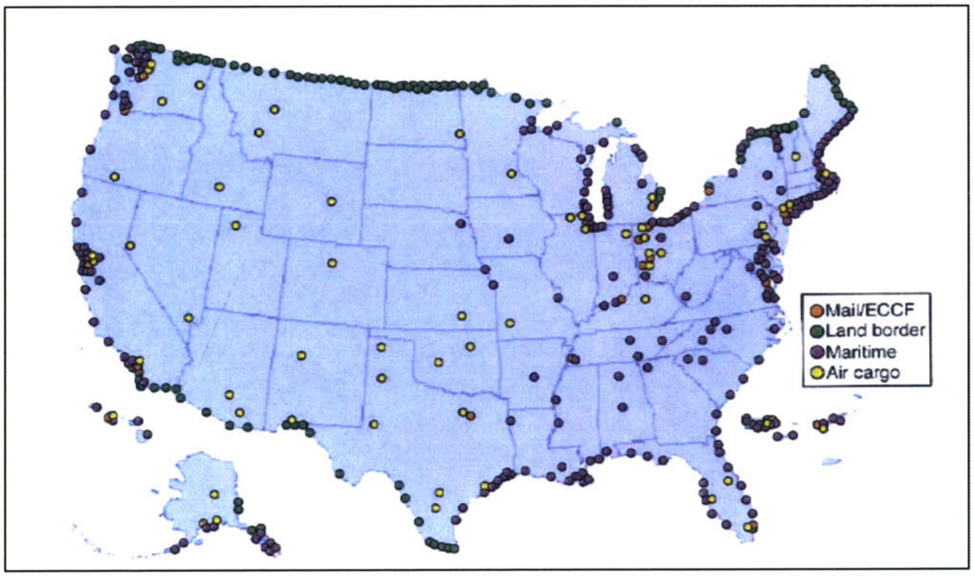

Figure 1. Locations of the more than 300 U.S. ports of entry (2002 data) [**27**]. The number and dispersion of the POEs, and vast expanse of the U.S. border, make securing the border a significant challenge.

1.6 The Holistic Effort to Secure the Border and the Nuclear Security Mission

An ideal screening process to allow the CBP to carry out its mandate would allow scanning of all cargo and personnel without impeding commerce, but no such process yet exists. To achieve the best possible practical solution, CBP employs a holistic approach to border security [**32**]. CBP works with domestic and foreign governments; private, public, national, multinational and international businesses; and participates in many national and international initiatives to increase the security surrounding the import of goods, services, and people into the United States and to help partners do the same [**33**], [**34**]. Through their collaborative efforts, the US and its partners seek to minimize the impact on commerce in balance with the need for security.

1.7 The Container Security Initiative

In response to the 9/11 terrorist attacks, the U.S. Customs Service created the Container Security Initiative (CSI) [**35**]. This program seeks to screen cargo before it is shipped to the U.S. The program is currently active at 59 ports in Africa, Asia, Europe, Latin and Central America, the Middle East, and North America. These operational posts lead to prescreen of 80% of maritime containers bound for the US. The CSI program has three core elements:

- ID high-risk containers through automated targeting, advance information, and strategic intelligence.
- Prescreen containers before they are shipped.
- Use technology for rapid prescreen of high-risk containers.

1.8 Border SNM Detection Systems

The current procedure at borders and ports to detect SNM is to conduct a rapid scan using radiation portal monitors (RPM) and, if required, to conduct a secondary screening to isolate and identify the source [27]. Typical fixed RPMs, with both gamma ray and neutron detection capabilities are located at traffic choke points. Mobile RPMs, such as truck mounted or towed systems, are frequently used at seaports, airports, rail yards, and for vehicle cargo operations to add capacity and increase unpredictability of where the scanning will occur.

1.9 Overview of Detectors used at POEs

Large volume polyvinyl toluene (PVT) plastic scintillator detectors are used for large-area portal monitors [27]. These detectors are used to detect gamma rays from tens of keV to 3 MeV, covering the range of interest for passive emissions from SNM and most industrial and medical sources. Further, these detectors are relatively low-cost and can be made quite large, thus potentially reducing the scan time required to detect a signal. However, an important drawback is that their signal to background ratio is very low due to a lack of energy resolution. Inorganic scintillators, such as NaI(Tl), are also frequently used. Other detectors, such as high purity germanium (HPGe) or cadmium zinc telluride (CZT), may also be used for gamma ray detection but are significantly more expensive. HPGe and CZT detectors' use is limited mainly to secondary screening with hand-held devices. In general, the PVT detectors are preferred because they are more rugged. A comparison of the advantages and disadvantages of NaI(Tl) and PVT based detection systems is seen in Table 1 [**36**].

Table 1. Comparison of NaI and PVT based detection systems. For purposes of the current work, NaI(Tl) detectors provide the best option due to a combination of resolution, efficiency, and cost.

Detector	Advantages	Disadvantages
NaI	• Spectral capability • Ability to change crystal geometry • Crystals come in large sizes • High intrinsic efficiency • Inexpensive (~ $5k for 2x4x16") [**37**]	• Sensitive to shock • Hygroscopic • Fair resolution (22.6 keV @ 300 keV, 30 keV @ 1332 keV) [**37**]
HPGe	• Spectral capability • Excellent resolution (0.86 keV @ 300 keV, 1.60 keV @ 1332 keV)	• Must be cooled • Expensive • Low geometric efficiency • Low intrinsic efficiency
PVT	• Lightweight • Ability to create large, flat geometry • Rugged and resistant • Inexpensive (~$2.5k for 2x4x16")	• No incident energy resolution • Lower intrinsic efficiency

The use of neutron signatures and neutron detectors is not considered in this thesis. However, basic information on the use of neutron detectors at POEs is provided in Appendix A.

1.10 Detector Applicability to the Proposed Method

For the proposed system, the required detector properties are low-cost, high-intrinsic efficiency, geometric efficiency, and an ability to discriminate between high energy gammas between 1 and 20 MeV. Figure 2 shows a comparison of the spectra for a plastic scintillator, HPGe, NaI, and CZT detectors. It is readily apparent that the plastic scintillator has no energy resolution and is therefore not useful for the proposed scanning method. The CZT has very poor efficiency and is also not practical for the proposed scanning method. The HPGe has significantly better energy resolution than in the NaI(Tl) spectra but the ^{208}Tl and ^{40}K peaks are still visible in the NaI(Tl) detector. For the proposed scanning method, which uses gamma rays that are separated by over 10 MeV, energy resolution is not an issue. Further, the HPGe detectors cannot be made as large as the NaI detectors so they have significantly lower geometric efficiency. Additionally, HPGe has lower intrinsic efficiency as compared to NaI. This is largely due to the much lower Z of Ge (32) than that of I (53). Finally, the NaI(Tl) detectors cost an order of magnitude less than the HPGe detectors. Therefore, the practical choice for the proposed method is the 2"x4"x16" NaI(Tl) detector.

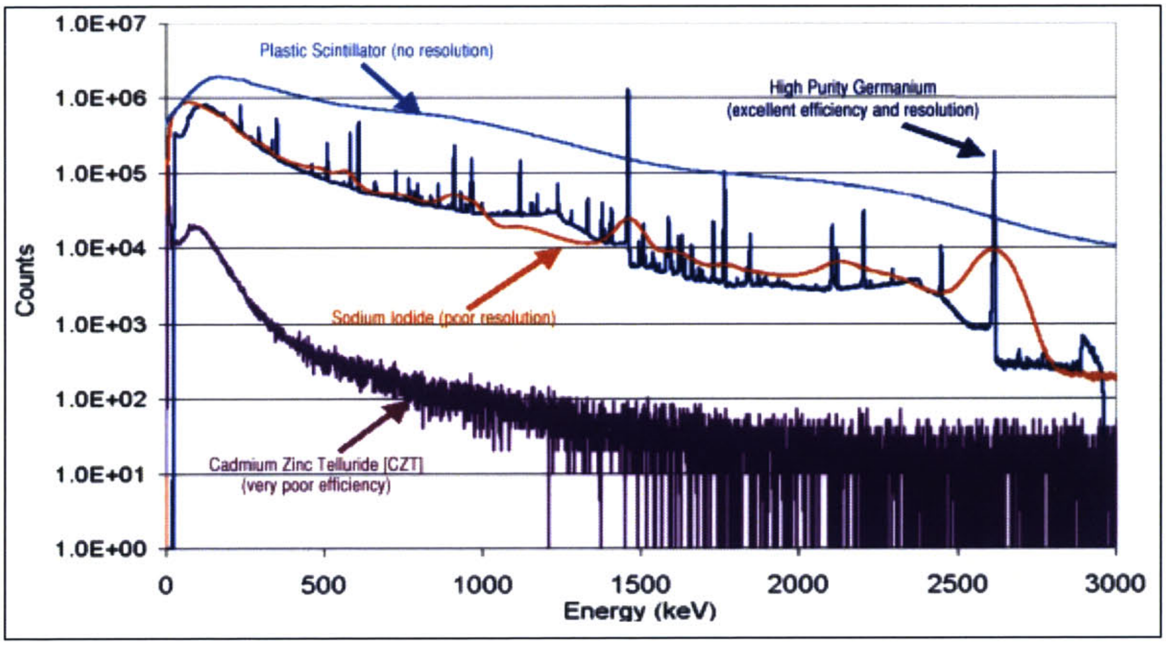

Figure 2. Comparison of Gamma Spectra of Natural Background for Plastic scintillator, NaI(Tl), HPGE, and CZT **[38]**. Plastic scintillators lack the resolution and CZT has inadequate efficiency for this application. HPGe has lower geometric efficiency and better resolution than NaI(Tl). However, the greater resolution is not important to the current application. NaI(Tl) is less expensive, has better geometric efficiency, and its higher Z (I = 53 vs Ge = 32) makes it better for higher energy gamma detection.

1.11 Characterization of Cargo passing through U.S. Ports

This thesis does not attempt to address securing all borders but focuses on increasing the ability to screen the containerized cargo passing through the POEs.[3] While it is physically possible to screen every container, such an operation would severely impede the flow of commerce. The manpower and resources would be cost prohibitive. For purposes of this research, which is focused on identifying the presence of high-Z materials in cargo, a successful system would be one that can scan containers with minimal to no impact on cargo throughput and without adverse effects on the cargo itself. Development of such a system requires, among other things, an understanding of the composition and disposition of the cargo.

Lawrence Livermore National Laboratory (LLNL) conducted an analysis of cargo imported through North American ports on 14 days over a year period that provides insights into the composition of typical cargo passing through US ports [**39**]. Their data included nearly half a million cargo manifests for shipments originating in 325 different ports and passing through 44 US import ports. The tabulated percentages by classification of the imported goods are shown in Table 2. Their research indicated toys and furniture, base metals, plastic, base metal articles, and plastic and rubber as the most common categories of materials. They estimated 60% of US imports are plastics or organics, 28% are metal based, and 12% are stone, ceramics, minerals or other products. They also noted general merchandise, including household goods and miscellaneous cargo, accounted for 3% of the cargo.

---

[3] One reason to focus on clearance of cargo containers is 90% of world trade is transported via the international shipping industry, which uses cargo containers extensively [**54**].

Table 2. Typical distribution of goods passing through US ports based on data from 14 days randomly taken during one year **[**39**]**. Goods are classified by category and ranked by percentage of Twenty Foot Equivalent Units (TEU). The TEU is a standard unit of measurement equivalent to the volume of one standard 20' cargo container. The first three categories account for over 46% of US imports.

Category	[%] TEU
Furniture, Toys, Miscellaneous Manufacturing Articles	20.18
Machinery & mechanical appliances	15.48
Textiles & textiles articles	10.75
Base metals & articles thereof	7.11
Plastic and rubber	7.00
Prepared foodstuffs	5.29
Transportation equipment	5.04
Articles of stone, plaster, cement, asbestos	4.00
Footwear, headgear	3.98
Wood & Wood products	3.64
Chemical products	3.12
General merchandise	3.09
Vegetable Products	2.66
Wood pulp products	2.47
Hides and skins	2.24
Animals & animal products	1.60
Instruments measuring-musical	1.41
Mineral products	0.63
Animal or vegetable fats	0.15
Works of art	0.07
Pearls, precious & semi-precious stones, metals	0.05
Arms & ammunition	0.03

To perform the most accurate possible assessment of what cargo can and cannot be scanned, thereby determining the fraction of cargo that can be cleared with the proposed scanning system, requires knowledge of the distribution and densities of the cargo and the maximum areal density the scanning method can effectively clear. While the maximum areal density that can be scanned can be experimentally determined, the areal densities of the cargo are unknown. Currently, the best possible data includes only average density. Thus, if using a side view scanning system, the average areal density is then the product of the average density of the cargo and the 235 cm interior width of the typical cargo container.[4]

LLNL's research also considered the average densities of the shipments. They estimated the cargo density as the weight of the cargo container divided by the volume of the container. Within the data they found certain peaks in average cargo density related to the types of materials in the cargo, as seen in Figure 3.

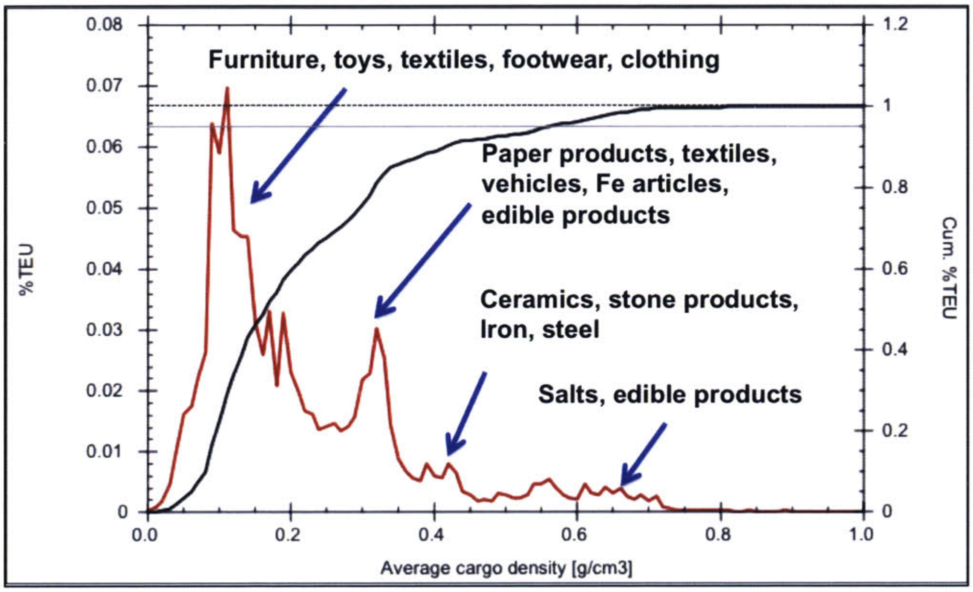

Figure 3. An average cargo density histogram shows different cargo categories account for different peaks. The peak at ~0.1 g/cm^3 is from furniture and toys, textiles, footwear and clothing. From 0.2-0.4 g/cm^3 is largely due to paper products, textiles, vehicles, iron articles, and edible products. The peak around 0.4 g/cm^3 is from ceramics, stone products, iron, and steel, while the peak around 0.6 g/cm^3 is from salts and edible products. Only a small fraction of commodities, mainly ceramics and stone products, have densities greater than 1 g/cm^3. Note the dashed line represents the level where the cumulative fraction of TEUs equals 1. The gray line at 0.95 indicates where 95% of all TEUs are accounted for. Dropping a vertical line from the intersection of the 0.95 TEU fraction line to the average cargo density indicates that 95% of all TEUs have an average density of 0.6 g/cm^3 or less.

---

[4] It should be noted that, if a scanning system is designed to scan from the top of the cargo, the average areal density is then the product of the average density of the cargo and the 239 cm interior height of the typical cargo container.

It is important to note that average cargo densities and actual areal densities seen scanning across the container are only somewhat related. Lower density products, which are transported in bulk, do not approach the load limits of the containers so they are likely to be distributed rather uniformly. High-density materials, for which bulk shipments approach load capacities, are more likely to be located in the center and lower portions of the container.

Runkle and others developed a histogram based on the LLNL data relating the average areal density of cargo containers and the frequency with which they are encountered as seen in Figure 4 [**40**]. It is important to note that these areal densities assume complete and uniform filling of the containers. Thus, the utility of this histogram is somewhat limited since it provides only average areal densities and not the actual maximum areal density for the cargo in each container. For example, a container of textiles may be nearly full and the average areal density would be a reasonable measure of true areal density. However, a container with marble or stone that is near the maximum allowable load is unlikely to be loaded uniformly. It could be expected the material in this container would be located more toward the bottom and closer to the center of the container. Thus, the areal density of the top and ends of the container would be significantly different from that of the center. If the marble slabs are two-meter long sheets inside the 2.35 m wide container, at a density of $2.6\,\frac{g}{cm^3}$, the areal density across the slab would be $520\,\frac{g}{cm^2}$.

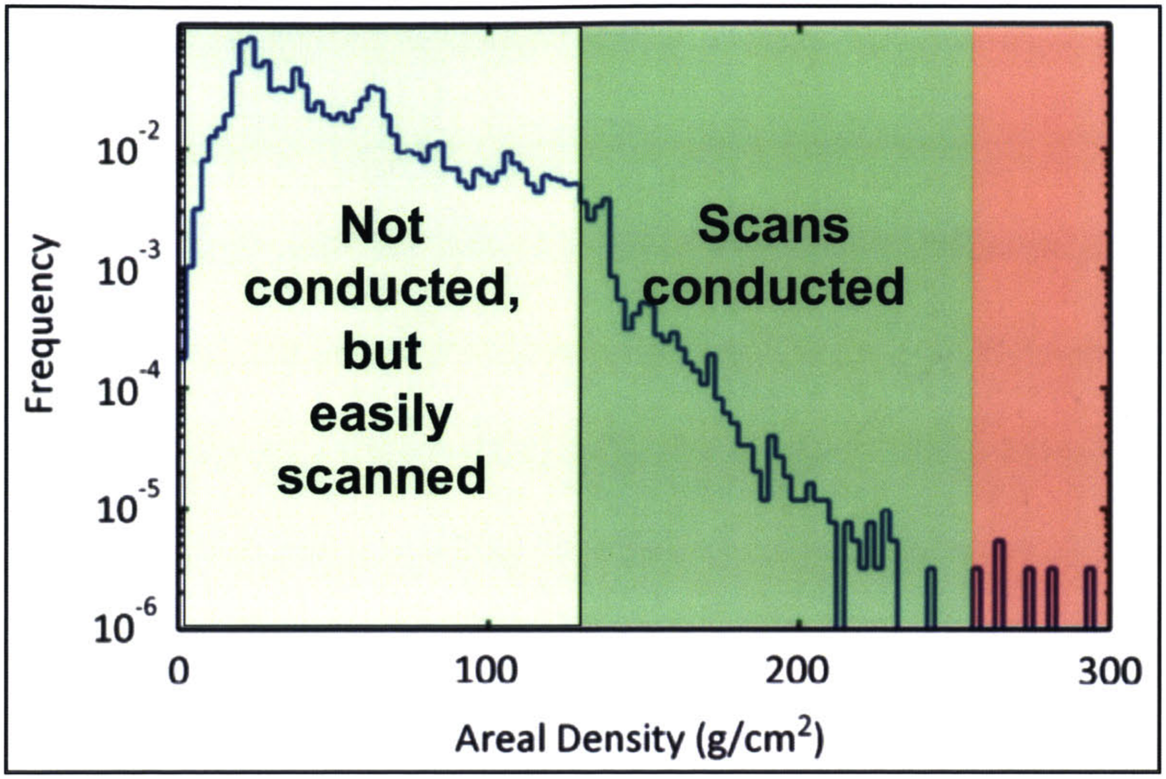

Figure 4. Histogram of areal density of cargo containers derived from cargo masses assuming complete and uniform filling of the cargo container [40]. Note these are derived based on the average density of the container (load divided by the volume) and the width of the container. The actual areal density across the container at any point depends on the cargo distribution and load plan. The shaded area from 120-255 g/cm^2 represents the areal densities considered in this thesis. Areal densities below 120 g/cm^2 are easily scanned but not experimentally validated. Areal densities above 255 g/cm^2 were not experimentally validated in this thesis because low count rates,[5] large backgrounds, and large statistical uncertainty made these measurements impractical with the current system configuration.

The LLNL report also indicates that potential sources of interference[6], while common, only account for a small fraction of the cargo containers. Potential sources of interference with the proposed scanning method, cargo of interest and their TEU percentage, and the frequency within which these cargos may appear are found in

---

[5] Reconfiguration of the shielding plan could be conducted to allow increased current and therefore increased count rates. The present current limitations were a result of the need to maintain dose rates below a proscribed limit.

[6] Sources of interference are naturally occurring and industrial radioactive materials or those items that would interfere with determination of the presence of SNM.

Table 3. It should be noted that the radioactive sources and fuel cycle related materials originated from the EU or Russia so it is probable that this cargo will be properly checked and labeled prior to shipment to the U.S. and will therefore be readily identifiable. The report identifies miscellaneous cargo as a category because the cargo is not clearly identified and may contain many different types of materials.

The Pb and W ores and products may be very difficult, if not impossible, to properly scan because of their potentially large areal densities, however these are a very small fraction of the total TEUs. The rock / salt, cut stones, and ceramics are of interest because they cumulatively account for 3.38% of TEUs and, depending on cargo loading and distribution, may be difficult to properly scan.

Table 3. Potential sources of interference and cargo of interest **[**39**]**. The selected products may be difficult to image (e.g. rock/salt, cut stones, Pb/W ores, etc.) or contain radioactive materials (e.g. U metal, UF6, radiation sources, etc.) and account for approximately 6% of TEUs. The rock/salt, cut stones, and ceramics are all dense materials that make up 3.38 % of total TEUs. The Pb and W ores and articles only account for a small portion of TEUs but may be difficult, if not impossible, to properly scan. The radioactive and fuel cycle related materials originate in the EU and Russia and are therefore likely to be annotated properly and these shipments can be readily identified. Determining the difficulty of scanning the miscellaneous category is problematic because little to no information is provided about the cargo on the manifests.

Product	TEU [%]	# days / year
Rock / Salt	0.49	364
Cut Stones	0.58	364
Ceramics	2.31	364
U metal	1.24e-6	26
UF6	2.80e-5	130
U	6.02e-6	26
Rad Sources	3.30e-6	52
Pb ores / articles	3.0e-3	26
W ores	2.4e-3	312
W articles	7.0e-4	52
Miscellaneous	2.43	364

Some additional key findings from the LLNL research important to this work [**39**]:

- Difference in payload between 20' and 40' containers. 40' containers are more frequently used to ship low-density products while 20' containers are used more frequently for more dense commodities. Typical 20' and 40' payloads are 21 and 27 metric tons, respectively.
- 94% of TEU traffic is handled by 12 U.S. ports, with Los Angeles and Long Beach accounting for 47% of the total U.S. imports.
- Roughly 60% of U.S. imports are organics[7], 28% are metal based, and 12% are made of stone, ceramics, or are classified as other.
- 40' cargo containers account for the majority of overall containers and are predominantly loaded with toys, furniture, and textiles.
- The mean cargo density is just below 0.2 $\frac{g}{cm^3}$, which is roughly one-third of the theoretical cargo density reference limit of 0.65 $\frac{g}{cm^3}$.[8] (From Figure 3, roughly 97% of all TEUs have an average volumetric density below this level so approximately 3% of containers are loaded in excess of rated capacity.)

While this information and the previous cargo density descriptors are not the ideal metric, they do allow determination of some valuable insights. For instance, it is likely that a large portion of containers, particularly those with lower density materials like textiles, will be stacked to maximum capacity and the average density will be close to the actual areal density. These materials account for a large fraction of overall cargo and are easily scanned. It is also reasonable to assume that a small fraction of containers, such as those with heavy ores or stone, may present scanning challenges. The determination as to whether or not other containers falling between these two extremes can be effectively scanned depends on the materials, cargo configuration, and the limits of the scanning system.

It should be noted that cargo is normally loaded with heavier material at the bottom and lighter materials stacked on top. Therefore, if cargoes contain heavy

---

[7] Organics here is defined as those materials consisting mostly of C, H, O, and N.

[8] This density is the maximum theoretical cargo density that is calculated by dividing the 21.6 metric ton maximum load for a 20' container by the volume of a 20' container.

materials, this would lead to higher average areal densities across the bottom of the container than near the top of the container. Thus, if one considers a top-down view of the cargo container, unless the materials are completely uniform and loaded from floor to ceiling, the areal density for a vertical slice of the material will be lower than the areal density of a side view of the container. Thus, a scanning system looking down through the cargo may be more effective than a scanning system looking horizontally through the cargo. Furthermore, the average volumetric density shown in Figure 3 and the average areal density shown in Figure 4 likely provide a more accurate description of the cargo encountered by a top-down scanning system than a horizontal scanning system.

Absent additional information about the cargo and without full knowledge of the actual areal densities the proposed system can effectively scan, it is not yet possible to determine exactly what percentage of cargo containers can be cleared. As a reasonable estimate, if we assume a mean density of $1.0 \frac{g}{cm^3}$, which is more than five times the mean cargo density value, and we conservatively assume the cargo fills the entire 235 cm of the container width, this equates to an areal density of 235 $\frac{g}{cm^2}$. This areal density accounts for over 99.99% of the average areal densities from Figure 4. Therefore, this study considers scanning of materials up to an areal density of $250 \frac{g}{cm^2}$.

1.12 The Weapons Signature Problem

One of the most significant challenges of detecting SNM, and particularly highly enriched uranium, is the difficulty associated with detecting radiation signatures from shielded material. The most useful passive signatures of SNM are neutrons and gamma rays. However, due to their low abundance or the ease with which they can be shielded and complications from background, the detection problem is not easy. The signatures of hypothetical U and Pu based weapons with W or depleted U (DU) tampers and the difficulties associated with detection of a nuclear weapon in general are further discussed in Appendix B. In comparing potential weapon signatures, a U based weapon with W tamper is the most difficult to passively detect because it provides the least favorable signature. Therefore, any detection mechanism must be able to detect this type of shielded weapon.

Since deliberately or incidentally shielded SNM may have a very low signature, detection may require eliciting an induced response from the SNM or using the impact of SNM on an incident radiation to detect its presence. Using heavy charged particles as a means to elicit a response is not useful because of their short range in matter. Use of low energy gamma rays is of limited utility because they are easily shielded and there is an abundance of low-energy background gammas in the natural environment. Two promising means of detection are using gammas and neutrons to induce fission or using attenuation of gamma lines to detect the presence of high-Z materials. This thesis focuses on use of differential attenuation of gammas at different energies to detect the presence of high-Z material. The proposed method seeks to make detection of such a weapon possible by detecting the presence of high-Z material ($Z \geq 74$). This method would also apply to detection of Pu-based weapons.

1.13 The Problem Defined

As previously discussed, nuclear proliferation is a real issue and the threat of a nuclear attack anywhere in the world is a global game changer. Countries throughout the world are cooperating to counter the nuclear terror threat. One of the most significant challenges is the pure scope and scale of the border security issue and the fact that 90% of international trade travels via maritime vessels. The sheer volume of cargo makes detailed inspection nearly impossible and certainly impractical.

The CBP spearheads the effort to keep borders secure and the BP maintains primary responsibility for preventing a nuclear weapon from entering the U.S. The CSI program, in its current form, prescreens (in one form or another) 80% of the cargo at foreign ports before it embarks for the U.S. At the U.S. borders and ports fixed and mobile RPMs are used to passively search for radioactive sources and weapons. The RPMs mainly use plastic scintillators and NaI(Tl) detectors to look for gamma signatures. At this point, the cargo passing through ports is not defined well enough to determine what can and cannot be scanned with the proposed method. However, enough information is known about the physics (to be discussed in Chapter 3) and the cargo to determine that NaI(Tl) detectors will work for the proposed method.

This thesis will show that, based on the previously mentioned assumptions about the characteristics of the cargo passing through POEs and the LANL data, the proposed scanning method is very likely capable of clearing a majority of the maritime cargo.

CHAPTER 2
A SNAPSHOT OF SNM DETECTION EFFORTS

The current chapter provides a brief overview of SNM detection efforts, including descriptions of both passive and active detection efforts. This chapter provides an introduction to the two basic approaches to detection of SNM. It also explains the basic principles of passive detection, discusses current detection systems deployed at POEs, and the limitations of passive detection. The basic principles of active detection are discussed and an example of why active detection systems are needed to overcome the limitations of passive detection systems is also provided.

2.1 Two Basic Detection Approaches

The two basic approaches to identifying the presence of special nuclear material are passive and active interrogation. There are numerous detection techniques associated with each method [**40**]. Passive interrogation involves reading the signatures—which may include charged or neutral massive particles and massless particles—naturally emanating from materials. Active interrogation involves probing the material with particle beams and subsequently looking at the natural and induced signatures radiating from the material. The proposed scanning method is a type of transmission radiography and is an active interrogation technique. The scanning method uses particles to probe the materials but instead of looking for induced radiation signatures from the material it looks for gammas transmitted through the cargo. Consideration of a single gamma line from the scanning system provides a densitometry image similar to what may be created with an x-ray imaging system.[9,10]

2.2 Basic Principles of Passive Detection

Passive detection relies on detection of nearly unique signatures from nuclear material. The gamma and neutron signatures emanate from the nuclear material, are altered by the surrounding environment, and are then registered by a detector. The gammas and neutrons are emitted in all directions so their signature falls off at one over the square of the distance, $\frac{1}{r^2}$. Detection is made more difficult by further signature reduction by the material between the source and the detector. Even if a source is above background near the source, at some distance away from the source the additional signature is not detectable above background. As will be shown later in this section, the signals from SNM (particularly shielded U) are weak and make passive detection of SNM at a distance extremely difficult.

2.3 Systems Currently Deployed at POEs[11]

The U.S. Customs and Border Protection agency describes six major inspection technologies currently deployed at US POEs [**41**]:

- Radiation Portal Monitors (RPM). Large passive systems used to detect signatures emanating from cargo. Currently over 1,000 RPMs

---

[9] For purposes of this paper, scanning methods are considered an active interrogation method.

[10] Rebuffel and Dinten provide an overview of x-ray imaging in the article Dual-Energy X-ray Imaging: Benefits and Limits [**81**].

[11] Kouzes provides an excellent overview of the history of the radiation portal monitor project, the CBP's approach to radiation interdiction, and an overview of passive and active cargo interrogation techniques [**24**].

are deployed in the field. Manufacturers of such systems include Ludlum [**42**], Rapiscan Systems [**43**], and Presidio Systems, Incorporated [**44**].

- Personal Radiation Detectors (PRD). Small passive devices worn by CBP personnel at POEs. Currently over 16,200 in the CBP inventory. Examples of PRDs can be found at [**45**].
- Radiation Isotope Identifiers (RIID). Small, passive handheld instruments with an ability to detect and characterize gamma emission and detect neutron emissions. CBP has over 1,200 handheld systems.
- Large-Scale Gamma-ray/X-ray Imaging Systems. Produce transmission and detection images of cargo in containers and vehicles. Over 200 systems are currently fielded.
- Explosives and narcotics detection systems. Require physical contact with material to obtain wipe samples.
- Portable Contraband Detector 'Buster'. Uses low intensity gamma radiation and a scintillation detector to locate density anomalies [**46**].

Of the six major inspection technologies deployed, the proposed scanning method would only serve as a replacement or complement to the RPMs and large-scale gamma-ray/X-ray imaging systems. The proposed scanning technique would not depend on the gamma and neutron signatures originating from radioactive material in the cargo but, if run without the mono-energetic gamma lines, could serve as a passive detector. It should be noted that when the system is operating, the gamma lines originating from a radioactive source in the cargo would only be visible in the spectra if the gamma fluxes reaching the detector from the source are close to or above the gamma strength of the attenuated monoenergetic beams. The attenuation of the lower energy mono-energetic gamma line from the proposed method would provide similar information to the large-scale gamma-ray/X-ray scanning system. However, the use of both gamma lines provides additional information about the potential composition of the material and will be discussed in subsequent chapters. The PRDs, RIIDs, explosives and narcotics detection systems, and 'Buster' detector would continue to serve their current purposes.

2.4 Limitations of Passive Systems[12]

Some of the most important limitations of passive detection include:

- Signals are usually weak.
- Time requirements to acquire sufficient counts.
- Signals fall off as $1/r^2$.
- Background interferences and/or changing backgrounds.
- Deliberate shielding and other materials attenuate or change the signal.

The combination of these factors makes it extremely difficult to detect SNM, especially shielded WGU with its very weak signal, at a distance. The difficulty of detecting SNM at a distance will be discussed through an example detection problem later in this chapter.

The single greatest limitation of passive detection systems is that they depend on the signature of the material in the presence of background radiation. The signal to noise ratio (SNR) serves as a measure of the sensitivity of a system to detect radiation. It can be thought of as the ratio of the signal to the standard deviation of the signal plus any background present. There are three general cases: (1) there is no background, (2) background is known and well characterized, and (3) background is unknown and variable.

---

[12] It should be noted that several techniques have been applied to passive detection systems that make them more effective such as directional sensitivity based on multiple events [**65**], neutron scattering cameras [**66**], and directional detection [**67**]. However, the low neutron signatures make these methods impractical for shielded U detection in a reasonable amount of time.

For the first possibility, if there is no background, the signal to noise ratio is $SNR = n_s/\sigma_s = \sqrt{n_s}$, where n_s is the number of counts and σ_s is the standard deviation of the number of counts and is equal to $\sqrt{n_s}$. Therefore, absent background, the ability to detect a source is purely limited by statistics. This is the SNR case where a gamma is produced and there are no other gammas that can interfere with the signal.

For the second possibility, the case where there is a known and measureable background, $SNR = \frac{(n_s+n_b)-n_b}{\sqrt{\sigma^2_{n_s+n_b}+\sigma^2_{n_b}}} = \frac{n_s}{\sqrt{n_s+2n_b}}$, where n_b is the number of background counts and σ_b is the standard deviation. This condition, where background is well characterized, allows setting a certain SNR as an alarm level. This can be set as any signal above a certain SNR, which assumes the second SNR method is the most accurate descriptor. Unfortunately, this can lead to false negatives and false positives. A false negative would be when a radioactive source passes through without alarming the system. A false positive is identification of a potential radioactive source when one is not present.

The third possibility is for an unknown and variable background, $SNR = n_s/n_b$. This is the case for mobile detection operations. It is also the case for static detection operations when the incident material not actively being scanned also emits radiation or if the local background changes due to weather or industrial / medical isotope use.

It is clear there is background radiation present at ports so the first SNR measure is not applicable at least at the energies of significant gamma emissions from SNM. The reality, since there is substantial cargo present, which contains many tons of various materials which contribute to the changing background, and there is a relatively fixed background from the environment where the detector is located, the true characterization falls somewhere between a known and fixed background and an unknown and variable background.

It should be noted that future improvements to radiation detectors could result in better passive detection results. Cited areas for improvement include [27]:

- Improvement of energy resolution.
- Increased efficiency, especially for gammas.
- Increased ruggedness and reliability.
- Decreasing prices to make fielding of large systems more cost effective.
- More intelligent scanning systems to reduce false alarms.

It should be noted that first four improvements would also increase the effectiveness of active detection systems.

2.5 Basic Principles of Active Detection[13]

Unlike passive techniques, active interrogation involves probing the material with particle beams and subsequently looking at the induced signatures radiating from the material or the transmitted signature. The major methods use neutrons, gammas or X-rays as source particles. Neutrons are frequently created by nuclear reactions or spallation, gammas are created by nuclear reactions or nuclear interactions, and X-rays from bremsstrahlung from acceleration of electrons into a high-Z conversion target. If induced interactions or reactions are observed, that

---

[13] Runkle provides an excellent overview of active interrogation of special nuclear material [27].

characteristic signatures of those interactions or reactions are measured. If neutrons are the observed particles they may be prompt or delayed.[14] If the transmitted signature is observed the original particles that pass through the material are measured.

2.6 Why Active Detection Systems are needed to overcome the limitations of Passive Detection Systems

An easy means of showing why active detection systems are needed to detect SNM, and specifically shielded WGU, is to provide an example of detection of a possible nuclear device. As an example consider the use of a passive detection system to identify the presence of a 12 kg WGU weapon with a 3 cm W tamper weapon hidden in cargo. The radius of the device is 8.33 cm.[15] From Table 19 in Appendix B the gamma activity at 1.001 MeV is 30/s and the neutron activity is 30/s at the device surface. Therefore the neutron and gamma fluxes at the surface are $\frac{30\ particles/s}{4\pi(8.33\ cm)^2} = 0.034\ \frac{particles}{cm^2 \cdot s}$. If left unshielded at the center of a standard shipping container[16] and attenuation and interactions are not considered, the respective fluxes are reduced to $1.73 \cdot 10^{-4}\ \frac{particles}{cm^2 \cdot s}$ at the container surface. These fluxes are small compared to typical background count rates and could not be easily detected using a passive interrogation system. Figure 5 shows a typical background spectrum. A

---

[14] Note there are many other possible detection scenarios that can be involved, e.g. looking at angular response or for specific gamma lines, but these techniques are not considered as they are not applicable to the current thesis.

[15] Calculated from 12000 g = 18.95 $\frac{g}{cm^3} \cdot \frac{4}{3}\pi \cdot r^3$, where r is the radius of the U sphere. An additional 3 cm is added to r to account for the W tamper.

[16] A standard shipping container has an inside width of 235 cm. Half this distance is 117.5 cm.

gamma flux of $1.73 \cdot 10^{-4} \frac{\gamma}{cm^2 \cdot s}$ on a 4" NaI(Tl) detector, with a 50% peak efficiency taken for one hour, would yield an expected count of 32 gammas compared to a background of 650 counts. This would yield a SNR of 0.87 using the case of a known background. For a 1 minutes scan, the SNR would only be 0.11. According to NCRP Report No. 94, the typical flux of neutrons at sea level is $0.00646 \frac{n}{cm^2 \cdot s}$ **[47]**. This typical neutron flux is 37 times larger than the neutron flux from the ^{235}U device. Thus, the limited neutron and gamma signatures from the ^{235}U-based weapon with a W tamper would not produce a statistically significant change in the count rate.

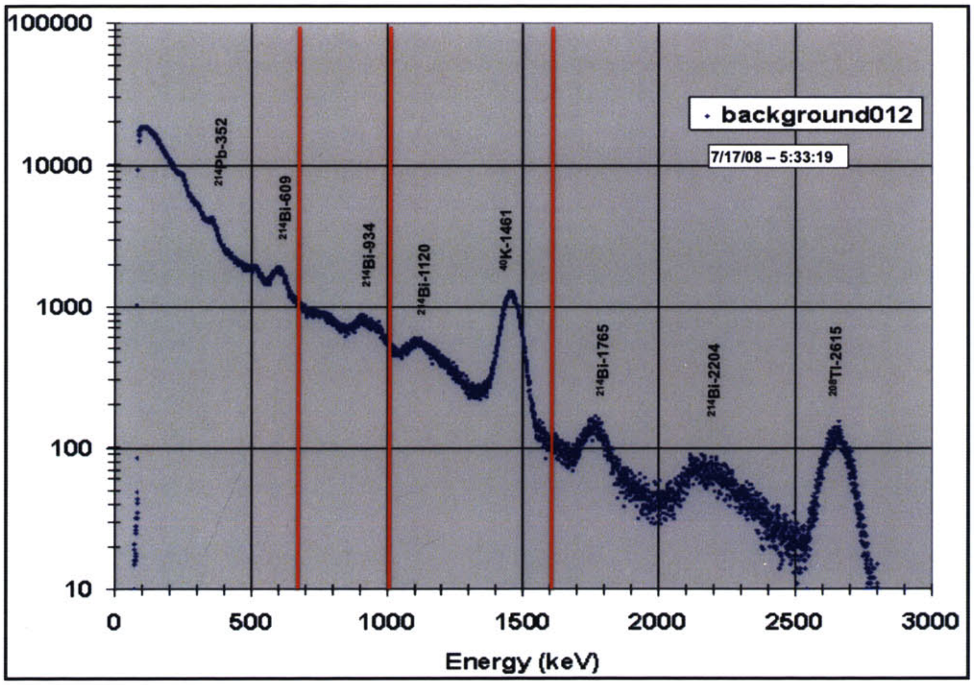

Figure 5. Background spectrum taken with a 4" cube NaI(Tl) detector in Sudbury, MA for 1 hour. Note the lack of background gammas above the ^{208}Tl peak at 2.6 MeV means gamma interactions that deposit energy above this energy are not convoluted by background. However, the 1.001 MeV gammas originating from ^{234M}Pa (a decay product of ^{238}U) and 0.662 MeV gammas from ^{241}Am (a decay product of ^{241}Pu) are located in the vicinity of peaks in the natural background. The origin of the 1.6 MeV line is from neutron-induced gammas in W (neutrons originating mainly from ^{240}Pu).

The example above demonstrates the need for active interrogation systems to detect the presence of SNM in cargo. The passive signature is below practical detection limits. Active interrogation or the proposed scanning technique will have a much better chance of detecting the SNM because detection does not depend on the weak signal of the device. The type of system used would determine its ability to detect the weapon. In the simplified case presented, even simple X-ray radiography would show a suspect object in the container. However, if the scenario is changed somewhat, to include incidental material of high density between the weapon and the sides of the container and spread throughout the container, detection becomes more difficult. An X-ray radiographic image will show the presence of dense material and the outline of the suspect object but if the device is placed in substantial dense material the outline of the device may not be readily apparent.

This thesis will demonstrate that the proposed scanning technique will easily detect the 10.66 cm (4.2") diameter sphere of WGU. The remainder of this thesis will explain the physics behind the proposed technique, how the method is employed and why it works, methodology of the experiments conducted, report "proof of principle" findings for use of monoenergetic gammas to detect the presence of SNM, and will provide recommendations for future work on the proposed scanning system.

CHAPTER 3
THE UNDERLYING PHYSICS OF MULTIPLE MONOENERGETIC GAMMA IMAGING

This chapter presents the underlying physics important to the multiple-monoenergetic gamma line imaging method and defines critical concepts key to characterization of cargo. A discussion of the production of the mono-energetic gamma lines used in this thesis is provided, as well as a discussion of the materials considered in this thesis and their mass attenuation coefficients. Means of estimation of areal density, to include estimation of the areal density[17] of a cargo using 4.44 and 15.11 MeV gamma lines is discussed. The use of attenuation of both gamma lines to distinguish between materials is addressed. The energy and atomic number dependence of gamma interaction processes and the relative importance of these processes for each material used in this research are also discussed. The behavior of the mass coefficients for all elements is considered, to include their use in defining materials as ratio enhancers or ratio reducers and the classification of materials as low-, medium-, and high-Z. Finally, the range of effective mass attenuation coefficients for a cargo and how the range of effective mass attenuation coefficients for an effective atomic number limits the range of possible ratios of 15.11 to 4.44 MeV gammas is also discussed. These discussions provide the physics foundation for the experimental setup discussed in the subsequent chapter.

---

[17] The areal density of a material, measured in [g/cm^2], is equal to the density of the material ([g/cm^3]), times the thickness of the material in cm.

3.1 Gamma lines and their production

Photons appearing in gamma spectra can originate from changes in the structure of the nucleus, annihilation events, light charged particle bremsstrahlung, x-rays from atomic de-excitation, or as the residual gamma from a Compton event. The gammas used for cargo interrogation in this experiment originate from de-excitation of an excited nuclear state. The energy of the emitted gamma is equal to the difference between the energy levels of the initial and final nuclear states, less a negligible nuclear recoil. In this particular experiment, a radio-frequency quadrupole (RFQ) accelerator (Appendix D) is used to bombard an elemental boron (B) target with 3.0 MeV deuterons to produce a variety of monoenergetic gammas. The primary interaction of interest in this experiment, $^{11}B(d,n\gamma)^{12}C^*$, produces gammas at 4.44, 10.67, 12.71, and 15.11 MeV. For purposes of this thesis, only the 4.44 and 15.11 MeV gamma lines were used. A discussion of why only these two gamma lines were used in this thesis is found in the subsequent chapter.

It should be noted that additional gamma lines are also produced in the B target. For example, it was observed that the $^{11}B(d,p\gamma)^{12}B^*$ reaction produces 0.953 and 1.674 MeV gammas which were present in the histogram. It is also known that $^{11}B(n,g)^{12}B$ interactions are also possible. However, during this thesis no attempt was made to characterize or quantify gamma yields from these other interactions.

3.2 Materials and their mass attenuation coefficients

For this experiment a broad range of materials were used as simulated cargo: Al (Z=13), Fe (26), Cu (29), Mo (42), Sn (50), W (74), Pb (82) and U (92). For purposes of this thesis, Al, Fe, and Cu are classified as low-Z, Mo and Sn as medium-Z, and W, Pb, and U as high-Z materials.[18] Figure 6 shows the mass attenuation coefficients for these materials as a function of gamma energy. The energies of the monoenergetic gamma lines used in this thesis research are denoted as vertical black lines. The relative strengths of the mass attenuation coefficients for each material at the monoenergetic energies and how the ratios of these coefficients differ for each of the materials provide the physical basis behind the proposed method of scanning cargo.

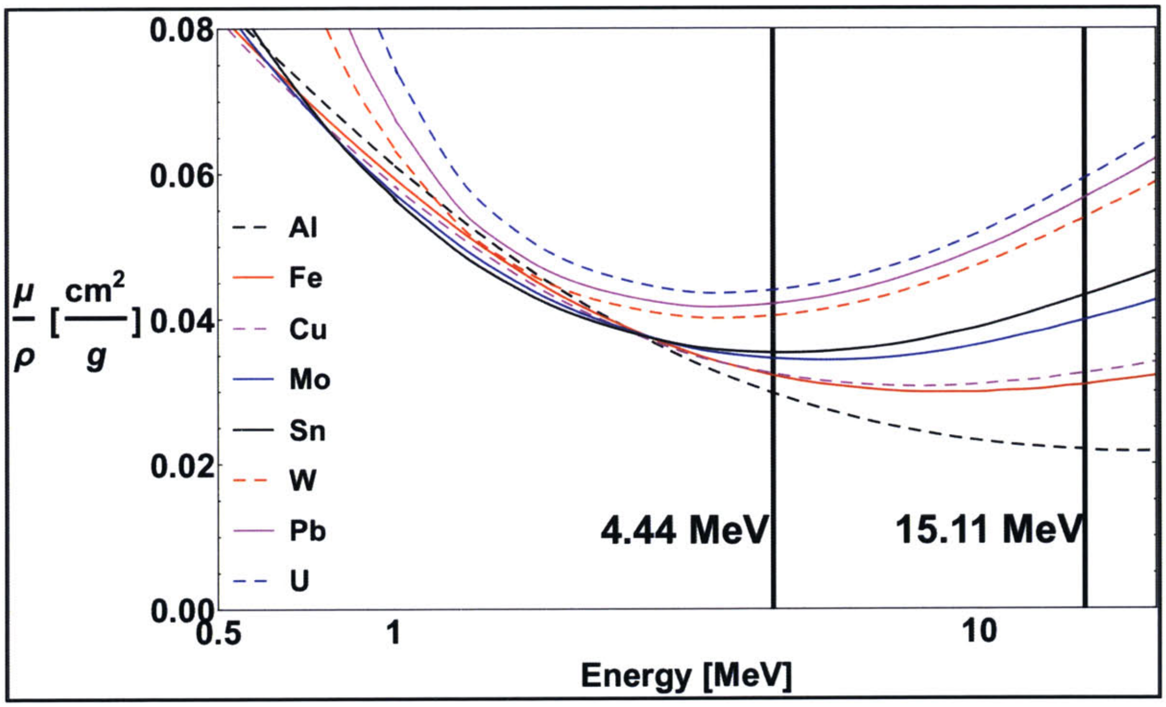

Figure 6. Mass attenuation coefficients versus gamma energy for the materials considered in this thesis. Derived from data taken from the NIST database **[48]**. The energies of the 4.44 and 15.11 MeV monoenergetic gamma lines used in this thesis are shown as vertical lines. Note the mass attenuation coefficients at 15.11 MeV are larger than at 4.44 MeV for the medium- and high-Z materials.

---

[18] The rationale for dividing materials into these categories is provided later in this section after an explanation of the physics involved.

3.3 Estimation of cargo areal density

If the mass attenuation coefficients among materials are similar for a given gamma energy, attenuation of the gamma line can be used as a means of estimating the areal density. The areal density, α, is related to the initial flux I_o, final flux $I(\alpha)$, and mass attenuation coefficient $\frac{\mu}{\rho}$ by the simple attenuation relationship:

$$\boldsymbol{I(\alpha) = I_o e^{-\frac{\mu}{\rho}\alpha} \therefore \alpha = ln\left[\frac{I(\alpha)}{I_o}\right] / \left(-\frac{\mu}{\rho}\right)} \qquad (1)$$

This research used the 4.44 MeV gamma line as a measure of areal density. While there are some differences among mass attenuation coefficients, the spread is only half that of the differences at 15.11 MeV. It should be noted that comparison of the incident and transmitted 4.44 MeV gammas[19] provides a measure of the product $\frac{\mu}{\rho} \cdot \boldsymbol{\alpha}$ and not the areal density directly. The fact this is the measurement of the product $\frac{\mu}{\rho} \cdot \boldsymbol{\alpha}$ and not the areal density directly is important because it is possible to obtain the same product by combining each material's mass attenuation coefficient or each material combination's effective mass attenuation coefficient[20] with a specific areal density. Thus, what is measured provides a range of potential areal densities specific to every material or combination of materials.

---

[19] Incident is defined as those produced and moving toward the cargo in the solid angle subtended by the detector and transmitted as those gammas that pass unattenuated through the cargo within the solid angle subtended by the detector.

[20] The effective mass attenuation coefficient of a cargo is derived from a simple linear weighting of the individual component's mass attenuation coefficients based on their mass contribution to the cargo.

3.4 The range of areal densities for an unknown cargo derived from 4.44 MeV attenuation

For the materials considered in this thesis, U has the largest mass attenuation coefficient at 4.44 MeV with a value that is 1.5 times that of Al.[21] The spread between their respective mass attenuation coefficients sets the range for potential areal densities. The difference in their mass attenuation coefficients at 4.44 MeV dictates the areal density of Al must be 1.5 times larger to achieve the same attenuation as U. All other materials considered in this thesis would require areal densities between these two extremes because their mass attenuation coefficients fall between the values for Al and U. Figure 7 shows the relationship between the fraction of 4.44 MeV gammas remaining for each material as a function of the areal density. This graphic was developed from $\boldsymbol{e}^{-\frac{\mu}{\rho}\alpha}$ for each material. Note the graph is log-linear and the slope is equal to $\frac{\mu}{\rho}$ for each material. To achieve the same attenuation, which is the same $e^{-\frac{\mu}{\rho}\alpha}$ as the reference material U, each material must have an areal density such that $\frac{\mu}{\rho}\ \alpha$ equals that of the reference. Therefore, based on our measurements of 4.44 MeV attenuation alone, and not considering other sources of error, it is possible to estimate the areal density of a material to between 66% (if the material was Al and the value for U is used) and 150% (if the material was U and the value for Al is used) of the actual value.

---

[21] The mass attenuation coefficients are more closely grouped together at 1.5-3 MeV so use of attenuation of a gamma line in this energy range to measure the areal density of cargo could potentially provide a more accurate measure of areal density. However, no such interaction was available for this research.

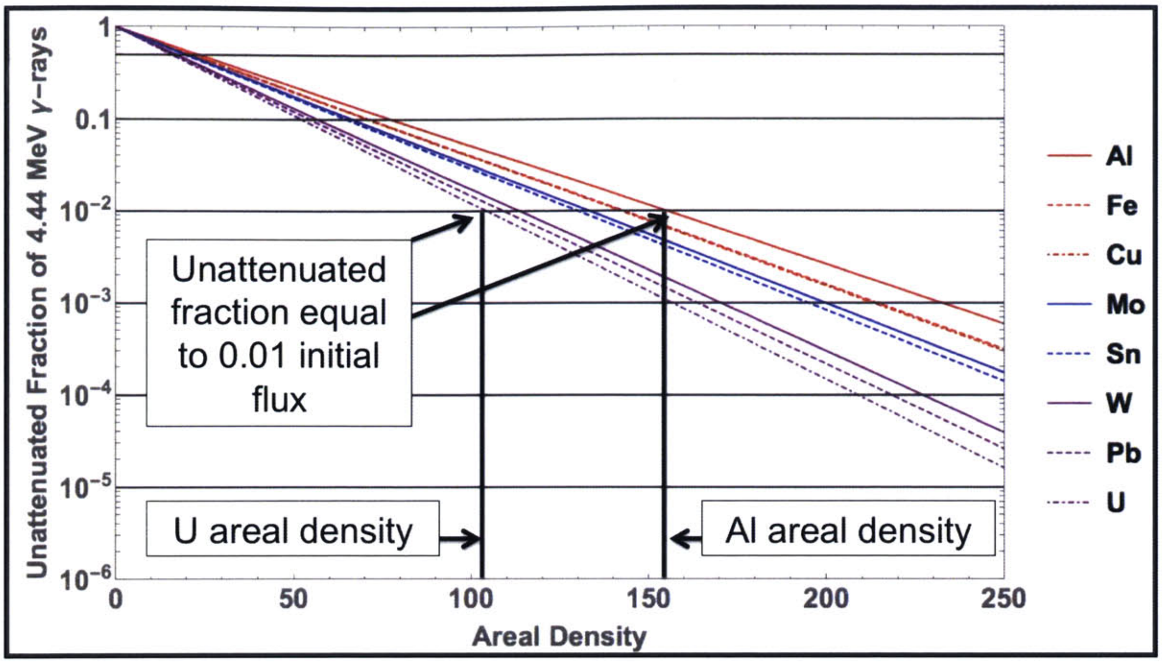

Figure 7. Relationship between the unattenuated fraction of 4.44 MeV gammas and areal density for all materials considered in this thesis. Note the log scale. To determine the areal density required for a material to attenuate the incident 4.44 MeV gamma flux to a certain fraction, drop a vertical line from where the desired unattenuated fraction and material line intersect to the areal density axis. For example, approximately 100 g/cm^2 of U will attenuate the 4.44 MeV gamma flux by a factor of $\mathbf{10^{-2}}$ (left vertical line) while Al requires about 155 g/cm^2 of material to achieve the same effect (right vertical line).

In all cases, the lowest-Z material requires 50% more areal density to have the same attenuation as the highest-Z material.

3.5 The range of areal densities for an unknown cargo derived from 15.11 MeV attenuation

At 15.11 MeV, the mass attenuation coefficients for the three high-Z materials are roughly 1.5 times that of the medium-Z materials and 2-2.5 times that of the low-Z materials. These relative difference in mass attenuation coefficients between materials mean that high-Z material will absorb 15.11 MeV gammas more readily than medium-Z materials and significantly more than low-Z materials. Figure 8 shows the relationship between the unattenuated fraction of 15.11 MeV gammas and areal density for all materials considered in this thesis. The areal density of Al required to achieve the same attenuation at 15.11 MeV as U is 2.7 times larger. This much larger range of potential areal density values makes it less practical to use the 15.11 MeV gamma line as a measure of areal density.

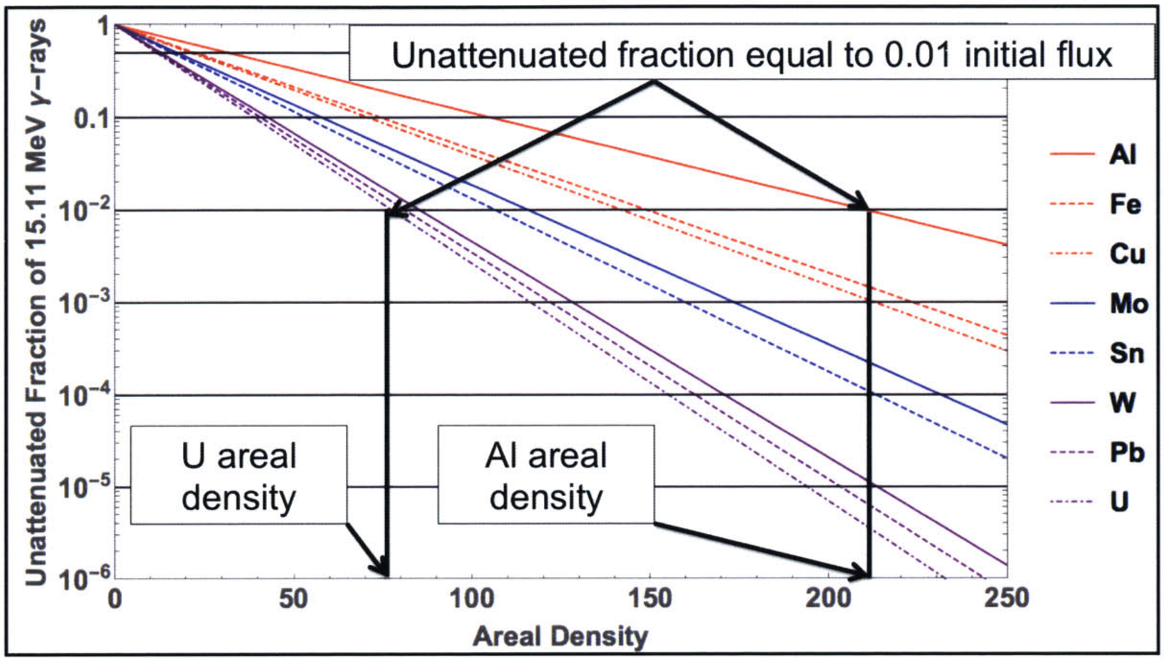

Figure 8. Relationship between the unattenuated fraction of 15.11 MeV gammas and areal density for all materials considered in this thesis. To achieve the same amount of attenuation, Al requires 2.7 times the areal density of U.

3.6 Use of attenuation of both gamma lines to distinguish between materials

The significant behavioral differences between attenuation and areal density of the two monochromatic gamma lines do, however, make it possible to distinguish between materials. Figure 9 shows the ratio of the unattenuated fractions for each material as a function of areal density. While gammas at both 4.44 and 15.11 MeV are attenuated as they pass through materials, the impact that low-Z materials have on the unattenuated ratio is substantially different than medium-Z and high-Z materials. Addition of Cu has a neutral effect while Al and Fe both preferentially absorb 4.44 MeV gammas and therefore lead to an increased ratio. The medium- and high-Z materials both preferentially attenuate 15.11 MeV gammas but the areal density of the medium-Z materials require almost twice the areal density to have the same impact on the 15.11 to 4.44 MeV gamma ratio as the high-Z materials.

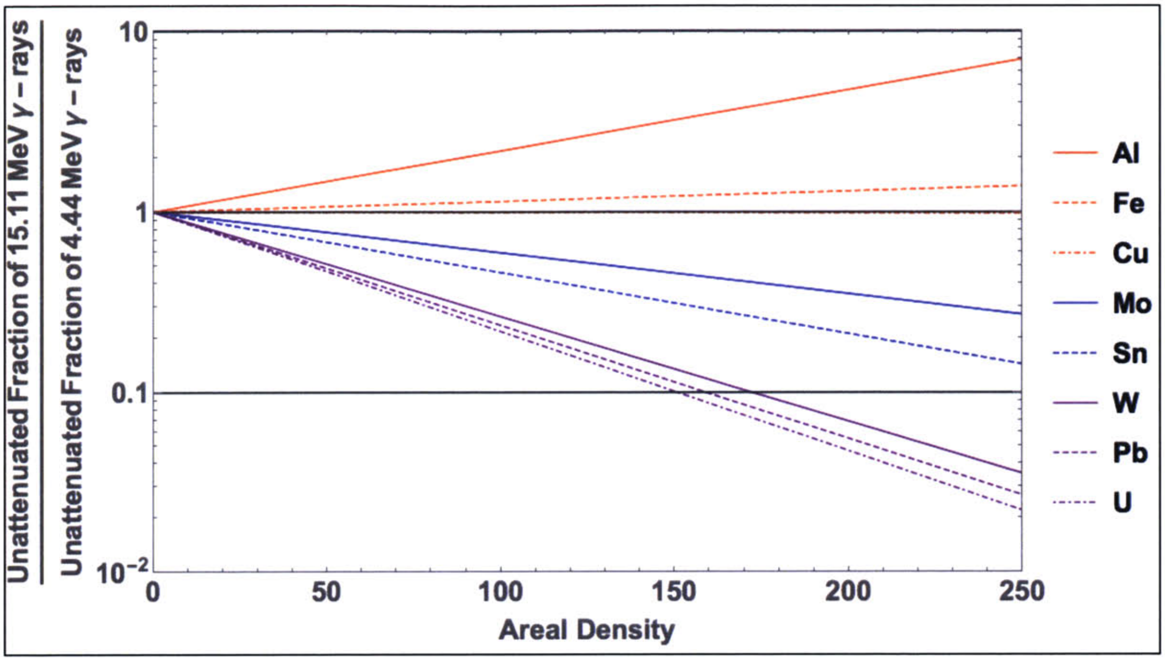

Figure 9. Relationship between the ratios of the unattenuated fraction of the two monoenergetic gammas and areal density for all materials considered in this thesis.

There are three important pieces of information we can infer from Figure 9. First, at low areal densities of only a few $\frac{g}{cm^2}$ the impact on the ratio of the unattenuated fractions is small enough that when material is mixed in a larger cargo the impact may be unnoticeable. This is important because the ability to differentiate between materials at very small areal densities sets the limits of sensitivity for this cargo scanning method. Second, beyond a few $\frac{g}{cm^2}$ there is a range of areal densities where the impact of low-, medium-, and high-Z materials are all noticeably different. However, in this range it is possible to include different combinations of materials together with a near constant areal density such that they create similar unattenuated ratios. This will be shown in a series of experiments using near constant total areal densities with different combinations of materials. Third, since this is a log-linear plot, it should be noted that at very high areal densities, the overall attenuation of medium- and high-Z materials could be substantial enough such that the counting statistics and error bars make it impractical to discriminate between the two.

3.7 The energy and atomic number dependence of gamma interaction processes

The differences in the mass attenuation coefficients for each material arise from the differences in atomic number and the Z and energy dependence of gamma interaction processes. At the incident gamma energies of 4.44 and 15.11 MeV both the Compton and pair production processes will occur for all of these materials. The Compton process is independent of Z but directly proportional to the electron density and decreases at 1/E at high energy. The pair production process is proportional to Z^2 and has a slight positive logarithmic dependence on energy.

3.8 The importance of gamma interaction processes as a function of energy and atomic number for materials considered in this thesis

Figure 10 and Figure 11 show the photoelectric, Compton, pair production, and total mass attenuation coefficients for U and Al, respectively. For U, at 4.44 MeV, the Compton and pair production are equally important but at 15.11 MeV pair production accounts for most of the total mass attenuation coefficient. At 4.44 MeV the Compton portion of the mass attenuation coefficient is much larger than pair production for Al while they are equally important at 15.11 MeV.

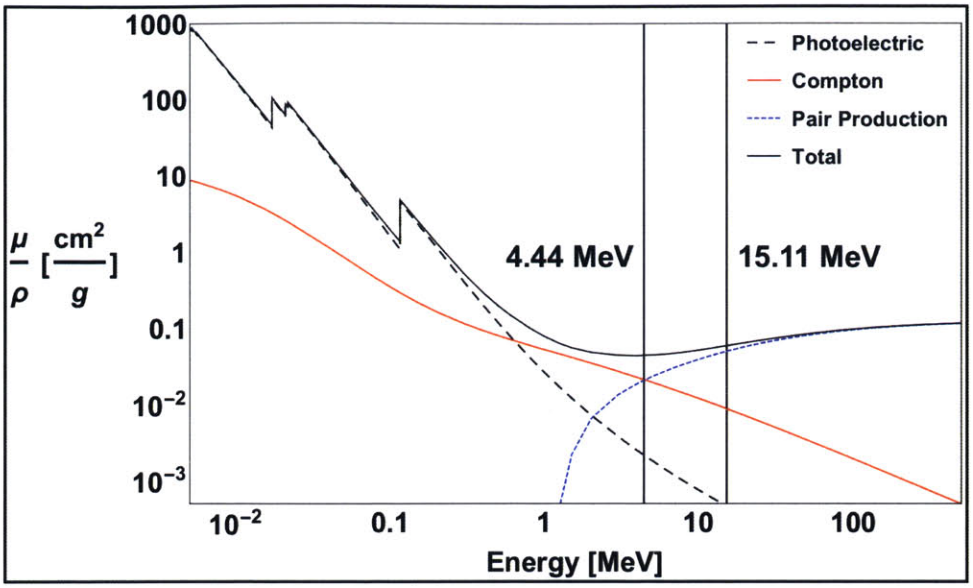

Figure 10. Total and Component Mass Attenuation Coefficients for U. At 4.44 MeV, Compton effect and pair production are equally probably processes. At 15.11 MeV, pair production is more important than the Compton effect. Graphic developed from data retrieved from National Institute of Standards and Technology Physical Measurements Laboratory XCOM database (NIST) **[48]**.

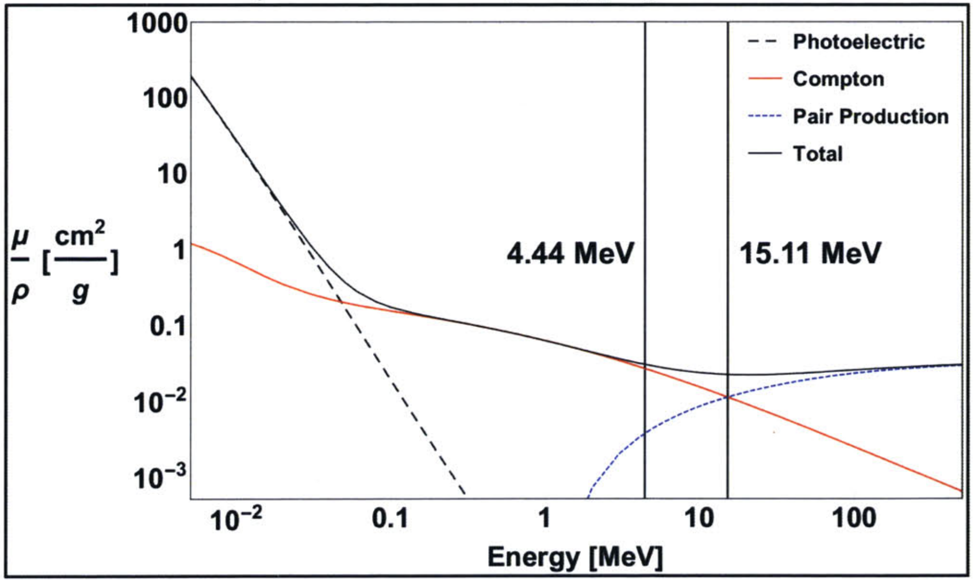

Figure 11. Total and Component Mass Attenuation Coefficients for Al. For Al, at 4.44 MeV the Compton effect is the most important gamma interaction while Compton and pair production are equally important at 15.11 MeV. Graphic developed from data retrieved from NIST database **[48]**.

The importance of the Compton and pair production interaction mechanisms at the two energies is different for each material. The ratios of the Compton to pair production components of the mass attenuation coefficient are shown in Table 4. At 4.44 MeV the Compton effect is significantly more important for Al, Fe, and Cu; slightly more important than pair production for Mo and Sn; and on parity with pair production for W, Pb, and U. At 15.11 MeV, pair production is on par with the Compton effect for Al; slightly more important for Fe, Mo, and Sn; and dominant for W, Pb, and U.

Table 4. Ratio of Compton to Pair Production Mass Attenuation Coefficients for materials used in this thesis. Derived from data retrieved from NIST [48]. At 4.44 MeV, Compton interactions are 7.15 times more likely than pair production events in Al but are equally probably in U. At 15.11 MeV, Compton and pair production are equally likely in Al but pair production dominates for interactions in U.

Element	Al	Fe	Cu	Mo	Sn	W	Pb	U
4.44 MeV	7.15	3.59	3.22	2.21	1.85	1.24	1.12	1.00
15.11 MeV	0.99	0.52	0.47	0.33	0.28	0.20	0.19	0.17

The fact that the Compton and pair production processes occur to different extents for each material at 4.44 MeV contributes to the difficulty in using attenuation of this gamma line as a measure of areal density.[22] It cannot be assumed the 4.44 MeV attenuation that occurs is solely through Compton interactions and therefore a direct measure of the amount of mass the gammas have passed through.

3.9 The behavior of mass attenuation coefficients at 4.44 and 15.11 MeV for all the elements

The mass attenuation coefficients at 4.44 MeV and 15.11 MeV incident gamma ray energy for the elements, shown in Figure 12, vary smoothly and

---

[22] Use of a lower energy gamma line may provide a better measure of areal density. A gamma line below 1.02 MeV would eliminate competition from pair production with the Compton effect.

consistently with Z. In general, the further elements are away from Cu (Z = 29), the more pronounced these differences in attenuation become. Additionally, the 15.11 MeV mass attenuation coefficients increase at roughly twice the rate of the 4.44 MeV mass attenuation coefficients for materials with Z > 29 and decrease at roughly half the rate of the 4.44 MeV mass attenuation coefficients for Z < 29.

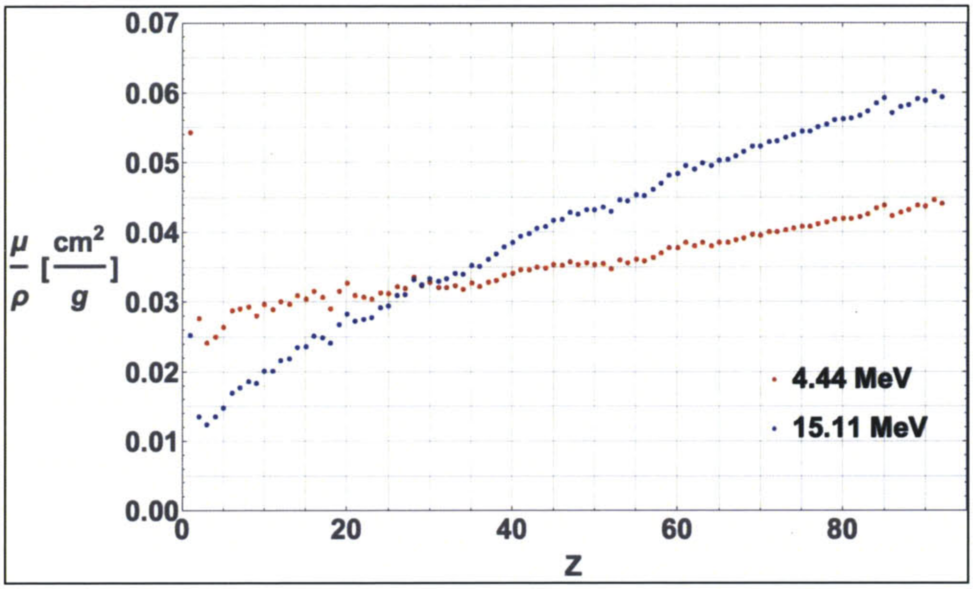

Figure 12. Mass Attenuation Coefficients by Atomic number for 4.44 and 15.11 MeV gamma rays. The mass attenuation coefficient at 4.44 MeV is greater than that at 15.11 MeV for Z < 29. Therefore, these materials preferentially attenuate the lower energy gammas. The opposite is true for Z > 29. Mass Attenuation Coefficients taken from the NIST database **[48]**.

3.10 Ratio enhancers and ratio reducers

As previously noted, the difference between the mass attenuation coefficients at 15.11 and 4.44 MeV dictates the behavior of the ratio of unattenuated gammas. Enhancement or reduction of the ratio is directly proportional to the exponential of the product of the areal density and difference in mass attenuation coefficients. The difference in mass attenuation coefficients has an even simpler relationship with the Z of the material involved. Figure 13 shows that the ratio of the mass coefficient at

15.11 MeV to 4.44 MeV varies smoothly with Z. The slope of curve provides insight into the ability to discriminate among different Z materials. For low-Z materials the slope is relatively steep so differentiation between materials with closer Z values is easier. The decreasing rate of change in the ratio of the mass attenuation coefficients for medium- to high-Z materials makes it more difficult to differentiate between closely located materials in this range. For a known areal density of pure but unknown material and known 4.44 MeV and 15.11 MeV attenuation with error bars the range of potential Z values would be smaller for a lower Z material than for higher Z materials because the error bars would encompass fewer potential Z values due to the steeper slope of the ratio of mass attenuation coefficients curve.

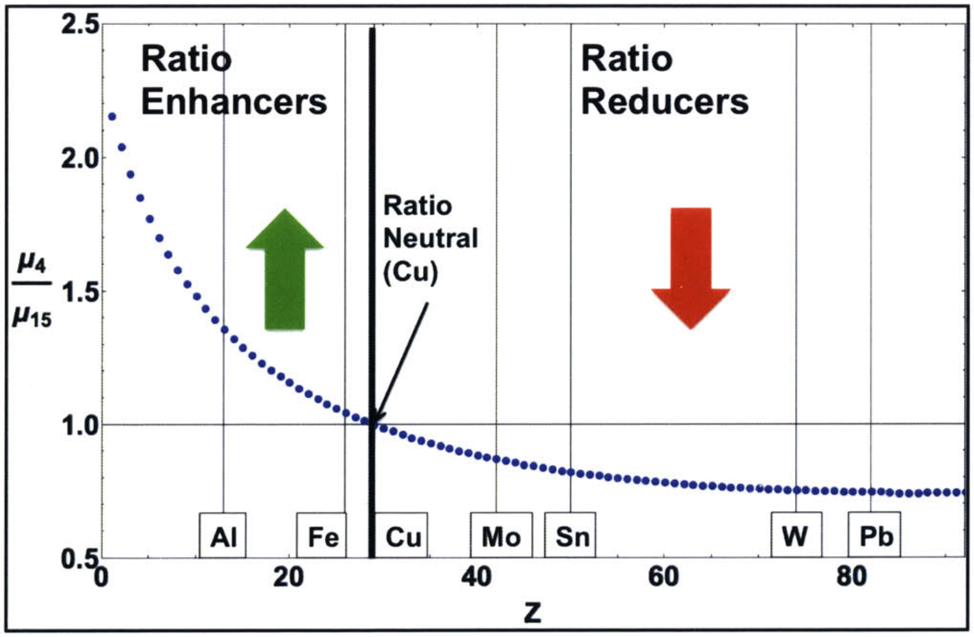

Figure 13. Ratio of Mass Attenuation Coefficients at 4.44 MeV to 15.11 MeV by Atomic number. Vertical lines indicate the materials used in this study: Al, Fe, Cu, Mo, Sn, W, Pb, and U. Ratio-neutral Cu is denoted by a thick black vertical line. Materials to the left are net ratio enhancers and materials to the right are net ratio reducers. The further a material is from Cu the greater its impact on the ratio for a given areal density. Derived from data taken from NIST [48].

3.11 Definition of low-, medium-, and high-Z materials

The relationships between how the mass attenuation coefficients and the areal density and Z of each material drive the ratio provides the rationale for the division of materials into low-, medium-, and high-Z materials. We noted that Cu was ratio neutral, with increases to areal density not impacting the ratio of unattenuated gammas. Al and Fe both preferentially attenuated 4.44 MeV gammas and were net ratio enhancers. Since these materials cannot reduce the ratio they are classified as low-Z materials.

The differentiation between medium- and high-Z is subtler.[23] The non low-Z materials all decrease the ratio but the rapidity with which they do so varies. As seen in Figure 14, W, Pb, and U all have a similar impact on the ratio, with approximately 45-52 $\frac{g}{cm^2}$ of each material cutting the expected ratio in half. Mo and Sn would require 89.2 and 132.5 $\frac{g}{cm^2}$ of material, respectively, to cause to the same ratio reduction. This can be determined from the graph by dropping a vertical line from the intersection of the ratio for the material and the ratio equals 0.5 to the areal density axis. For purposes of this study, we term materials that can cut the ratio in half with 55 $\frac{g}{cm^2}$ of material or less as high-Z (W, Pb, and U) and the remaining non low-Z materials as medium-Z (Mo and Sn).

---

[23] If we were to plot the ratios for all materials with Z > 29 we would see a near continuum of ratios with Z and areal density so there is no specific cutoff to differentiate among materials. For example, Tantalum (Z-73) would create ratios nearly identical to Tungsten (Z=74).

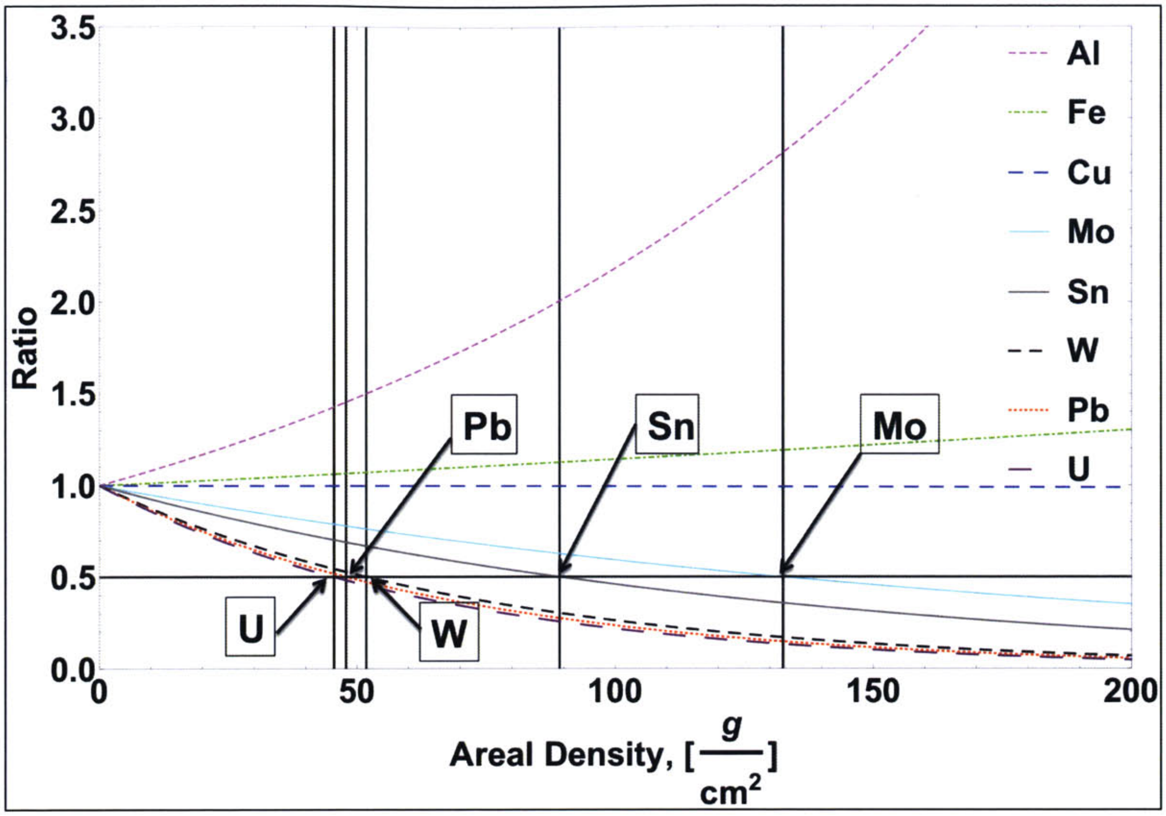

Figure 14. Impact of attenuation on 15.11 MeV gamma to 4.44 MeV gamma ratio for various materials as a function of areal density. The areal densities required for each medium- and high-Z material to reduce the ratio in half is shown by the intersection of the vertical black lines with the areal density axis. W, Pb, and U require approximately 50 g/cm^2 of material to reduce the ratio to 0.5 while Sn and Mo require approximately 90 and 130 g/cm^2 to have the same impact.

3.12 The range of effective mass attenuation coefficients for a cargo

Given the importance of the effective mass attenuation of a cargo to this scanning method, it is important to consider the range of physically allowable effective mass attenuation coefficients a cargo configuration can have. The maximum or minimum Z_{eff} value a combination of materials can have is bounded by linear combinations of the effective mass attenuation coefficients for materials that are outliers.[24] The effective mass attenuation coefficient bounds, NIST mass attenuation coefficients by Z, and the effective mass attenuation coefficients for all experiments conducted are shown Figure 15. The reasoning for not including H in this simple model is discussed below.

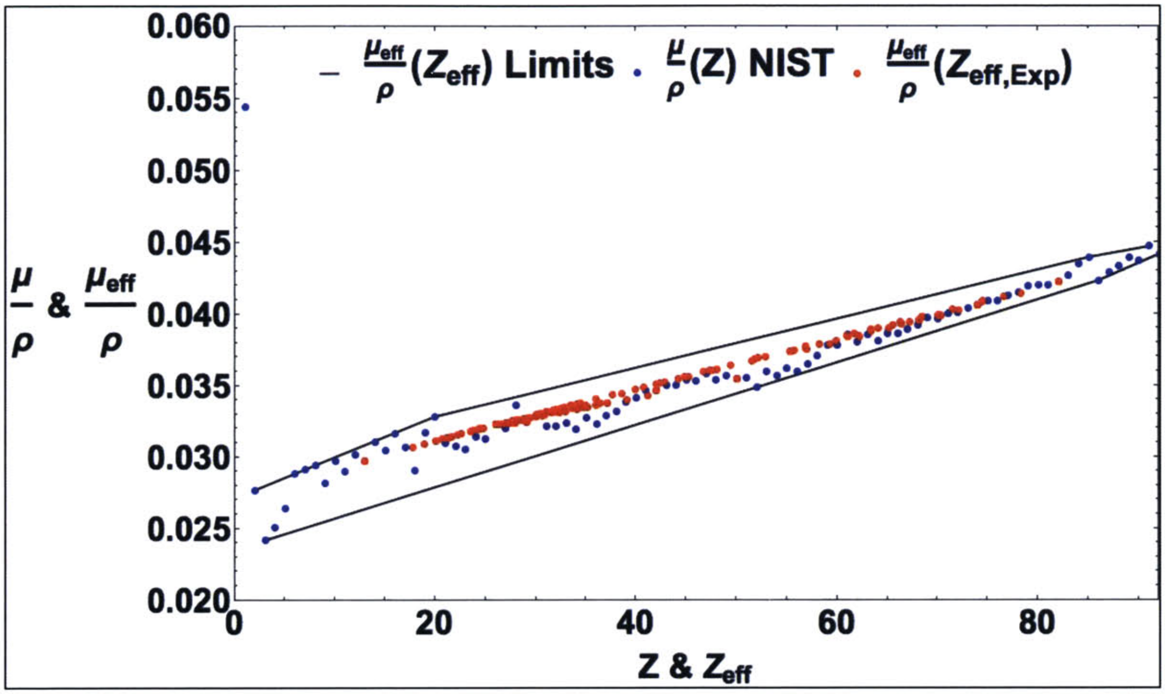

Figure 15. The range of physically allowable effective mass attenuation coefficients, $\frac{\mu_{eff}}{\rho}(\boldsymbol{Z}_{eff})$, for all possible combinations of materials (except hydrogen) are shown as solid black lines. These values are determined by connecting the mass attenuation coefficients outliers, where outliers are defined as those mass attenuation coefficients that enclose all mass attenuation coefficients between their Z values. The mass attenuation coefficients by Z, $\frac{\mu}{\rho}(\boldsymbol{Z})$, taken from NIST are shown in blue. The effective mass attenuation coefficients for the experimental configurations used in this experiment, $\frac{\mu_{eff}}{\rho}(\boldsymbol{Z}_{eff,Exp})$, are annotated in red. If H, seen in the top left of the graphic, is not considered, no possible combination of materials can be combined at a Z_{eff} value that falls outside of the bounds outlined in black.

---

[24] Outliers here are defined as those mass attenuation coefficients that, when connected by a line no line from any two materials will cross not cross those lines.

The one exception to this simplified model is material that combines with H such that the effective mass attenuation coefficient would fall outside of the area defined by the outliers. H has a mass attenuation coefficient of $0.055 \frac{cm^2}{g}$ at 4.44 MeV so the combination of an appropriate amount of hydrogen with other materials may lead to the creation of compounds that violate these bounds. Further study is warranted to determine which materials and to what extent the potential effective mass attenuation bounds may need to be adjusted because of H rich compounds.

3.13 The range of effective mass attenuation coefficients for Z_{eff} limits the range of R_{Th} values at a given areal density

The range of R_{Th} values at a specific areal density are limited by the range of the effective mass attenuation coefficients for Z_{eff}. A similar analysis for 15.11 MeV gammas would also yield a bounded region for the effective mass attenuation coefficients. When the effective mass attenuation coefficients at 4.44 MeV and 15.11 MeV are combined together and used in the R_{Th} formula, bounds for R_{Th} for a specific areal density can be determined. Figure 16 shows that the measured ratios for the combinations of materials and U fall within the R_{Th} values derived from the theoretical effective mass attenuation bounds. While the experimental areal densities varied from $155\text{-}165 \frac{g}{cm^2}$, the bounds were established assuming an areal density of $160 \frac{g}{cm^2}$. The small difference in areal densities does not significantly impact the bounds. The experimental ratios, which all contained high-Z material, tend to fall in the bottom half of the R_{Th} range.

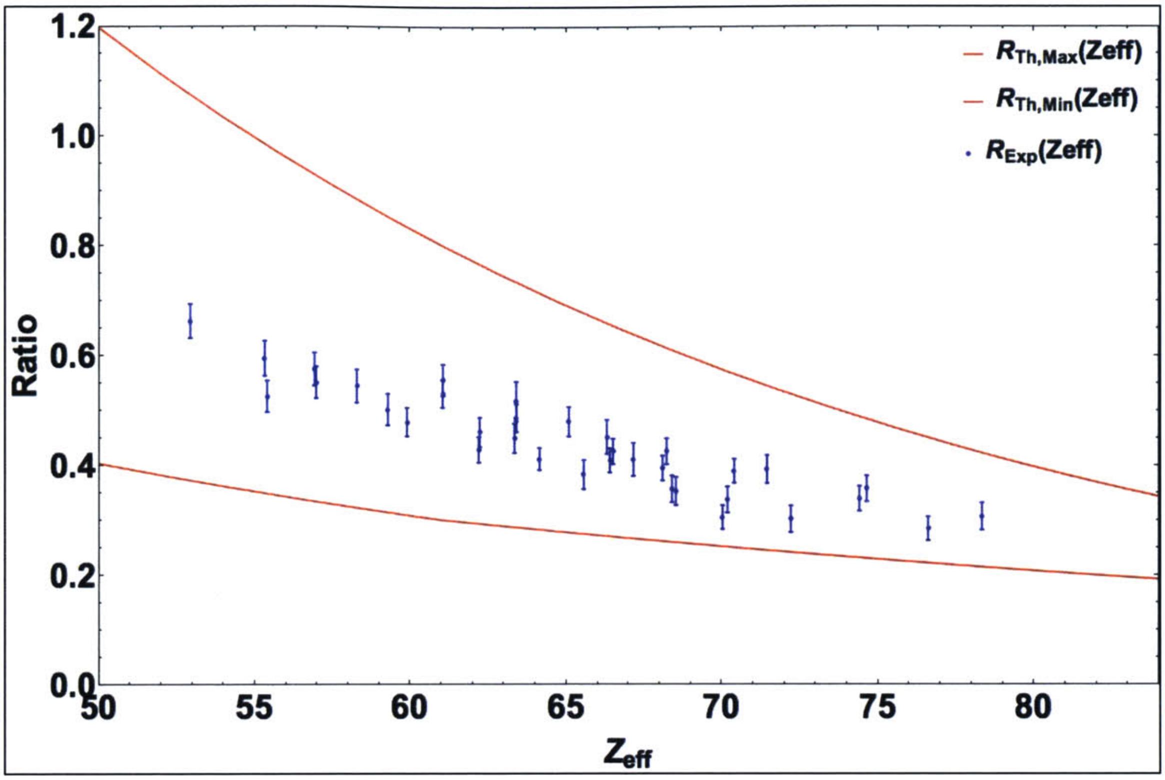

Figure 16. R_{Th} upper and lower bounds and R_{Exp} for combinations of materials with a total areal density of 160 g/cm^2. 57 g/cm^2 of the areal density is from 21" of 5% borated polyethylene (HDPE) in the beam line and the remainder from the cargo. The upper $R_{Th,Max}$ (Z_{eff}) curve is the theoretical maximum ratio value for the given areal density for any cargo configuration (without H) with an effective atomic number of Z_{eff}. The $R_{Th,Max}$ (Z_{eff}) curve is calculated using the minimum effective mass attenuation value at 15.11 MeV and the maximum effective mass attenuation value at 4.44 MeV for Z_{eff}. The $R_{Th,Min}$ (Z_{eff}) is calculated in a similar way using the maximum effective mass attenuation value at 15.11 MeV and minimum effective mass attenuation coefficient at 4.44 MeV.

The upper and lower R_{Th} bounds are based on the effective mass attenuation coefficients for the possible combinations of all materials from He to U.

Similar analyses for materials with $Z < 74$ and with a minimum areal density detection threshold of $Z > 74$ material could also be conducted. Thus, if a means of experimentally determining Z_{eff} and areal density are developed, it will be possible to establish automatic clearance of cargo based on the measured ratio. This specific ratio for automatic clearance would depend on a high-Z material areal density detection threshold. With a definitive high-Z areal density detection threshold, a lower R_{Th} bound for each Z_{eff} and areal density can be established based on the RTh value for a high-Z areal density detection threshold. This would allow, especially at lower-Z_{eff} values, establishment of an “automatic clearance ratio.” Such an automatic clearance threshold would be defined as the R_{Th} value for a given cargo areal density at which it is impossible to hide high-Z material with an areal density equal to or greater than the detection threshold.

CHAPTER 4

CONCEPT AND SETUP OF THE EXPERIMENT

This chapter provides an overview of the experimental concept and setup, to include development of a theoretical model to predict imaging counts, simulations conducted in support of the experiment, the presence and mitigation of neutrons in the beam line, major equipment and materials used, and the data acquisition and analysis software programs employed. The overall goal, general concept, and experimental layout of this thesis research are provided. Gamma production, selection of an appropriate low-threshold nuclear reaction, choice of monoenergetic gamma lines, and the potential use of additional gamma lines are addressed. A description of the path unattenuated gammas take from production until ultimate deposition in the detector array, and a simple model of this physical process that allows prediction of a theoretical ratio of 15.11 to 4.44 MeV gammas (R_{Th}) is developed. Use of a GEANT 4 simulation to determine the detector intrinsic efficiencies and experimental measurement of gamma yields is discussed. The use of detector efficiencies and gamma yields to simplify the R_{Th} model is also discussed. A discussion of the presence of neutrons in the beam line, use of a GEANT 4 simulation to model the impact of neutron-induced events on the spectrum, and actions taken to mitigate their impact is conducted. Finally, a brief description of the major equipment and materials used in the experiment, and the data acquisition and analysis software programs used are provided.

4.1 The Goal

This thesis provides a proof of principle for development of a low-dose imaging system to rapidly screen cargo using multiple lines of monochromatic gammas from 1-20 MeV produced at known rates from low-threshold nuclear interactions. Specifically it will show that use of two monochromatic gamma lines can be used to identify the presence of high-Z material in non high-Z materials.

4.2 The General Concept

When passing through material, the ratio of the monoenergetic gammas changes with the energy-specific mass attenuation coefficients and areal density,[25] α, of each material. Attenuation of the lower energy gamma rays provides a measure of the areal density of the material.[26] The ratio[27] of the attenuated monochromatic gamma ray lines provides information about the presence or absence of high-Z materials shielded by low- to medium-Z materials.

The basic concept, as depicted in Figure 17, is to accelerate an ionized particle into a target nucleus creating an excited nucleus that decays producing monoenergetic gammas at known rates. Concrete collimators allows a fan beam of the monoenergetic gammas to pass toward the cargo but limits the forward passage of additional gammas not in the beam line. The fan beam of monoenergetic gammas then passes through or interacts with the cargo depending on its composition and

---

[25] Areal density is equal to the product of the density of a material and its thickness, $\alpha = \rho \cdot \Delta x$, and is measured in g/cm^2.

[26] Measurement of the attenuation actually provides the product of the areal density and the effective mass attenuation coefficient for the material.

[27] For purposes of this thesis, unless otherwise specified, the term ratio refers to the 15.11 MeV gamma counts divided by the 4.44 MeV gamma counts. The "counts" here denotes the number of events whose energy deposition falls within a well-defined window.

the gamma energies. A small Pb collimator immediately following the cargo allows gammas parallel to and within the beam line to pass forward through a second set of concrete collimators and toward the detector. The second collimators limit the forward passage of gammas not in the beam line thereby reducing secondary scatters into the detection array. Pb shielding to the sides and front of the detector array limits interactions in the detectors from gammas outside of the beam line. Analysis of the quantity and ratio of the detected monoenergetic gammas provides information about the areal density and cargo composition.

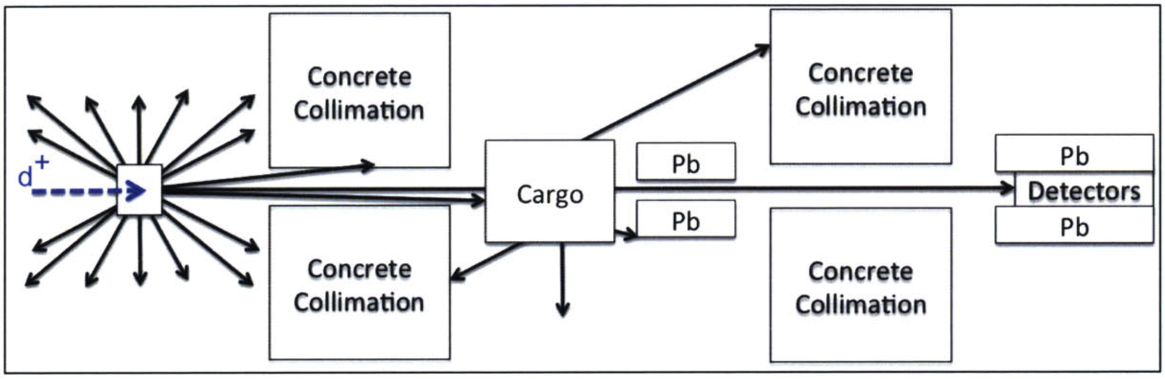

Figure 17. Experimental concept showing the layout of the accelerator beam target, collimation and shielding, cargo, and detector array. An excited daughter product from a low-threshold nuclear interaction decays emitting monoenergetic gammas at known rates. A fan beam of gammas passes forward through collimators and cargo to a detector. The quantities and ratio of the original monoenergetic gammas detected provides information about the areal density and composition of the interrogated cargo.

4.3 The Experimental Layout

Figure 18 shows a side view of the accelerator, concrete collimators with an inset of a typical cargo configuration with Pb shielding, and the detector array with Pb shielding. An AutoCAD schematic of the warehouse housing the experiment and the major equipment, description of the setup, summary of key dimensions, and pictures of the equipment and experiment area are found in Appendix C.

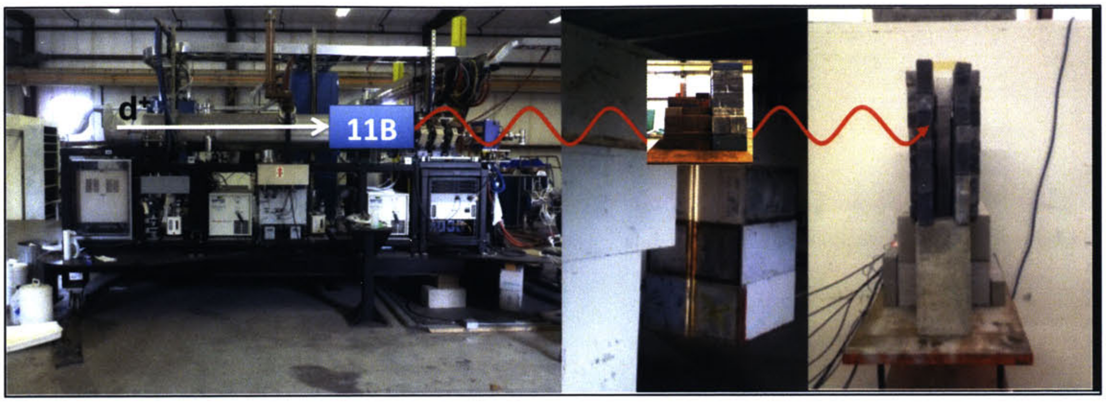

Figure 18. Collage of pictures of the main components of the experimental setup. From left to right, the accelerator, concrete collimators with inset picture of typical interrogation material and Pb collimator, and the detector array with Pb shielding and collimator.

The major equipment used in this experiment included Model DL-3 Linac System (Appendix D) and associated computerized controls, 2"x4"x16" NaI(Tl) Saint-Gobain scintillation detectors with 2" PMT (Appendix G), a CAEN V1724 digitizer, a CAEN VME crate, CAEN power supply, and various connectors and cables. Standard and dual-density concrete was used for gross beam collimation, standard 2" x 4" x 8" Pb bricks for fine collimation and detector shielding, and Shieldwerx SWX-201HD 5% Borated Polyethylene Neutron Radiation Shielding (HDPE) **[49]**.

4.4 Gamma production

As previously mentioned, 3.0 MeV deuterons were accelerated into an ^{11}B target to produce an excited ^{12}C nucleus and a multiple MeV neutron. (The level scheme for ^{12}C is found in Appendix E.) The deuteron and ^{11}B interact to form a compound intermediate nucleus $^{13}C^*$ or from a stripping reaction an excited $^{12}C^*$

compound nucleus. The kinetic energy of the neutron emitted is equal to the inverse mass ratio of the reaction products times the sum of the kinetic energy of the deuteron (assuming the ^{11}B is initially at rest) and the Q value of the reaction. The ^{11}B(d, nγ)^{12}C* interaction produces 4.44 MeV gammas at roughly an order of magnitude (OOM) more frequently than the 15.11 MeV gammas.[28] Additional gamma lines produced from this interaction include a 12.71 MeV gamma from an excited state decay to the ground state and a 10.67 MeV gamma from 15.11 MeV excited state decay to the 4.44 MeV excited state but these decays occur an OOM less frequently than the 15.11 MeV decays.

The difference between the frequency of the various gamma decays is largely explained by initial production of the ^{12}C* excited states. The 12C* excited state may form if the neutron and recoil of the nucleus do not carry off all of the excess energy. The excited ^{12}C* states seek to decay via available transitions to a more favorable state. For ^{12}C*, de-excitation via gamma decay provides a readily available mechanism. How quickly and which gamma emissions occur can be explained by the gamma decay selection rules. The basic rules are that gammas must carry off integer non-zero values of angular momentum and the integer value of angular momentum is bounded by the difference of the initial and final states, $|I_i - I_f|$, and the sum of the initial and final nuclear spin states, $I_i + I_f$. Since the gamma must carry off at least one unit of angular momentum, 0^+ to 0^+ transitions are strictly forbidden. The types of transitions are characterized as electric or magnetic. If there is no

---

[28] Estimates of production rates were determined from data provided by R.L. Sheffield from the data used to develop a paper on neutron and gamma-ray production using the ^{11}B(d, nγ)^{12}C* interaction [**80**].

change in parity, as is the case for the $^{12}C^*$ decay, only even electric and odd magnetic decays are possible. Table 5 depicts the possible transitions for the four gamma energies previously discussed. Note that the $^{12}C^*$ state at 15.11 MeV can decay either directly to the ground state through an M1 transition or to the 4.44 MeV state through M1, E2, or M3 transitions. The decay constant, $\lambda(\text{M1})$ is proportional to the E^3 [**50**] so decay to the ground state (G.S.) is favored over decay to the 4.44 MeV excited state.

Table 5. Allowable transitions of the four major gamma rays considered in this thesis. The gamma energy, initial and final nuclear states and parities, lower bound for angular momentum carried off by the gamma, allowable angular momentum values for the gamma, upper bound for angular momentum, and possible electric (E) and magnetic (M) transitions are tabulated.

E_γ [MeV]	Initial State	Final State	|Ii – If|	≤ L ≤	Ii + If	Possible decays
15.11	15.11 (1^+)	GS (0^+)	|1-0| = 1	1	1+0= 1	M1
12.71	12.71 (1^+)	GS (0^+)	|1-0| = 1	1	1+0 = 1	M1
10.67	15.11 (1^+)	4.44 (2^+)	|1-2| = 1	1,2,3	1+2 = 3	M1, E2, M2
4.44	4.44 (2^+)	GS (0^+)	|2-0| = 2	2	2+0 = 2	E2

It is important to note that there are no stopping-power thickness gamma production cross sections available for 3.0 MeV deuterons on B. Further, there is not sufficient experimental total and angular cross section data to construct a stopping power thickness cross section for production of the 4.44 and 15.11 MeV gammas. Therefore, one part of this thesis was to measure the absolute production yields at 0° into the solid angle subtended by the detector per μA of d^+ source particles per second. The details of this experiment will be discussed in the subsequent chapter.

4.5 Selection of the low-threshold nuclear reaction

The nuclear reaction employed in this thesis research is not necessarily the best interaction for this method. A broad study of potential nuclear reactions is necessary to make that determination. However, the reaction does have some excellent qualities that enable it to be used to conduct a "proof of principle" for the proposed method. In particular, the 4.44 and 15.11 MeV gamma production rates are sufficiently high to penetrate more than 9" of Fe. Additionally, while not used in this research, a fast neutron spectrum is created that could be used to gain additional information about the cargo (e.g. induce fissions to look for delayed neutrons to confirm the presence of SNM, neutron radiography).

An ideal interaction would produce multiple, well spaced 1-20 MeV gamma lines without the accompanying neutrons. Perhaps an ideal low-threshold reaction would produce a 1-3 MeV gamma (where mass attenuation coefficients for all materials are much closer together) and a gamma where pair production dominates for most materials. Previous research suggests using a cyclotron for $^{12}C(p,p')$ with an incident proton energy of 18-19 MeV. This may provide the same gamma lines without the accompanying neutrons **[51]**. An alternate reaction that eliminates or reduces the neutron production would greatly reduce the dose rate and shielding requirements for such a system. It should also be noted that use of a beam target material made of multiple materials instead of B might result in the production of ideal monoenergetic gammas for this work.

4.6 Monoenergetic gamma line selection

In addition to production rates that made their transmission and detection through cargo feasible, the two gamma lines used in this thesis were selected because the mass attenuation coefficients at 4.44 MeV (except for H) were sufficiently close to allow reasonable estimation of areal density and the 15.11 MeV gamma was of sufficient energy to allow pair production to occur in all the material considered and to be the dominant process for high-Z materials.

Two potential considerations for future work include use of a monochromatic gamma line lower than 4.44 MeV and use of additional gamma lines between 4.44 and 15.11 MeV. The rationale for considering a lower energy gamma line is, as seen in Figure 6, that the mass attenuation coefficients are closer together from 1.5-3 MeV. Use of a gamma line in this region could reduce the error associated with estimation of the areal density. Further, it should be noted that the mass attenuation coefficients at these lower energies are approximately equal to those of the medium-Z materials at 15.11 MeV. Therefore, in addition to the greater attenuation that would occur at this line, it would also shift the definition of what constitutes a low-Z material to the current middle-Z materials. All materials with a mass attenuation coefficient at this energy equal to or larger than the mass attenuation coefficient at the higher energy would be considered ratio enhancers. This would make it easer to distinguish these materials from the non low-Z materials.

4.7 Use of additional gamma lines

If additional gamma lines of known origin had been available, they would have been included in this thesis. Unfortunately, experimental measurements verified that the 10.67 and 12.71 MeV gamma lines were not produced in sufficient quantities to allow their use in the current experiments. It should be noted that gammas of unknown origin at approximately 6-7 and 8-9 MeV were also present in all spectra, as seen in Figure 19. Some potential sources of these gammas include neutron capture in $^{10}B(n,\gamma)^{11}B$, $^{10}B(d, n\gamma)^{11}C$, $^{11}B(n,\gamma)^{12}B$, $^{27}Al(n, \gamma)^{28}Al$, and $^{206}Pb(n, \gamma)^{207}Pb$. Neutron inelastic scattering may also be a potential source of these gammas. Further study, using materials and a higher resolution detector (e.g. HPGe) may lead to identification of the source of these gammas.

Once the origin of these peaks can be determined and their production quantified, it may be possible to use information about their attenuation to determine additional information about the cargo. Suggestions for research to determine the presence of these peaks will be discussed later in recommendations for future work. The potential impact of including additional gamma lines between 4.44 and 15.11 MeV is discussed below.

The use of additional gamma lines between 4.44 and 15.11 MeV could be used in conjunction with the 4.44 MeV or another lower energy gamma to provide several unique ratios. The use of multiple ratios potentially provides a way to better estimate Z_{eff} and areal density of an unknown cargo. Since each ratio depends on the product of $\frac{\mu_{eff}}{\rho}$ and α, and α must be the same from ratio to ratio, comparison of

$\frac{\mu_{eff}}{\rho} \cdot \alpha$ allows elimination of some potential Z_{eff} values. If the α values among ratios do not match up, the associated Z_{eff} values can be eliminated from consideration. Use of additional gamma lines could also result in increased sensitivity to small amounts of high-Z materials since any ratios that raise the current low-Z range cutoff into the current medium-Z range would now allow easier differentiation between these newly classified low-Z materials and the high-Z materials. Thus, the use of multiple, independent complimentary ratios may allow increased confidence in determining the presence or absence of high-Z materials for an unknown cargo.

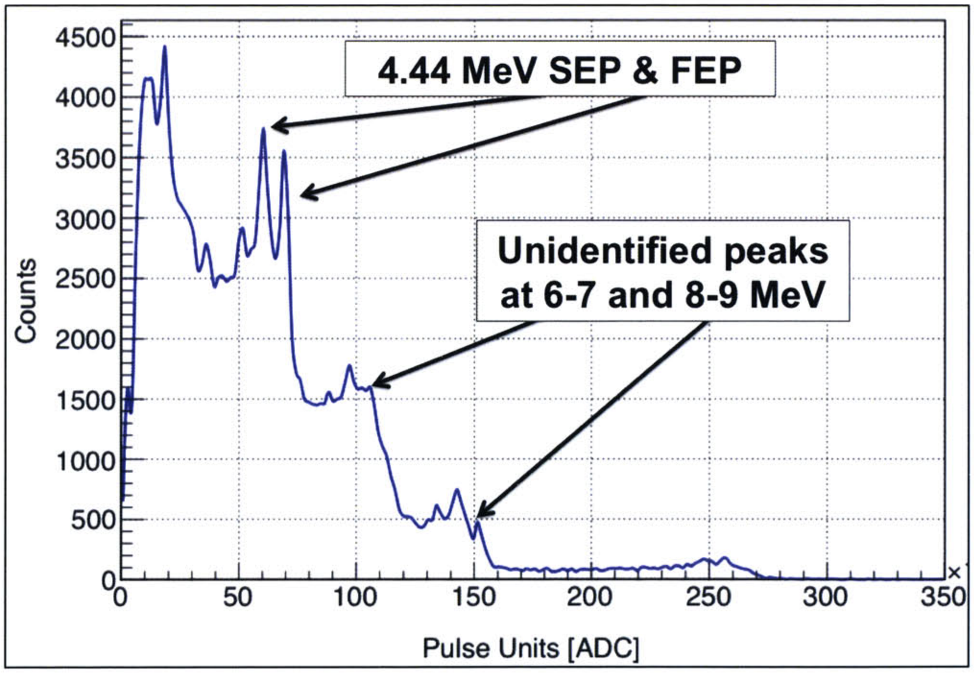

Figure 19. Typical gamma spectrum showing 4.44 MeV single escape peak (SEP) and full energy peak (FEP) and unidentified peaks at 6-7 and 8-9 MeV.[29] Pulse Units [ADC] are the channels used for binning the events and are proportional to the energy deposited by the incident gammas in the detector. A total of 350,000 ADC channels were used to bin events over the entire range of the energy spectrum.

---

[29] The FEP results from full deposition of the gamma energy in the detector. The SEP results when all energy from the gamma is deposited in the detector except for the escape of a single annihilation gamma.

4.8 Passage of gammas from production to the detector array

Upon generation of the 4.44 and 15.11 MeV gammas in the B target (shown in Figure 17), a fraction of the gammas and neutrons produced travel in the direction of the NaI(Tl) detector. These gammas and neutrons pass through an empty, lead-lined radiation channel within borated high-density polyethylene (HDPE)[30] shielding as seen in Figure 20. Gammas and neutrons not in the beam line were shielded with Pb and HDPE.

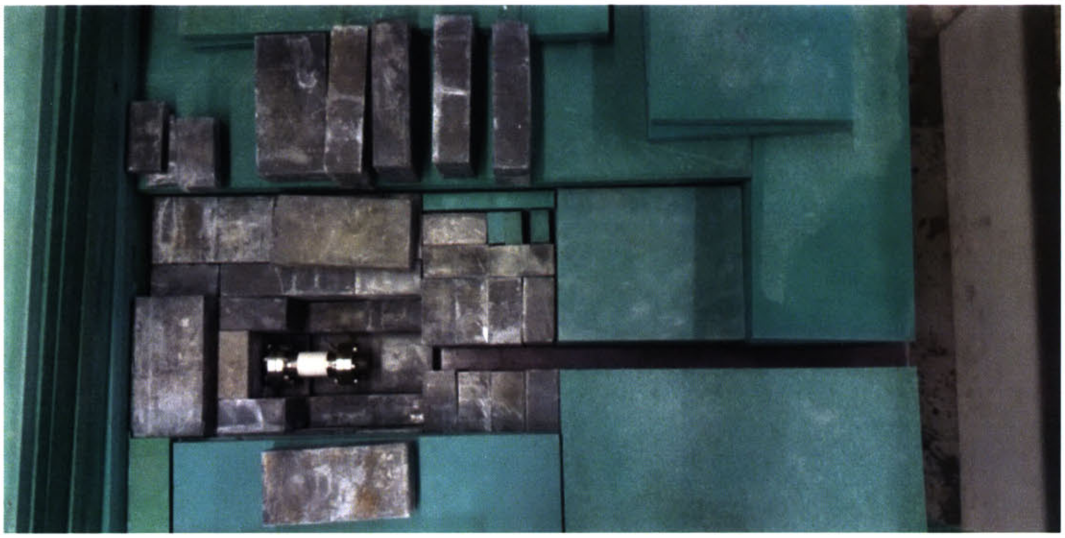

Figure 20. Pb and HDPE shielding and radiation channel surrounding the B target housing. An inner layer of Pb and an outer layer of HDPE were used to shield gamma close to the B and neutrons out of the beam line. A channel was left open for gammas and neutrons to pass down the beam line. It should be noted the HDPE has 5% boron which potentially undergoes interactions that confound the spectrum.

To further enhance the ability to detect the unattenuated 4.44 and 15.11 MeV gammas, several layers of shielding and collimators were placed to limit the introduction of scattered gammas rays into the beam line.[31] Two sets of double

---

[30] HDPE throughout this work refers to Shieldwerx SWX-201HD 5% Borated Polyethylene Neutron Radiation Shielding.

[31] There are no naturally occurring terrestrial sources of gamma rays that are of sufficient energy to interfere with the 4.44 MeV FEP and 15.11 MeV peak integration area so collimation and shielding

density concrete collimators, as shown in Figure 21, were used as collimators and shielding to limit gamma rays not in the beam line from moving toward the detector. The first set of concrete collimators greatly reduced neutron and gamma flux originating from interactions between the d^+ and ^{11}B. It also reduced neutron capture gammas originating from events in the HDPE surrounding the radiation channel. The second set of concrete collimators allowed the fan beam of unattenuated gammas to pass but greatly reduced scattered radiation in the cargo from reaching the detector array.

Figure 21. Double density concrete collimators. A flood light was used to shine light through the collimation channels to verify the detector array was correctly positioned in the beam line. Cargo to be scanned was placed in the beam line between the two sets of concrete collimators.

---

efforts were focused on radiation originating from the $^{11}B(d, n\gamma)^{12}C$ interaction and prompt gammas from neutron capture.

The cargo was placed between the two sets of concrete collimators. A Pb collimator, as seen in Figure 22, was placed immediately after the cargo as fine collimation. The Pb collimator greatly reduced the amount of gammas originating from scatter in the cargo from entering the beam line.

Figure 22. Pb collimator immediately after cargo. The Pb collimator was placed immediately after the interrogation cargo to limit the amount of scattered radiation entering into the beam line. Keeping a gap between the interrogated cargo and Pb collimator limited the acceptance angle for scattered radiation into the beam line.

Finally, the NaI(Tl) detector array was shielded with 4" of Pb along the sides for the length of the detector and an additional 2" Pb shielding was placed extending 8" in front of the detector as seen in Figure 23. This Pb shielding reduced the amount of radiation entering the detectors from outside of the beam line by limiting the acceptance angle. It should be noted that extending the length of the Pb collimator in front of the beam line would reduce the acceptance angle and could potentially further reduce unwanted gammas. A measurement of gammas outside of the beam line would determine if extension of the collimator is warranted.

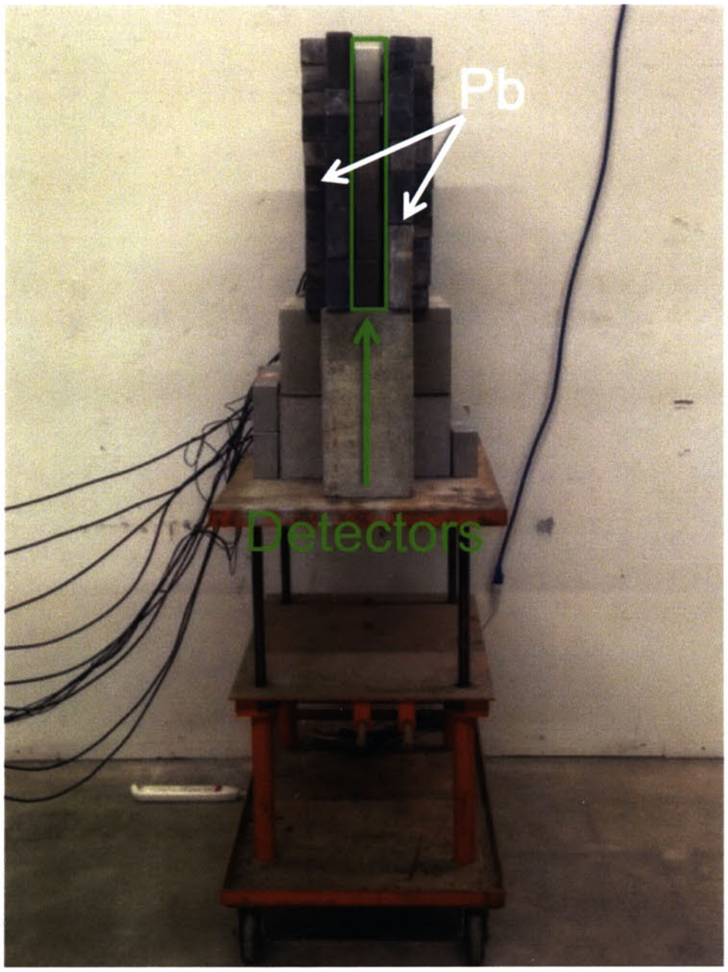

Figure 23. NaI(Tl) array with Pb shielding. 4" thick Pb shielding was placed along the sides for the length of the detector. An additional 2" thick Pb shielding was placed extending 8" in front of the detector. The Pb placed directly to the sides of the NaI(Tl) scintillators and the Pb collimator directly in front of the detectors greatly reduced the acceptance angles for in-scatter of gammas originating outside of the beam line.

In summary, unattenuated gammas from the B source travel through 21" of HDPE, a gap in the first set of concrete collimators, the cargo, fine Pb collimator, a gap in the second set of concrete collimators, and several meters of air[32] prior to reaching and interacting with the NaI(Tl) scintillation detectors.

4.9 A simple model to predict the ratio of 15.11 MeV to 4.44 MeV gammas transmitted through the cargo

One of the goals of this thesis is to create a model that predicts what is actually seen at the detectors for the scan of any cargo configuration. The ability to accurately predict experimental results is important because it allows an increased ability to understand and interpret these results. Additionally, a theoretical model that accurately predicts experimental results can also be used to inform more complex modeling efforts used to develop, optimize, and field a complete cargo scanning system.

One of the key goals of developing a model to predict observed 15.11 to 4.44 MeV gamma ratios was to make the simplest model possible that accurately predicts the experimental results. The model was developed to describe the aforementioned process of gammas passing from production to ultimate detection in the NaI(Tl) array. It relates the ratio of the 15.11 and 4.44 MeV gammas produced in the B and moving in the direction of the detector to the expected ratio of 15.11 to 4.44 MeV detected. The simple model developed to predict the expected 15.11 to 4.44 MeV gamma counts, hereafter referred to as the theoretical ratio, R_{Th}, can be described as:

---

[32] Attenuation by the air was not considered in this analysis. The attenuation length for 4.44 and 15.11 MeV gammas are approximately 278 and 452 m for air sea-level air at standard temperature and pressure.

$$R_{Th} = \frac{Y_{15.11\,MeV\,\gamma}}{Y_{4.44\,MeV\,\gamma}} \frac{\epsilon_{15.11\,MeV\,\gamma}}{\epsilon_{4.44\,MeV\,\gamma}} \frac{\prod e^{-\alpha \frac{\mu_{15.11\,MeV\,\gamma}}{\rho}}}{\prod e^{-\alpha \frac{\mu_{4.44\,MeV\,\gamma}}{\rho}}} \quad (2)$$

where Y represents the gamma yield, ϵ the intrinsic efficiency of the detector, and $\prod e^{-\alpha \frac{\mu}{\rho}}$ is the product of the exponentials of the mass attenuation coefficient and the areal density for each material the gammas pass through. The R_{Th} equation assumes that if a gamma interacts, it is no longer part of the un-interacted gammas moving toward the detector. It also ignores other reactions, such as neutron capture or inelastic neutron scatter, which could create 15.11 and 4.44 MeV gammas. Thus, the theoretical prediction will match the experimental measurements only if other gamma production mechanisms are sufficiently small to be neglected from the model.

Note the yield production ratio[33] and not the absolute yields of the 15.11 MeV to 4.44 MeV are necessary to find the theoretical ratio. However, determining the areal density estimate, or more specifically the $\alpha \cdot \frac{\mu}{\rho}$, does require knowledge of the 4.44 MeV gamma production rate.

4.10 Use of a GEANT 4 simulation to determine the detector intrinsic efficiencies at 4.44 and 15.11 MeV

Use of the R_{Th} model requires knowledge of the gamma production yields, detector efficiencies, and knowledge of the cargo characteristics. However, at the

---

[33] The need for only knowing the ratio, and not the absolute production, is nice in that it greatly simplifies a lot of detailed analysis that is necessary to determine absolute production yields (i.e. gamma production cross sections for 3.0 MeV deuterons on a stopping power thickness target of B). However, research is ongoing to determine these production cross sections.

onset of this thesis neither the gamma production yields nor the detector efficiencies at 4.44 and 15.11 MeV were known. A collaborator conducted a GEANT simulation to determine the intrinsic efficiencies of the NaI(Tl) detectors at 4.44 and 15.11 MeV [**52**]. For purposes of this thesis, the intrinsic efficiency of the detector for a specific energy is defined as the number of counts recorded within a specific integration region divided by the total number of gammas at that energy incident on the face of the detector. The simulation geometry was similar to the experimental setup.

The intrinsic efficiency[34] of the detector for the 15.11 MeV gammas, $\epsilon_{15.11\ MeV}$, was determined to be 0.464 ± 0.003 for an energy window from 12.605 MeV to 15.870 MeV. The 15.11 MeV integration region is depicted in Figure 24. The limits of integration were selected to limit the inclusion of gammas from inelastic scatter and high-energy neutron capture. This was important because there are neutrons produced from the $^{11}B(d, n\gamma)^{12}C^*$ in excess of 16.7 MeV. These high energy (< 20 MeV) neutrons can produce 15-20 MeV gammas through inelastic (n,n') reactions with ambient material in the experiment and would represent a source of error.

The intrinsic efficiency for the 4.44 MeV gammas, $\epsilon_{4.44\ MeV}$, was determined to be 0.158 ± 0.001. After removal of background[35], a Gaussian fit was used to fit the 4.44 MeV FEP to determine the peak counts. The lower limit of integration was

---

[34] For this research, the efficiency of the detector is defined as the number of counts recorded within a specified energy integration window by the total number of gammas incident on the face of the detector at the specified gamma energy.

[35] Note the 4.44 MeV background spectrum is from the continuum created by partial energy deposition of higher energy gammas in the detector and not from the natural background.

the local minimum between the FEP and the SEP and the upper limit was extended until the counts go to zero with background subtracted. These integration limits were selected because it was easy to consistently identify these features in the experimental spectra. The intrinsic efficiency for the 4.44 MeV gammas was defined as the total number of counts falling in the above integral divided by the total number of incident 4.44 MeV gammas on the face of the detector. Figure 25 shows the 4.44 MeV FEP integration region. The SEP and double escape peak (DEP) are also seen in the spectra at 3.93 and 3.42 MeV.

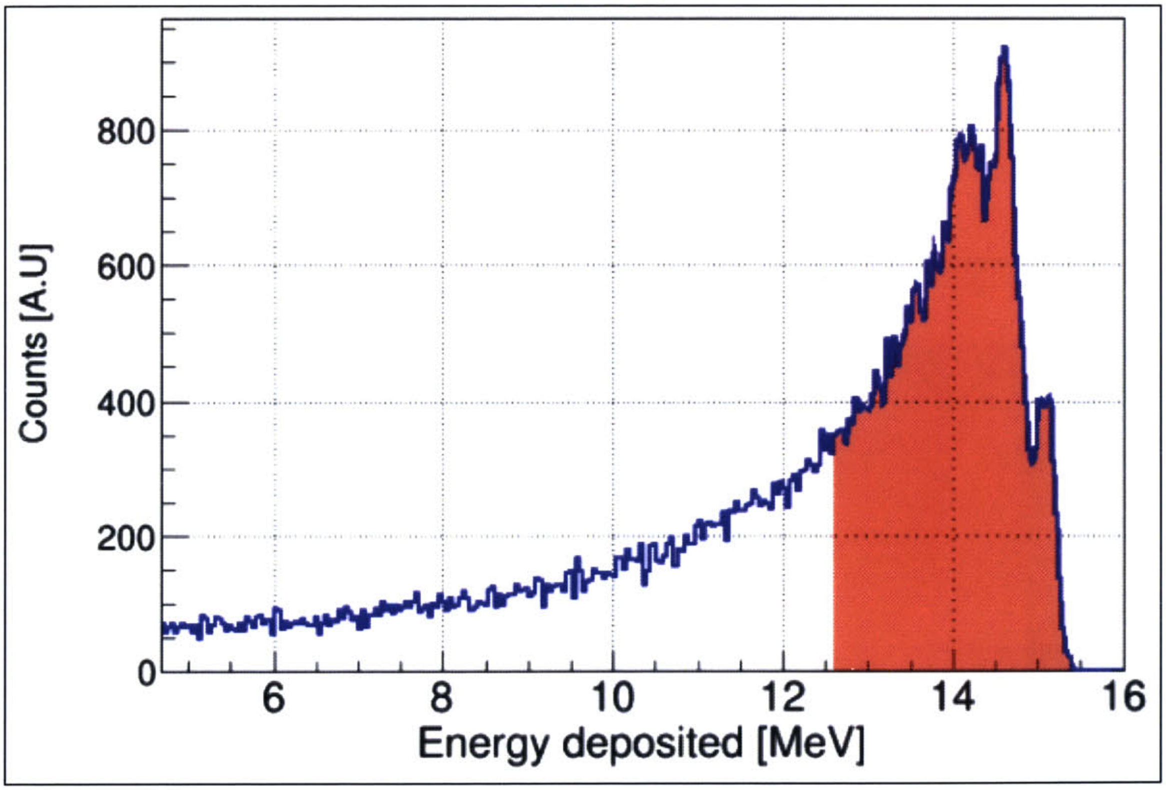

Figure 24. GEANT-4 simulated data showing the integration region for 15.11 MeV gamma NaI(Tl) intrinsic efficiency calculation. The long tail associated with the 15.11 MeV gammas is a result bremsstrahlung radiation escaping the detector.

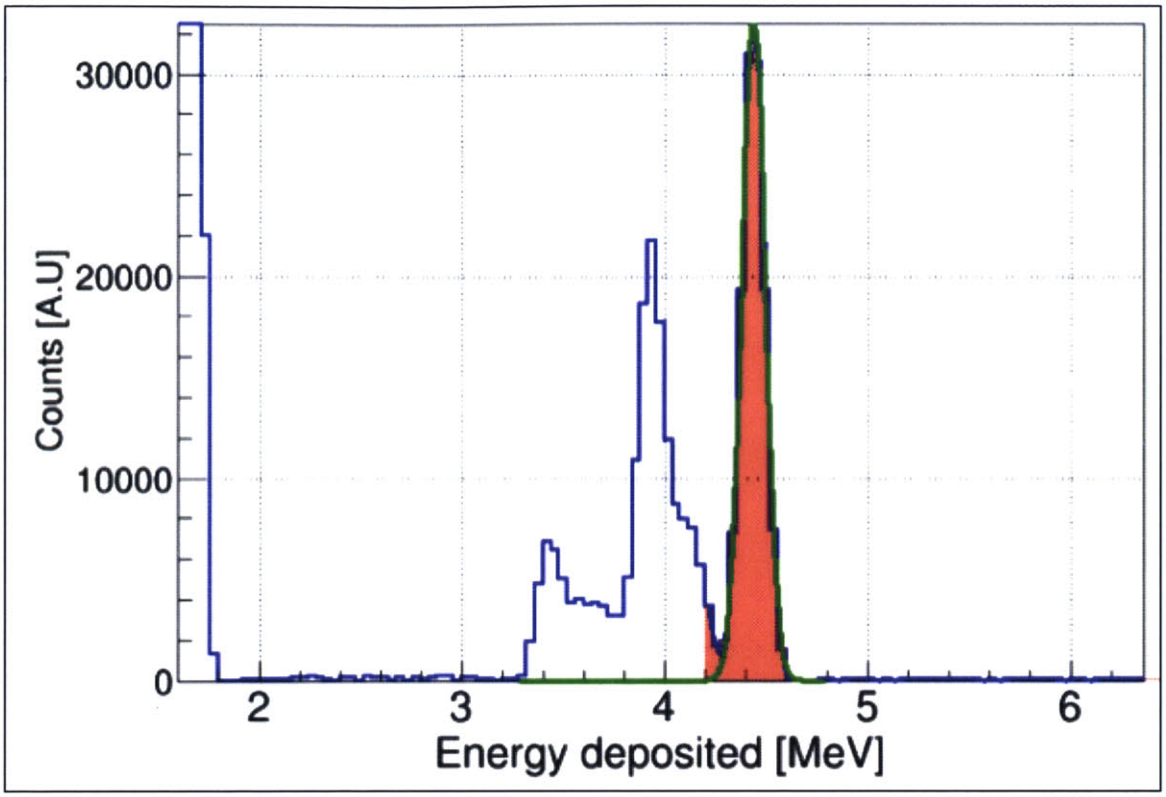

Figure 25. GEANT-4 simulated data showing the integration region for 4.44 MeV gamma NaI(Tl) intrinsic efficiency calculation. In all experimental tests, the 4.44 MeV FEP and SEP are visible. However, the much smaller double escape peak (DEP) was frequently not visible in higher total areal density cargo configurations.

It should be noted the model used to determine the efficiencies of the NaI(Tl) detector was previously successfully used to determine the efficiency of two different NaI(Tl) detectors and a LaBr detector, and was experimentally validated against data gathered using numerous check sources.

4.11 Determination of 4.44 and 15.11 MeV gamma production yields

The 4.44 MeV to 15.11 MeV gamma production yield ratio was found to be 6.0 ± 0.2 from a measurement of HDPE-only in the beam line and will be discussed further in the subsequent chapter. Analysis of the experimental results of the mixed materials tests and material combination tests demonstrated an estimated yield ratio of 5.8 ± 0.3. The material combination tests showed estimated yield ratio of 5.9 ± 0.4. Both results are in agreement with the HDPE-only test.

4.12 Definition and determination of the prefactor and simplification of R_{Th}

The prefactor, PF, which accounts for the experimentally measured gamma yields, $\frac{Y_{15.11\,MeV\,\gamma}}{Y_{4.44\,MeV\,\gamma}}$, and the detector efficiencies determined from GEANT-4 simulation, $\frac{\epsilon_{15.11\,MeV\,\gamma}}{\epsilon_{4.44\,MeV\,\gamma}}$, terms in the R_{Th} equation, was determined to be 0.505 ± 0.026 and will also be discussed in the subsequent chapter. Accounting for PF, R_{Th} now becomes:

$$\boldsymbol{R_{Th}} = \boldsymbol{PF}\,\frac{\prod e^{-\alpha\frac{\mu_{15.11\,MeV\,\gamma}}{\rho}}}{\prod e^{-\alpha\frac{\mu_{4.44\,MeV\,\gamma}}{\rho}}} \qquad (3)$$

This simple equation allows determination of the R_{Th} for any cargo material configuration.

4.13 The presence of neutrons in the beam line

In this experiment, neutrons are not desirable and, through (n,γ), (n,n'), and other interactions, may create gammas that complicate the spectra and make integration of the 4.44 MeV gamma counts more difficult. The ^{11}B(d, nγ)^{12}C reaction creates a neutron with every ^{12}C* produced. It was experimentally confirmed that if left unshielded, the neutron flux in the beam line was so high that gammas from fast neutron inelastic scatter and neutron capture created a gamma continuum and pulse pile-up issues that greatly inhibited the ability to identify the 4.44 and, to a lesser extent, 15.11 MeV events in the NaI(Tl) detectors.

4.14 Use of a GEANT 4 simulation to model the impact of neutron induced events on the spectra

A collaborator conducted a GEANT4 simulation of the NaI(Tl) response to the incident gamma spectrum with and without the associated neutrons [**53**]. The presence of the neutrons resulted in interactions that added a continuum of gammas onto the gamma spectrum. The addition of HDPE removed neutrons from the beam line and changed the qualitative behavior of the spectra, as seen in Figure 26 [**52**]. The higher energy events did not significantly change the peak area of the 15.11 MeV gammas but added counts above the high-energy edge and a noticeable number of counts up to 12.5 MeV in the continuum. The neutrons also led to a change in the ability to discern between the 4.44 MeV FEP and SEP. The importance of removing neutrons from the beam line so they do not interfere with the gamma spectra will be discussed when the processes for determining the 4.44 MeV FEP and 15.11 MeV counts are addressed later in this section.

As seen in Figure 26, the presence of neutrons in the beam line introduces additional counts at energies above the 15.11 MeV edge and on top of the continuum. However, within the current 15.11 MeV integration region (previously shown in Figure 24) the detection of gammas from neutron-induced events does not appear to significantly alter the total number of counts. Nonetheless, reduction of the neutron flux in the beam line should lead to a more accurate measure of 15.11 MeV counts.

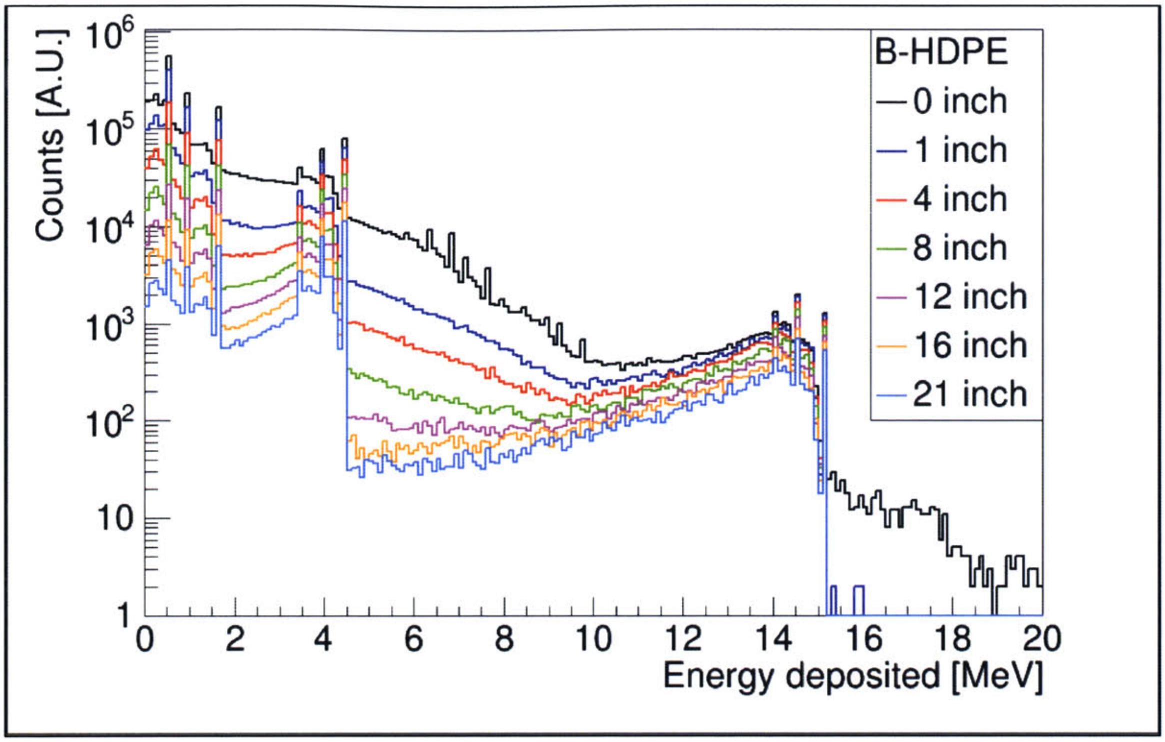

Figure 26. GEANT simulation of NaI(Tl) response to incident 4.44 and 15.11 MeV gammas with varying thicknesses of borated HDPE to remove neutrons. The presence of the neutrons leads to higher energy events beyond the right edge of the 15.11 MeV counts. Additionally, the presence of the neutrons changes the shape of the spectra near the 4.44 MeV full energy and single escape peaks. Thus, neutrons must be removed from the spectra to allow appropriate determination of 4.44 MeV peak counts.

The gamma continuum from neutron captures and inelastic scatters has a more profound effect on the 4.44 MeV FEP and SEP. (For a reminder of the 4.44 MeV FEP integration region see Figure 25.) Their presence changes the qualitative shape of the spectra and complicates identification of the 4.44 MeV FEP counts. Therefore, the reduction of neutrons in the beam line is necessary to ensure accurate identification of 4.44 MeV counts.

4.15 Testing the neutron spectra

To test the impact of the neutron flux on the spectra a 2"x2" organic scintillator (EJ309) with a 2" PMT was used to detect the fast neutrons using the same experimental setup as for experiments with the NaI(Tl) detectors. The data from the organic scintillator was used to compare the spectra of two separate configurations. The first configuration included 21" of HDPE but no attenuating materials. The second configuration consisted of 3" of Pb to attenuate gammas and no HDPE. The Pulse Shape Discrimination (PSD) results for both experiments are shown in Figure 27.

The PSD analysis compares the area of the pulse within the long gate, defined as 10 ns before pulse rise until 1000 ns after pulse peak, and the short gate, defined as 28 ns after pulse peak until 1000 ns after pulse peak. The recoil electrons (liberated in Compton events) deposit their energy over a much longer path length than the recoil ions (liberated by neutron scatters). The recoil ions deposit their energy over a much smaller path length, causing increased molecular interactions within the scintillator molecules, which leads to increase in emission of light as delayed fluorescence. Thus, comparing the tail of the pulses from electrons (smaller tail) with recoil ions (larger tail) allows discrimination between gamma and neutron induced events. This leads to a shift of the neutron-induced pulses upward in the PSD spectrum as compared to an equal sized pulse originating from a gamma interaction.

The mishandled events are due to pulse pile up issues. When several events are close enough together so that the signal does not fall below the lower level discriminator, the events are calculated as if they are only one pulse. Thus, several pulses can combine to create "apparent" pulses that do not fall into the neutron or gamma lobes.

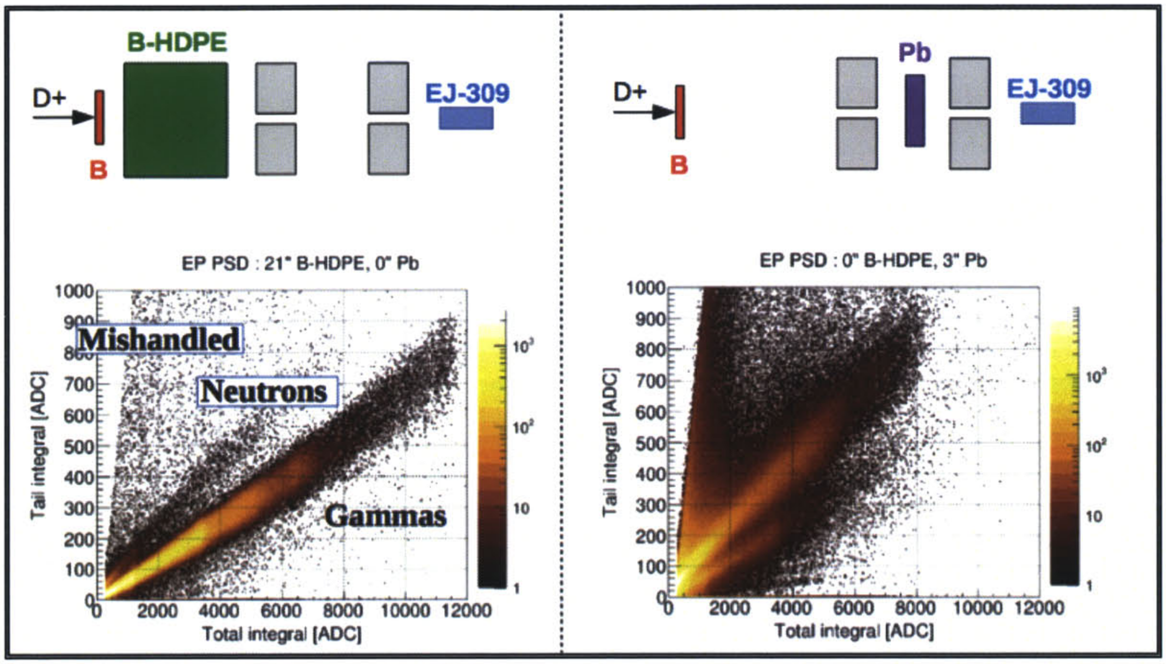

Figure 27. Impact of HDPE on Neutron and Gamma Spectra **[53]**. In the case of 21" of HDPE, shown to the left, most of the neutrons are removed from the spectra. A clear line of gammas remains. With no HDPE and 3" of Pb present, shown to the right, a strong neutron and low energy gammas are present. Pulse pile-up issues resulted in the strong third line in the case of no HDPE and 3" of Pb.

The presence of the HDPE, as seen to the left in the above graphic, greatly reduced the neutron counts, especially the higher energy events, but allowed passage of gammas. The absence of HDPE, seen in the above graphic to the right, showed significant neutron events, including higher energy events that could interfere with the identification of higher energy peaks. In both cases, mishandled pulses were the result of pulse pileup from excessive count rates and did not appear in the neutron or gamma bands.

4.16 Use of HDPE to reduce the impact of neutron-induced events on the spectra

An effort was made to remove neutrons from the beam line as early as possible to limit the acceptance angle of gammas from these events in the detector array. HDPE was placed immediately prior to the first set of collimators and spectra were taken with a NaI(Tl) detector and HDPE thicknesses from 11-21" to verify the 4.44 MeV peaks and 15.11 MeV continuum increased in clarity with the addition of more HDPE.

While it may be possible that additional HDPE could have produced additional benefits, the HDPE thickness was set to 21" for all subsequent experiments since geometric constraints precluded adding additional material between the radiation channel and the first set of collimators. The inclusion of the HDPE to reduce the neutron flux and nearly eliminate higher energy neutrons from the beam line reduced the 15.11 MeV flux to 35% and 4.44 MeV flux to 16% of their original values but significantly increased the ability to discern 4.44 and 15.11 MeV events.

4.17 Data acquisition and analysis software programs

ADAQAcquisition and ADAQAnalysis codes were used to acquire and process experimental and modeling data. These are locally developed software packages. These codes are part of the ADAQ data acquisition framework, which is being actively developed at MIT for general purpose radiation detector data acquisition with digital systems [**54**], [**55**]. The ADAQ framework is built with the ROOT toolkit and provides full control of digital data acquisition systems as well as comprehensive online and offline analysis capabilities. The ADAQAcquisition code was used to acquire all experimental and modeling data. The ADAQAnalysis code was used to analyze spectra using the same settings and procedures for both experimental and modeling data. The settings used during data acquisition and data analysis are included in Appendix F.

CHAPTER 5

HOMOGENEOUS AND NON-HOMOGENEOUS CARGOES, THEIR VULNERABILITIES, AND FUTURE EFFORTS TO ADDRESS VULNERABILITIES

This chapter addresses scanning of homogeneous and non-homogeneous cargoes, and potential scanning system vulnerabilities to high-Z material smuggling and future efforts to address these vulnerabilities. It provides a theoretical exploration of topics that are important to the experimental results addressed in subsequent chapters. Consideration is given to scanning a known homogeneous cargo, the limitations of scanning unknown homogeneous cargo, and the difficulties associated with characterizing an unknown homogeneous cargo. The complexities of scanning non-homogeneous cargoes are then addressed. Finally, the potential vulnerabilities of the proposed scanning system to the smuggling of high-Z materials and future efforts to address these vulnerabilities are addressed.

5.1 The Case of known Homogeneous Cargoes

The easiest cargo to scan and characterize is one consisting of a pure material. Figure 28 shows experimental spectra of Al, Fe, Cu, Mo, Sn, W, and Pb at an areal density of 68 $\frac{g}{cm^2}$ plus 57 $\frac{g}{cm^2}$ of HDPE for a total areal density of 125 $\frac{g}{cm^2}$. As the Z of the cargo increases 15.11 MeV integration region counts are reduced. The figure also shows less pronounced differences in 4.44 MeV counts. This is primarily a result of the differences in mass attenuation coefficients at 4.44 MeV previously addressed but is also impacted by other factors such as differences in deuteron current.[36] As we will see in the subsequent chapter, the experimental data is sufficient to discriminate with high confidence each material from the adjacent test materials and definitively state whether high-Z materials are present.

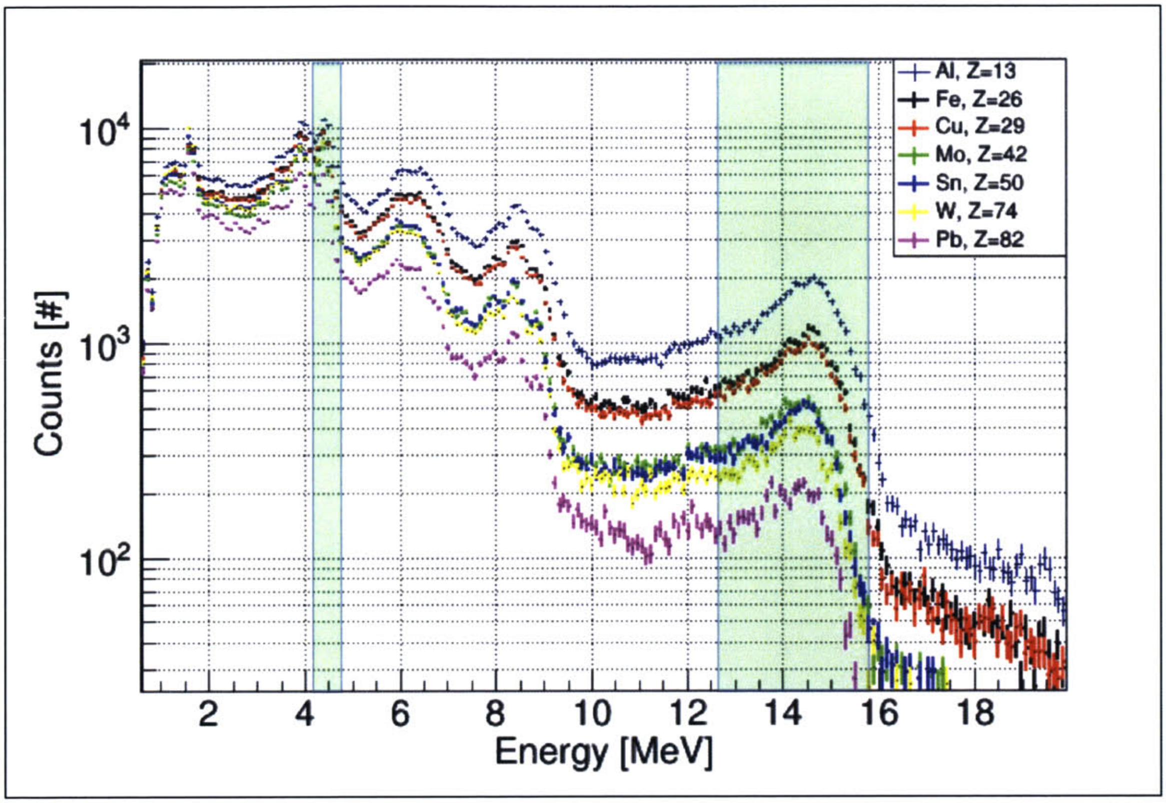

Figure 28. Experimental spectra of pure materials scanned using the proposed method. All pure materials have areal densities of approximately 68.3 g/cm^2. For each test there was also 57 g/cm^2 of HDPE present yielding a total areal density of approximately 125 g/cm^2. The shaded areas indicate the locations of the 4.44 MeV and the 15.11 MeV integration regions. Note the 4.44 MeV peak counts among materials does not change as dramatically as the 15.11 MeV integration region counts. The high-Z cargo more strongly attenuates the 15.11 MeV counts. Counts are normalized to a current of 10.5 μA. All data were taken for 1200 s.

---

[36] Integration of the deuteron beam current will allow better determination of the actual 4.44 MeV production rates and provide the ability to normalize out differences to beam current. Current estimates for the current are based on manual measurements at different times.

5.2 Limitations of Unknown Homogeneous Cargoes

The case of homogeneous cargo was a simplified problem. First, the areal density was known. Second, the materials were pure. Knowledge of the areal density, that the material is pure, and the number of produced and counted gammas, allowed use of the attenuation equation to determine the mass attenuation coefficient with error bars. The range of potential Z values includes all Z with mass attenuation coefficients (at both 4.44 and 15.11 MeV) that fall within the error bars. Without knowledge that the materials are pure and the areal density, the discrimination problem would have been more complicated. Without this information, the known gamma yields and detected counts would only provide the product of the mass attenuation coefficients and the areal densities.

A lack of knowledge about the areal density requires considering the full range of areal densities based on the 4.44 MeV attenuation. Using simple exponential attenuation and the produced and recorded 4.44 MeV counts and their associated errors it is possible to establish absolute upper and lower bounds of areal density. Calculating the lower and upper areal density bounds assumes the reduction of 4.44 MeV counts is a result of attenuation by the material with the greatest mass attenuation coefficient, U, or the lowest mass attenuation coefficient, Li.[37] It should be noted, even for a mixture of materials, this method still applies since any combination of mass attenuation coefficients for the materials tested cannot fall outside the range established by Li and U.

---

[37] Neptunium actually has a larger 4.44 MeV mass attenuation coefficient but U is chosen for practical purposes.

The relationship between attenuation of the 4.44 MeV line and the required areal density for the materials considered in this thesis to create a specific 4.44 MeV attenuation is shown in Figure 7. The same analysis for Li and U is depicted in Figure 29. Li requires an areal density 1.82 times that of U to achieve the same attenuation. This calculation assumed the 4.44 MeV counts were without uncertainty. The addition of error bars to counts expands this range but only by a few percent.

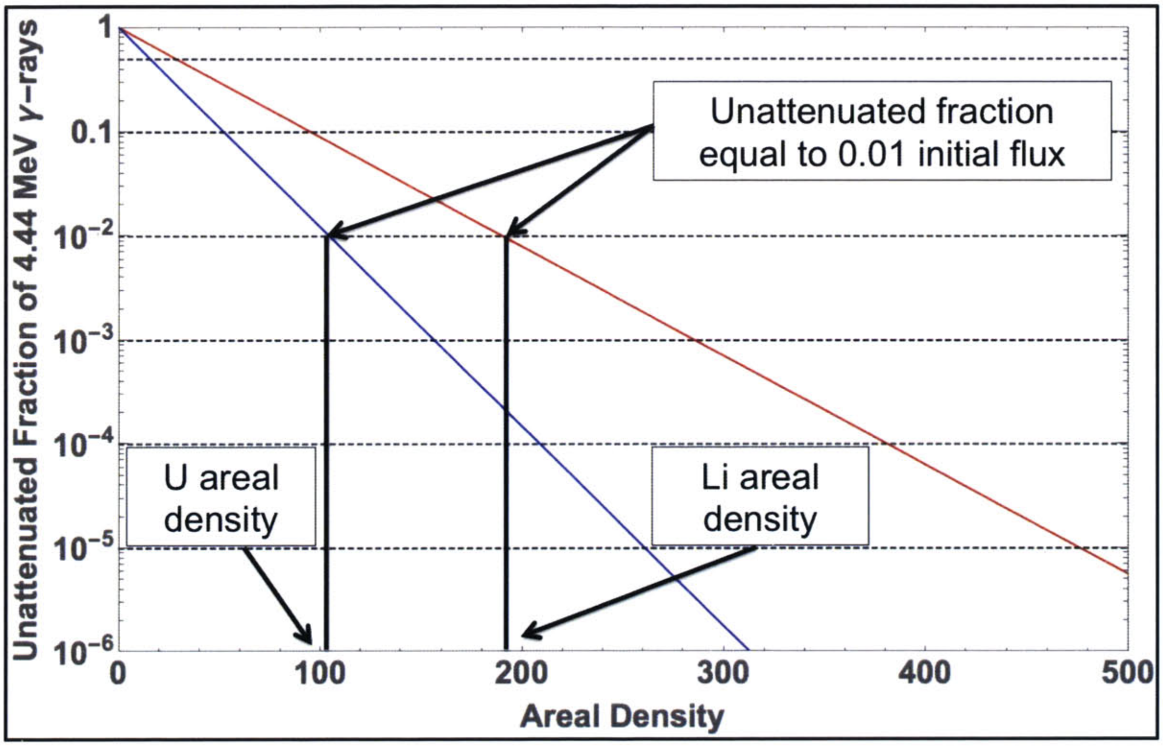

Figure 29. Relationship between the unattenuated fraction of 4.44 MeV gammas and areal density for Li and U. Note the log scale. As seen in the graph, Li must have an areal density 1.82 times greater than that of U to result in the same unattenuated fraction. This is because at 4.44 MeV, U has a mass attenuation coefficient (0.04414 cm^2/g) that is 1.82 times larger than that of Li (0.02419 cm^2/g). Since Li has the smallest mass attenuation coefficient at 4.44 MeV of all materials and U has the largest (Np actually has a larger mass attenuation coefficient but is not a practical consideration here), areal density estimations using the 4.44 MeV are always within a factor of 1.82 of the true value.

5.3 Characterization of unknown Homogeneous Cargoes

As an example of the best possible case for determining Z_{eff} for a cargo, an analysis was conducted of the pure materials test. For purposes of this example, the estimated attenuation, $f_{atten,i}$, for the HDPE in combination with the i^{th} material for a known areal density $\alpha(i)$ was calculated as

$$f_{atten,i} = e^{-\frac{\mu_{4.44\,MeV,\ HDPE}}{\rho_{HDPE}}\alpha(HDPE)} e^{-\frac{\mu_{4.44\,MeV,\ i}}{\rho_i}\alpha(i)} \qquad (4)$$

This estimation of the initial number of 4.44 MeV gammas produced, n_o, moving into the solid angle subtended by the detector was calculated by the product of the 4.44 MeV gamma production rate, deuteron current, and experimental run time. The lower bound of attenuation $f_{atten,LB}$ was calculated by adding three standard deviations to the recorded total 4.44 MeV counts: $f_{atten,LB} = (n_{4.44} + 3\,SD)/n_o$. The upper bound of attenuation $f_{atten,UB}$ was calculated by subtracting three standard deviations. The lower bound equates to less 4.44 MeV gamma attenuation and the upper bound to more attenuation. These values of attenuation were then substituted into (4) to solve for α for each material. The areal density, α, to achieve the same 4.44 MeV gamma attenuation was then calculated for every material Z for f_{atten}, $f_{atten,UB}$, and $f_{atten,LB}$.

The R_{Th} was calculated for the estimated, lower, and upper bounds for areal density for every material. The R_{Th} values were then plotted against the experimental measured ratio, R_{Exp}, and a graphical analysis was conducted to estimate the range of potential Z values. The estimated ranges of Z values for measurements of all materials are included in Table 6.

Table 6. Estimated Range of Z values for measurements of pure materials. The estimated Z range (Z_{Est}) is the range of potential Z values based on $R_{Exp} \pm 3\boldsymbol{\sigma}_{R_{Exp}}$. The R_{Th} values for all Z values were calculated and compared to $R_{Exp} \pm 3\boldsymbol{\sigma}_{R_{Exp}}$. The lower bound of the Z Est value is the Z where R_{Th} equals $R_{Exp} + 3\boldsymbol{\sigma}_{R_{Exp}}$. The upper bound of the Z Est value is the Z where R_{Th} equals $R_{Exp} - 3\boldsymbol{\sigma}_{R_{Exp}}$. The same method was used to calculate Z upper bound (Z_{UB}) and Z lower bound (Z_{LB}) ranges. Z_{Tot} accounts for the entire range of Z estimates.

	Al (13)	Fe (26)	Cu (29)	Mo (42)	Sn (50)	W (74)	Pb (82)
Z_{Est}	11.8-14.5	23.6-27	28-31.6	39.9-45	47-53	62.8-76.9	69-92
Z_{UB}	11.4-14.2	23.6-27	28-31.6	40.2-45.4	47.6-53.6	64-77	72-92
Z_{LB}	12.1-14.8	23.8-27	28-31.5	39.7-44.6	46.7-52.5	61.8-74	67-92
Z_{Tot}	11.4-14.8	23.6-27	28-31.6	39.7-45.4	46.7-53.6	61.8-76.9	67-92

Figure 30 shows the results for Sn. The range of Z-values is calculated based on R_{Th} values within three standard deviations of the measured value. The $R_{Exp} \pm 3\sigma_{R_{Exp}}$ for Sn are shown as dark horizontal lines. The potential Z-values are those Z with RTh values that fall between $R_{Exp} \pm 3\sigma_{R_{Exp}}$.[38]

The use of estimated error in attenuation is directly related to the observed 4.44 MeV gamma counts and associated error. Therefore, use of the known gamma production rates and detected counts allows establishment of a range of Z if the areal density is known. It should be noted that for this analysis, the actual experimental measurements were used. Table 7 shows number of standard deviations that the R_{Exp} differs from the R_{Th}. In the case of W, the measured ratio differed by 2.6 SD but the analysis still showed the potential Z-value range contains high-Z material. However, this was a very simplified case for homogenous cargo. As

---

[38] It should be noted that the Z upper bound signifies less 4.44 MeV attenuation and equates to a decrease in the areal density. For net enhancers, this should mean a slight decrease in ratios and therefore will shift the Z estimated range lower. For net reducers, this means a slight increase in ratios and will therefore shift the Z estimated range higher. The converse is true for Z lower bound. This pattern is seen in the data.

will be shown in the next section, non-homogeneous cargo is a much more complex problem.

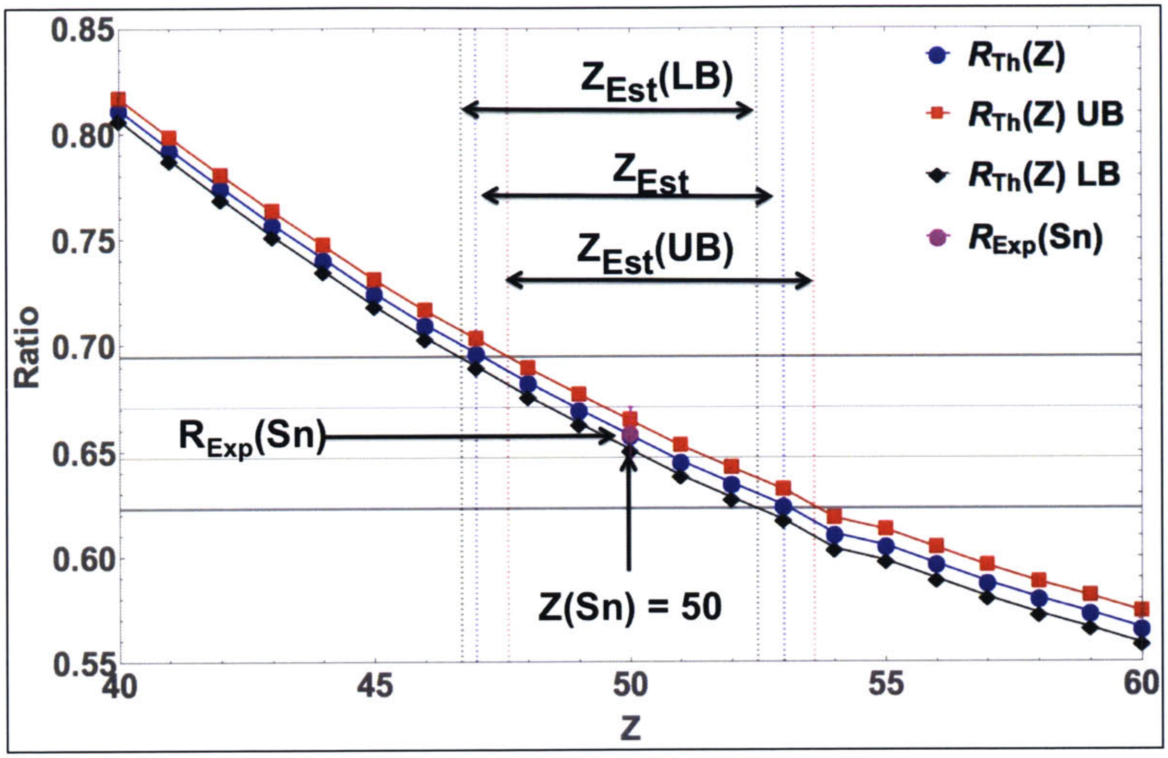

Figure 30. The range of potential ratios for all materials for a known attenuation of the 4.44 MeV gamma line compared with the experimentally measured ratio for Sn. For each Z, the ratio R_{Th} is shown. The actual data point with error bars is also present. Horizontal lines representing one standard deviation (thin) and three standard deviations (thick) in the experimental measurement were also added. Vertical lines, representing the potential range of Z values were added where the experimental ratio ± three standard deviations intersected with the R_{Th} values, were drawn to represent the potential Z values. For this particular case, the range of the potential Z values is 46.7 to 53.6, where 46.7 is calculated from the $R_{Th}(Z)$ lower bound and 53.6 from the $R_{Th}(Z)$ upper bound.

Table 7. R_{Exp}, R_{Th}, and their difference in number of standard deviations (# σ) for homogeneous cargo with an approximate areal density of 68.3 g/cm^2 of pure materials and 57 g/cm^2 HDPE for a total areal density of approximately 125g/cm^2.

	Al	Fe	Cu	Mo	Sn	W	Pb
R_{Exp}	1.892 ±0.034	1.248 ±0.022	1.090 ±0.019	0.760 ±0.015	0.659 ±0.012	0.486 ±0.009	0.405 ±0.010
R_{Th}	1.889	1.214	1.106	0.762	0.654	0.463	0.401
# σ	0.103	1.602	0.843	0.174	0.408	2.596	0.371

5.4 Complexities of Non-Homogeneous Cargoes

The material discrimination problem for non-homogeneous cargo is significantly more difficult. Some of the factors making discrimination of non-homogeneous cargo more challenging include:

- Combination of multiple materials, all with differing mass attenuation coefficients, creates a continuum of possible Z_{eff} values and effective mass attenuation coefficients[39], $\frac{\mu_{eff}}{\rho}$, for any given areal density.
- Uncertainty in areal density, α. It was previously noted that if pure materials are involved, the range in areal density is a factor of 1.82. The lack of knowledge about the cargo composition precludes reduction of this potential bound. This is further compounded by the errors associated with production and detection of the 4.44 MeV gammas used as a measure of areal density.
- Uncertainty in the ratio. The combination of the uncertainty in the areal density and the ratio of the 15.11 MeV to 4.44 MeV counts and relatively smooth variation in mass attenuation coefficients leads to a range of potential Z_{eff} values qualitatively similar to that seen for pure materials. However, the ability to determine Z_{eff} and the reliability of such measurements for combinations of materials is currently unknown.
- Uncertainty in the product of the areal density and effective mass attenuation coefficient. The measured reduction in 4.44 MeV counts and the known quantity of 4.44 MeV gammas produced in the direction of the detector actually provide a measure of the product of α and $\frac{\mu_{eff}}{\rho}$.

The difficulty in discriminating between two combinations of two pure materials with additional HDPE demonstrates some of the major challenges. As a simple example, a cargo with 57 $\frac{g}{cm^2}$ of HDPE, 62 $\frac{g}{cm^2}$ of Fe, and 138 $\frac{g}{cm^2}$ of Iodine (I) with Z_{eff} = 44.6[40] will attenuate 4.44 MeV gammas by a factor of $1.50\ x\ 10^{-4}$ and result in a R_{Th} of 0.367. A cargo with 57 $\frac{g}{cm^2}$ of HDPE, 175 $\frac{g}{cm^2}$ of Mo, and 25 $\frac{g}{cm^2}$ of I

---

[39] The effective mass coefficient attenuation coefficient is equivalent to μ/ρ for a mixed cargo.

[40] Zeff is the simple linearly weighted Z values, i.e. $\frac{62\frac{g}{cm^2}\cdot 26+138\frac{g}{cm^2}\cdot 53}{62\frac{g}{cm^2}+138\frac{g}{cm^2}} = 44.6$.

with a Z_{eff} of 43.4 will attenuate 4.44 MeV gammas by a factor of $1.52\ x\ 10^{-4}$ and result in a R_{Th} of 0.360. Figure 31 shows the ratios of the respective cargos with I replaced with all possible materials from $40 \leq Z \leq 92$. While this is one example of two material cargos providing similar signatures, not all materials at a given areal density can be combined to get both the same ratio and attenuation.[41]

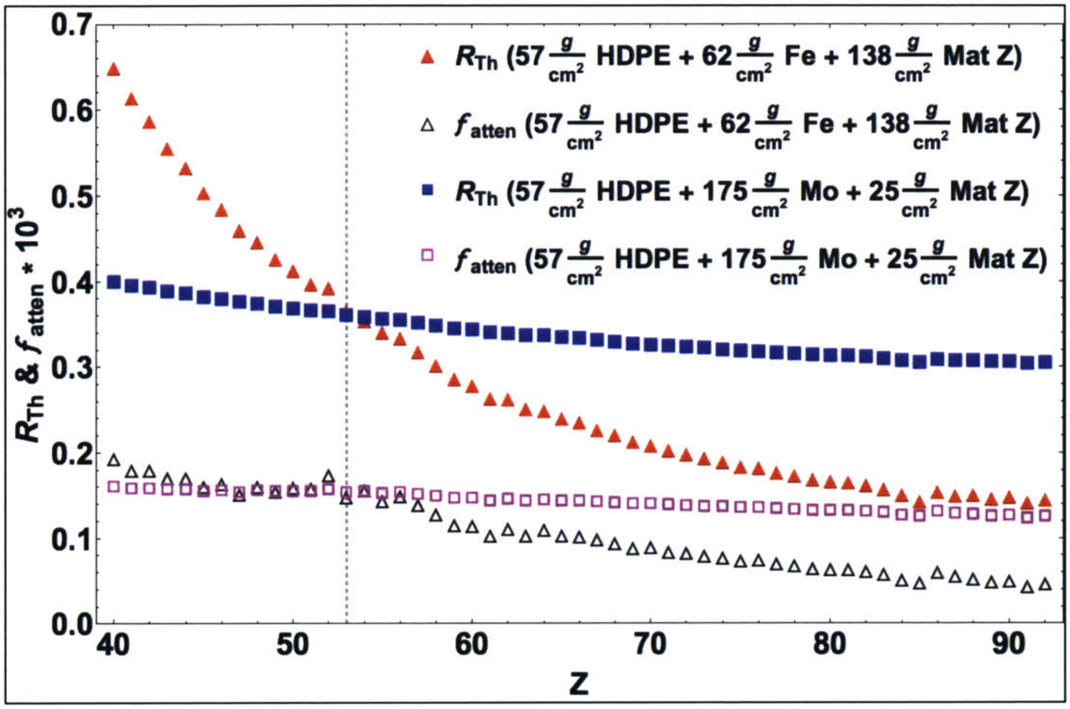

Figure 31. Comparison of Ratios and 4.44 MeV gamma attenuation for two equal-areal density cargos. One cargo configuration has 57 g/cm^2 of HDPE, 62 g/cm^2 of Fe, and 138 g/cm^2 of material Z while the other has 57 g/cm^2 of HDPE, 175 g/cm^2 of Mo, and 25 g/cm^2 of material Z. The respective ratios and attenuations for the two different configurations of HDPE, Fe, and I and HDPE, Mo, and I, which intersect the vertical line at Z = 53, are nearly identical. (Replacement of I with Xe is even more similar but is not a practical configuration.) This is an example of two different cargo configurations yielding almost identical signatures. Note the attenuation is scaled by a factor of 10^3 so the two graphs could be plotted together.

---

[41] The ability or inability to combine materials together to mask a high-Z material will be discussed more in the vulnerabilities section later in this chapter.

Determination of the areal density α for a known cargo requires knowledge of the initial flux I_o, detected flux I, and the mass attenuation coefficient of the materials $\frac{\mu_{4.44\,MeV}}{\rho}$. From rearranging the attenuation equation, the areal density is:

$$\boldsymbol{\alpha = Log\left(\frac{I}{I_o}\right)/\left(-\frac{\mu_{4.44\,MeV}}{\rho}\right)} \tag{5}$$

The uncertainty associated with areal density estimates for the cargo depends on the deuteron current, 4.44 MeV production rate, and 4.44 MeV full energy peak (FEP) counts with and without background.[42]

For an unknown cargo, neither the areal density nor the mass attenuation coefficients are known. With two unknowns, and only one equation, only a range of areal densities associated with a range of effective mass attenuation coefficients can be determined. The upper and lower boundaries for areal density remain those defined from attenuation by Li and U. The range of the effective mass attenuation coefficients is defined by all possible combinations of the weighted mass attenuation coefficients within the range of areal densities that lead to the product of α and $\frac{\mu_{eff}}{\rho}$ with error bars. The potential range of areal densities and effective mass attenuation coefficients will be discussed in a subsequent section.

In the course of the experiment, since the cargo configurations were known, it was possible to demonstrate that measured effective mass attenuation coefficient results matched closely to values calculated from known material thicknesses, densities, and NIST mass attenuation coefficients. To do so required knowledge of I, I_o, and their associated errors. I was directly measured by correcting the number of

---

[42] For purposes of this study no uncertainty is attributed to the mass attenuation coefficients or material densities.

4.44 MeV gamma counts recorded by the intrinsic efficiency of the detector. The uncertainty attributed to I was estimated from the FEP counts with (N_{bg}) and without background (N) from (6).

$$\boldsymbol{\sigma = \sqrt{2\,N_{bg} - N}} \tag{6}$$

Precise determination of I_o required knowledge of the deuteron current and stopping power thickness cross-section. The accelerator used for this experiment was not configured to provide the integrated current and the stopping power thickness cross sections were not known so it was not possible to determine theoretical I_o. As a substitute, a measurement of detected counts with only HDPE in the beam line was used to provide an estimate of the production rates of 4.44 and 15.11 MeV gammas per μC per second. To estimate the production rates, a measurement of a 21" of HDPE was conducted for one hour with current measurements taken every two minutes. The 4.44 and 15.11 MeV gamma production rates in the direction of the detector were determined to be 85.2 $\pm$ 0.7 and 31.1 $\pm$ 0.1 $\frac{\gamma}{\mu A \cdot s}$, respectively, at 1056 cm from the B target to the detector array for the set of combined material experiments. For the embedded material experiments this equated to gamma production rates of 107.8 $\pm$ 0.4 and 39.4 $\pm$ 0.1 $\frac{\gamma}{\mu A \cdot s}$, respectively, at 939 cm.

As a check of production rate estimates for 4.44 MeV, experimental $\frac{\mu_{eff}}{\rho}$ results were compared with theoretical results calculated from NIST data and show excellent agreement as seen in Figure 32. Z_{eff} was determined from a simple mass weighting $Z_{eff} = \prod_i Z_i \rho_i \Delta x_i \ / \ \prod_i \rho_i \Delta x_i$, where Z_i is the atomic number, Δx_i the material thickness, and ρ_i the density of each material.[43] The $\frac{\mu_{Th,eff}}{\rho}$ values were calculated in the same manner, with μ_i substituted for Z_i.

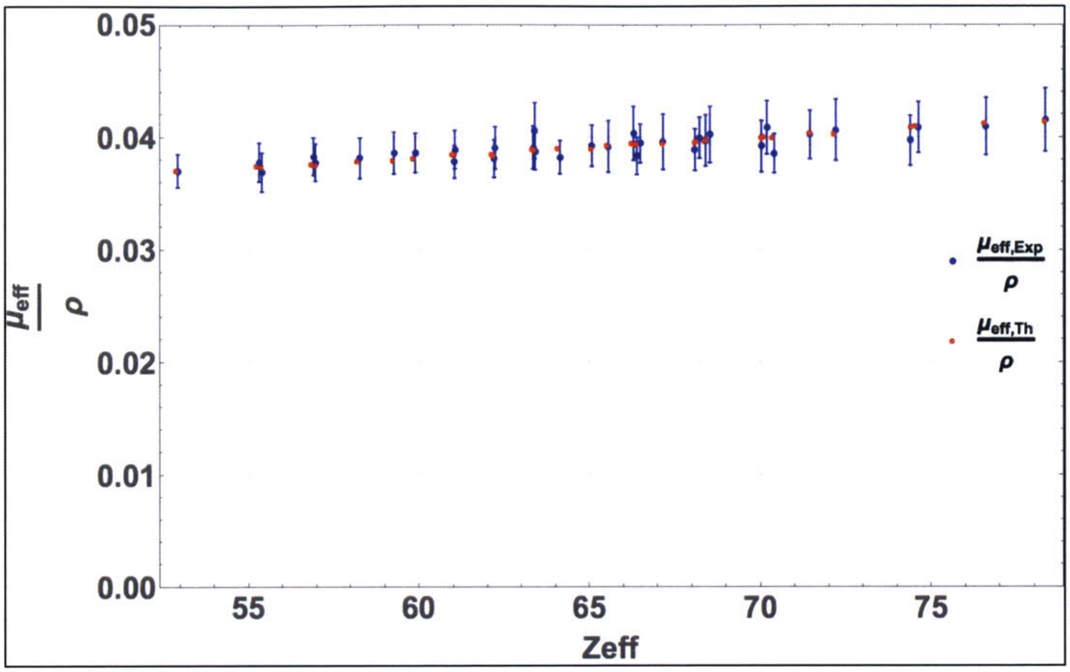

Figure 32. Comparison of theoretical effective mass attenuation coefficients at 4.44 MeV calculated from NIST values and experimental results for combinations of materials with total areal densities of 155-165 g/cm^2. Experimental mass attenuation coefficients were calculated based on experimental measurements for 4.44 MeV FEP counts, known cargo areal densities, and known 4.44 MeV gamma production. Theoretical mass attenuation coefficients were based on known cargo configurations and NIST values **[56]**.

As seen in this section, there are two major impediments that limit the capability of this scanning method. First, different cargo configurations can lead to the same attenuation and ratio, which makes them indistinguishable absent additional information. Second, the inability to decouple α and $\frac{\mu_{eff}}{\rho}$ presents a constraint that ultimately impacts how well this scanning method will perform in identifying the presence of high-Z material. While these are significant obstacles,

---

[43] The HDPE is considered part of the experimental apparatus and is not included in Z_{eff} calculations for the cargo.

there are potential solutions. For example, the use of additional gamma lines may increase the ability to differentiate between seemingly indistinguishable cargoes since it is less likely that two different cargoes will have the same effective mass attenuation coefficient at a third energy. The additional gamma lines provide additional measures of attenuation and ratios that can be used to reduce the range of potential areal densities and Z_{eff} values and will be discussed in subsequent chapters.

5.5 System Vulnerabilities to high-Z material smuggling

It should be noted the primary problem is determining if high-Z material is present and not differentiating between similar cargoes. The introduction of a threshold for detection, defined as the minimum areal density of high-Z material in a cargo that must be detected, simplifies the problem. The three major methods of concealing high-Z material in cargo are to either make the cargo "ratio neutral," attempting to hide high-Z material in significant quantities of medium-Z material through replacement of material, or placing the high-Z material in massive amounts of non high-Z material to increase statistical error and thereby reduce the ability to differentiate medium- and high-Z material.[44]

The "ratio neutral" method seeks to counteract the ratio reduction caused by the high-Z material by using low-Z material to preferentially reduce 4.44 MeV

---

[44] This list is not exhaustive. Other potential methods of smuggling material exist. For example, two additional potential smuggling methods include attempting to change the geometry of the high-Z material (e.g. hiding sheets thinner than the detection threshold) or changing the areal density. Changing the areal density may involve changing the physical character of the material, such as grinding into a fine powder. It could also involve modifying the chemical character, such as including the high-Z compound from which it can later be separated.

gammas. The neutral ratio impact is achieved through placement of enough low-Z material with the high-Z material such that the product of the ratios is one. For a given material, the areal density required to achieve a neutral impact on the ratio is defined as:

$$\alpha_{R_{Th}\,Complement} = \frac{\left(-\left(\frac{\mu_{15.11\,MeV,ref}}{\rho_{ref}} - \frac{\mu_{4.44\,MeV,ref}}{\rho_{ref}}\right) \cdot \alpha_{ref}\right)}{\frac{\mu_{15.11\,MeV,i}}{\rho_i} - \frac{\mu_{4.44\,MeV,i}}{\rho_i}} \qquad (7)^{45}$$

It should be noted that inclusion of the low-Z and high-Z material in the cargo still impacts the 4.44 MeV attenuation. Therefore, to "spoof" the system, the uncertainty in the $\alpha \cdot \frac{\mu_{eff}}{\rho}$ needs to be sufficient to mask the presence of the additional areal density associated with the net-enhancer and high-Z material. From (7) the areal density for low-Z materials from $3 \leq Z \leq 20$ requires 20-60 $\frac{g}{cm^2}$ of material to counteract the attenuation from a 1 cm thickness of W. Above Z = 20 the material areal densities required increase significantly. Table 8 shows the required low-Z material areal density to combine with a high-Z reference material to have a neutral impact on overall R_{Th}, the impact on attenuation of the low-Z separately and low- and high-Z materials together, and the total areal density added to a cargo to hide a 1 cm thickness of W in a cargo.[46] The areal density required and impact on attenuation increases significantly for material with Z > 20 making them less practical for use to hide high-Z materials using this method.

---

[45] Calculated by setting the product of the R_{Th} values equal to one and solving for the areal density of the low-Z material.

[46] W was selected instead of U because it has the lowest atomic number of the high-Z materials. With the proposed method, U is easier to determine than W so the more difficult material was considered.

Table 8. Required areal density of a low-Z material to combine with $R_{Th,ref}$ neutral impact on the overall R_{Th}, low-Z material attenuation, total areal density of the low- and high-Z material, and total attenuation of low- and high-Z reference material to hide a 1 cm thickness of W. Note the presence of the Li and C plus the 1 cm of W reduce the 4.44 MeV flux to about 1/4th (0.27 and 0.24, respectively), Al about 1/6th (0.17), and Fe to about 1/1000th (0.0008) of the value for the rest of the cargo. Since more low-Z material is required to mask the presence of a greater thickness of high-Z material this would have an even greater impact on attenuation and make this smuggling method less likely to succeed.

Low-Z Material	Areal density of low-Z material $\alpha_{R_{Th}\,Complement}$	Attenuation from low-Z material $f_{atten,material}$	Areal density of low-Z plus W α_{Total}	Attenuation from low-Z plus W $f_{atten,material+W}$
Li (3)	22.1	0.59	41.4	0.27
C (6)	21.8	0.53	41.1	0.24
Al (13)	33.1	0.37	52.4	0.17
Fe (26)	195.6	0.0018	214.9	0.0008

The second means of attempting to hide high-Z material through replacement of medium-Z material in cargo attempts to make the attenuation and ratio close to the surrounding cargo. A portion of the medium-Z cargo could be removed and replaced with high-Z material. The areal density to be removed and replaced by the reference material to have the same impact on R_{Th} is:

$$\alpha_{R_{Th}\,Equal} = \frac{\left(\left(\frac{\mu_{15.11\,MeV,ref}}{\rho_{ref}} - \frac{\mu_{4.44\,MeV,ref}}{\rho_{ref}}\right) \cdot \alpha_{ref}\right)}{\frac{\mu_{15.11\,MeV,i}}{\rho_i} - \frac{\mu_{4.44\,MeV,i}}{\rho_i}} \tag{8}$$

While there are differences in the impact on the ratio and attenuation between medium- and high-Z materials, the difference is less pronounced. Table 9 below shows the amount of incidental medium-Z material that a 1 cm or 1" thickness of W could replace without impacting the R_{Th} value for pure medium-Z material. The $f_{\alpha_{R_{Th}\,Equal}}/f_W$ represents the ratio of the attenuation from the pure material removed to that of the W it was replaced with. It is clear that the differences in relative attenuation are more significant for lower medium-Z materials but, as the material moves closer to Z = 74, the differences become more difficult to discern. Thus, medium-Z materials closer to Z = 74 serve as better materials in which to hide high-Z material.[47]

It should be noted that as the areal density of the high-Z material increases, differences in attenuation become more pronounced except for the highest of medium-Z materials. Thus, the 4.44 MeV gamma density measurement will show a dearth of 4.44 MeV gammas in the area and call attention to the potential presence of hidden high-Z materials.

Table 9. Areal densities of medium-Z materials impacting R_{Th} the same as a 1 cm and 1" thicknesses of W. The ratio of the attenuation by the material to that of a 1 cm thickness of W is also shown. A 1 cm or 1" thickness of W could replace the cited areal density of the medium-Z material and result in the same overall ratio but would result in an increased attenuation. For example, replacing 125.4 g/cm^2 of Mo with 1" of W would yield the same ratio but since the attenuation ratio of Mo to W is 0.10 the overall attenuation of the cargo would be reduced to 1/10th of the value for the cargo configuration without the W. Thus, higher medium-Z materials—which require areal densities more similar to that of the W material and have attenuation similar to W—are more effective at hiding the presence of high-Z materials.

	W = 1 cm		W = 1”	
Material (Z)	Areal density of material Z that has the same R_{Th} as W $\alpha_{R_{Th}\,Equal}$	Ratio of attenuation from material Z to that of W $f_{\alpha_{R_{Th}\,Equal}}/f_W$	Areal density of material Z that has the same R_{Th} as W $\alpha_{R_{Th}\,Equal}$	Ratio of attenuation from material Z to that of W $f_{\alpha_{R_{Th}\,Equal}}/f_W$
Y (39)	62.9	0.25	160.0	0.03
Mo (42)	49.4	0.40	125.4	0.10
Sn (50)	33.2	0.67	84.4	0.37
La (57)	26.7	0.83	67.8	0.62
Ce (58)	25.7	0.84	65.4	0.65
Eu (63)	22.7	0.91	57.7	0.79
Ta (73)	19.5	0.995	49.6	0.99

---

[47] It should also be noted that additional work should be done to determine which, if any, of the higher medium-Z materials are actually frequently transported in bulk and could be used to hide high-Z material.

The third means of attempting to hide high-Z material in cargo is to use significant mass to reduce the statistics to the point where error bars are large and discrimination of high-Z materials is problematic. This method could use low-Z, medium-Z, or a mix of medium-Z materials. Substantial quantities of any materials could lead to enough attenuation to make error bars large and discrimination of high-Z materials more difficult. However, significantly reducing the attenuation of a cargo container draws additional scrutiny.[48] This may lead to secondary screening or other additional protocols.

This thesis does not directly consider the "poor statistics" problem or the compensation tactic. It does, however, consider related problems. This thesis studies the problem of attempting to determine the presence of small amounts of high-Z material embedded in various areal density carrier materials. It also studies the ability to differentiate between small amounts of materials embedded in other cargo. Finally, it considers the impact of using various combinations of materials to shield U from detection. Specific efforts should be taken in the future to address these vulnerabilities.

5.6 Future Efforts to address scanning system vulnerabilities to high-Z material smuggling

Significant work should be conducted to determine the appropriate high-Z material areal density detection threshold. This thesis does not determine a high-Z material areal density threshold for the proposed system but it does consider the

---

[48] Research should be conducted to determine the frequency with which high areal density cargo passes through port facilities. Currently available data does not provide the areal density information needed for this analysis.

difficulty in detecting 1 cm, 1", and 3.54 cm of high-Z material in various areal densities of incident materials and can be used to inform further study.[49] A study of the higher medium-Z (> 50) materials should be undertaken to determine what materials are transported in bulk that could be used to shield high-Z material. Further study should consider detection of high-Z materials embedded in any lanthanides that may be transported in bulk since their impact on attenuation and R_{Th} are most similar to the high-Z materials. The results of such a study may lead to redefining what constitutes a high-Z material.

It should be noted that in any of the three potential smuggling techniques addressed, creation of images using multiple detectors in an array makes it less likely high-Z material in cargo can pass through undetected.[50] For example, in the "ratio neutral" case, images will show significantly more attenuation in one detector pixel as compared to the surrounding pixels.[51] The same is true for images created of cargo in which the second method is tried. Unless the hidden high-Z material is embedded in substantial quantities of medium-Z material so that statistical differentiation is no longer possible, the third smuggling technique will also be subject to probable detection. Any attempt to build an elaborate masking method using the three previously mentioned methods may be defeated by taking multiple

---

[49] Preliminary calculations showed that thicknesses associated with the Fetter devices would be relatively easy to detect. Therefore, smaller, more conservative thicknesses, were selected to gain insights about the possible areal density detection limits.

[50] It should be noted this thesis research used only one detector and, since only static cargoes were scanned, would only account for a single pixel in an image. The scanning system characteristics (e.g. linear scanning speed, detector array placement, detector dimensions, and temporal data processing) will ultimately determine image creation and resolution. Creation of an imaging system was beyond the scope of this research.

[51] It should also be noted that if there is a small area in the image where there is dearth of gamma counts, a system that uses high energy gammas to induce photofissions can be used to check for the presence of delayed neutrons. Photofission induction is not considered in this thesis.

images at different angles. Therefore, the proper size, spacing, and placement of detector arrays should be considered. The optimal size and type of detectors should also be considered.

CHAPTER 6
RESEARCH SCOPE AND OVERVIEW OF EXPERIMENTS

This chapter introduces and provides an overview of the experimental research for which the subsequent chapter provides detailed results. Specifically, this chapter reiterates the research and objectives and describes the experiments conducted.

6.1 Research Scope

The thesis demonstrates that multiple monochromatic gammas can be used to screen cargo to determine the presence or absence of high-Z materials shielded by low- to medium-Z materials. While this thesis does not solve the problems of accurately determining the areal density and Z_{eff} for an arbitrary configuration of materials it does provide insights into what might be possible. This work establishes two distinct sets of data that can be used as a future basis to develop models to address these challenges. The first set of experiments establishes how different Z materials embedded in Fe impacts the ratio. The second set of experiments explores how the ratio changes when U is shielded with combinations of various Z materials.

The major objectives of this thesis include:

- Demonstrate proof of principle that multiple monochromatic gammas can be used to screen cargo to determine the presence or absence of high-Z materials shielded by low- to medium-Z materials.
- Determine the validity of the R_{Th} model.
- Demonstrate the ability to discriminate among pure materials.
- Demonstrate the ability to discriminate between medium- and high-Z materials embedded in Fe.

- Experimentally establish how different Z materials embedded in Fe impact the 15.11 to 4.44 MeV gamma ratio.
- Explore how the 15.11 MeV to 4.44 MeV gamma ratio changes when U is shielded by combinations of various Z materials at near constant total areal density.
- Determine the ability to differentiate between medium- and high-Z material 19.3 g/cm^2, 49.0 g/cm^2, and 68.3 g/cm^2 areal densities.
- Determine the major theoretical and experimental challenges that must be addressed to develop a system to be placed in the field.

6.2 Overview of Experiments

This thesis explores the sensitivity, material combinations, and material discrimination issues. It does not seek to set a limit to sensitivity of the cargo screening method. However, it does consider the equivalent of a 1 cm thickness of high-Z material ($\sim 19\,\frac{g}{cm^2}$) to determine what is possible. The 19 $\frac{g}{cm^2}$ areal density threshold was selected to determine if it is possible to determine the presence of a 1 cm thickness of U hidden in cargo. Areal densities of 49 and 68.3 $\frac{g}{cm^2}$ of material are also considered to determine if 2.54 cm (1") and 3.54 cm thicknesses of high-Z material hidden in cargo can be identified. Consideration of these densities shows how small amounts of high-Z material can be identified even when hidden in larger amounts of low- and medium-Z cargo.

This thesis research involved two major experiments. The first set of experiments sought to determine the ability to identify the presence of Al, Fe, Cu, Mo, Sn, W, and Pb (test materials) embedded in various thicknesses of Fe. Each test also included 21" (57 $\frac{g}{cm^2}$) HDPE neutron absorber.[52] Four series of tests were conducted:

---

[52] The rationale for use of the HDPE was previously explained in sections 4.13-4.15.

- 19.3 $\frac{g}{cm^2}$ of test materials plus 57 $\frac{g}{cm^2}$ of HDPE and additional Fe for total areal densities of 155-255 $\frac{g}{cm^2}$. An experiment was conducted for each test material with six different Fe areal densities for a total of 42 individual tests.
- 49.0 $\frac{g}{cm^2}$ of test materials plus 57 $\frac{g}{cm^2}$ of HDPE and additional Fe for total areal densities of 165-245 $\frac{g}{cm^2}$. An experiment was conducted for each test material with five different Fe areal densities for a total of 35 individual tests.
- 68.3 $\frac{g}{cm^2}$ of test materials plus 57 $\frac{g}{cm^2}$ of HDPE and additional Fe for total areal densities of 165-245 $\frac{g}{cm^2}$. An experiment was conducted for each test material with five different Fe areal densities for a total of 35 individual tests.
- 68.3 $\frac{g}{cm^2}$ of test materials plus 57 $\frac{g}{cm^2}$ of HDPE for a total areal density of approximately 125 $\frac{g}{cm^2}$. No additional Fe shielding was included. Experiments were conducted on each material at two different distances from the natural boron target to the detector array for a total of 14 individual tests.

A total of 18 different configurations were tested for each of the seven test materials for a total of 126 individual tests. The 19.3 $\frac{g}{cm^2}$ embedded material tests accounted for 6 configurations, the 49.0 $\frac{g}{cm^2}$ and 68.3 $\frac{g}{cm^2}$ embedded material tests each accounted for 5 configurations, and the 68.3 $\frac{g}{cm^2}$ of test materials plus 57 $\frac{g}{cm^2}$ of HDPE accounted for the remaining two configurations. Table 10 lists the material (α_{Mat}), HDPE (α_{HDPE}), Fe (α_{Fe}), and total (α_{Tot}) areal density for each configuration. Note, as a reference, that 20 $\frac{g}{cm^2}$ is approximately equivalent to a 1" thickness of Fe.

The second set of experiments involved all possible combinations of three materials from Al, Fe, Cu, Mo, Sn, W, and Pb with a 1.1" diameter U rod for a total of 35 individual tests. The total areal densities for these experiments ranged from 155-165 $\frac{g}{cm^2}$. For all experiments, the 21" of HDPE accounts for 57 $\frac{g}{cm^2}$ of the total areal density.

Table 10. Areal density ($\boldsymbol{\alpha}$ $[\frac{g}{cm^2}]$) configurations of all series of tests conducted. The approximate areal density of the surrogate material (Al, Fe, Cu, Mo, Sn, W, and Pb) for each row of tests is listed under the $\boldsymbol{\alpha}$ of the material ($\boldsymbol{\alpha}$ Mat) column. All tests included 57 g/cm^2 of HDPE listed under $\boldsymbol{\alpha}$ HDPE. All series of tests in a row include the $\boldsymbol{\alpha}$ Mat and $\boldsymbol{\alpha}$ HDPE listed in the first two columns. The areal density of Fe for each test is listed under $\boldsymbol{\alpha}$ Fe and immediately followed by the total areal density of the test ($\boldsymbol{\alpha}$ Tot). For example, all tests in the first row include 19.3 g/cm^2 of embedded material and 57 g/cm^2 of HDPE. The first test in this series also includes 79 g/cm^2 of Fe plus for a total areal density (19.3 g/cm^2 + 57 g/cm^2 + 79 g/cm^2) of 155 g/cm^2. The second test in the series includes 99 g/cm^2 of Fe plus for a total areal density (19.3 g/cm^2 + 57 g/cm^2 + 99 g/cm^2) of 175 g/cm^2.

α_{Mat} $[\frac{g}{cm^2}]$	α_{HDPE} $[\frac{g}{cm^2}]$	α_{Fe} $[\frac{g}{cm^2}]$	α_{Tot} $[\frac{g}{cm^2}]$	α_{FE} $[\frac{g}{cm^2}]$	α_{Tot} $[\frac{g}{cm^2}]$	α_{FE} $[\frac{g}{cm^2}]$	α_{Tot} $[\frac{g}{cm^2}]$	α_{FE} $[\frac{g}{cm^2}]$	α_{Tot} $[\frac{g}{cm^2}]$	α_{FE} $[\frac{g}{cm^2}]$	α_{Tot} $[\frac{g}{cm^2}]$	α_{FE} $[\frac{g}{cm^2}]$	α_{Tot} $[\frac{g}{cm^2}]$
19.3	57	79	155	99	175	119	195	139	215	159	235	179	255
49.0	57	59	165	79	185	99	205	119	225	139	245	-	-
68.3	57	40	165	60	185	80	205	100	225	120	245	-	-
68.3	57	0	125	0	125	-	-	-	-	-	-	-	-

This thesis directly addresses the material combination issue through both sets of experiments.[53] Additionally, both experiments are used to study the behavior of the 15.11 MeV to 4.44 MeV ratio as a function of both effective atomic number Z (Z_{eff})[54] and areal density. The results of these experiments are used to validate the use of a simple model to predict the theoretical ratio of 15.11 to 4.44 MeV gammas within the experimental conditions considered. The impact of counting statistics and the associated error bars is considered in determining the ability to discriminate among different cargo configurations. Specifically, this thesis studies the ability to differentiate between the presence of medium- (Sn) and high-Z (W) material embedded in low- and medium-Z cargo.

---

[53] Numerous trial runs were conducted before the major experiments to optimize collimation and shielding, optimize data acquisition, determine the best HDPE placement to shield neutrons, and verify that order of the placement of materials in the beam line was not important.

[54] Z_{eff} is the simple linearly weighted Z values, i.e. $\sum_i \alpha_i Z_i / \sum_i \alpha_i$. For purposes of this work, HDPE is not considered for calculation of Z_{eff}.

CHAPTER 7

EXPERIMENTAL RESULTS AND ANALYSIS

This chapter includes experimental results and analysis. Calculation of the 4.44 and 15.11 MeV gamma yields is reported. The criterion for differentiation of medium- and low-Z materials is presented. The results for pure material, embedded material, and material combination tests are presented. The problem of identification of the 12 kg WGU weapon with 3 cm W tamper is revisited. The potential use of information gained from this scanning method for automatic clearance of cargo and creation of transmission and ratio images are also explored.

7.1 Calculation of the 4.44 to 15.11 MeV Gamma Yields for HDPE-only experiment

A single run of the experiment with no materials in the beam line except for the 21" HDPE was conducted to determine an independent measure of the production rates of 4.44 and 15.11 MeV gammas for the experimental configuration.

- Experiment run time: 3600 s
- Distance from the natural B source to the detector array: 1056 cm
- Deuteron current recorded every two minutes
- Recorded 4.44 MeV FEP counts: $N_4 = 64{,}933 \pm 522$
- Recorded 15.11 MeV FEP counts: $N_{15} = 69{,}632 \pm 264$
- Intrinsic efficiency for 4.44 MeV integration region = 0.158 ± 0.001
- Intrinsic efficiency for 15.11 MeV integration region = 0.464 ± 0.003

Based on the observed count rates, the gamma production rate (I_o) and error (σ_{Io}) in $\gamma/(\mu A \cdot s)$ into the solid angle subtended by the detector and error were found to be 85 ± 2 and 31.1 ± 0.7 $\gamma/(\mu A \cdot s)$ for 4.44 and 15.11 MeV gammas from:

$$I_o = \frac{N_{det}}{\epsilon_i \cdot time \cdot \mu A} \tag{9}$$

$$\sigma_{I_o} = \frac{N_{det}}{\epsilon_i \cdot time \cdot \mu A} \cdot \sqrt{\left(\frac{\sigma_N}{N_{det}}\right)^2 + \left(\frac{\sigma_{\mu A}}{\mu A}\right)^2 + \left(\frac{\sigma_{\epsilon_i}}{\epsilon_i}\right)^2} \tag{10}$$

Where N_{det} is the recorded counts (N_4 and N_{15}), σ_N the N_{det} error (σ_4 and σ_{15}) ϵ_i detector efficiency (ϵ_4 and ϵ_{15}), time is experimental run time, and μA is the average deuteron current.

As the deuteron slows down in the B target, the cross section for 4.44 and 15.11 MeV changes with the deuteron energy. At a deuteron kinetic energy of 1.63 MeV, excitation of the nucleus to the 15.11 MeV excited state is no longer possible. However, 4.44 MeV gammas can still be produced until the deuteron energy is not sufficient to allow the deuteron to approach within the range of the nuclear strong force.

To ensure maximum production of 15.11 and 4.44 MeV gammas, a 2 mm thick B target was used.[55] This exceeded the stopping power thickness of 3.0 MeV deuterons on B. The measured 4.44 to 15.11 MeV gamma production rate (GYR) was determined to be 6.0 ± 0.2. These were calculated from:

$$\boldsymbol{GYR = \frac{N_4/\epsilon_4}{N_{15}/\epsilon_{15}} \cdot \frac{e^{\mu_{HDPE,4} \cdot \Delta HDPE}}{e^{\mu_{HDPE,15\,MeV} \cdot \Delta HDPE}}} \tag{11}$$

$$\boldsymbol{\sigma_{GYR} = GYR \cdot \sqrt{\left(\frac{\sigma_4}{N_4/\epsilon_4}\right)^2 + \left(\frac{\sigma_{15}}{N_{15}/\epsilon_{15}}\right)^2}} \tag{12}$$

Where N_4 and N_{15} are recorded counts, ϵ_4 and ϵ_{15} detector efficiencies, σ_4 and σ_{15} the associated propagated errors, and the $\boldsymbol{e^{\mu_{HDPE} \cdot \Delta HDPE}}$ terms correct for attenuation in the HDPE.

---

[55] The stopping power thickness of 3.0 MeV deuterons on B was calculated as 48.57 μm ($4.857 \cdot 10^{-2}$ mm) from SRIM [77].

Geometrical limitations and high count rates prevented measurement of the GYR of the unshielded beam. This matches with the gamma yield ratio of 5.8 ± 0.3 for the entire experimental data set. The GYR for each test were calculated based on the observed number of counts using:

$$\frac{N_4/\epsilon_4}{N_{15}/\epsilon_{15}} \frac{\prod e^{\alpha \frac{\mu_4}{\rho}}}{\prod e^{\alpha \frac{\mu_{15}}{\rho}}} \tag{13}$$

Where N and ϵ remain as defined above, Π represents multiplication of the subsequent terms, α is the areal density of the ith material, and $\frac{\mu}{\rho}$ is the energy specific mass attenuation coefficient of the ith material. Figure 33 shows the GYR values calculated from experimentally measured 4.44 and 15.11 MeV gammas. The values have a Gaussian shape, with 70.7 % of measurements falling with one standard deviation (SD) of the mean, 87.1 % within 2 SD, and 96.5% within 3 SD.

As mentioned previously, there is insufficient 4.44 and 15.11 MeV gamma production cross section data to determine theoretical stopping power thickness production rates of 4.44 and 15.11 MeV gamma for 3.0 MeV deuterons on a B target. This precluded comparison of measured and theoretical production rates. Additionally, calculation of the experimental production yields depends on the intrinsic efficiencies calculated for the NaI(Tl) detectors used in this experiment. Any errors in the efficiency calculations would propagate through to the GYR calculation. While it is believed the efficiency calculations are reliable, an independent validation using a second model to determine intrinsic efficiencies or a different detector should be conducted.[56] Finally, in its current configuration, the DL-3 accelerator does not allow charge integration. Modifying the setup to allow the DL-3 to integrate charge could potentially improve production rate calculations, determination of cross sections, and produce more accurate GYR estimates.[57]

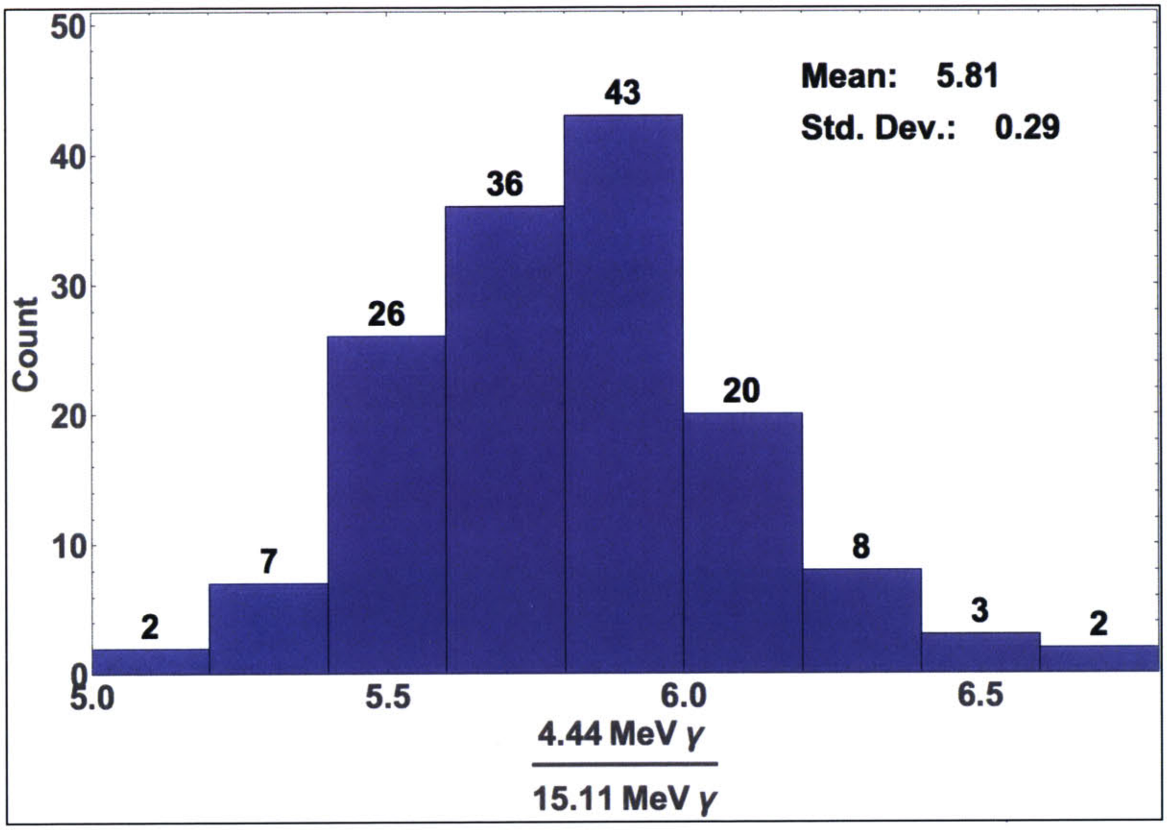

Figure 33. Histogram of measured ratio of 4.44 MeV gamma counts to 15.11 MeV gamma counts. The ratios are derived from experimental data from sixteen tests of materials embedded in various Fe areal densities and 35 tests for combinations of materials with U. Measured counts were corrected for detector efficiency and attenuation in cargo and HDPE.

---

[56] It should be noted the GEANT-4 model used was previously employed to accurately predict the experimental results for a LaBr and two NaI(Tl) detectors using various check sources.

[57] It should be noted that the theoretical Ratio equation only uses the ratio and not absolute rates of gamma production. However, the absolute production rate of 4.44 MeV gammas is needed to allow estimation of the areal density of the cargo.

7.2 Discrimination between low-, medium-, and high-Z materials

For purposes of this study, the ability to distinguish between materials falls into one of four categories:

- *indistinguishable* if the measurements are not different by more than a standard deviation (SD),
- *distinguishable* if they are different by more than one SD but less than two SD, *distinguishable with high confidence* if they are different by more than two SD but less than three SD, and
- *distinguishable with very high confidence* if they are different by more than three SD.

The measure of how different two measurements are in terms of the number of standard deviations separating them is described by:

$$\#SD = \frac{R_{Exp1} - R_{Exp2}}{\sqrt{\sigma^2_{R_{Exp1}} + \sigma^2_{R_{Exp2}}}}. \tag{14}$$

Where the R_{Exp} terms represent the experimental ratios and $\sigma_{R_{Exp}}$ the error of the experimental ratio for the two materials.

For example, to discriminate between medium- and high-Z materials, consider data from approximately 49.0 g/cm^2 Sn and W in 7" of Fe. The Sn and W ratios were measured as 1.01 ± 0.13 and 0.67 ± 0.06. The number of SD separating the two measurements is $\#SD = \frac{1.01-0.67}{\sqrt{(0.13)^2+(0.06)^2}} = 2.37$. Therefore, since the two measurements are separated by more than two standard deviations, we can be 95% confident that in a dedicated test we can differentiate between the medium-Z material Sn and high-Z material W.

7.3 Interrogation of Pure Materials

Each of the materials Al, Fe, Cu, Mo, Sn, W, and Pb was interrogated with approximately 68.3 $\frac{g}{cm^2}$ of the pure material and 57 $\frac{g}{cm^2}$ of HDPE for a total areal density of approximately 125 $\frac{g}{cm^2}$. The experiment was conducted twice, with the detector array at 939 cm (Test 1) and 1056 cm (Test 2) from the B target.[58] The measured values with errors, predicted values, and number of standard deviations of the error are included in Table 11.

Table 11. R_{Exp} with Error, R_{Th} Ratio, and # of Standard Deviations of the R_{Exp} from R_{Th} for Pure Materials with HDPE.[59]

	Al	Fe	Cu	Mo	Sn	W	Pb
R_{Th}	1.889	1.214	1.106	0.762	0.654	0.463	0.401
R_{Exp} Test 1	1.946 ±0.044	1.235 ±0.026	1.134 ±0.025	0.764 ±0.019	0.647 ±0.012	0.504 ±0.012	0.424 ±0.013
# σ	1.306	0.785	1.130	0.068	0.610	3.446	1.765
R_{Exp} Test 2	1.892 ±0.034	1.248 ±0.022	1.090 ±0.019	0.760 ±0.015	0.659 ±0.012	0.486 ±0.009	0.405 ±0.010
# σ	0.103	1.602	0.843	0.174	0.408	2.596	0.371

Note, as previously seen in Figure 28, the significant change in 15.11 MeV counts with increasing Z while the changes in 4.44 MeV peaks are much more subtle. This clearly shows the trend in differential attenuation of gammas for the materials that serves as the basis for this method. The origins of the peaks at 6-7 and 8-9 MeV have not yet been determined. These peaks are present in all of the experimental data, to include the HDPE only and pure material tests. The peak heights appear to

---

[58] Only one current measurement was taken for Test 1. Current estimations for Test 2 were taken every two minutes.

[59] Note that in both W tests, the R_{Exp} values were more than 2.5 σ larger than the predicted value. For the 1.39" W + Fe experiments, the R_{Exp} values were 1-2.5 σ greater than the R_{Th} values. The behavior was not as prominent at other W areal densities. Additional research and experiments should be conducted to determine if gammas produced from neutron interactions in W are impacting the 4.44 MeV FEP counts and/or 15.11 MeV integration region.

change with changes to the incident material, showing greater attenuation with greater cargo areal density and more for higher-Z material so they likely originate prior to the cargo in the B target area.[60]

7.4 Results from various material areal densities embedded in Fe

Three sets of experiments were run with different thicknesses of Al, Fe, Cu, Mo, Sn, W, and Pb embedded in various thicknesses of Fe:

- Six tests with embedded material thickness of approximately 19.3 $\frac{g}{cm^2}$
    - 57 $\frac{g}{cm^2}$ of HDPE
    - Fe areal densities in increments of 20 from 80-180 $\frac{g}{cm^2}$
    - Total areal densities of 155-255 $\frac{g}{cm^2}$
- Five tests with embedded material thickness of approximately 49.0 $\frac{g}{cm^2}$
    - 57 $\frac{g}{cm^2}$ of HDPE
    - Fe areal densities in increments of 20 from 60-140 $\frac{g}{cm^2}$
    - Total areal densities of 165-245 $\frac{g}{cm^2}$
- Five tests with embedded material thickness of approximately 68.3 $\frac{g}{cm^2}$
    - 57 $\frac{g}{cm^2}$ of HDPE
    - Fe areal densities in increments of 20 from 40-120 $\frac{g}{cm^2}$
    - Total areal densities of 165-245 $\frac{g}{cm^2}$

All experiments were carried out with a distance of 939 cm from the B target to the detector array. Run time varied from 20 minutes for the lowest areal densities to 90 minutes for the highest areal densities. The range of deuteron currents varied from 8.5 to 13 μA among tests.[61] It should be noted that the areal

---

[60] Future work is planned to determine the origins of the two peaks and to quantify their production. Subsequent work using the existing data will then be pursued to analyze these lines to gain additional information about cargo composition.

[61] During this set of experiments the current was only recorded once. Some drift was noted to the current during the experiments but was not accounted for.

densities were close, not equal, to 19.3 g/cm^2, 49.0 g/cm^2, and 68.3 g/cm^2. The actual areal densities used are found in Table 12.

Table 12. Comparison of nominal and actual areal densities of embedded materials used in the experiment in g/cm^2. The nominal areal density is listed in the first column. The actual areal density for each embedded material is listed underneath the material identifier. For example, for experiments with a nominal areal density of 49 g/cm^2, the Mo areal density used was 52.1 g/cm^2. Note the Sn areal densities are closer to the nominal values than the W areal densities.

Nominal Areal Density	Al	Fe	Cu	Mo	Sn	W	Pb
19.3 $\frac{g}{cm^2}$	20.4	17.6	19.3	19.9	19.2	16.2	21.6
49.0 $\frac{g}{cm^2}$	49.0	56.8	48.8	52.1	48.9	49.0	50.4
68.3 $\frac{g}{cm^2}$	69.4	74.4	68.1	72.0	68.1	65.2	72.0

Since the specific goal of this method is to discriminate between medium- and high-Z materials, the differences in material areal densities from the nominal reference values for Sn and W are important. The Sn areal densities are close to the reference values in all cases. However, the W areal densities are lower in two cases (16.2 vs. 19.3 and 65.2 vs. 68.3 $\frac{g}{cm^2}$) than the nominal values. The lower W areal densities in these cases make it more difficult to discriminate between Sn and W.

Results for material nominal areal density of 19.3 $\frac{g}{cm^2}$ embedded in Fe

The first embedded material tests were conducted for a nominal areal density of 19.3 $\frac{g}{cm^2}$. The actual areal densities for each embedded material are specified in the first row of Table 12. Tests included the specified embedded material areal density, 57 $\frac{g}{cm^2}$ of HDPE, and areal densities of Fe in 20 $\frac{g}{cm^2}$ increments from 80-180 $\frac{g}{cm^2}$ for total areal densities of approximately 155-255 $\frac{g}{cm^2}$. The measured R_{Exp} values for the tests closely approximated the R_{Th} values. Figure 34 shows the ratio of R_{Exp} to R_{Th} for all 42 tests with the R_{Exp} error bars shown.

The R_{Exp} versus Z_{eff}[62] values for these tests are shown in Figure 35. As expected, the ratio values generally decrease with an increase in Z_{eff}. As seen in the data, a small difference of only approximately 19.3 $\frac{g}{cm^2}$ of the embedded material can make a significant difference in observed ratios. For example, at all but the highest areal density, the ratios for configurations with embedded Al were approximately 50% larger than those with Pb. This same difference in ratios was not noted in the data with a total areal density of 255 $\frac{g}{cm^2}$. However, it is believed that changes to background and poor counting statistics are the reason the behavior was not observed and will be discussed later in this chapter.

---

[62] Z_{eff} is defined in section 3.2.

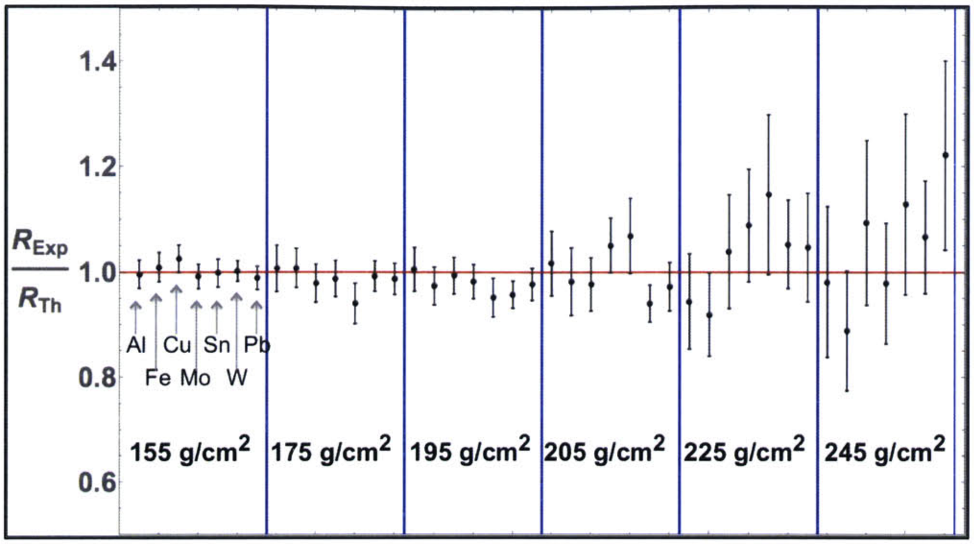

Figure 34. Ratio of the Experimental Ratio (R_{Exp}) to the Theoretical Ratio (R_{Th}) with R_{Exp} error bars. The vertical lines separate the six different total areal density tests ranging from 155-255 g/cm^2 in increments of 20 g/cm^2. Within each test, data points are for Al, Fe, Cu, Mo, Sn, W, and Pb. Each test contains approximately 19.3 g/cm^2 of the embedded material and 57 g/cm^2 of HDPE. Fe accounts for the balance of the areal density for each test.

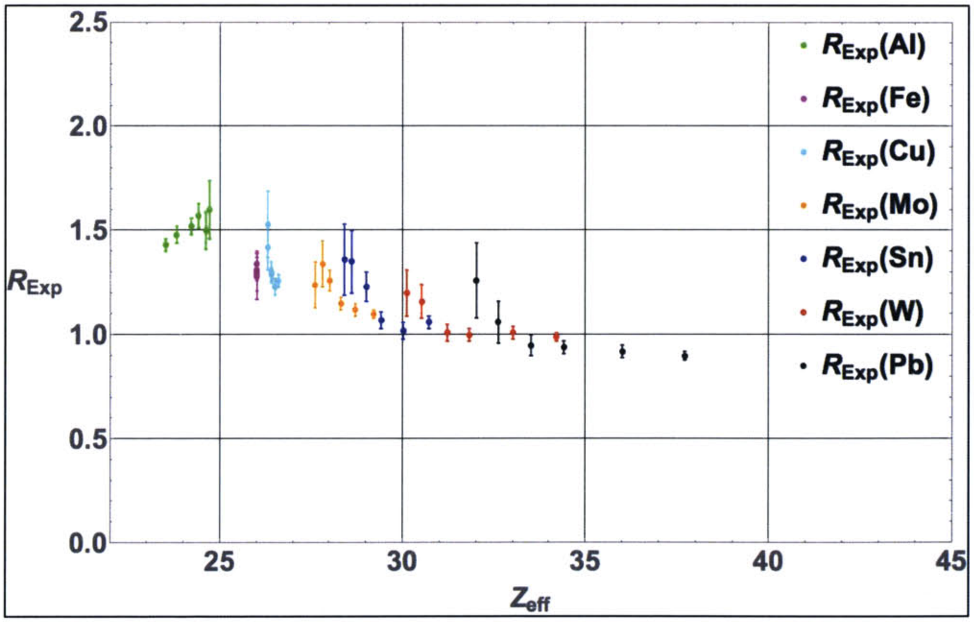

Figure 35. Experimental ratios (R_{Exp}) versus effective Z (Z_{eff}) for the approximately 19.3 g/cm^2 embedded material tests. For Al tests the total areal density of the tests increases from left to right since addition of Fe increases Z_{eff}. For Fe configurations Z_{eff} remains the same for all trials. All other materials have Z greater than 26 so increases in total areal density are from right to left since addition of Fe decreases Z_{eff} values. The closeness of the Sn (blue) and W (Red) ratios makes it difficult to distinguish between the materials.

Table 13 gives that number of standard deviations difference between Sn and W at each areal density for experiments with a nominal embedded material areal density of 19.3 $\frac{g}{cm^2}$. At four of the six areal densities it was possible to distinguish between medium- and high-Z materials. However, at 175 $\frac{g}{cm^2}$ the Sn and W ratios were indistinguishable. While the experimental data demonstrates the potential to identify a 1 cm thickness of high-Z material embedded in low- or medium-Z material, the results are inconclusive. The cargo with W was distinguishable from the cargo with Sn on three occasions and distinguishable with high confidence on one occasion. It was not possible to differentiate W from Sn at 175 and 255 $\frac{g}{cm^2}$. It is notable that at 255 $\frac{g}{cm^2}$, low count rates led to large error bars that make differentiating between materials difficult.

Table 13. Discrimination capability between medium- and high-Z materials for various areal densities with a nominal areal density of 19.3 g/cm^2 material embedded in Fe and HDPE. The discrimination capability is defined as the number of standard deviations between $R_{Exp}(Sn)$ and $R_{Exp}(W)$ as defined in Equation (14). The current and run time are also specified.

Areal Density	155 $\frac{g}{cm^2}$	175 $\frac{g}{cm^2}$	195 $\frac{g}{cm^2}$	215 $\frac{g}{cm^2}$	235 $\frac{g}{cm^2}$	255 $\frac{g}{cm^2}$
Discrimination Capability	1.94	0.20	1.40	2.73	1.12	0.79
Current (μA)	12	10.9	11.6	13.5	12	14
Run Time (s)	1200	1200	3600	3600	3600	5400

Results for material nominal areal density of 49.0 $\frac{g}{cm^2}$ embedded in Fe

The second embedded material tests were for a nominal areal density of 49.0 $\frac{g}{cm^2}$. The actual areal densities for each embedded material are specified in Table 12. Tests included the specified embedded material areal density, 57 $\frac{g}{cm^2}$ of HDPE, and areal densities of Fe in 20 $\frac{g}{cm^2}$ increments from 60-140 $\frac{g}{cm^2}$ for total areal densities of approximately 165-245 $\frac{g}{cm^2}$. The measured R_{Exp} values for the tests again closely approximated the R_{Th} values, as seen in Figure 36.

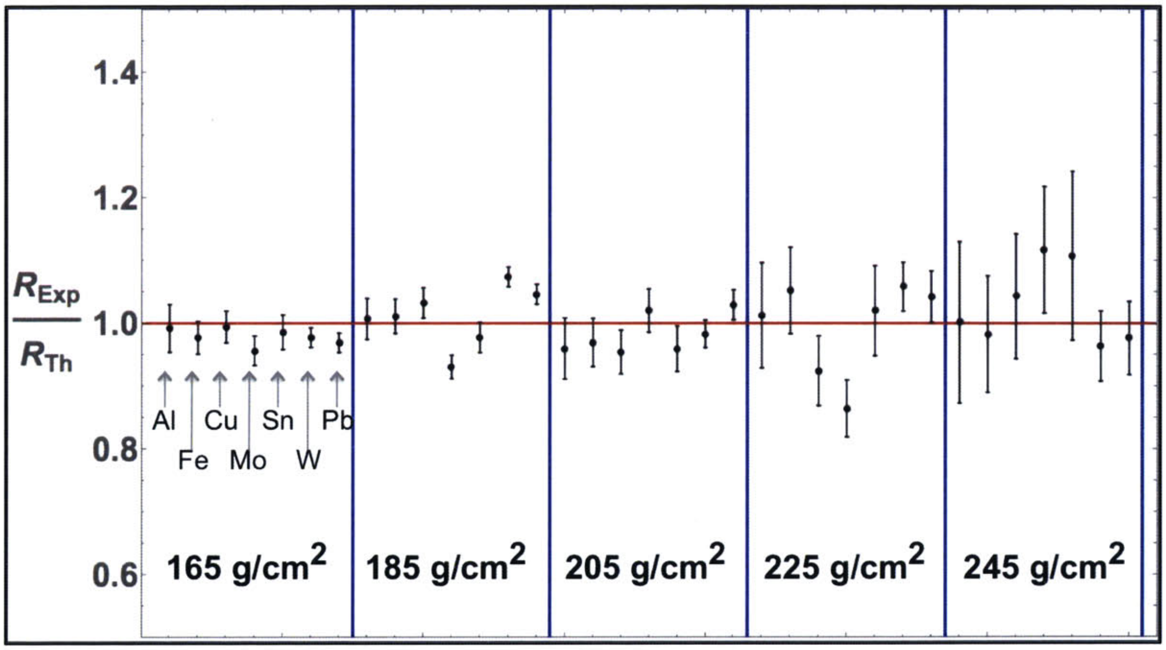

Figure 36. Ratio of the Experimental Ratio (R_{Exp}) to the Theoretical Ratio (R_{Th}) with R_{Exp} error bars. The vertical lines separate the five different total areal density tests ranging from 165-245 g/cm^2 in increments of 20 g/cm^2. Within each test, data points are for Al, Fe, Cu, Mo, Sn, W, and Pb. Each test contains approximately 49.0 g/cm^2 of the embedded material and 57 g/cm^2 of HDPE. Fe accounts for the balance of the areal density for each test.

The R_{Exp} versus Z_{eff} values for the 49.0 $\frac{g}{cm^2}$ embedded material tests are shown in Figure 37. The ratios exhibit the same dependence on Z_{eff} as previously observed. The increase in embedded material thickness further increases the difference between the ratio values for Al and Pb configurations. The Al ratios are now approximately 3-3.5 times larger than the Pb ratio values. More importantly, the increase in areal density of the embedded material makes it easier to discriminate between medium-Z Sn and high-Z W. The R_{Exp}(Sn) values are larger than the R_{Exp}(W) values for all total areal densities.

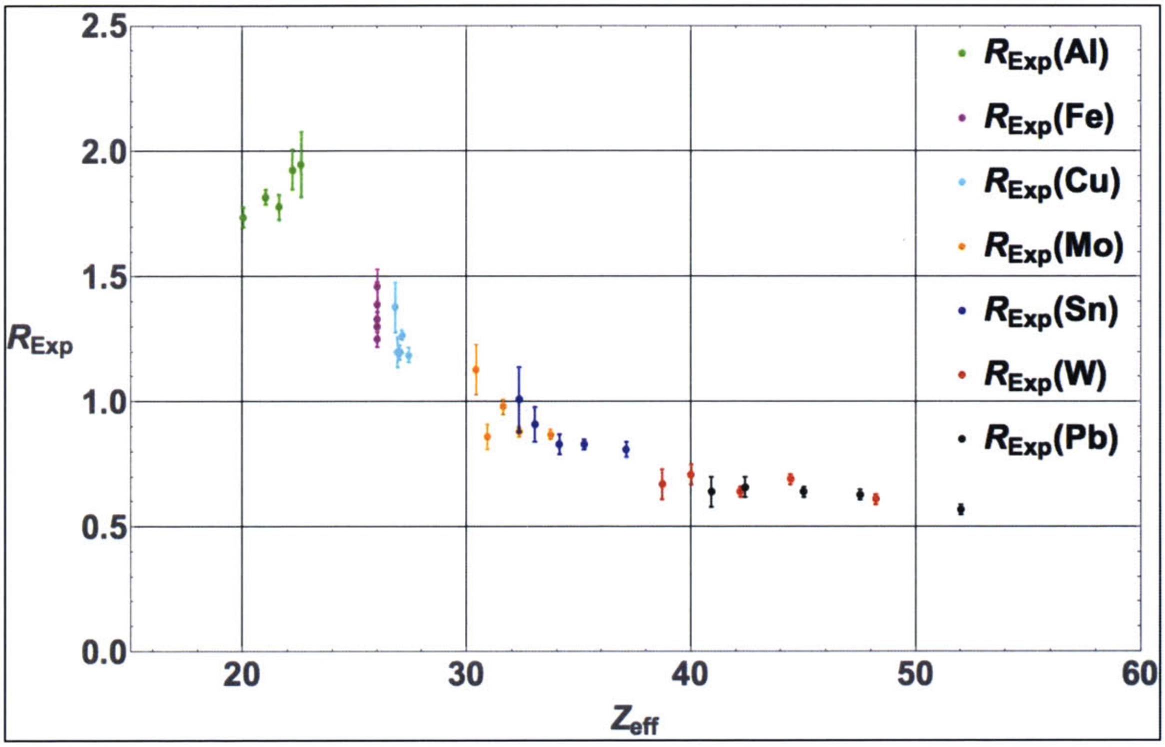

Figure 37. Experimental ratios (R_{Exp}) versus effective Z (Z_{eff}) for the approximately 49.0 g/cm^2 embedded material tests. The increase in embedded material areal density makes discrimination of Sn (in blue) and W (red) much easier.

The experimental data from embedding 49.0 $\frac{g}{cm^2}$ of materials in five different total areal densities from 165-245 $\frac{g}{cm^2}$ demonstrates the ability to identify the presence of high-Z material and distinguish medium- and high-Z materials. Table 14 shows the ability to differentiate between hidden medium- and high-Z material with very high confidence at three and with high confidence at an additional two areal densities. This is a notable increase in the ability to discriminate among embedded medium- and high-Z materials.

Table 14. Discrimination capability between medium- and high-Z materials for various areal densities with 49.0 g/cm^2 material embedded in Fe. The embedded material accounts for 49.0 g/cm^2 and HDPE for 57 g/cm^2 of the areal density. The balance of the areal density is from Fe.

Areal Density	165 $\frac{g}{cm^2}$	185 $\frac{g}{cm^2}$	205 $\frac{g}{cm^2}$	225 $\frac{g}{cm^2}$	245 $\frac{g}{cm^2}$
Discrimination Capability	5.55	4.95	4.24	2.48	2.37
Current (μA)	14.3	13.5	12.5	12.5	13.5
Run Time (s)	1200	3600	3600	3600	5400

Results for material nominal areal density of 68.3 $\frac{g}{cm^2}$ embedded in Fe

The third embedded material tests were for a nominal areal density of 68.3 $\frac{g}{cm^2}$. The actual areal densities for each embedded material are specified in Table 12. Tests included the specified embedded material areal density, 57 $\frac{g}{cm^2}$ of HDPE, and areal densities of Fe in 20 $\frac{g}{cm^2}$ increments from 40-120 $\frac{g}{cm^2}$ for total areal densities of approximately 165-245 $\frac{g}{cm^2}$. The measured R_{Exp} values for the tests again closely approximated the R_{Th} values, as seen in Figure 38.

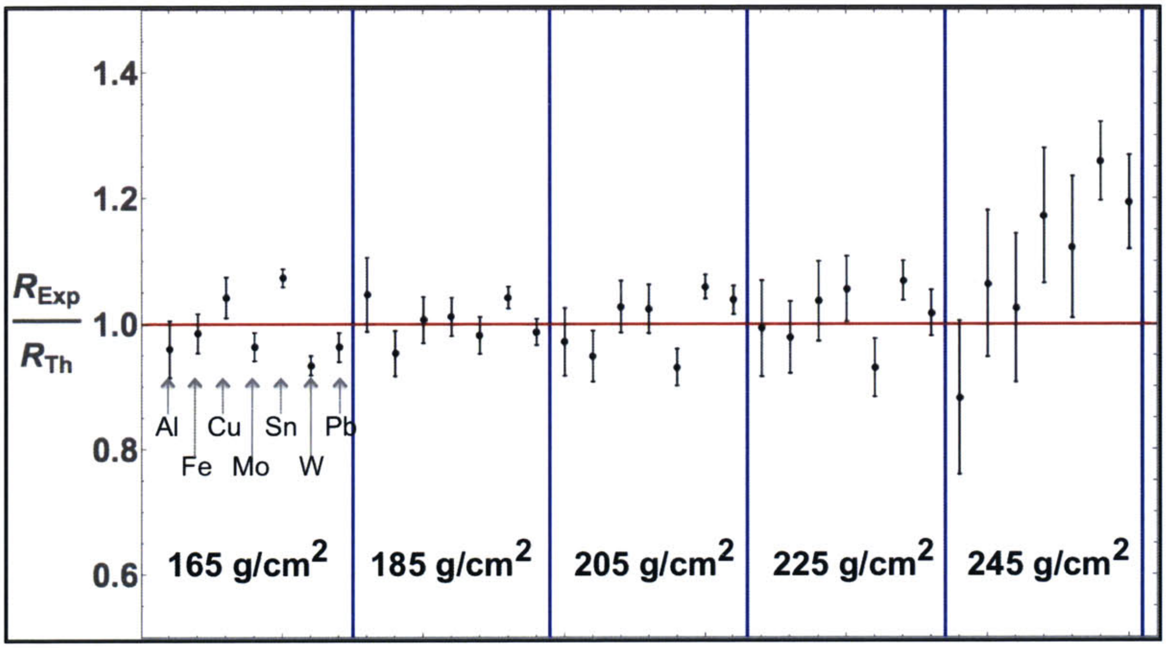

Figure 38. Ratio of the Experimental Ratio (R_{Exp}) to the Theoretical Ratio (R_{Th}) with R_{Exp} error bars. The vertical lines separate the five different total areal density tests ranging from 165-245 g/cm^2 in increments of 20 g/cm^2. Within each test data points are for Al, Fe, Cu, Mo, Sn, W, and Pb. Each test contains approximately 68.3 g/cm^2 of the embedded material and 57 g/cm^2 of HDPE. Fe accounts for the balance of the areal density for each test.

The R_{Exp} versus Z_{eff} values for the 68.3 $\frac{g}{cm^2}$ embedded material tests are shown in Figure 39. The ratios exhibit the same dependence on Z_{eff} as seen in the previous two sets of tests. The increase in embedded material thickness further increases the difference between the ratio values for Al and Pb configurations to almost a factor of 4. It is notable that the R_{Exp}(Sn) and R_{Exp}(W) are well separated at all but the highest areal density. These data points are the leftmost points of their respective data sets in the graphic. For the 245 $\frac{g}{cm^2}$ total areal density case, R_{Exp}(W) was 2.24 standard deviations higher than R_{Th}(W) but, as will be shown below, it was still possible to differentiate between Sn and W embedded in the Fe.

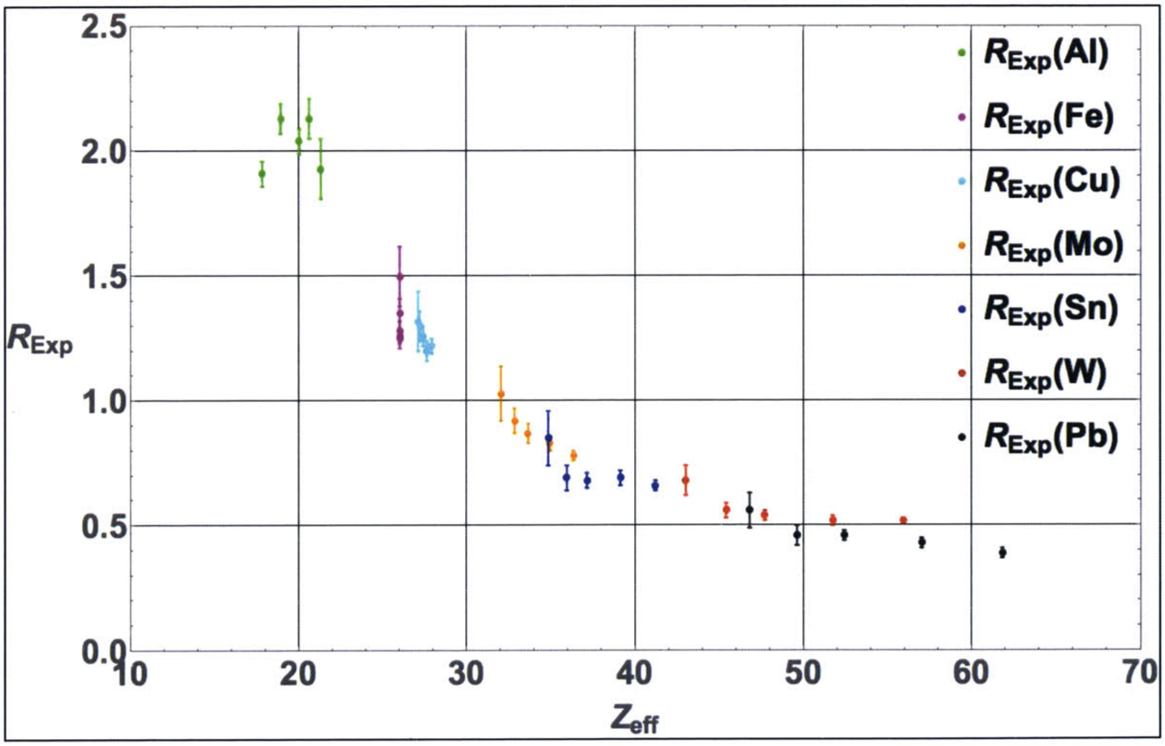

Figure 39. Experimental ratios (R_{Exp}) versus effective Z (Z_{eff}) for the approximately 68.3 g/cm^2 embedded material tests.

Table 15 depicts that number of standard deviations difference between Sn and W at each areal density for experiments with a nominal embedded material areal density of 68.3 $\frac{g}{cm^2}$. At all five areal densities tested, it was possible to differentiate between low-, medium-, and high-Z materials. At the three lowest areal densities it was possible to differentiate cargo with high-Z material from medium-Z materials with very high confidence, with high confidence at 225 $\frac{g}{cm^2}$, and with confidence at 245 $\frac{g}{cm^2}$. The discrimination capability at an embedded material areal density of of 68.3 $\frac{g}{cm^2}$ was similar to that at of 49.0 $\frac{g}{cm^2}$ for all but the highest areal density configuration. At this configuration, the discrimination capability was only a 1.36 versus 2.37 for the case of 49.0 $\frac{g}{cm^2}$. However, the run time was also only 3600 seconds instead of 5400 seconds and likely accounts for much of this difference.

Table 15. Discrimination capability between medium- and high-Z materials for various areal densities with 69.3 g/cm^2 material embedded in Fe. The embedded material accounts for 69.3 g/cm^2 and HDPE for 57 g/cm^2 of the areal density. The balance of the areal density is from Fe.

Areal Density	165 $\frac{g}{cm^2}$	185 $\frac{g}{cm^2}$	205 $\frac{g}{cm^2}$	225 $\frac{g}{cm^2}$	245 $\frac{g}{cm^2}$
Discrimination Capability	6.26	4.71	3.88	2.23	1.36
Current (μA)	14.5	14.3	13	13	14.3
Run Time (s)	1200	1800	3600	3600	3600

7.5 Observed trends in the results from embedded material configurations

The data did not determine an absolute minimum areal density threshold for detection of high-Z material embedded in low- and medium-Z material. The 19.3 $\frac{g}{cm^2}$ areal density tests were inconclusive. However, the data did demonstrate that, within the conditions of the experiment, areal densities of 49.0 $\frac{g}{cm^2}$ and above are detectable. Differentiation was possible at these larger embedded material areal densities because the impact on the ratio for the high-Z materials increased the relative separation between the R_{Exp} values for medium- and high-Z materials. Larger embedded material areal densities would make high-Z materials increasingly separated from low- and medium-Z materials.[63] Figure 40 shows experimental results for embedded material areal densities of 49.0 $\frac{g}{cm^2}$ and 68.3 $\frac{g}{cm^2}$ corrected to standard current and scan times.

The lack of success at an embedded material areal density of 19.3 $\frac{g}{cm^2}$ and substantial success at larger areal densities indicates additional theoretical and experimental work should be conducted to determine the potential limits of detection for the proposed system and to establish a minimum areal density detection threshold.[64]

---

[63] It should be noted that if overall areal densities are increased to the point where total counts are low and error bars are large, differentiation becomes more difficult and, in some cases, impractical.

[64] It should also be noted that the detection threshold depends on the number of counts so increasing the current and/or scan time leads to a lower detection threshold. Therefore, a practical threshold will depend on the allowable dose and scan time. This may vary for primary and secondary scanning.

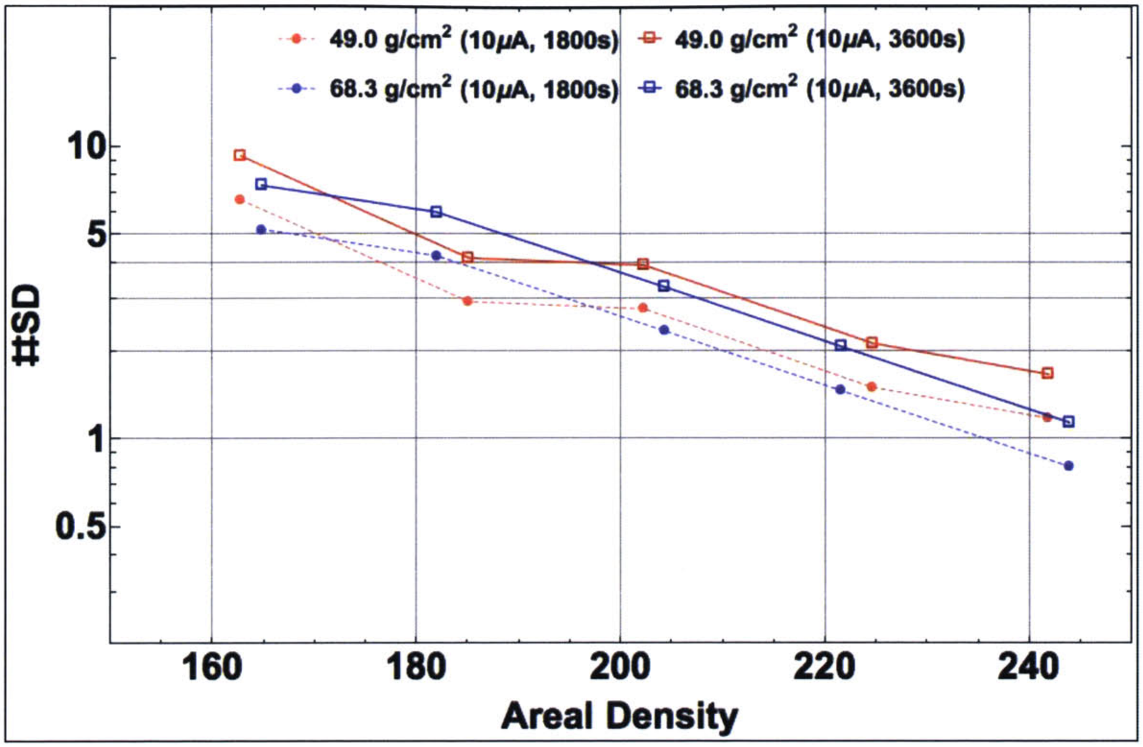

Figure 40. Differences in Sn and W at 49.0 and 68.3 g/cm^2 embedded material areal density as a function of total areal density for two separate scan times. An increase in scan time (or current) increases counts, reduces uncertainty, and leads to an increased ability to differentiate between embedded medium- and high-Z materials.

It was also noted that for all embedded material areal densities, at 230 $\frac{g}{cm^2}$ and higher total areal densities, R_{Exp} values were consistently higher than R_{Th} values (See Figure 34, Figure 36, and Figure 38). It is believed that experimental values are higher because of increased difficulty in determining the actual 4.44 MeV counts. As the areal density increases, more radiation scatters into the vicinity of 4.44 MeV and lower energies and the character of the spectra changes. These changes make it more difficult to accurately determine the number of 4.44 MeV FEP counts. The increased background is reflected in an increase in the size of the error bars at larger areal densities as seen in Figure 34, Figure 36, and Figure 38. At the same time, the changing background has no noticeable impact on the 15.11 MeV integration region. The impact of the changing background spectrum on the 4.44 MeV FEP integration and coupled with no noticeable impact on the 15.11 MeV integration region leads to consistently higher R_{Exp} values. These results indicate additional work should be conducted to determine if a better algorithm for background removal could lead to more consistent results.

An additional problem that occurred for all embedded material areal densities, at 230 $\frac{g}{cm^2}$ and higher total areal densities, was that large error bars from increased background in the vicinity of the 4.44 MeV gammas made discrimination between medium- and high-Z materials more challenging. Low counts at 4.44 and 15.11 MeV directly contributed to the large error bars. Therefore, one potential solution is to increase the deuteron current from the current low rate of approximately 10 μA to closer to the rated capacity of 90 μA. This would increase does rates and require modification of existing data acquisition techniques and update of the shielding configuration. This maximum current that can be used is also dependent on the incident flux on the detector since an excessive flux could lead to pulse pile-up. Another potential solution is to increase the scan time. However, it should be noted the current count times are excessively long and that in a fielded system count times must be necessarily short to prevent impedance of commerce. Finally, a more practical solution may be to vary beam current with observed count rates. This would avoid pileup issues for low attenuation cargoes and reduce the scan time for high attenuation cargoes.

It was also noted that changes to the areal density of materials also changed the character of the background. As seen in Figure 41, which plots histograms for variable thicknesses of pure Fe experiments, the adjacent gamma ray counts began to approach the 4.44 MeV FEP and SEP counts with increases in areal density. This flattening of the peaks relative to the counts in adjacent bins made background removal more difficult. Alternative approaches to background removal should be considered. Additionally, better results may be achieved by considering counts in both the 4.44 MeV FEP and SEP instead of just the FEP.

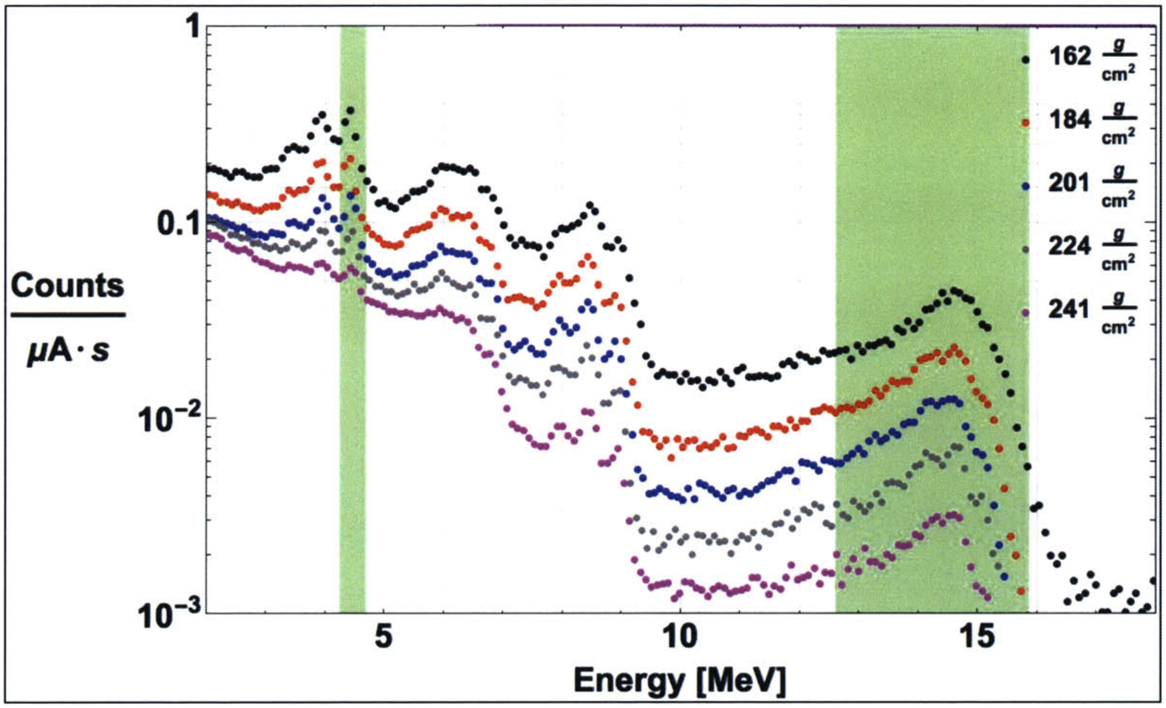

Figure 41. Actual spectra for pure Fe for various thicknesses. Histograms are normalized to account for differences in deuteron current and detection time. As Fe thickness increased, representing areal density changes in increments of 20 from 160 to 240 g/cm^2, the 4.44 MeV FEP and SEP peak heights decreased relative to adjacent bins. This made background removal more difficult.

7.6 Observed trends in the results from embedded material configurations shows the utility of the R_{Th} model

Figure 42 shows a plot of all R_{Th} and R_{Exp} values for the sixteen embedded material configurations. This plot clearly shows the R_{Th} model predicts the impact of Z_{eff} on the R_{Exp} value and does a good job predicting R_{Exp} values.

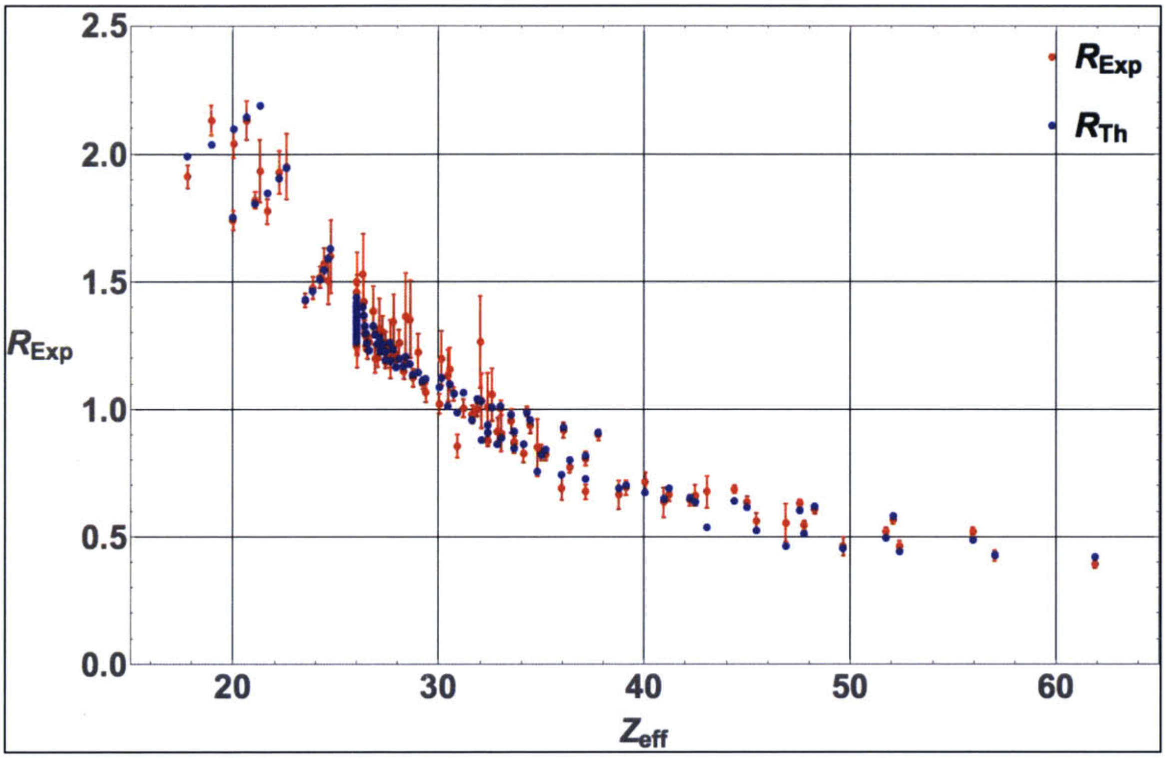

Figure 42. R_{Th} and R_{Exp} versus Z_{eff} for all embedded material configurations. The R_{Th} model reproduces observed experimental results and predicts dependence of the ratio on Z_{eff} of the scanned cargo.

The success of the R_{Th} model is an important accomplishment because this indicates it can be used to support further development of the proposed scanning technique. For example, a program could be developed to pull gamma production data from low-threshold nuclear reactions and mass attenuation coefficients for all materials to determine which interactions or combinations of interactions can be used to best identify the presence of high-Z materials embedded in low- and medium-Z materials.

The locations where R_{Th} did not perform as well were limited to those where areal density was very high and counting statistics were poor. Ideas to improve experimental performance, which should bring experimental values for these problem areas closer to predicted values will be discussed in Chapter 8.

7.7 Results from combinations of materials and a U rod

Thirty-five experiments were conducted using all 35 possible combinations of three of Al, Fe, Cu, Mo, Sn, W, and Pb each at a nominal areal density of 19.3 $\frac{g}{cm^2}$. The actual areal density (α) for each material is shown in Table 16. In addition to the areal density associated with each of the three materials used for each configuration, 57 $\frac{g}{cm^2}$ HDPE and a 1.1" diameter natural U rod were placed in the beam line. The total areal density for each test was between 155-165 $\frac{g}{cm^2}$.

Table 16. Material areal densities ($\boldsymbol{\alpha}$) for combination tests.

Material	Al	Fe	Cu	Mo	Sn	W	Pb
$\alpha\ [\frac{g}{cm^2}]$	20.4	17.6	19.3	19.9	19.2	16.2	21.6

This experiment studied the effect of using various combinations of materials to shield U and the impact of Z_{eff} on the ratio for near constant areal density. The experiment was conducted with the detector array at 1056 cm from the B target. Run times were 20 minutes for all tests and the current varied among tests from 8.3 to 10.6 μA. Current measurements were recorded at least every five minutes during the tests.

Figure 43 shows the R_{Th} and R_{Exp} versus Z_{eff}[65] for the complete set of tests. Figure 44 shows the same results but with Z_{eff} replaced by areal density. All materials had low R_{Exp} values due to the presence of U. Increasing the Z_{eff} of the cargo by increasing the Z values of the component parts led to expected reduction to R_{Th} values. The experimental results confirmed this trend.

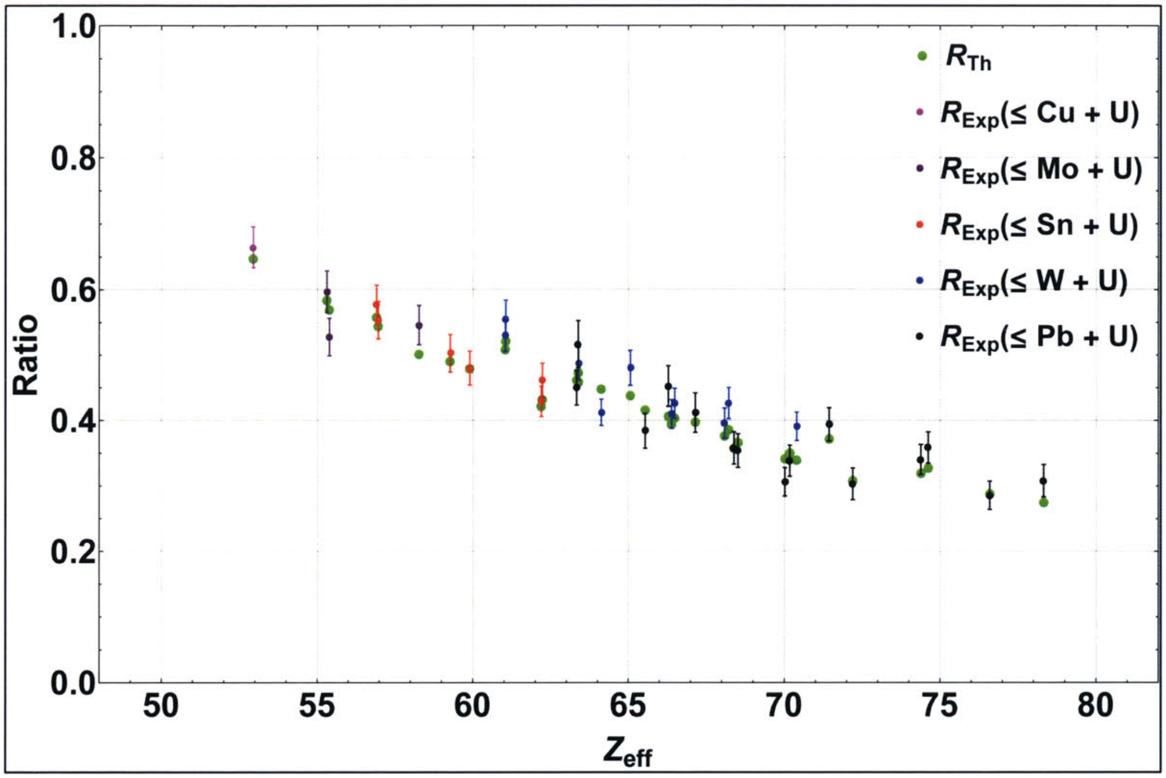

Figure 43. Ratio vs. Z_{eff} for combinations of three materials each at approximately 19.3 g/cm^2, 57 g/cm^2 HDPE, and a U rod for a total areal density of 155-165 g/cm^2. Theoretical values are shown as green circles. Experimental values are shown as circles with error bars.

---

[65] Z_{eff} is defined in Section 3.2. It includes the simple linear weighting $(\sum_i \alpha_i Z_i / \sum_i \alpha_i)$ of all materials except HDPE where α_i and Z_i are the areal density and atomic number of the ith material.

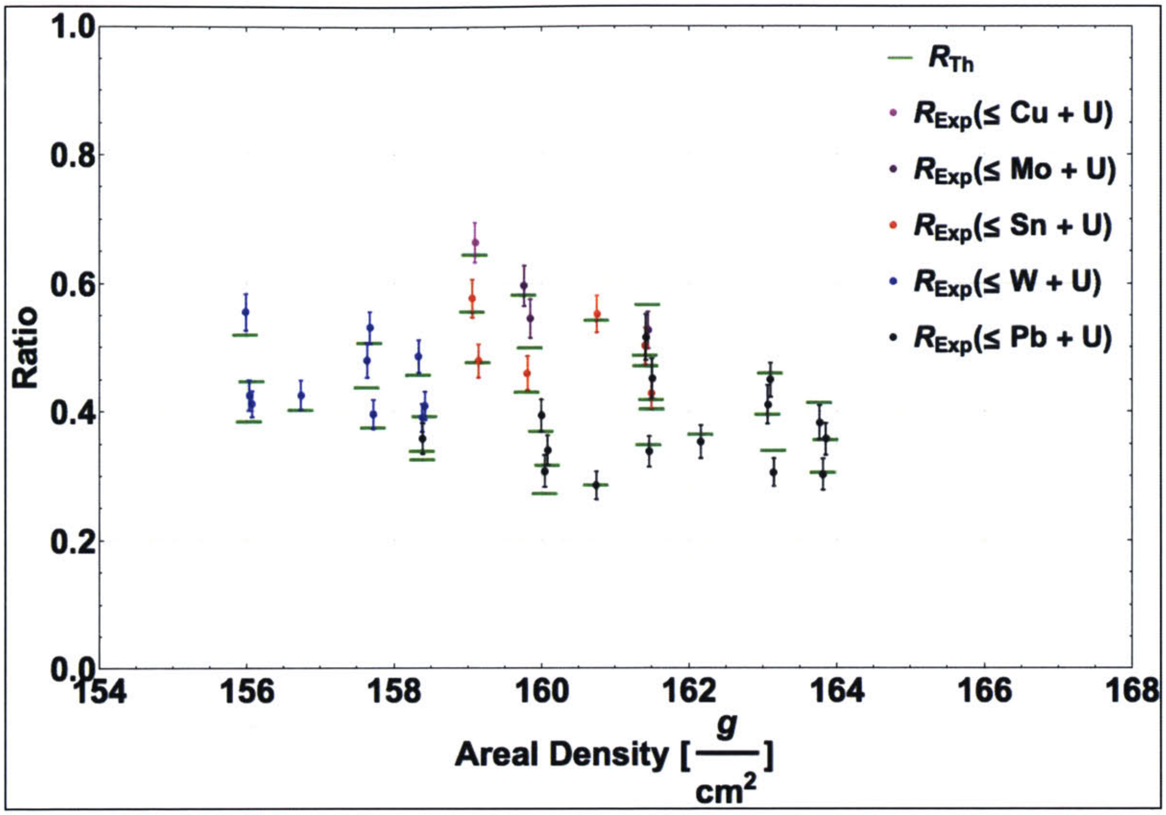

Figure 44. Ratio vs. areal density for combinations of three materials each at approximately 19.3 g/cm^2, 57 g/cm^2 HDPE, and a U rod for a total areal density of 155-165 g/cm^2.

7.8 Observations from results from combinations of materials and a U rod

The experimental data from combinations of materials provided two important results:

- Medium-Z materials can be combined to create similar ratios to a mix of low- and high-Z materials
- R_{Exp} values closely approximated the R_{Th} values

First, the experiment demonstrated that medium-Z materials can be combined to create similar ratios to a mix of low- and high-Z materials. As seen in Figure 43, two experiments with $R_{Exp}(\leq W+U)$ located at $Z_{eff} = 61$ had higher R_{Exp} values than the $R_{Exp}(\leq Sn+U)$ located at $Z_{eff} = 62$. The $R_{Exp}(\leq W+U)$ trials were composed of Al+Fe+W+U and Al+Cu+W+U while the $R_{Exp}(\leq Sn+U)$ trials were composed of Fe+Mo+Sn+U and Cu+Mo+Sn+U. Since the U areal density was the same this provides an example of low- and medium-Z materials (Fe+Mo+Sn and Cu+Mo+Sn) effectively attenuating the gammas to create a lower R_{Exp} than a combination of low- and high-Z materials (Al+Fe+W and Al+Cu+W). If U is removed from consideration, this would have been the equivalent to the inability to discriminate between medium- and high-Z materials at an embedded material areal density of 19.3 $\frac{g}{cm^2}$. It should also be noted the $R_{Exp}(\leq W+U)$ with Al+Fe+Pb+U and Al+Cu+Pb+U would not have been distinguishable from the same $R_{Exp}(\leq Sn+U)$ tests. This finding reinforces previous results suggesting more experimental work should be done to determine the practical limits of the high-Z areal density detection threshold.

Second, it demonstrated that the R_{Exp} values closely approximated the R_{Th} values. This reinforces previous findings that the R_{Th} model does an excellent job of predicting R_{Exp} results for non-low Z_{eff} cargo when background and counting statistics are not problematic.

7.9 Sensitivity of Method (1cm, 1", 3.54 cm in material)

Of the sixteen experimental series conducted and two tests with pure materials, it was possible to differentiate medium- and high-Z cargo embedded in Fe on fifteen occasions. The limited success at 19.3 $\frac{g}{cm^2}$ of embedded material indicates the practical threshold may lie above this areal density. It is, however, premature to rule out the possibility of a 19.3 $\frac{g}{cm^2}$ areal density threshold. Improvements to shielding and collimation of the beam line and improved algorithms for 4.44 MeV background removal may make 19.3 $\frac{g}{cm^2}$ or lower areal densities feasible.

7.10 Revisiting identification of the 12 kg WGU weapon with 3 cm W tamper

Revisiting the 12 kg WGU weapon with 3 cm W tamper hidden in the cargo container demonstrates the efficacy of the proposed scanning method. However, instead of the simplified problem with no additional cargo, consider the weapon is placed in a 40 cm thick block of Fe. The difference in 4.44 MeV gamma attenuation between the center of the weapon and the surrounding Fe is four orders of magnitude as shown in Figure 45. The difference in R_{Th} between the weapon and the surrounding Fe is two orders of magnitude, as seen in Figure 46.

Substitution of other shielding materials for Fe leads to similar differences in the relationship between the center of the device and the incident shielding material as seen in Table 17. Note these are point measurements but what the detectors actually record will depend on averages over the materials between the source and detector that fall within the solid angle subtended by the detector and there will be errors in counts, current, etc. However, the fact that the differences in attenuations are several orders of magnitude and the differences in ratios are also more than an order of magnitude make it very probable the device will not pass undetected through the scanning process.

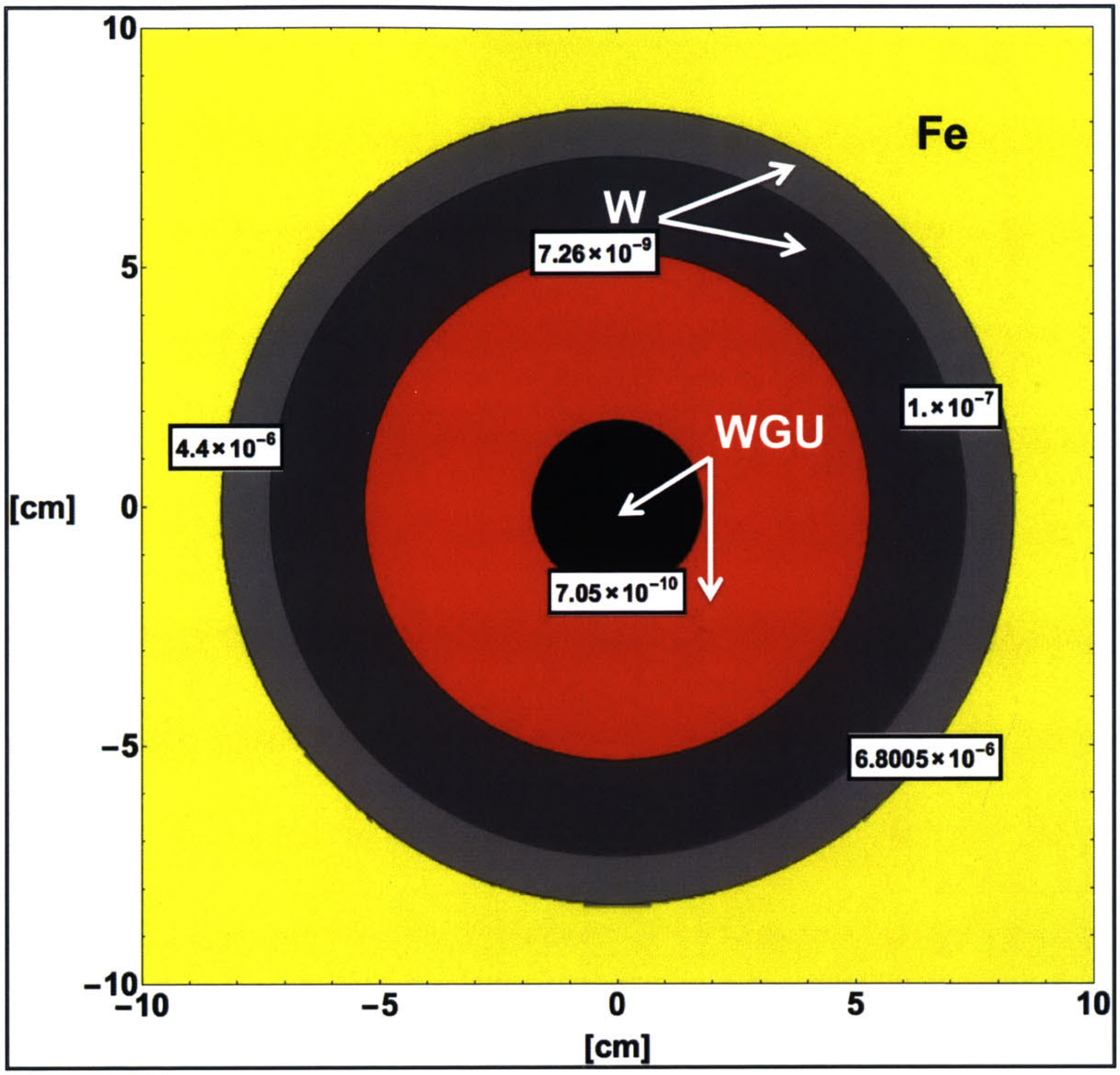

Figure 45. Radiography transmission image of 12 kg WGU weapon (radius (r) of 5.33 cm) with W tamper (r_{inner} = 5.33 cm, r_{outer} = 8.33 cm) embedded in 40 cm thick block of Fe. Image shows equipotential transmission fraction of 4.44 MeV gammas.[66] Transmission fraction through 40 cm of Fe (in yellow) leads is $6.8 \cdot 10^{-6}$. Gammas transmitted through the light and dark gray areas must pass through Fe and W. Gammas transmitted through the red and black areas must pass through Fe, W, and WGU. The difference in 4.44 MeV transmission between the center of the weapon and the surrounding Fe is four orders of magnitude.

---

[66] Note this is not a cross section of the WGU weapon with W tamper. However, the shaded areas are geometrically true to what a cross section of the weapon would look like. The areas in black and red would be WGU and the light and dark gray areas would be W. The yellow area would be where Fe is located.

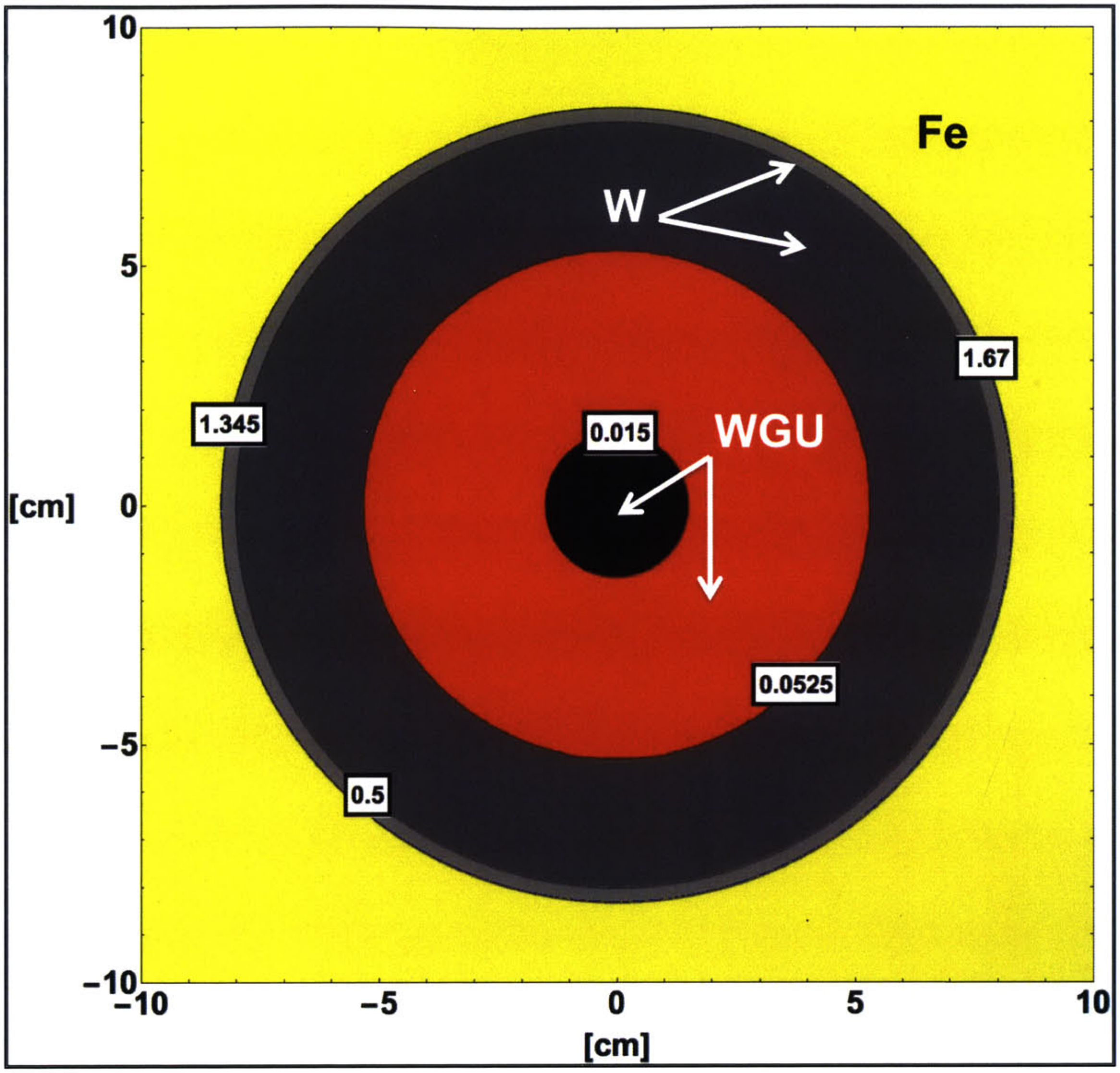

Figure 46. Alternative dual energy radiography transmission image based on equipotential R_{Th} lines for a 12 kg WGU weapon (r = 5.33 cm) with 3 cm W tamper (r_{inner} = 5.33 cm, r_{outer} = 8.33 cm). WGU is shown in black and red. The light and dark gray areas are W contours. The area in yellow is the surrounding Fe. The difference in R_{Th} between the center of the weapon and the surrounding Fe is two orders of magnitude.

Table 17. Monoenergetic 4.44 MeV transmission ratios, $\mathfrak{f}_{atten}(\boldsymbol{Shield})$ / $\mathfrak{f}_{atten}(\boldsymbol{Weapon})$, and dual energy transmission ratios, R_{Th}(Shield) / R_{Th}(Weapon) for 12 kg WGU weapon with 3 cm W tamper embedded in 40 cm of shielding material (none, Al, Fe, Cu, Mo, Sn, or HDPE). Shield calculations are based on transmission through 40 cm of the noted material. Weapon calculations are based on transmission through the centerline of the WGU core, W tamper, and surrounding shielding material. Both transmission images easily show the presence of the embedded high-Z material.

	None	Al	Fe	Cu	Mo	Sn	HDPE
$\frac{\mathfrak{f}_{atten}(Shield)}{\mathfrak{f}_{atten}(Weapon)}$	$8.2 \cdot 10^5$	$2.2 \cdot 10^5$	$1.2 \cdot 10^4$	$6.6 \cdot 10^3$	$2.3 \cdot 10^3$	$1.1 \cdot 10^4$	$4.6 \cdot 10^5$
$\frac{R_{Th}(Shield)}{R_{Th}(Weapon)}$	$1.0 \cdot 10^2$	$1.5 \cdot 10^2$	$1.2 \cdot 10^2$	$1.0 \cdot 10^2$	$4.2 \cdot 10^1$	$4.0 \cdot 10^1$	$1.3 \cdot 10^2$

7.11 Exploration of Automatic Clearance using the proposed scanning method

Experimental ratio measurements can be used in an automated cargo clearing system. For a defined high-Z material areal density detection threshold and a given cargo areal density, select cargo can be cleared based on ratio measurements. If the Z_{eff} of the cargo is unknown, an upper bound of areal density can be established by considering the cargo is made of low-Z material. Carbon (C) is used as the reference material because it is common in cargo and is a significant ratio enhancer.[67]

A graphic describing the relationship between automatic clearance, cargo areal density, and the measured ratio is shown in Figure 47. The green portion of the figure shows the range of cargoes, by areal density and ratio, which can be automatically cleared. The lower bound of the automatic clearance region is established by using the using the R_{Th} equation to calculate the theoretical ratio for a cargo. For a given total areal density (on the x-axis), the material measured is

---

[67] The combination of its density and mass attenuation coefficient make C a more favorable and realistic material choice for hiding high-Z material than H, He, Li, Be, and B.

composed of 57 g/cm^2 of HDPE (from the scanning system), a detection threshold equivalent areal density of W, and the balance from the C reference material. The upper bound of the automatic clearance region is established based on the ratio limits for a Li cargo.[68] The light-red region represents those areal densities and ratios for which the entire areal density (except the 57 g/cm^2 of HDPE from the scanning system) is composed of high-Z material. The yellow region, which is bounded by the two previous regions, contains the range of ratios for which a cargo at a specific areal density may include an amount of high-Z material equal to or in excess of the high-Z areal density detection threshold.

The elemental symbols present in the graphic show the theoretical ratios for a cargo of the pure material for the stated areal density minus the 57 g/cm^2 for the HDPE. For example, the Li listed at a total areal density of 150 g/cm^2 with a ratio of approximately 3.5 is the R_{Th} value for a Li cargo of 93 g/cm^2 (150 g/cm^2 total areal density - 57 g/cm^2 of HDPE). The combinations of materials are the theoretical ratio for the specified configuration. For example, the Sn/Al (30/70) shown above 160 g/cm^2 areal density has a ratio of approximately 3.6. The actual cargo has an areal density of 103 g/cm^2 (160 g/cm^2 total areal density - 57 g/cm^2 of HDPE), of which 30% is Sn and 70% is Al.

The black dots show the ratios for different mixes of U and HDPE. From lowest to highest ratio, the U content was 103, 77, 51, 26 and 0 g/cm^2. The balance of the areal density is from the presence of HDPE. These areal densities were selected so the U accounted for 100, 75, 50, 25, and 0% of the total cargo. As

---

[68] The region in gray shows those ratios that are not physically possible for a cargo at the given areal density.

expected, the cargo with 103 g/cm^2 U falls into the region showing the presence of high-Z material is confirmed. The additional three U cargoes (77, 51, and 26 g/cm^2) all fall within the range of ratios requiring material discrimination.

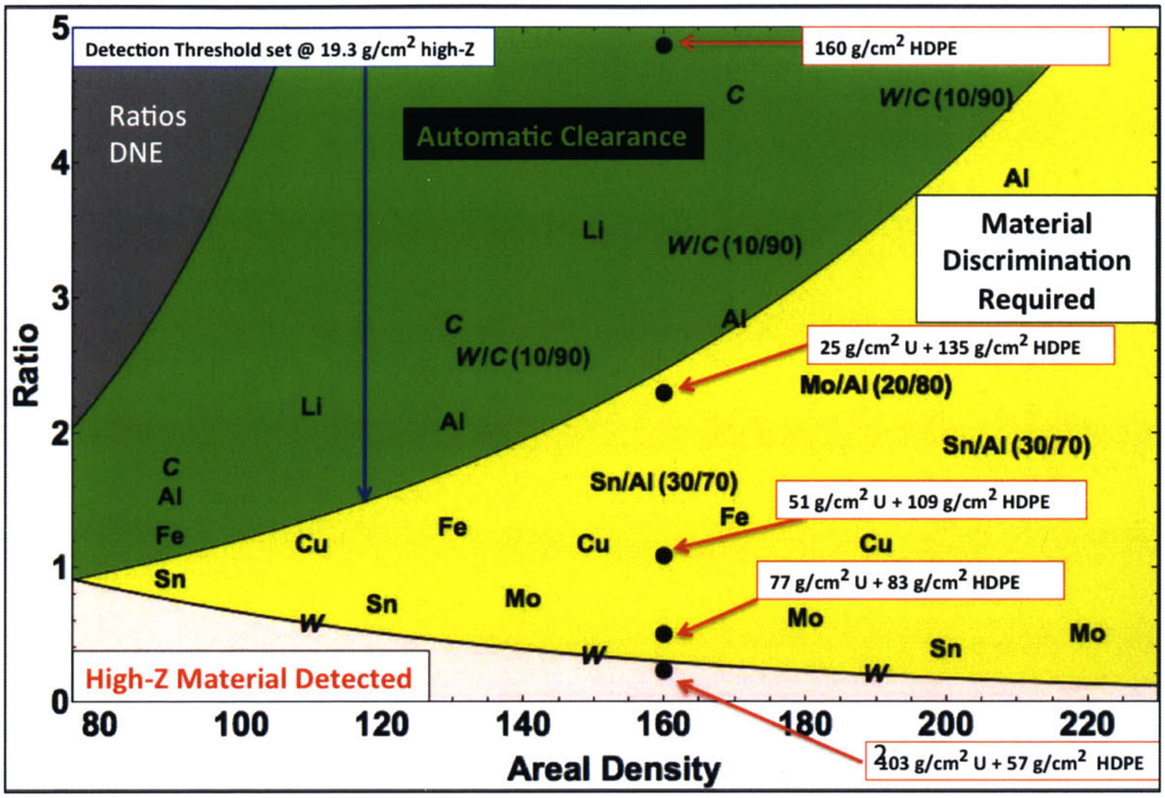

Figure 47. Automatic clearance graphic showing certain cargoes can be automatically cleared based on the high-Z areal density detection threshold, measured areal density of the cargo, and the measured gamma ratio. The area shaded in green represents automatic clearance. No cargoes at the specified ratios can contain high-Z material at or above the detection threshold. The area shaded in light red shows the ratios and areal densities where the cargo must contain high-Z material equal to or in excess of the detection threshold. No cargoes can have ratios within this range unless they have high-Z material at or above the detection threshold. The area in yellow depicts the ratios and ranges of areal densities for cargoes that require further analysis. This graphic assumes that the areal density is estimated based on attenuation of 4.44 MeV gammas in Carbon.

The previous automatic clearance method assumed no knowledge about the material composition. If the Z_{eff} of the cargo is known, a different reference material may be substituted for C. For example, if a Fe cargo is being scanned, the use of Fe as the reference material provides different automatic clearance ratios. Figure 48 shows the expanded range of cargoes that can be cleared based off of an assumed cargo with Z = 26. This graphic also shows the ratios for the U smuggling configurations with Fe substituted for HDPE in the cargo from the previous scenario. (Note the 57 g/cm^2 of HDPE associated with the scanning mechanism is still present.)

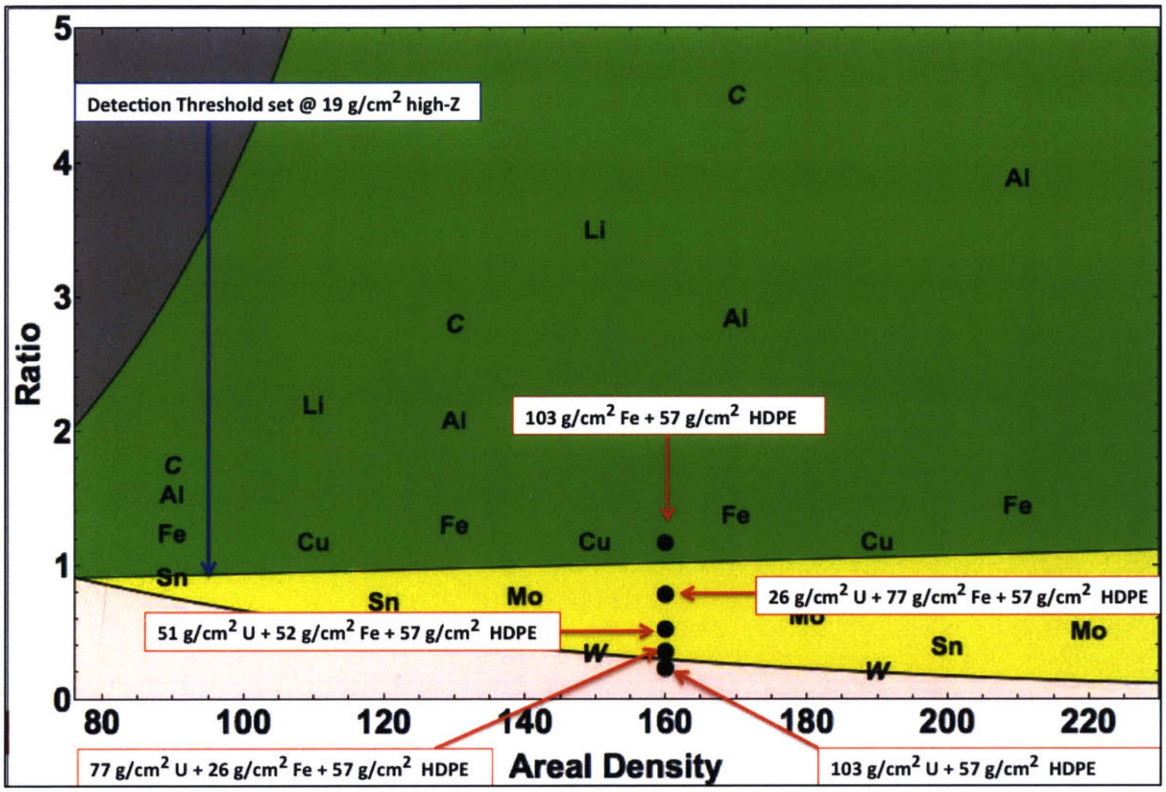

Figure 48. Automatic clearance graphic showing certain cargoes can be automatically cleared based on the high-Z areal density detection threshold, measured areal density of the cargo, and the measured gamma ratio. This graphic assumes that the areal density is estimated based on attenuation of 4.44 MeV gammas in Fe.

It should also be noted that the specification of the high-Z areal density detection threshold impacts the portion of cargoes that can be automatically cleared. A higher detection threshold expands the range of ratios for a specific areal density that can be cleared. A lower detection threshold has the opposite effect.

7.12 Exploration of Basic Imaging Using Transmission and Ratios

Creation of an imaging system was beyond the scope of this resource. However, a Mathematica simulation was used to produce sample transmission and ratio images for a random cargo configuration with a hidden nuclear device. For both cases, a resolution of 1 cm x 1 cm was used. The weapon was placed at different locations in a 2 m x 2 m x 2 m container and the incidental cargo was populated for each cubic centimeter randomly selecting materials from Z = 3 to Z = 50. Typical results from these simulations are seen in Figure 49 and Figure 50.

While the weapon can be identified in both pictures, the image of the ratios provides a much clearer indication of the anomaly. The transmission image shows that there are many areas where there is a substantial areal density of material. It can be expected that in the presence of real cargo, the presence of large pieces of high-density material will create black spots that become locations of interest. However, as the ratio images shows, the difference in impacts on the ratio makes identification of the anomaly easier. It should be reiterated significant amounts of medium-Z material can have the same impact on the ratios as the high-Z material. However, since a significantly higher areal density of medium-Z material (roughly 2-2.5 times the areal density for Sn and Mo) is required to have the same impact on the ratio as a high-Z material, an analysis of attenuation and ratios together may better enable differentiation.

It should be noted that these simulated images were created using a static scanning configuration. The purpose of these simulations was to show the knowledge of the ratio potentially provides a valuable means of detecting the presence of high-Z materials. For these simulations, no uncertainty was associated with the calculated 4.44 MeV transmission and ratios. Additionally, the resolution size was set to 1 cm x 1 cm so a practical image may not have the same level of resolution. Finally, since the simulation determined the exact transmission factor and ratios, scan time and current were not considered.

Figure 49. Results from a transmission simulation for a weapon enclosed in a 2 m x 2 m x 2 m container. Cargo was randomly populated with low- and medium-Z material for every cc surrounding the weapon. A dark spot in the lower right of the graphic shows the presence of the weapon.

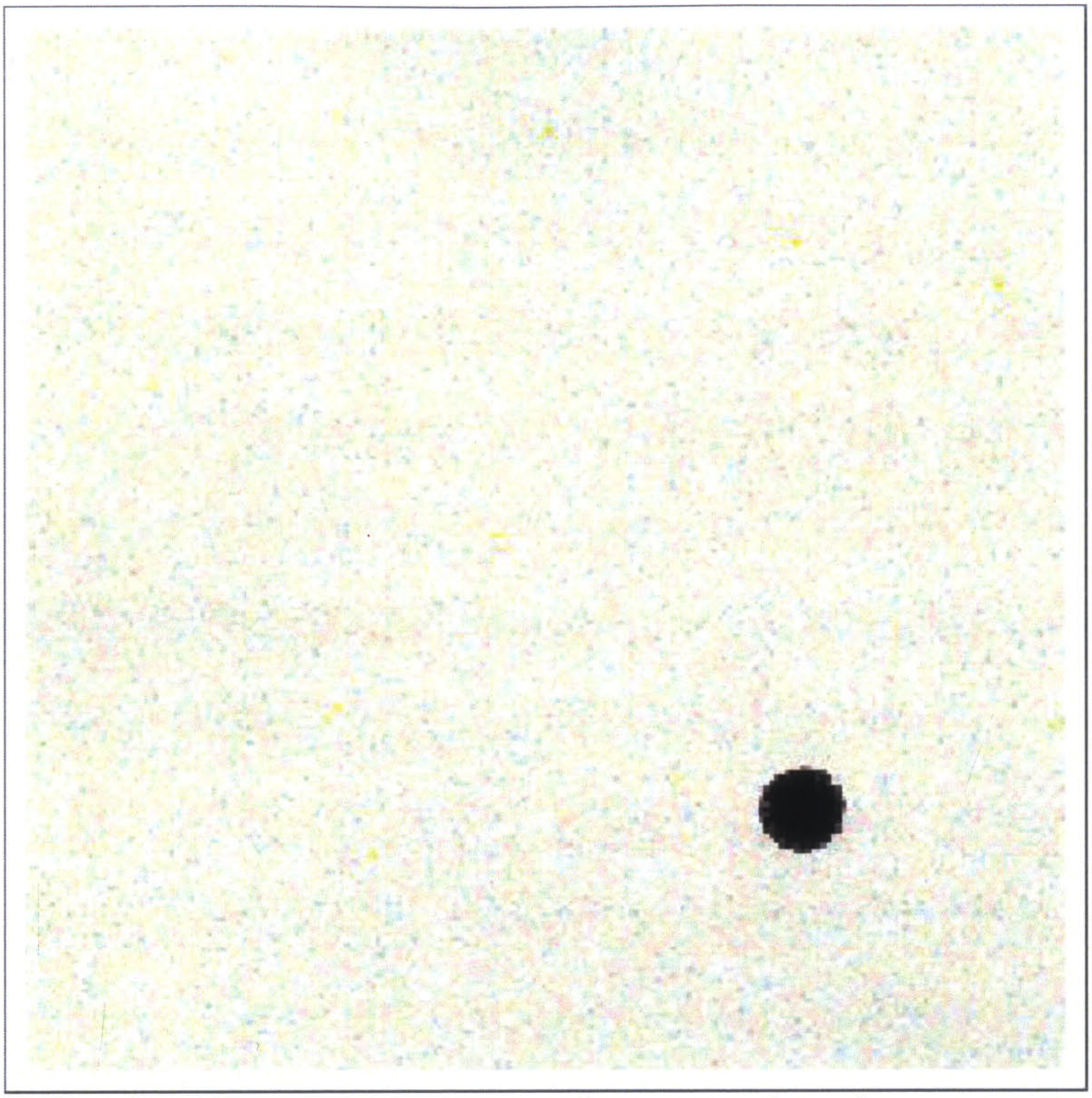

Figure 50. Ratio image produced from a Mathematica simulation for interrogation of a weapon surrounded by low- and medium-Z materials in a 2 m x 2 m x 2 m container. Cargo was randomly populated for every cc surrounding the weapon. A dark spot in the lower right of the graphic shows the presence of the weapon. Note the significant difference in clarity between this image and **Figure 49**.

CHAPTER 8
CONCLUSIONS AND RECOMMENDATIONS

This chapter reports conclusions and provides recommendations for future work that could lead to development of a better cargo scanning system.

8.1 Conclusions

This thesis demonstrated the ability to use multiple monoenergetic gamma lines to determine the presence or absence of high-Z materials in cargo. The success demonstrated in discriminating small amounts of high-Z material embedded in low- and medium-Z material justifies further research in this area. Specifically, this thesis demonstrated that the current scanning system consistently discriminates between medium- and high-Z materials embedded in cargo at high-Z areal density detection thresholds of 49.0 and 68.3 $\frac{g}{cm^2}$ for total areal densities of 125-250 $\frac{g}{cm^2}$.[69] It did not conclusively determine if a 19.3 $\frac{g}{cm^2}$ high-Z areal density detection threshold is possible.

This thesis also achieved several other successes. One key achievement was the validation of the R_{Th} model as a predictor of the ratio of 15.11 MeV to 4.44 MeV gammas for a known cargo configuration. The model can also be modified and used to predict the behavior and characteristics of unknown cargo. It allows establishment of the range of potential areal densities and effective mass

---

[69] Note this statement refers to the specific conditions as defined in this thesis, which did not include all possible medium- and high-Z materials.

attenuation coefficients. The R_{Th} model also serves as a starting point for the development of future "automatic clearance" models. This thesis research also resulted in the compilation of a large range of complete spectral data for numerous cargo configurations that can be processed offline. This will allow future researchers and collaborators to use actual data to use to further develop the proposed scanning system. This data can also serve as the raw data necessary to inform development of a scanning system with real-time feedback.

Another substantial success of this thesis is that it provides insights into some of the areas that must be further researched prior to deploying an operational system. These major areas include:

- Determination of the full range of potential areal density that can be scanned.
- Determination of the high-Z areal density detection threshold.
- Reduction of the estimated areal density range.

8.2 Recommendations for Future Work

While the proof of principle is promising, during this research it became apparent that there are numerous areas for future theoretical and experimental work that could ultimately lead to development of an even more successful system. A list of these potential areas of research and their impact on the system is included below. Suggestions and insights on how to conduct this research are included in Appendix H.

Potential areas of future research include, but are not limited to, the following:

1. Charge integration improvements will allow better determination of 4.44 and 15.11 MeV gamma production yields, provide the instantaneous production

rates necessary for fielding a near real-time scanning system, and allow better estimation of cargo areal density.

2. Quantification of 4.44 and 15.11 MeV gamma production rates for 3.0 MeV deuterons on a B target without the presence of HDPE will allow more accurate determination of cross sections and optimization of shielding design.
3. Changes to the Data Acquisition System (DAQ) will reduce the amount of data that must be recorded, reduce the amount of information passed to the computers for processing and analysis, and data storage requirements.
4. Optimization of 4.44 and 15.11 MeV counting intervals will allow better understanding of the dependence of Z reconstruction resolution on the integration limits.
5. Optimization of 4.44 MeV background removal may result in more accurate determination of experimental counts, ratios, areal density, and estimation of the Z_{eff} of the cargo.
6. Incorporation of multiple arrays and alternate arrays may decrease system vulnerability to smuggling, facilitate secondary scanning and searches, and allow combination of data to provide more information about the cargo than any single detector array can provide.
7. Consideration of alternative low-threshold nuclear interactions and reactions may lead to better estimation of areal density or reduced shielding requirements.
8. Possible use of additional or alternative gamma lines may increase system ability to discriminate among materials and allow better estimation of the cargo areal density and Z_{eff}.
9. A general study of the optimal gamma energies for maximum penetration and Z discrimination may allow determination of the best possible gamma energy combinations to use and potential source interactions.
10. Quantification of neutron and gamma dose rates will allow comparison of the proposed system and existing systems, and will provide a means of setting interrogation source production limits.
11. Determination of the areal density interrogation range will allow better estimation of the fraction of cargo passing through POEs the system can reliably scan and determination of how source production should be changed when scanning various areal densities.
12. Reduction of interrogation time to the minimum necessary will increase the potential of creating a system that can be used for primary and secondary scanning without adversely impacting commerce.
13. Establishment of the high-Z areal density detection threshold will quantify what high-Z areal density quantities the system can detect.
14. Validation of detector efficiencies will allow use of the NaI(Tl) detectors to determine 4.44 and 15.11 MeV gamma production rates and increased confidence in using these detector efficiencies as part of a full system model.
15. Testing the ability of smuggling methods to defeat the system will inform how the system should be modified to reduce vulnerability to smuggling.

16. Detailed study of the impact of lanthanides on discrimination of medium- and high-Z materials will inform eventual tests to discriminate between medium- and high-Z materials, provide insights into if and how these materials may be used to hide high-Z materials, and possibly inform redefinition of the dividing line between medium- and high-Z materials.
17. Acquisition of more realistic information on the distribution of cargo in containers will inform determination of what cargo can and cannot be cleared using the proposed system and the development of scanning system operating parameters.
18. Further removal of neutrons produced from the 3.0 MeV deuteron interactions with the B target may reduce their impact on the recorded spectra.
19. Development of algorithms for automatic clearance will inform development of an automated system to report estimated areal density and Z_{eff} of the cargo.
20. Development of sophisticated algorithms, other than simple ratios, could be developed to maximally use the statistical information and thus reduce the necessary scan time and dose.
21. Exploration of the relationship between count rates and ratios will inform development of the cargo scanning control system.
22. Exploration of the possibility of placing three columns of detectors (one in the beam line and adjacent detector arrays) and summing the signals may allow recovery of lost counts and result in improved statistics.
23. Study of gamma lines in the 6-9 MeV range that appear in the spectra from unknown processes will allow determination of their origin and determine if these gamma lines can be used in the detection system.
24. Use of alternative accelerators for the production of monochromatic sources may allow development of a more effective scanning system with lower shielding requirements and lower dose.
25. Utilization of the fast neutrons produced in $^{11}B(d,n\gamma)^{12}C^*$ for fast neutron radiography may allow improved reconstruction of areal densities and Z_{eff} of the cargo.
26. Use of delayed neutrons emanating from the cargo would allow confirmation of the presence of SNM.
27. Variation of beam energy (e.g. by building a 2-piece target, one with ^{11}B, one with ^{11}B covered by a thin energy degrader) to allow for control over the 15.1 MeV line will allow use of non-spectroscopic detectors to reconstruct Z while operating in charge integrating mode.
28. Tests should be undertaken to ensure actual scanning of cargoes, reconstruction of cargo images, and tests of penetration comply with ANSI N42.46 standards.
29. Uncoupling of the areal density and Z_{eff} (equivalent to the effective mass attenuation coefficient of the cargo) or reliable determination of Z_{eff} or a small range of Z_{eff} for an unknown cargo would have a dramatic impact on the effectiveness of the proposed scanning system.

APPENDIX A. NEUTRON DETECTORS

The USG's preferred choice for neutron detection is the ^{3}He-based detector. Shortfalls in availability of ^{3}He increase the cost of fielding and maintaining such a system. Alternative detection technologies include boron-line and BF_3 detectors. The low neutron signatures for ^{235}U based weapons makes neutron detection with these relatively small detectors much more difficult, although they may be more effective in secondary screening of suspect cargo when more time can be spent scanning. However, even spending more time scanning does not guarantee a weapon can be identified. As discussed in the Appendix B, the neutron signatures from a W shield ^{235}U weapon in extremely low (more than a factor of 25 less than background at 1 m from the weapon) and undetectable.

A brief comparison of ^{3}He, BF_3, and ^{10}B-based detection systems is seen in Table 18.

Table 18. Comparison of advantages and disadvantages of popular neutron detection systems.[70]

Detector	Advantages	Disadvantages
^{3}He	• Large thermal cross section (5333 b) • Higher operating pressure than BF_3	• Gaseous form • Limited availability
BF_3	• Lower x-section than ^{3}He (3837 b for ^{10}B)	• Fluorine toxicity • Gamma background from isomeric transition interferes with ID algorithms
^{10}B	• Lower cross-section than ^{3}He (3837 b for ^{10}B)	• Gamma background from isomeric transition interferes with ID algorithms

---

[70] Thermal neutron cross sections retrieved from [**71**].

APPENDIX B. THE DIFFICULTIES OF DETECTING NUCLEAR DEVICES

The difficulties of detecting the presence of SNM are largely a result of their limited signatures and the surrounding environment. The most useful signatures for four hypothetical weapon configurations are summarized in Table 19. The origin of the 0.662 MeV gammas found in WGPu is from a decay product of ^{241}Pu (^{241}Am) and the 1.001 MeV gammas are from a decay product of ^{238}U (^{234M}Pa). The low 1.001 MeV gamma emission rate from the 12 kg WGU with W tamper is because there is not much 238U present and W is a good attenuator of 1 MeV gammas. The lack of 0.662 MeV gammas for the 4 kg WGPu with 52 kg DU tamper is because the gammas are significantly attenuated by the DU tamper. Thus, weapon design has a direct effect on available signatures and therefore on the ability to detect the nuclear device.

Table 19. Signatures from four Hypothetical Weapons [57]. The WGU weapon in W tamper is by far the most difficult to detect because it has the smallest signature.

Fissile Material	Tamper Material	Neutron emission rate at surface [#/s]	Gamma emission rate at surface [#/s]	Gamma energy [MeV]
12 kg WGU	Tungsten (3cm)	30	30	1.001
12 kg WGU	79 kg Depleted Uranium	1,400	100,000	1.001
4 kg WGPu	Tungsten (3cm)	400,000	600 1,000	0.662 1.6
4 kg WGPu	52 kg Depleted Uranium	400,000	60,000	1.001

Since WGPu weapons have significant neutrons present, they are easier to detect than WGU weapons. Based on the signatures, the WGU with W tamper has by far the smallest signature and is therefore frequently the benchmark used for detection of a nuclear device. The specific neutron and gamma activities for weapons-grade uranium and weapons-grade plutonium are included in Figure 52 and Figure 53 at the end of this appendix. One should note that if reprocessed uranium is used, the ^{232}U decay chain daughter products have high activity gamma decays (238.59, 510.61, 583.02, and 2614.35 keV) that, even at 1 ppm, provide the strongest signature [**57**].

Continually changing environmental conditions during scanning to detect radioactive material occurs in a border security scenario greatly compounds the detection challenge. The intrinsic site background—that associated with the site in the absence of vehicles and cargo—continually changes in energy, spatially, and temporally. The presence of natural radioactive materials found in legitimate cargo (e.g. 40K in bananas and fertilizer, U and Th in granite) both within and adjacent to the detection site further compounds the detection challenge.

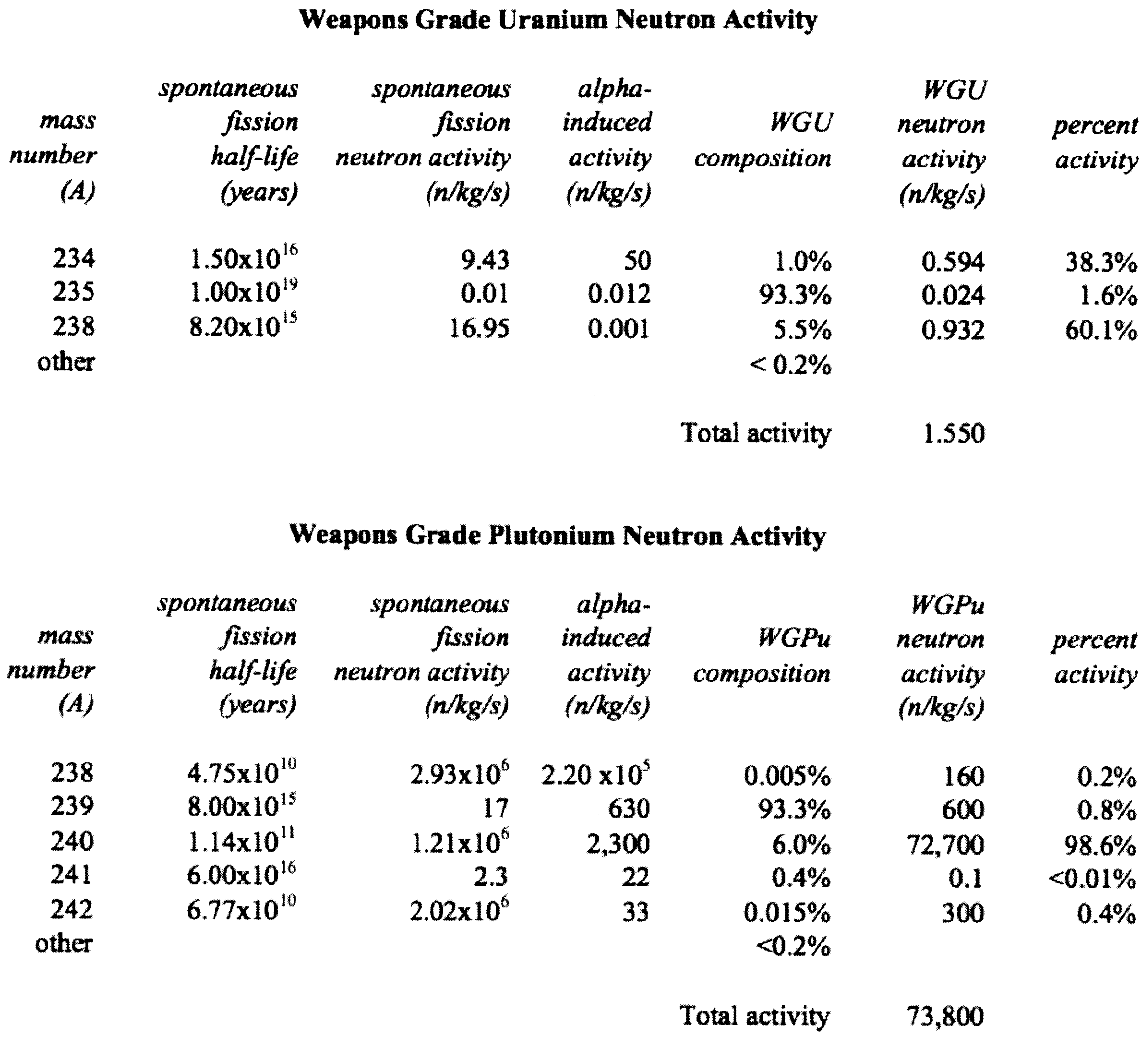

Weapons Grade Uranium Neutron Activity

mass number (A)	*spontaneous fission half-life (years)*	*spontaneous fission neutron activity (n/kg/s)*	*alpha-induced activity (n/kg/s)*	*WGU composition*	*WGU neutron activity (n/kg/s)*	*percent activity*
234	$1.50x10^{16}$	9.43	50	1.0%	0.594	38.3%
235	$1.00x10^{19}$	0.01	0.012	93.3%	0.024	1.6%
238	$8.20x10^{15}$	16.95	0.001	5.5%	0.932	60.1%
other				< 0.2%		
				Total activity	1.550	

Weapons Grade Plutonium Neutron Activity

mass number (A)	*spontaneous fission half-life (years)*	*spontaneous fission neutron activity (n/kg/s)*	*alpha-induced activity (n/kg/s)*	*WGPu composition*	*WGPu neutron activity (n/kg/s)*	*percent activity*
238	$4.75x10^{10}$	$2.93x10^{6}$	$2.20 x10^{5}$	0.005%	160	0.2%
239	$8.00x10^{15}$	17	630	93.3%	600	0.8%
240	$1.14x10^{11}$	$1.21x10^{6}$	2,300	6.0%	72,700	98.6%
241	$6.00x10^{16}$	2.3	22	0.4%	0.1	<0.01%
242	$6.77x10^{10}$	$2.02x10^{6}$	33	0.015%	300	0.4%
other				<0.2%		
				Total activity	73,800	

Figure 51. Neutron Activities from Nuclear Materials [58].

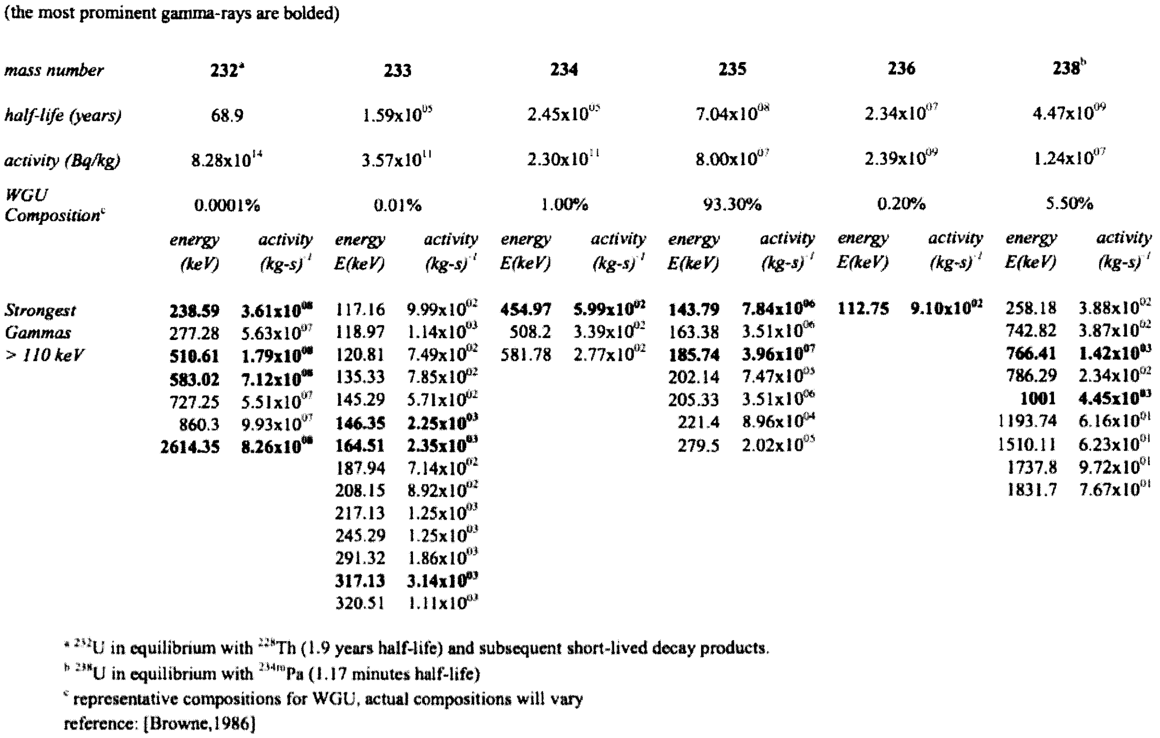

(the most prominent gamma-rays are bolded)

mass number	**232^{a}**		**233**		**234**		**235**		**236**		**238^{b}**	
half-life (years)	68.9		1.59x10^{05}		2.45x10^{05}		7.04x10^{08}		2.34x10^{07}		4.47x10^{09}	
activity (Bq/kg)	8.28x10^{14}		3.57x10^{11}		2.30x10^{11}		8.00x10^{07}		2.39x10^{09}		1.24x10^{07}	
WGU Composition^{c}	0.0001%		0.01%		1.00%		93.30%		0.20%		5.50%	
	energy (keV)	*activity (kg-s)$^{-1}$*	*energy E(keV)*	*activity (kg-s)$^{-1}$*	*energy E(keV)*	*activity (kg-s)$^{-1}$*	*energy E(keV)*	*activity (kg-s)$^{-1}$*	*energy E(keV)*	*activity (kg-s)$^{-1}$*	*energy E(keV)*	*activity (kg-s)$^{-1}$*
Strongest Gammas > 110 keV	**238.59**	**3.61x10^{08}**	117.16	9.99x10^{02}	**454.97**	**5.99x10^{02}**	**143.79**	**7.84x10^{06}**	**112.75**	**9.10x10^{02}**	258.18	3.88x10^{02}
	277.28	5.63x10^{07}	118.97	1.14x10^{03}	508.2	3.39x10^{02}	163.38	3.51x10^{06}			742.82	3.87x10^{02}
	510.61	**1.79x10^{08}**	120.81	7.49x10^{02}	581.78	2.77x10^{02}	**185.74**	**3.96x10^{07}**			**766.41**	**1.42x10^{03}**
	583.02	**7.12x10^{08}**	135.33	7.85x10^{02}			202.14	7.47x10^{05}			786.29	2.34x10^{02}
	727.25	5.51x10^{07}	145.29	5.71x10^{02}			205.33	3.51x10^{06}			**1001**	**4.45x10^{03}**
	860.3	9.93x10^{07}	**146.35**	**2.25x10^{03}**			221.4	8.96x10^{04}			1193.74	6.16x10^{01}
	2614.35	**8.26x10^{08}**	**164.51**	**2.35x10^{03}**			279.5	2.02x10^{05}			1510.11	6.23x10^{01}
			187.94	7.14x10^{02}							1737.8	9.72x10^{01}
			208.15	8.92x10^{02}							1831.7	7.67x10^{01}
			217.13	1.25x10^{03}								
			245.29	1.25x10^{03}								
			291.32	1.86x10^{03}								
			317.13	**3.14x10^{03}**								
			320.51	1.11x10^{03}								

[a] ^{232}U in equilibrium with ^{228}Th (1.9 years half-life) and subsequent short-lived decay products.

[b] ^{238}U in equilibrium with ^{234m}Pa (1.17 minutes half-life)

[c] representative compositions for WGU, actual compositions will vary

reference: [Browne,1986]

Figure 52. Gamma-Ray Activities per Kilogram of Weapons Grade Uranium [58].

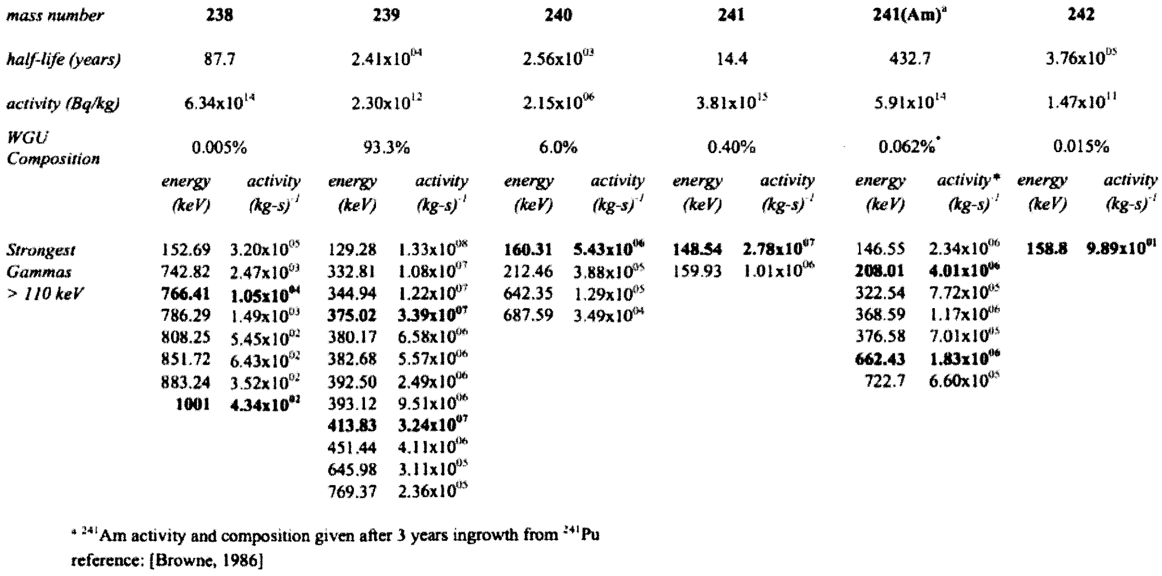

mass number	**238**		**239**		**240**		**241**		**241(Am)^{a}**		**242**	
half-life (years)	87.7		2.41x10^{04}		2.56x10^{03}		14.4		432.7		3.76x10^{05}	
activity (Bq/kg)	6.34x10^{14}		2.30x10^{12}		2.15x10^{06}		3.81x10^{15}		5.91x10^{14}		1.47x10^{11}	
WGU Composition	0.005%		93.3%		6.0%		0.40%		0.062%*		0.015%	
	energy (keV)	*activity (kg-s)$^{-1}$*	*energy (keV)*	*activity (kg-s)$^{-1}$*	*energy (keV)*	*activity (kg-s)$^{-1}$*	*energy (keV)*	*activity (kg-s)$^{-1}$*	*energy (keV)*	*activity* (kg-s)$^{-1}$*	*energy (keV)*	*activity (kg-s)$^{-1}$*
Strongest Gammas > 110 keV	152.69	3.20x10^{05}	129.28	1.33x10^{08}	**160.31**	**5.43x10^{06}**	**148.54**	**2.78x10^{07}**	146.55	2.34x10^{06}	**158.8**	**9.89x10^{01}**
	742.82	2.47x10^{03}	332.81	1.08x10^{07}	212.46	3.88x10^{05}	159.93	1.01x10^{06}	**208.01**	**4.01x10^{06}**		
	766.41	**1.05x10^{04}**	344.94	1.22x10^{07}	642.35	1.29x10^{05}			322.54	7.72x10^{05}		
	786.29	1.49x10^{03}	**375.02**	**3.39x10^{07}**	687.59	3.49x10^{04}			368.59	1.17x10^{06}		
	808.25	5.45x10^{02}	380.17	6.58x10^{06}					376.58	7.01x10^{05}		
	851.72	6.43x10^{02}	382.68	5.57x10^{06}					**662.43**	**1.83x10^{06}**		
	883.24	3.52x10^{02}	392.50	2.49x10^{06}					722.7	6.60x10^{05}		
	1001	**4.34x10^{02}**	393.12	9.51x10^{06}								
			413.83	**3.24x10^{07}**								
			451.44	4.11x10^{06}								
			645.98	3.11x10^{05}								
			769.37	2.36x10^{05}								

[a] ^{241}Am activity and composition given after 3 years ingrowth from ^{241}Pu

reference: [Browne, 1986]

Figure 53. Gamma-Ray Activities per Kilogram of Weapons Grade Plutonium [58].

APPENDIX C. EXPERIMENTAL CONFIGURATION

The layout of the area housing the experiment and major components is seen in Figure 54 below. The DL-3 accelerator is seen in dark blue, HDPE in bright green, concrete collimators and shielding in gray, cargo material in light green, and detector array in yellow.

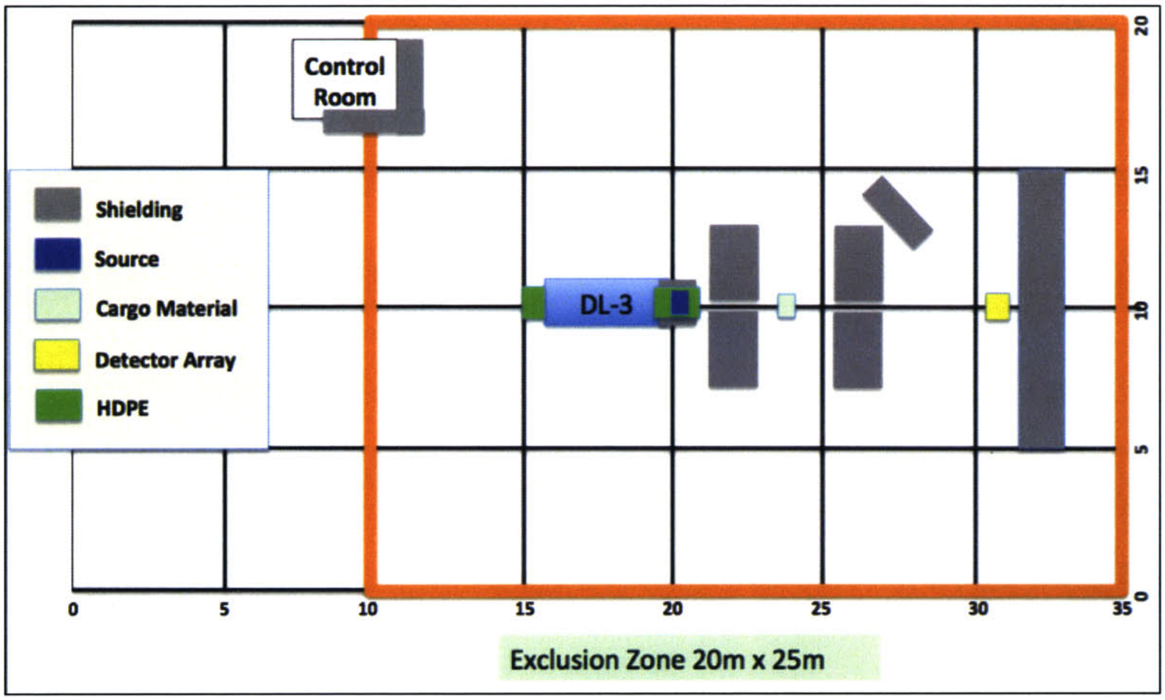

Figure 54. Facility and Experiment Layout.

HDPE was placed behind the DL-3 to shield for neutrons emanating backward through the beam port toward the edge of the exclusion zone. A layer of Pb 8" thick was placed immediately around the B source to shield gamma rays close to the nuclear interaction. Additional HDPE was placed immediately around the Pb to reduce the neutron flux. The combination of the Pb and HDPE near the B target ensured the dose rate outside of the exclusion zone remained below 1 mrem/hr at all times.[71] A channel inside the Pb and HDPE was left open to allow a fan beam of gamma rays and neutrons moving down the beam line.

An additional 21" of HDPE was placed between the end of the local Pb and HDPE shielding and the first set of dual-density concrete. This HDPE in the beam line reduced the neutron flux significantly while only minimally attenuating the 4.44 and 15.11 MeV gamma rays of interest. After passing through this HDPE, the gammas passed through the first set of concrete collimators with a 0.75" gap, any cargo if present, through a 1.5" cm 8" long lead collimators immediately after the cargo, and the second set of concrete collimators with a 1.25" gap. Gammas moving toward the detector then saw an 8" thick lead collimator with 2.25" gap prior to arrival at the detector. The detectors were shielded at the sides with 4" of Pb.

Key distances for the experimental setup are included in Table 20. All distances are from the location of the B target down the beam line to the point of interest.

Table 20. Key Distances for Experimental Setup.

Description	Distance [cm]
Front of 21" HDPE attenuating material	88
Front of first set of double density concrete collimators	142
Back of first set of double density concrete collimators	264
Front of second set of double density concrete collimators	443
Back of second set of double density concrete collimators	565
Front of array for first set of measurements	939
Front of array for second set of measurements	1056

Pictures of key pieces of the experimental setup are included below.

---

[71] The shielding plan was developed based on an MCNP simulation conducted to ensure the shielding plan kept dose rates outside of the exclusion zone below 1 mrem/hr at all times.

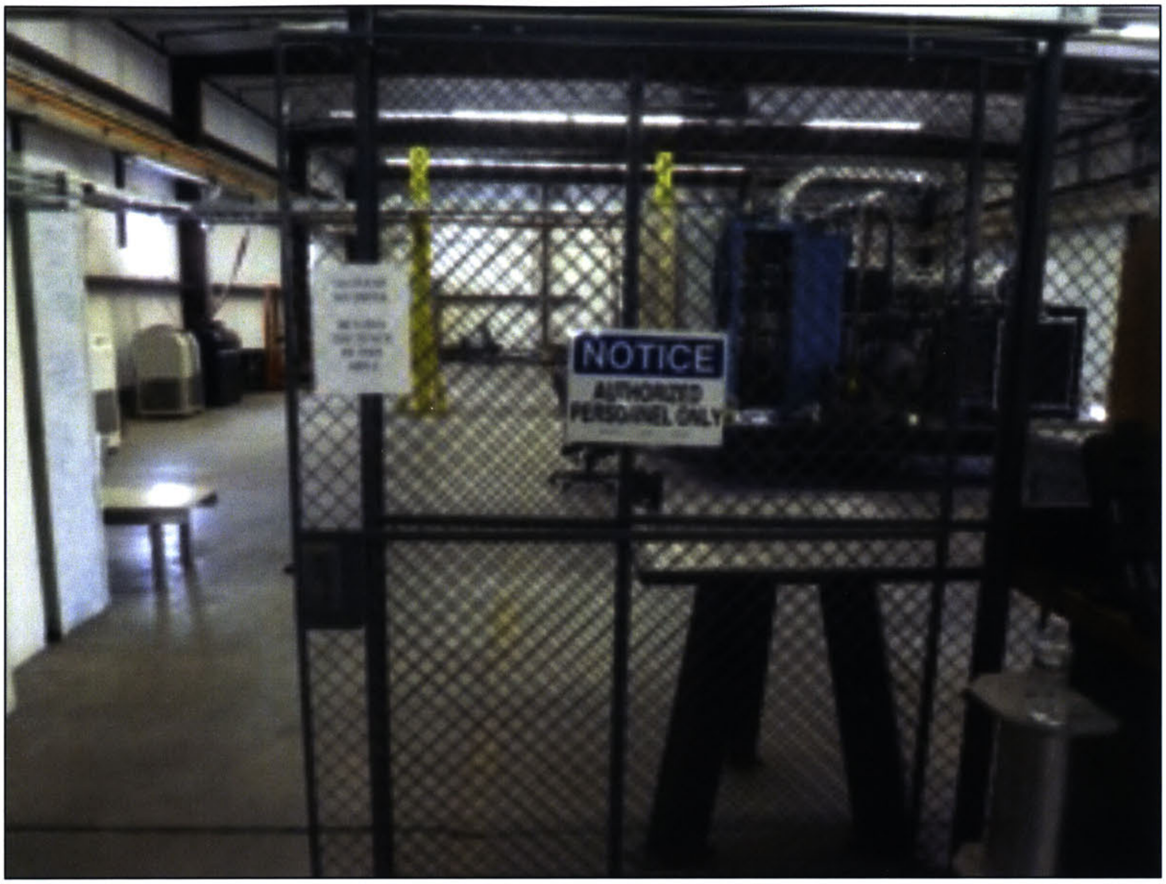

Figure 55. Access gate to experimental area. The DL-3 accelerator is located to the front right.

Figure 56. DL-3 accelerator with shielding in place. Note the HDPE to the back (left) of the accelerator to shield for neutrons traveling back through the vacuum.

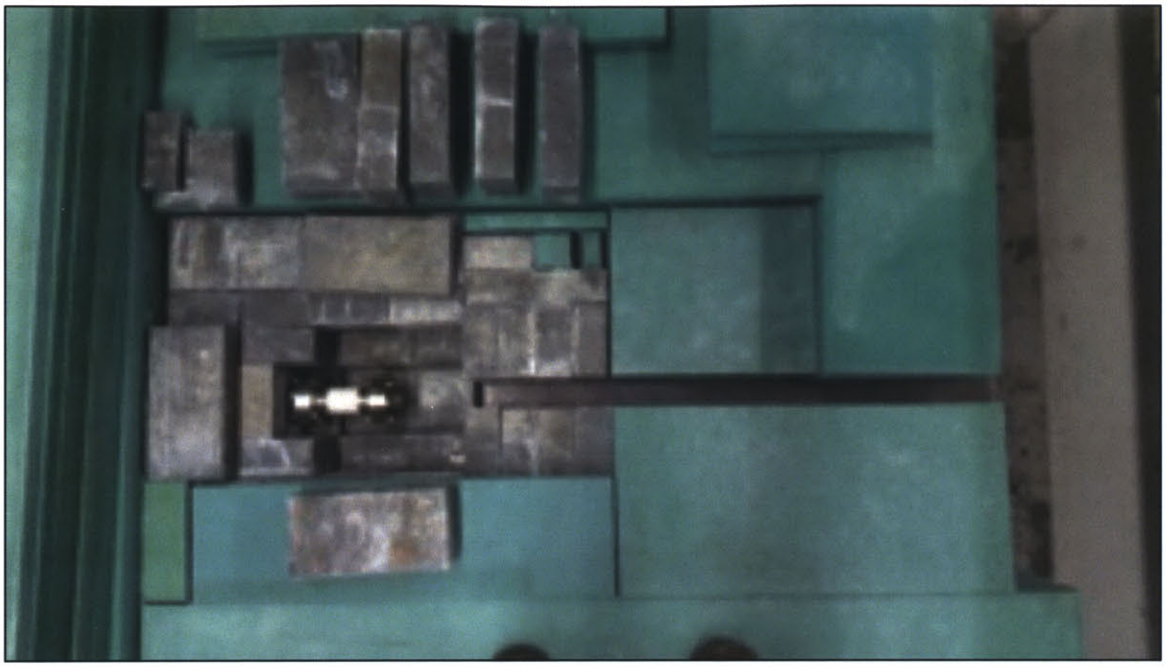

Figure 57. Pb and HDPE shielding for the B target. A channel was left open for the gammas and neutrons to travel down the beam line. An additional 21" of HDPE was placed after the channel to reduce the neutron flux down the beam line.

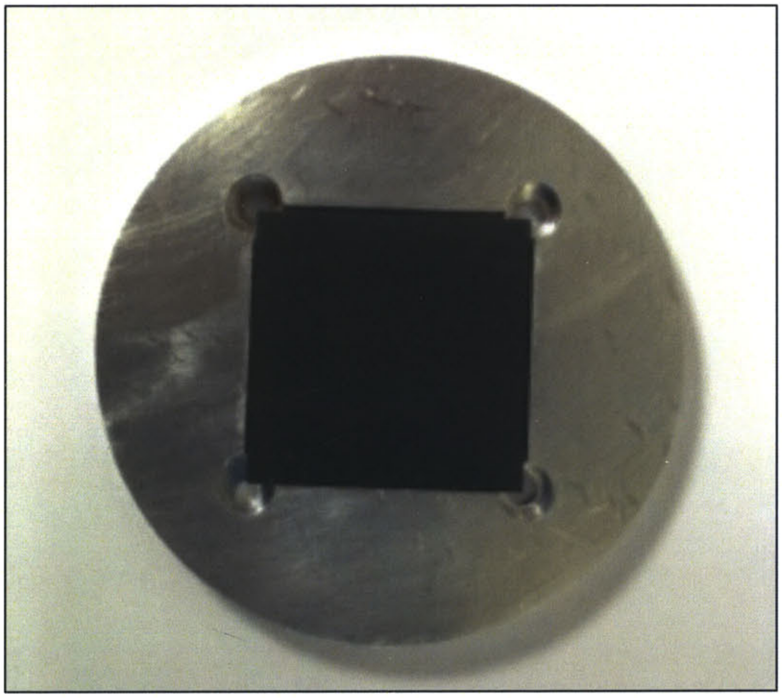

Figure 58. 1" x 1" x 2mm thick B target. Air was forced over the Al housing for the B target to help with cooling.

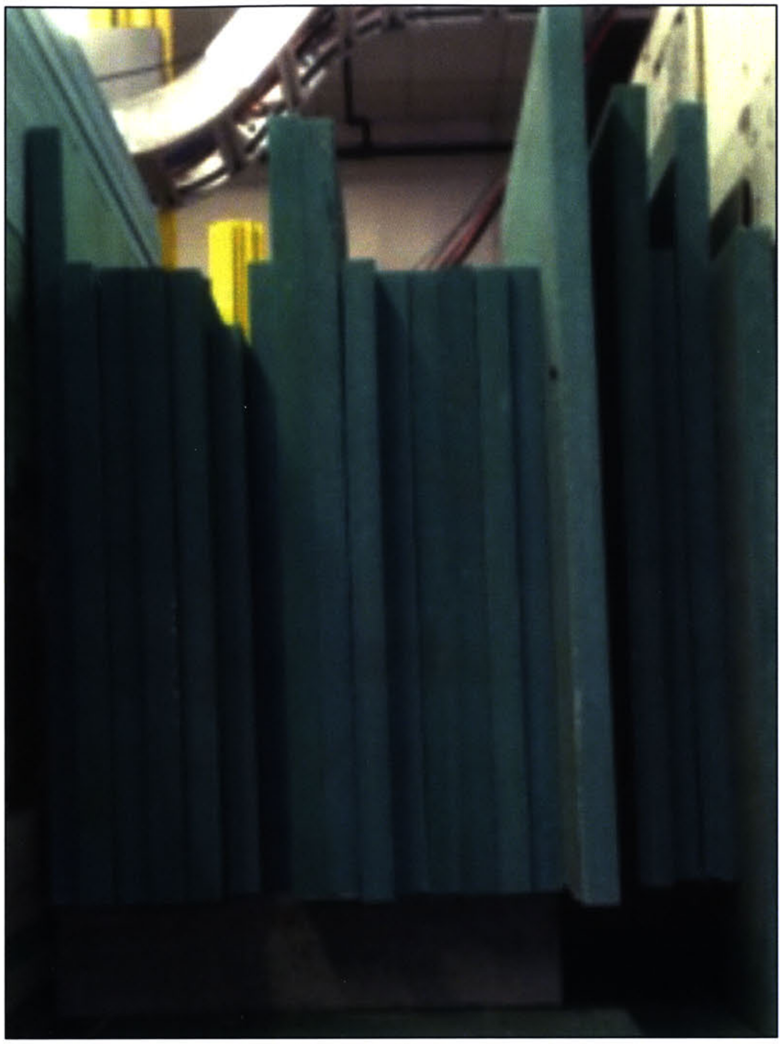

Figure 59. 21" of HDPE was placed immediately after the channel and prior to the first set of dual-density concrete collimators. The borated HDPE greatly reduced the fast and total neutron fluxes.

Figure 60. Using light to confirm daily alignment of the NaI(Tl) array with the beam line. Note the first and second sets of double density concrete collimators.

Figure 61. Typical configuration of materials for interrogation. Note the Pb collimator immediately down beam line (left) of the material interrogated.

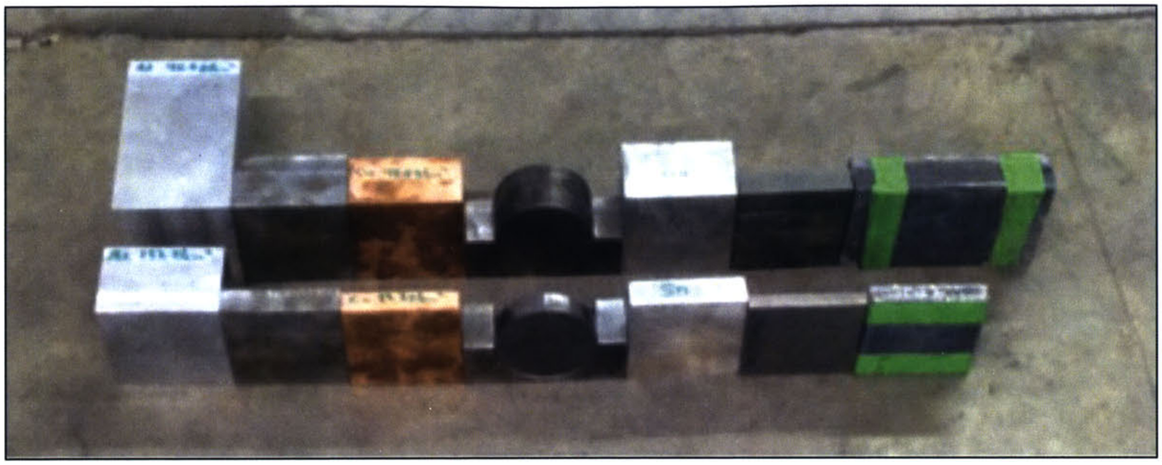

Figure 62. Materials used in the experiment including Al, Fe, Cu, Mo, Sn, W, and Pb. The near row of materials was cut to be equivalent areal density to a 1 cm thickness of W. The far row of materials was cut to be equivalent areal density to a 1" thickness of W.

Figure 63. A 1.1" U rod used in the experiments. The rod had an aluminum housing and a U diameter of 0.93".

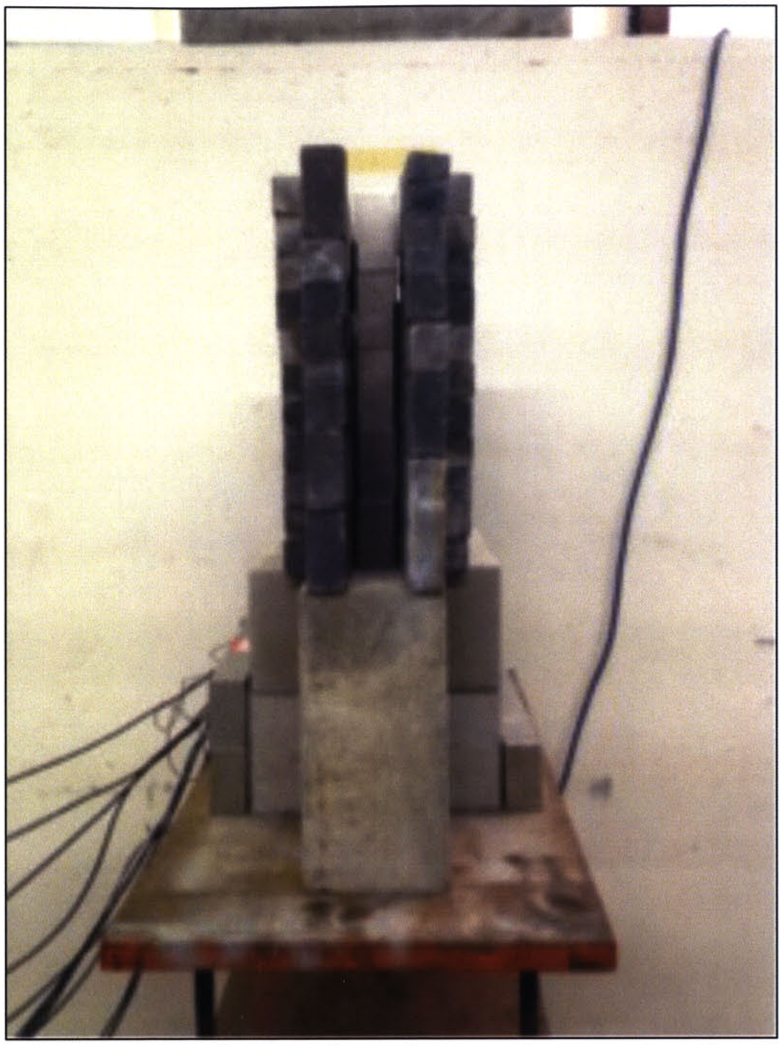

Figure 64. NaI(Tl) array used throughout the experiment. The data for the runs was taken with the second detector from the top. Note the 4" of Pb shielding to the sides and 2" thick Pb shielding extending 8" in front of the array. The concrete beam stop is seen behind the detector.

APPENDIX D. RFQ ACCELERATOR

The accelerator used in this experiment was a Model DL-3 Linac System S/N 05-0026. The information, show in Table 21 below, from tests and measurements carried out 17-21 November 2005 is included in an email from AccSyS Technology, Inc. to L-3 Communications [**59**].

Table 21. Model DL-3 Accelerator Operating Specifications **[60].**

Parameter Description	**Required Value**	**Measured Value**
Output d^+ beam energy	3.0 ± 0.1 MeV	3.02 MeV
Beam pulse width	5-150 µsec	2-150 µsec
Max RF duty factor (depends on rep rate)	1.2-1.6 %	1.6%
Output beam current (pulsed)	8-12 mA	6-10 mA
Beam diameter at target entrance	10 mm	10 mm
Vacuum pressure	$< 1 x 10^{-6}$ torr	$3 x 10^{-7}$ torr
Average current	0.1-120 µA	1-90 µA
RF Fill time	8-10 µsec	5-6 µsec

During the course of the experiment, the accelerator was operated with a pulse width of 25 µs a beam repetition rate of 100 Hz. Average current was between 9 and 14.5 µA for all runs involving borated HDPE, Al, Fe, Cu, Mo, Sn, W, Pb, and U. For two runs in which no material other than the HDPE was in the beam line, the current was run at 2-3 µA to prevent overwhelming the NaI(Tl) scintillators. After the initial runs, involving all materials except U were completed, the tech personnel adjusted the accelerator parameters to reduce the current to allow data acquisition with only HDPE in the beam line. While every attempt was made to restore the accelerator to its previous condition to conduct the experiment using attenuating materials and U, it was impossible to restore the exact configuration since not all values had been record. The average flux values per μA of current were 66% of their original values. The ratio of 15.11 MeV to 4.44 MeV gammas remained consistent. It is believed that the reduction in current is due to a change in overall defocusing of the beam current or due to a change of alignment such that the beam current was no longer interacting exclusively with the B target.

Figure 65. Side view of the DL-3 Accelerator used in the experiment.

APPENDIX E. ^{12}C LEVEL SCHEME

The level scheme for ^{12}C is included below.

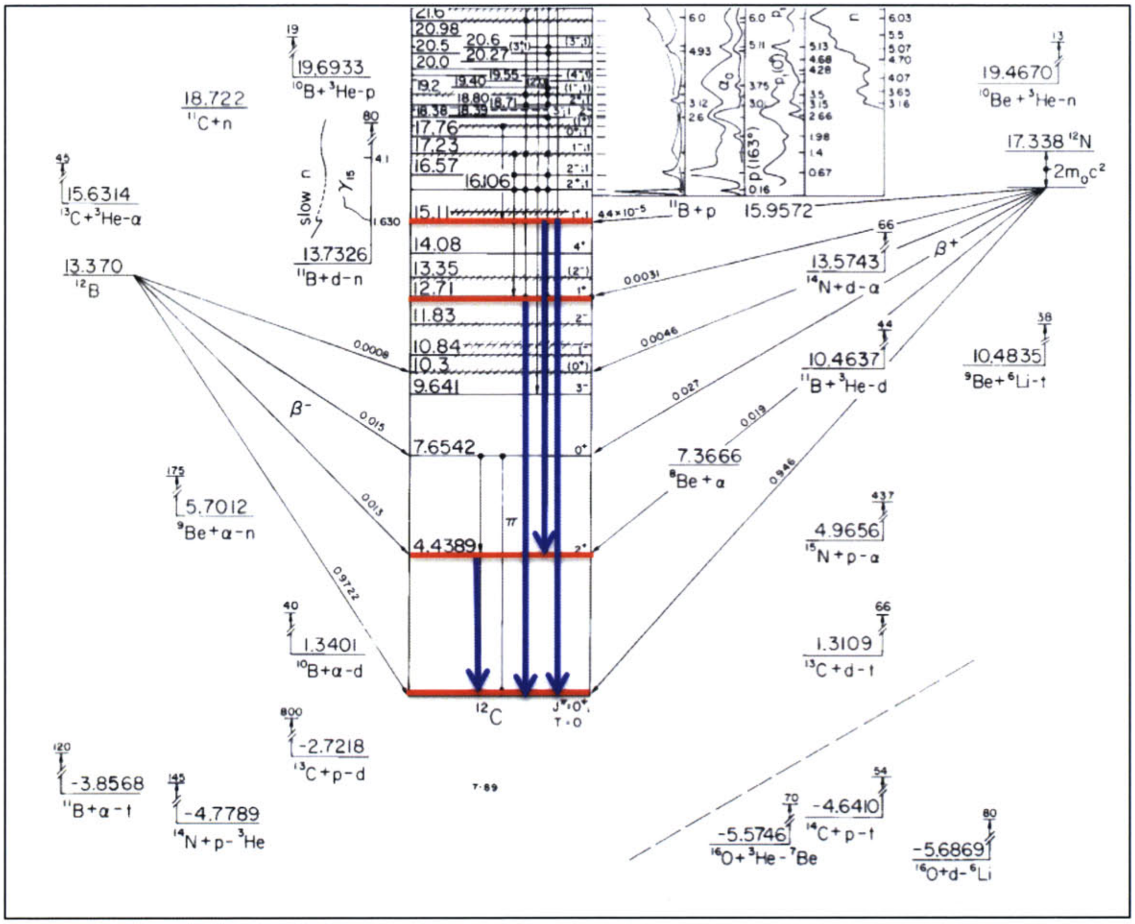

Figure 66. The Level Diagram for ^{12}C taken from [61] and modified to show the gamma lines of interest. From left to right, the 4.44 MeV gamma from decay from the first excited state to the ground state. This is the most prevalent gamma. The 12.71 MeV gamma from decay to the ground state. The 10.67 MeV gamma from decay from the 15.11 MeV state to the first excited state. The 15.11 MeV gamma from decay directly to the ground state.

APPENDIX F. ADAQACQUISITION AND ADAQANALYSIS SETTINGS

Prior to acquiring data for each experimental run, the ADAQAcquisition program's built-in oscilloscope feature was used to confirm the acquisition window was set correctly and that count rates would be acceptable. The accelerator was operated at 100 Hz with a beam with of 25-μs, and a current from 2.75-14.5 μA. A 35-μs delay was used from when the computer sent a signal to the accelerator to prepare a pulse and the digitizer opening a 30-μs data acquisition window with a 10 ns digitization frequency. The delay and the width of the data acquisition window allowed approximately 3 μs digitization before the pulse to establish baseline and 3 μs after the pulse to ensure digitization of the entire pulse and limit digitization of delayed gammas. A typical series of waveforms obtained during digitization is seen in Figure 67.

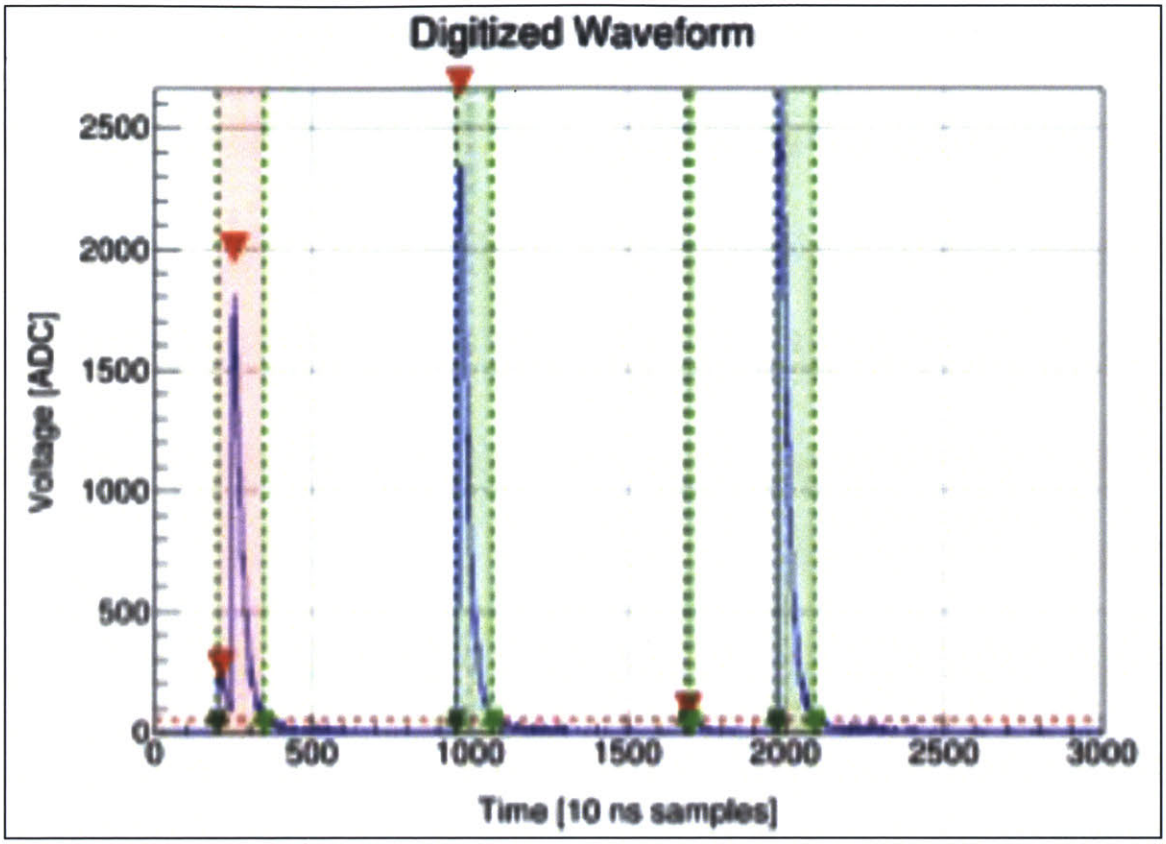

Figure 67. Waveforms obtained during digitization process. The waveforms are digitized in 10ns intervals. The two pulses to the left are thrown out due to pulse pile-up. The remaining three pulses are accepted.

The ADAQAcquisition was then operated in high-rate non-updateable mode using an automatic timer to digitize and write all data to files for subsequent off-line analysis. If desired, the ADAQAcquisition could be operated in the high-rate (updateable) but this frequently led to data loss because the buffers were full.

The ADAQAnalysis program was used to analyze data offline. The ADAQAnalysis program features were used to process waveforms, create spectra, integrate peak areas, and create root file histograms. Additional features of the program used include options for manual energy calibration and prediction of escape peaks.

Graphics with the key ADAQAcquisition and ADAQAnalysis selection screens with comments are included below.

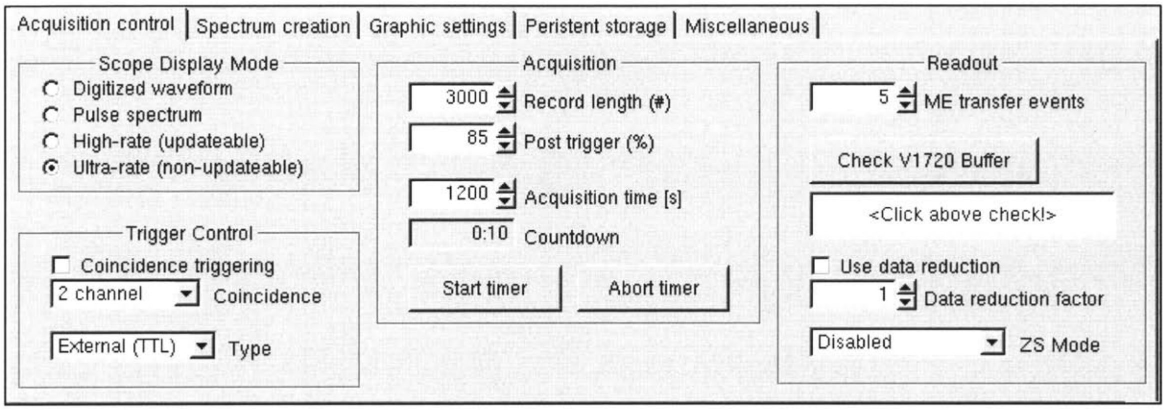

Scope Display Mode
○ Digitized waveform
○ Pulse spectrum
○ High-rate (updateable)
● Ultra-rate (non-updateable)

Trigger Control
☐ Coincidence triggering
2 channel Coincidence
External (TTL) Type

Acquisition
3000 Record length (#)
85 Post trigger (%)
1200 Acquisition time [s]
0:10 Countdown

Readout
5 ME transfer events
<Click above check!>
☐ Use data reduction
1 Data reduction factor
Disabled ZS Mode

Figure 68. ADAQAcquisition Acquistion Control settings. When observing the waveform, select scope display mode. For the best data acquisition capability, select the Ultra-rate (non-updateable) mode. This prevents you from observing data when acquiring but prevents loss of data because the buffers are full. External (TTL) was set for the external trigger. The record length was set to allow 2-3 μs of data capture before and after the pulse.

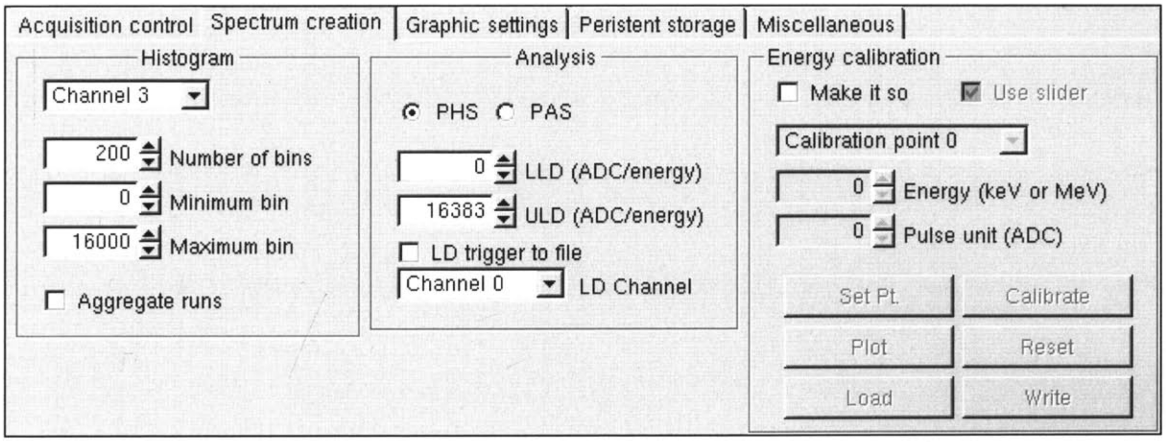

Histogram
Channel 3
200 Number of bins
0 Minimum bin
16000 Maximum bin
☐ Aggregate runs

Analysis
● PHS ○ PAS
0 LLD (ADC/energy)
16383 ULD (ADC/energy)
☐ LD trigger to file
Channel 0 LD Channel

Energy calibration
☐ Make it so ☑ Use slider
Calibration point 0
0 Energy (keV or MeV)
0 Pulse unit (ADC)

Figure 69. ADAQAcquisition control settings. Pulse height spectra (PHS) was selected. The maximum number of bins must be less than the upper level discriminator (ULD) and depends on the digitizer used.

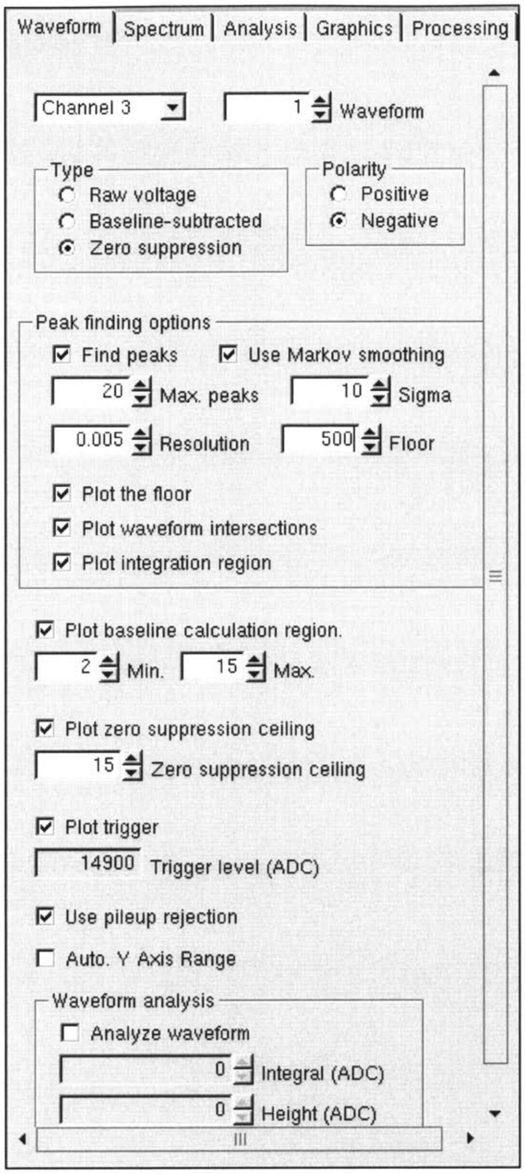

Channel 3

1 Waveform

Type
○ Raw voltage
○ Baseline-subtracted
● Zero suppression

Polarity
○ Positive
● Negative

Peak finding options
☑ Find peaks ☑ Use Markov smoothing
20 Max. peaks 10 Sigma
0.005 Resolution 500 Floor
☑ Plot the floor
☑ Plot waveform intersections
☑ Plot integration region

☑ Plot baseline calculation region.
2 Min. 15 Max.

☑ Plot zero suppression ceiling
15 Zero suppression ceiling

☑ Plot trigger
14900 Trigger level (ADC)

☑ Use pileup rejection

☐ Auto. Y Axis Range

Waveform analysis
☐ Analyze waveform
0 Integral (ADC)
0 Height (ADC)

Figure 70. ADAQAnalysis settings for waveform tab. The floor can be adjusted to optimal conditions for the data set but this will leave to a shift in the peak locations in ADC channels.

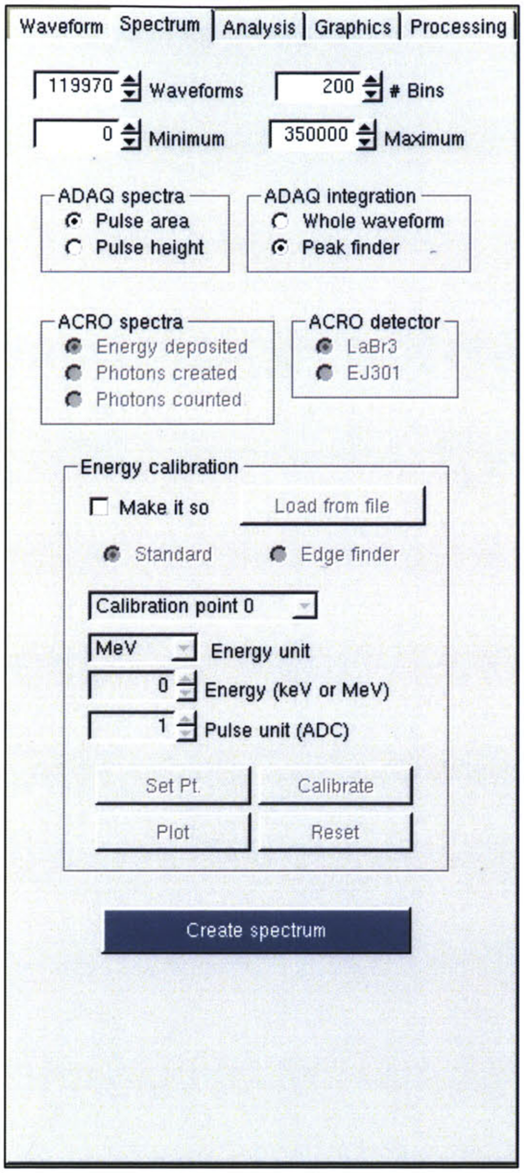

119970 Waveforms
200 # Bins
0 Minimum
350000 Maximum

ADAQ spectra
● Pulse area
○ Pulse height

ADAQ integration
○ Whole waveform
● Peak finder

ACRO spectra
● Energy deposited
● Photons created
● Photons counted

ACRO detector
● LaBr3
● EJ301

Energy calibration
☐ Make it so
● Standard
● Edge finder
Calibration point 0
MeV Energy unit
0 Energy (keV or MeV)
1 Pulse unit (ADC)

Figure 71. ADAQAnalysis settings for the Spectrum tab. Numerous analysis runs on various data sets were performed to determine 200 as the optimal number of bins. The maximum ADC channel of 350000 was selected such that the "edge" of the 15.11 MeV peak was at approximately 280000. The energy calibration option was used to calibrate spectra. When calibrated, the maximum was changed to 20 and plotted in units of MeV.

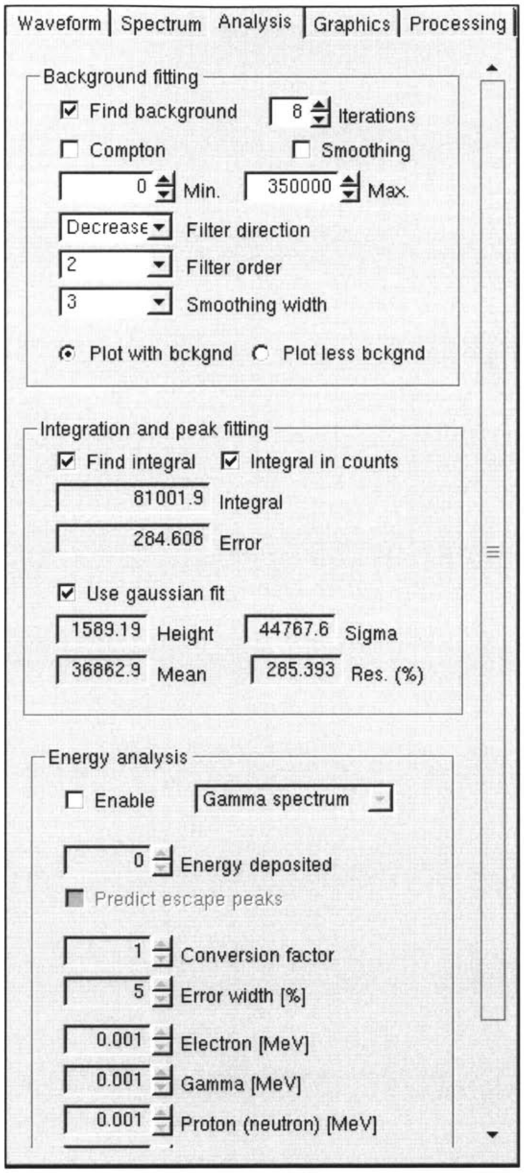

Background fitting

☑ Find background
8 Iterations
☐ Compton
☐ Smoothing
0 Min.
350000 Max.
Decrease Filter direction
2 Filter order
3 Smoothing width
● Plot with bckgnd
○ Plot less bckgnd

Integration and peak fitting

☑ Find integral
☑ Integral in counts
81001.9 Integral
284.608 Error
☑ Use gaussian fit
1589.19 Height
44767.6 Sigma
36862.9 Mean
285.393 Res. (%)

Energy analysis

☐ Enable
Gamma spectrum
0 Energy deposited
☐ Predict escape peaks
1 Conversion factor
5 Error width [%]
0.001 Electron [MeV]
0.001 Gamma [MeV]
0.001 Proton (neutron) [MeV]

Figure 72. ADAQAnalysis settings. Background subtraction was only used when finding the counts in the 4.44 MeV FEP and SEP. For consistency, a background subtraction of 8 iterations was used for all data sets. Gaussian fits (with the find integral, integral in counts, use Gaussian fit options selected, and plot less background) were made to the background-subtracted FEP and SEP to determine the number of counts in the FEP and SEP without background. The same areas of integration were used but the plot with background option selected and use Gaussian fit not selection to find the FEP and SEP counts with background.

APPENDIX G. DETECTOR SCHEMATIC

A 2” x 4” x 16” Saint Gobain NaI(Tl) detector with 2” PMT was used during this experiment. A schematic of the detector is seen in Figure 73.

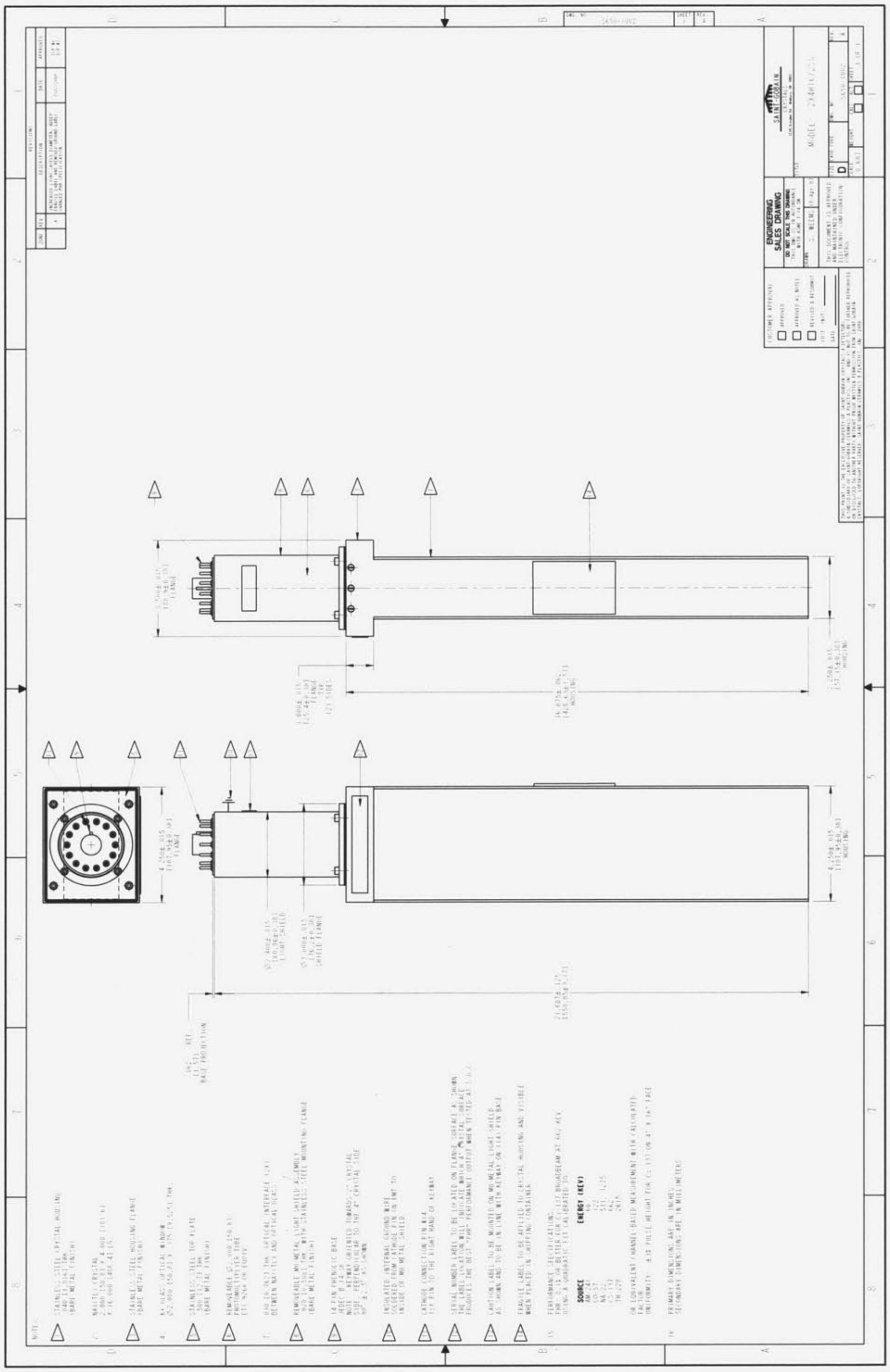

Figure 73. Schematic of 2"x4"x16" Saint Gobain NaI(Tl) with 2" PMT.

APPENDIX H. RECOMMENDATIONS FOR FUTURE WORK

The recommendations for future work stated in Chapter 8 are elaborated on upon below:

1) Charge Integration.

Charge integration improvements will allow better determination of 4.44 and 15.11 MeV gamma production yields, provide the instantaneous production rates necessary for fielding a near real-time scanning system, and allow better estimation of cargo areal density.

One possible method of performing charge integration is to configure the DL-3 accelerator to output a frequency that is directly proportional to the instantaneous charge passing through a collar in the accelerator located immediately prior to the B target. A software program could then be developed to interpret this signal to provide the instantaneous current and integrated current (total charge) for any time interval.

Knowledge of the total charge will allow more accurate determination of the 4.44 and 15.11 MeV gamma production yields per μC (μA) of charge. The frequency can be sampled and averaged or integrated over the entire run time to more accurately determine the total number of deuterons that reach the B target. This will allow more accurate determination of the 4.44 and 15.11 MeV production yields and cross sections for a 3.0 MeV deuteron on a greater than 3.0 MeV deuteron stopping power thickness target of B.

Knowledge of the instantaneous current will also be integrated into the control mechanism for the scanning system. The detector count rates are a source of feedback into the control system that will be used to determine if the current should be increased or decreased. The instantaneous current can then be adjusted to bring count rates into an optimal count rate range.

If a means of decoupling the Z_{eff} and areal density (which is equivalent to determining both the effective mass attenuation coefficient for the cargo and its areal density), more precise knowledge of the deuteron current will allow more accurate estimation of the areal density of the cargo.

Specific work to be conducted should include:

- Configuration of the DL-3 accelerator to provide an output signal that is directly proportional to the instantaneous deuteron current impinging on the B target.
- Use of the DL-3 in integrated current mode to more accurately determine the 4.44 and 15.11 MeV gamma yields.
- Development and integration of a current control system to allow automatic adjustment to the current based on count rates to bring count rates into an optimal count rate range.

2) Quantification of 4.44 and 15.11 MeV gamma production rates for 3.0 MeV deuterons on a B target without the presence of HDPE.

Quantification of 4.44 and 15.11 MeV gamma production rates for 3.0 MeV deuterons on a B target without the presence of HDPE will allow more accurate determination of cross sections, and optimization of shielding design.

Accurate measurement of gamma yields is important because it will allow better determination of the 4.44 and 15.11 MeV total and angular cross sections for 3.0 MeV deuterons on a greater than stopping power thickness B target. A better understanding of these cross sections will allow optimization of shielding designs and inform employment of any system using this reaction in a fielded system. Further, measurement of the naked beam will allow determination of which processes, if any, are originating in the HDPE, and to what extent these radiations may impact the quality and character of detected spectra.

The gamma production rates experimentally measured in this research were taken with 21" of HDPE in the beam line. Excessive count rates and geometry limitations prevented accurate measurements without HDPE. Thus, gamma production estimates involved correcting for the presence of the HDPE.

There are several potential techniques that can be employed separately or together to allow measurement of the gamma counts without HDPE in the beam line:

- Reduce the beam current as much as the DL-3 allows. Presently, the lowest beam current used in this thesis research was 1.35 μA. The accelerator functioned reliably at this level and further reductions may be possible.
- Temporarily remove the beam stop or move it back to reduce the solid angle subtended by the detector. Removal of the beam stop and placement of the detectors against the back wall will reduce the count rate by a factor of 2-3. It is not believed that this method by itself will allow measurement of the naked beam.
- Use a detector with a faster recovery time to reduce pulse pile-up issues.
- Use a smaller detector.

Initial work in this area should seek to determine the lowest current at which the DL-3 can reliably operate. This can be done with the current setup, including the HDPE, and gradually reducing the deuterium input. When the limit is reach reached, the HDPE can be removed from the beam line and a measurement taken. If the data shows that a factor or 2 or 3 reduction of the flux would allow accurate measurement, temporary removal of the beam stop should be considered.

Finally, it should be noted that use of a different accelerator, such as the Deuterium Accelerator-based Neutron-producing Tandem Experiment (DANTE) at

MIT [62], it should be possible to quantify gamma production yields and determine energy and angular specific measurements.[72]

3) Changes to the Data Acquisition System.

Changes to the Data Acquisition System (DAQ) will reduce the amount of data that must be recorded, reduce the amount of information passed to the computers for processing and analysis, and greatly reduce data storage requirements.

The current data acquisition setup, with complete digitization of all pulses when the beam is on, can only support 8 detectors. Transitioning to a vertical array of a few dozen detectors will require additional digitizers. The current DAQ digitizes at 10 ns samples for a few μs before the accelerator beam is on, the duration of the beam pulse, and for a few μs after the beam is off. This is very inefficient since many data points are of no value. The DAQ needs to:

- Operate in event mode
- Conduct pileup rejection
- Time stamp events

An effort should be made to determine the requirements and capabilities for an operational system. While the system should work with the DL-3 accelerator, it should be flexible enough to allow use of other gamma production equipment. The requirements and capabilities should then inform procurement of the necessary

---

[72] An effort should also be made to better understand the neutron spectrum. An organic scintillator can be used to conduct PSD, to determine the magnitude of the neutron production issue. Additional experiments to gain better understanding of the neutron energy spectrum should also be conducted.

hardware and modification of existing data processing software or development of a new software suite.[73]

4) Optimization of 4.44 and 15.11 Counting Intervals.

Optimization of 4.44 and 15.11 MeV counting intervals will allow better understanding of the dependence of Z reconstruction resolution on the integration limits.

Current integration intervals were chosen ad-hoc. Changes to the regions used for counting could increase the overall counts and reduce the associated errors. For this thesis, the 4.44 MeV integration only counted those events in the FEP. Counting statistics will be improved if counts from the FEP and SEP are both used for 4.44 MeV counting. The 15.11 MeV integration region limits could also be changed. It should be noted that while an increase in the 15.11 MeV integration region will increase counts and therefore reduce associated error, if the region is expanded so that gammas not originating from 15.11 MeV gammas are included this could introduce inaccuracies.

A systematic optimization study needs to be performed to understand the dependence of Z reconstruction resolution on the integration limits. The existing data can be used to determine the optimal integration regions used for counting. Development of an automated system with 4.44 FEP and SEP and 15.11 MeV high-energy edge finding capability with adjustable integration parameters may provide

---

[73] It should also be noted that the existing analysis software package and procedures must be modified to allow receipt of data from the DAQ. Eventually, the transfer of information and processing must occur rapidly enough to allow near real-time imaging capability.

an easy and adequate solution. Inclusion of additional peaks (6-9 MeV discussed below) may also be considered.

Specific research in this area should:

- Conduct a systematic optimization study using existing data to understand the dependence of Z reconstruction resolution on the integration limits.
- Develop an automated system with 4.44 FEP and SEP and 15.11 MeV high-energy edge finding capability with adjustable integration parameters to process histogram files.
- Determine potential sources of gamma lines that may fall within the 15.11 MeV integration region. Quantify the potential for these gamma lines to interfere with 15.11 MeV count integration. If the impact is substantial, determine if a means of suppression is available.
- Determine potential sources of gamma lines that may fall within the 4.44 MeV FEP and SEP region. Quantify the potential for these gamma lines to interfere with 4.44 MeV count integration. If the impact is substantial, determine if a means of suppression is available.

5) Optimization of 4.44 MeV background removal and determination of peak area.

Optimization of 4.44 MeV background removal may result in more accurate determination of experimental counts, ratios, areal density, and estimation of the Z_{eff} *of the cargo.*

Currently, the backgrounds are removed for 4.44 MeV using the ROOT TSpectrum class as part of the ADAQAnalysis program. For background subtraction, the ADAQAnalysis program assumes that all the bins are uncorrelated, and calculates the error as the square root of the sum of the square of the counts for each bin. It may be possible that other background removal techniques will provide more reliable results. For example, a better approach might be to model the backgrounds using Monte Carlo techniques and to do numerical subtraction.

In addition to background removal algorithms, alternative methods of determining the peak should also be considered. One potential method is to perform Gaussian fits to both the 4.44 MeV FEP and SEP at one FWHM-wide ROIs centered on each peak. The total peak areas can be determined from these fits.

An analysis of the FEP raw data with background removed should be compared to results using both full FEP Gaussian fits as was used in this thesis and using a FWHM Gaussian fit as described above. This will provide insights into the validity of using Gaussian fits to determine peak areas. The integration region should be these same for all three cases. The existing data could be used to conduct this analysis.

It was also noted during the experiment that the background at 4.44 MeV and below changed with areal density (Figure 41).[74] This changing background complicated background removal and identification of the peak area. Research should be undertaken to better understand the origin of this changing background. Specifically, an effort should be made to determine how the material composition (Z_{eff}) and areal density impact the shape of the background spectrum. This may be accomplished by analyzing the data from conducting a series of pure material tests at several equal areal densities.

Specific research in this area should:

- Determine if other automated background removal techniques will provide more reliable results.
- Develop simulations to better understand the character of the background spectrum. Use this information to inform selection of automated background removal techniques.
- Consider the use of models as a means to numerically subtract background.
- Conduct a full de-convolution of spectra (with and without collimators and shielding; with and without cargo present) to gain a better understanding of

---

[74] No background removal was considered for the 15.11 MeV integration region.

spectral features. Specifically, determine how the Compton continuum from different interactions shows up in the final spectra.

- Consider alternative means of calculating peak area, such as performing Gaussian fits to both the 4.44 MeV FEP and SEP at one FWHM-wide ROIs centered on each peak and using parameters to calculate total peak area.
- Study the existing data to determine how well Gaussian fits and raw counts for background spectra match.
- Study the existing data to determine how the material composition (Z_{eff}) and areal density impact the shape of the background spectrum, and how this impacts the ability to accurately determine peak heights. Use information gained from this study to inform selection of background removal spectra and selection of ROI for peak areas.

6) Incorporation of Multiple Arrays and Alternate Arrays.

Incorporation of multiple arrays and alternate arrays may decrease system vulnerability to smuggling, facilitate secondary scanning and searches, and allow combination of data to provide more information about the cargo than any single detector array can provide.

Multiple arrays may be used to take different imaging slices through the cargo. This would make it more difficult to smuggle high-Z materials using the methods discussed in Chapter 3. This would require an additional two arrays and all associated data processing systems. Since the direction of each fan beam, location of each detector array, and knowledge of what line across the cargo is scanned as a function of time, the information gained from the three arrays could also provide information about the depth of any material of concern inside the cargo container. An additional possibility is to replace each side array with a different set of detectors to gather similar or complementary information. Either technique would provide different views of the same cargo and make attempts to defeat the system less likely to succeed.

Depending on how the arrays are oriented with respect to the B target and cargo, it may provide additional information relating to the depth of suspect high-Z material in cargo. This could facilitate secondary scans or searches. Specific multiple array research should include:

- Determination of the optimal angle of fan beams to gather the best positional information (rather than just simple geometry, consideration must be given to areal density distributions, areal density scanning limitations, and scanning time requirements).
- Determination of how well the system can determine the depth of high-Z material imbedded in the cargo.
- Determination if scanning with multiple arrays provides information to estimate the total volume and/or mass of the imbedded high-Z material.

The use of alternate arrays may allow employment of different detectors that are better suited to detect gammas at different energies. Specific alternate array research should focus on identification of detectors best suited to identify 4.44 and 15.11 MeV gammas (and possibly 6-9 MeV gammas discussed later in this chapter).

Consideration should also be given to how the information gained from using multiple or alternate arrays could be combined to provide more information about the cargo than any single detector or detector array can provide. A cost-benefit analysis of employment of multiple or alternate arrays should also be considered.

7) Consideration of Alternative Low-Threshold Nuclear Interactions and Reactions.

Consideration of alternative low-threshold nuclear interactions and reactions may lead to better estimation of areal density or reduced shielding requirements.

Searching for alternative low-threshold nuclear interactions may yield gamma lines that may lead to better estimation of areal density (likely to occur from gammas in the 1.5-3 MeV range where mass attenuation coefficients are more similar for materials) or reduced shielding requirements (from an interaction that does not produce significant amounts of neutrons).

Other low-threshold nuclear interactions with favorable gamma lines should be considered. One researcher has suggested a $^{12}C(p,p')^{12}C^*$ interaction with 18-19 MeV protons will provide the 4.44 and 15.11 MeV gamma lines used in this thesis research without the prolific neutrons and with an adjustment to 20 MeV could provide the neutrons [**51**]. The absence of neutrons would greatly reduce shielding requirements. It should also be noted that other alternatives could involve using a combined material target to create multiple gamma lines from different interactions or the possibility of an exchangeable target.

Key areas of research should include:

- Identification of potential sources of gammas from 1.5 to 3.0 MeV. The mass attenuation coefficients vary less among materials in this energy range and could provide a narrower range of areal density estimates.
- A theoretical analysis to determine the optimal gamma ray energies to provide the best estimates of areal density and Z_{eff} for an unknown cargo.
- A compilation and analysis of all possible low-threshold reactions and their gamma and neutron production rates.
- An analysis of the data available in the NIST tables may identify combinations of gamma lines that would allow better discrimination between medium- and high-Z and among high-Z materials.[75]
- Determination if combinations of interactions may yield the desired gamma rates.
- Dose rates from radiations produced by the reaction or combination of reactions.

---

[75] It should be noted that the selection of which gamma rays to use in combination determines what materials are ratio enhancers, ratio neutral, or ratio reducers. Therefore, using several combinations of gamma rays has the potential to provide more information about the cargo composition. For example, in the current analysis, Cu was ratio neutral but use of a lower energy gamma line with a larger mass attenuation coefficient will lead to Cu acting as a net enhancer since the new gamma line has a larger mass attenuation coefficient than at 15.11 MeV.

8) Possible use of additional gamma lines in the data.

Possible use of additional or alternative gamma lines may increase system ability to discriminate among materials and allow better estimation of the cargo areal density and Z_{eff}. This section is closely related to the immediately preceding section since low-threshold nuclear interactions and reactions dictate which potential gamma lines are available.

The use of additional gamma lines would provide additional information that provides a potential increased ability to discriminate among materials. For example, the two material cargo combinations that produced the same ratio and attenuation could be differentiated with use of a third gamma line. An increase in the number of gamma lines would allow better estimation of the areal density and Z_{eff} for a cargo.

The use of additional gamma lines also provides additional information about the cargo. The attenuation of each gamma line provides a measure of the product of the effective mass attenuation coefficient and the areal density of the cargo. An increase in the number of gamma lines provides a linear increase in the number of measures of the cargo. However, with n gamma lines, we can compare each gamma line to all the other gamma lines so there are $\frac{n!}{2!(n-2)!}$ available independent ratios. So an increase to three gamma lines provides three, four provides six, and five provides 10 potential independent ratios. This additional data also provides the possibility of using a more complex algorithm to better determine the characteristics of the cargo.[76]

The existing data shows currently unidentified gamma lines at approximately 6-7 and 8-9 MeV that are present in all of the data. It is believed these gamma lines are produced prior to the cargo. If the origin and production yields of these two gamma lines can be characterized, if used in conjunction with the 4.44 and 15.11 MeV gammas, the current experimental configuration would provide six R_{Exp} ratios that can be compared with R_{Th} ratios. This may allow better characterization of the cargo, reduction to the range of potential areal densities, and an increased ability to discriminate between different Z materials.

Specific research in this area should focus on:

- Determination of the penetrability and attenuation of gamma lines (discussed in further detail later)
- Determination of gamma energies or combinations of gamma energies that allow the best discrimination capability between medium- and high-Z materials. Additionally, determination of gamma energies or combinations of gamma energies that allow discrimination among high-Z materials should be considered.
- Determination of whether continued consideration of R_{Th} values is provides sufficient information or if a more complex algorithm (discussed in further detail later) should be implemented. It may be possible to incorporate ratios in a rapid clearance algorithm while the more complex algorithm may be more useful for discrimination of medium- and high-Z cargo.
- Finding the origin of the 6-7 and 8-9 MeV gammas present in the existing data. If their origin can be determined and quantified, use the existing data set as a test case to determine if incorporation of these gamma lines provides an improved ability to characterize the cargo.

9) Study of optimal gamma energies for maximum penetration and Z discrimination.

---

[76] It should be noted that inclusion of additional gamma lines makes development of a workable algorithm much more difficult. Therefore, the use of a simple algorithm, such as the one used in this research, for multiple combinations of gamma lines separately should also be considered.

A general study of the optimal gamma energies for maximum penetration and Z discrimination may allow determination of the best possible gamma energy combinations to use and potential source interactions. This area of study is intricately related to the previous sections on identification of alternative low-threshold interactions and possible use of additional gamma lines in the data.

While mass attenuation coefficients provide an easy determination of absolute penetration, additional effects (e.g. changes to the character of the background spectra and dose rates) must also be considered. A relatively simple approach would be to create a simulation or program that pulls gamma interaction characteristics *en masse* and simulates scanning of various areal density cargos. This research will complement the research addressed in "Consideration of alternative low-threshold nuclear interactions and reactions" section above and influence ultimate selection of target material and gamma lines.

10) Quantification of neutron and gamma dose rates.

Quantification of neutron and gamma dose rates will allow comparison of the proposed system[77] *and existing systems, and will allow provide a means of setting source interrogation production limits.*

Theoretical and experimental research must be conducted in this area to ensure development of a system that can be used in the field. It is also important to quantitatively compare any developed system to existing systems and to demonstrate compliance with regulatory requirements. Future research should

---

[77] During the course of the experiment no effort was made to quantify total dose rate from neutrons and gammas. Neutron does rates were measured for numerous experiments and were less than 1 mrem/hr at the front of the cargo for up to a 14 μA deuteron current.

include quantification of the dose rates from neutron and gammas per μA of deuteron current during operation of the accelerator to the cargo, potential stowaways, and the equipment operator. A full simulation of the system and surrounding area should also be created to allow optimization of shielding and collimation and determination of dose rates.

11) Determination of the areal density interrogation range.

Determination of the areal density interrogation range will allow estimation of the fraction of cargo passing through POEs the system can reliably scan and determination of how source production should be changed with areal density.

The range of areal densities considered in this thesis was 125-255 $\frac{g}{cm^2}$. The lower range of areal density was limited by detector response and excessive count rates due to an inability to reduce the deuteron current. The upper range was limited by the deuteron current and changes to the background that made 4.44 MeV FEP integration difficult. Additional experiments after data collection demonstrated an ability to reduce the deuteron current by almost an order of magnitude to no more than 1.3 μA. Additionally, changes to the HDPE to reduce neutron dose rates may allow operation of the machine at approximately 90 μA. Due to the exponential nature of attenuation, the ability to adjust the current to these ranges should expand the areal density interrogation range to 50-320 $\frac{g}{cm^2}$ without a significant negative impact on counting statistics.

Every effort should be made to attempt to expand the areal density interrogation range to at least 300 g/cm^2. While it is not achievable with the current system and gamma lines used, the development of a system capable of scanning a 520 g/cm^2 (equivalent to a 2m thick slab of marble or 26" of Fe) would represent a significant breakthrough and would likely clear most cargo passing through US ports. If such a system cannot be developed that meets existing dose and dose rate restrictions, it may be possible to employ a system at major POEs for high areal density cargo (with a very low chance of stowaways).

Research to determine the limits of areal densities that can be interrogated includes:

- Quantifying the dose rate relationship between the current system and the deuteron current. This should include a full simulation (e.g. MCNP6) of the current system using a current up to 90 μA. The total dose rate and neutron and gamma dose rates should be determined.
- Conduct the same simulation using the $^{12}C(p,p')^{12}C^*$ interaction.
- Conduct an analysis relating the current, gamma production rates, cargo areal density, dose rates, and scan time to determine the maximum cargo areal density that can be scanned.
- Conduct a simulation and experiments to determine if changes to collimators may improve spectra by removing background and allow scanning of larger cargo areal densities. Suggested experiments include taking data beyond the second set of large collimators and to the side and front of the detector to determine if secondary scatters are convoluting the spectra. If in-scatter is a problem, the addition of Pb to the channel immediately in front of the detector will reduce the acceptance angle and may reduce background in the vicinity of the 4.44 MeV peak.

12) Reduction to interrogation time.

Reduction of interrogation time to the minimum necessary will increase the potential of creating a system that can be used for primary and secondary scanning without adversely impacting commerce.

The scan times in this thesis research must be reduced substantially to allow development of a practical system. Dose rate quantification will inform the maximum allowable deuteron current that can be used for the current configuration. Improvements to DAQ capabilities will allow adjustment to the beam repetition rate and pulse width to increase count rates. The NaI(Tl) detectors also have a maximum count rate that limits the current that can be run. The use of an alternate detector or detectors with a faster recovery time should also be considered.

Research should be undertaken to reduce the interrogation time. During this thesis, no effort was made to optimize or minimize interrogation time. The accelerator was run with 30 μS pulses at 100 Hz representing a duty factor of 0.3 %. However, the accelerator can operate at a duty factor of 1.6% and, as previously mentioned, at an almost order of magnitude larger current. The ability to change the pulse width, repetition rate, and average current should allow significant reductions to interrogation time. Note the 90 μA average deuteron current is the limiting factor. It can be reasonably parsed into pulses of varying width and repetition rates but cannot be exceeded.

Specific research that should be undertaken includes:

- Development of an algorithm to determine when sufficient 4.44 and 15.11 MeV counts have been recorded to allow scanning to proceed to a different area.
- Improved background removal (previously addressed).
- Inclusion of 4.44 SEP counts (previously addressed).
- Optimization of counting integration regions (previously addressed).

13) Establishment of the high-Z areal density detection threshold.

Establishment of the high-Z areal density detection threshold will quantify what high-Z areal density quantities the system can detect.

A detailed study of areal densities of 49.0 g/cm^2 and lower should be undertaken to quantify the detection threshold. A simple theoretical model can be developed that determines number of counts (and thus the product of the current and scan time) and SNR necessary to confirm the presence of high-Z material in a non high-Z cargo. Development of a more robust model with GEANT 4 or MCNP6 would provide a more accurate estimate and more easily allow inclusion of the impact of changes to the underlying background on identification of 4.44 and 15.11 MeV counts. Different thicknesses of high-Z material can then be scanned with the system to validate the model. Further, theoretical and experimental work should be conducted to relate the high-Z areal density detection threshold and the total areal density of the cargo. This research should also seek to characterize how detection sensitivity changes with overall areal density of the cargo.

Specific research should:

- Use improved background removal (previously addressed) and inclusion of 4.44 MeV SEP counts (previously addressed) with the previous data set to determine if this reduces the high-Z areal density detection threshold to 19.3 g/cm^2 areal.
- Develop a simulation (and conduct experiments) to study the relationship between cargo areal density and changing background spectrum to determine how they impact the required number of counts (to the desired SNR) to identify various high-Z areal density detection threshold thicknesses.

14) Validation of detector efficiencies.

Validation of detector efficiencies will allow use of the NaI(Tl) detectors to determine 4.44 and 15.11 MeV gamma production rates and increased confidence in using these detector efficiencies as part of a full system model.

The detector efficiencies can be validated using several different methods. One method would be to use MCNP6 to model the system (since GEANT 4 was originally used) and compare the modeling results. A second method is to use alternate detectors to determine the 4.44 and 15.11 MeV production rates and compare the results with the experimentally measured results. A third method is to construct 4.44 and 15.11 MeV production cross sections for 3.0 MeV deuterons on a greater than stopping power thickness B target from existing data and data that can be obtained using another well-characterized detector and to compare the theoretical results with experimental results obtained with the NaI(Tl) detectors used in this thesis research.

Specific research in this area should include:

- Development of an MCNP6 model and comparison of the results with those obtained from the GEANT 4 simulation.
- Use of a PuBe source (if the 4.44 MeV production rate can be characterized) or another source with a known 4.44 MeV gamma production rate to validate the GEANT 4 results for 4.44 MeV.
- Use of the same GEANT 4 model to simulate other gamma ray energies that can be compared to experimental results from data taken with the NaI(Tl) detector..
- Use of another well-characterized detector (with known efficiencies) to measure the gammas from the system and compare with the results obtained from the NaI(Tl) detector
- Use the DANTE accelerator to obtain 4.44 and 15.11 MeV energy and angular cross sections (using a different detector) for 3.0 MeV deuterons on a similar target, using these cross sections to construct 3.0 MeV deuteron theoretical stopping power target thickness yields, and comparison of results with those measured by the 4.44 MeV detector.

15) Testing the ability of smuggling methods to defeat the system.

Testing the ability of smuggling methods to defeat the system will inform how the system should be modified to reduce vulnerability to smuggling.

Once the high-Z areal density detection threshold is determined and a full detector array is operational, the system should be tested using the smuggling methods outlined in Chapter 3. The findings should be incorporated into system development to eliminate or minimize potential means of defeating the system. Experiments should be designed to test the sensitivity of the scanning method to "ratio neutral" and "cargo replacement" smuggling methods.

Research should also be conducted to develop an inventory of potential hydrides or hydrogenous materials that may be capable of hiding high-Z material. If research determines that using hydrogen-rich material to smuggle high-Z material is a possibility, experiments should be conducted to determine the sensitivity of the scanning system to this smuggling technique.

Specific research should include:

- Developing an inventory of potential hydrides or hydrogenous materials that may be capable of hiding high-Z material.
- Conduct tests to determine system sensitivity to "ratio neutral" and "cargo replacement" smuggling methods.

16) Impact of lanthanides on discrimination of medium and high-Z materials.

Detailed study of the impact of lanthanides on discrimination of medium- and high-Z materials will inform eventual tests to discriminate between medium- and high-Z materials, provide insights into if and how these materials may be used to hide high-Z materials, inform a potential redefinition of the dividing line between medium- and high-Z materials, and impact potential high-Z areal density detection thresholds.

Greater understanding of lanthanides is critical because their atomic numbers fall between Sn and our current definition of high-Z material. Due to their radiation attenuation characteristics, they are more difficult to differentiate from W than Sn. Significant amounts of lanthanides, and particularly the higher-Z lanthanides, could be mistaken for or used to conceal high-Z material. Therefore, research should be conducted to determine which lanthanides are transported in sufficient quantities that would allow them to be used to conceal high-Z material.

Lanthanide-related research and experiments should include:

- Research and engagement with industry to determine which lanthanides are transported in bulk quantities[78] (and how often they are transported) that could make it difficult for the proposed system to discriminate between their presence and the presence of high-Z materials.[79]
- Tests of the ability of the scanning system to discriminate between the lanthanides listed above and high-Z materials embedded in cargo.
- Results of the two above listed tasks may lead to a redefinition of which materials are considered medium- and high-Z materials
- If lanthanides are determined to be a significant potential source of false positives, work should be done to determine potential other methods of discriminating between them and high-Z materials.

17) Acquisition of more realistic information on the distribution of cargo in containers.

Acquisition of more realistic information on the distribution of cargo in containers will inform determination of what cargo can and cannot be cleared using the proposed system and development of scanning system operating parameters.

The existing data does not provide the kind of detailed information that is necessary to determine what fraction of cargo the proposed system can effectively scan. An effort should be made to reach out to industry to determine if information exists that may inform development of the proposed system. Examples of such information include data and images from x-ray imaging of actual cargo, any

---

[78] For example, movement of lanthanum and cerium for catalytic cracking of heavy crude at oil refineries.

[79] It should be noted that correspondence with an industry expert indicates that while all Lanthanides can be shipped in bulk to only that are commonly shipped are Ce, La, and Nd [**19**].

industry-specific studies that may provide information about the frequency and magnitude of areal densities actually encountered, and container loading requirements and practices that could inform development of the system. If the information does not exist, efforts should be made to work with shippers and port facilities to gather this information.

Available cargo container density data generally describes the average density based on the total load and does not account for non-homogeneity of the materials and irregular loading. Average homogeneous areal density measurements have minimal utility. The potential range of cargo container areal densities is bounded on the lower end by empty space and on the upper end by a dense material of the maximum rated load for the container that is palletized and placed in the center of the container. For example, a standard size container filled with Fe sheets could have a maximum areal density of $235\ cm \cdot \frac{7.785\ g}{cm^3} = 1829.5\ \frac{g}{cm^2}$. This cargo could not be scanned without excessive dose rates and impractically long scan times. It should be noted that an inability to scan such excessive areal density cargo does not negate the value of the scanning system. The system will still function for all cargos below a yet to be determined maximum areal density. This maximum areal density, when compared to the overall distribution of maximum areal densities in cargoes, will provide a better estimate of the system's applicability.

Engagement with freight companies and port facilities, and consideration of shipping regulations, may provide insights into more typical cargo distributions. Acquisition of actual areal density data would be invaluable. At a minimum, a reasonable estimate of the frequency of cargos above a yet to be determined maximum areal density threshold should be determined. These containers would require some sort of alternate or secondary screening. Obtaining this information would allow development of models that inform development of the scanning control system and system fielding.

Engagement with industry and regulatory bodies should:

- Seek to gain access to any existing areal density data (other than average areal density data). If data is not available, seek to collaborate with industry to make such data available.
- Seek to gain access to information on maximal areal density cargo, to include common types of high-density loads and their shipment frequency.
- Seek to gain access to x-ray images or associated data. Determine if this data can be used to gain insights into areal density distributions within cargo containers.
- Engage industry to better define how cargo loads are actually configured (e.g. homogeneity or uniformity of loading, loading of dense materials, etc.)

Theoretical and experimental work should:

- Use available data to determine areal density test cases.
- Theoretical work to determine statistical variations to areal density that can be expected based on information gleaned from engagement with industry and regulatory bodies.
- Eventual field testing of any developed system (may be conducted on-site or at the Bates facility with cargo passing through)

18) Removal of remaining neutrons from the gamma source from the beam line.

Further removal of neutrons produced from the 3.0 MeV deuteron interactions with the B target may reduce their impact on the recorded spectra.

While it is not possible to remove all neutrons from the beam line since they can be produced from (g,n) reactions, theoretical work and experiments should be conducted to measure the neutron spectra in the beam line to determine if neutrons reach the cargo and/or the detectors in sufficient numbers such that their interactions adversely affect the spectra in the 4.44 and 15.11 MeV integration regions. The cost of removal of these neutrons from adding additional HDPE or replacing or supplementing with an alternate neutron removal material should be weighed against the reduction in 4.44 and 15.11 MeV counts to determine if these actions should be implemented.

Experiments should also be conducted to determine the impact of additional HDPE in the beam line, particularly to see if this leads to a reduction in unwanted gammas in the vicinity of the 4.44 MeV FEP and SEP. With the geometric constraints of the current system, consideration should be given to replacing some of the 5% borated HDPE with a HDPE with a higher B concentration.

For purposes of this proof of principle, gamma production from thermal and fast neutron captures was not considered. Removal of neutrons from the beam line would obviate the need to consider how thermal and fast neutron captures may result in gammas that complicate or interfere with the spectrum (although (g,n) reactions would remain a source of neutrons). However, if the remaining neutrons cannot be removed from the spectra work should be undertaken to identify if any neutron-induced reactions take place that significantly interfere with 15.11 and 4.44 MeV counting. An additional possibility is to use an alternative nuclear reaction, such as $^{12}C(p,p')^{12}C^*$, that produces the requisite gammas without significant neutrons.

Specific experiments that may be conducted:

- PSD experiments to determine if neutrons reach the cargo and/or the detectors in sufficient numbers such that their interactions adversely affect the spectra in the 4.44 and 15.11 MeV integration regions. (This should also consider the presence of neutrons in any adjusted integration regions previously addressed.)

- If it is determined that neutrons do impact the peak integration regions, The cost of removal of these neutrons by adding additional HDPE or replacing or supplementing with an alternate neutron removal material should be weighed against the reduction in 4.44 and 15.11 MeV counts to determine if these actions should be implemented.
- Experiments should be conducted to determine the impact of additional HDPE in the beam line, particularly to see if this leads to a reduction in unwanted gammas in the vicinity of the 4.44 MeV FEP and SEP.
- Consideration should be given to replacing some or all of the 5% borated HDPE with a HDPE with a higher B concentration.
- Alternative means of removing fast and thermal neutrons (and gammas from neutron interactions) should be considered. For example, a small layer of Cd may be used to further reduce neutrons. Changes to the radiation channel and placement of Pb and HDPE in the vicinity of the B target could also be considered.
- Work should be conducted to identify and quantify the presence of any neutron induced gammas in the beam line (related to the 6-9 MeV gamma identification addressed later)
- If neutrons are determined to be a substantial problem that cannot be adequately mitigated, consider use of an alternative nuclear reaction, such as $^{12}C(p,p')^{12}C^*$, that produces the requisite gammas without significant neutrons.

19) Development of algorithms for automatic clearance.

Development of algorithms for automatic clearance will inform development of an automated system to report estimated areal density and Z_{eff} of the cargo.

Given a defined high-Z areal density detection threshold, a simple algorithm can easily be developed to process 4.44 and 15.11 MeV to automatically clear many low total areal density cargos. Such an algorithm would entail determining the range of potential areal densities based on observed gamma attenuation. It the total areal density can be estimated, it can be determined if it is possible for an areal density of high-Z material equivalent to the high-Z areal density detection threshold can be hidden in the cargo. If, given error bar constraints, the observed ratio falls above the maximum possible ratio for a cargo of the total areal density with a fraction replaced by the high-Z areal density threshold, the cargo is automatically cleared.

Research should be conducted to gain a greater understanding of the relationship between areal density (4.44 MeV attenuation), R_{Th} (relative attenuation of 15.11 to 4.44 MeV), and Z_{eff}. This work should be used to inform development of an automated system to report the estimated areal density and Z_{eff} range of the cargo. Eventually, an automated graphics system should be developed to display an image of the cargo with annotated go (no high-Z material present), no-go (high-Z material present), and unclear (potential high-Z material or suspect cargo).

An automated system should be developed to insure scanning at each location is limited to what is necessary to determine the absence or presence of high-Z materials. In a fielded system, real time data available will include count rates, ratio, and associated error bars. Research and experimental work should be undertaken to better understand the relationship between count rates, ratios, and errors bars and how this information can be used to define how and when to adjust scanning rates.

In summary, development of algorithms should entail:

- Development of a simple algorithm to automatically clear low-areal density cargo.
- Theoretical work and experiments to gain a greater understanding of the relationship between areal density (4.44 MeV attenuation), R_{Th} (relative attenuation of 15.11 to 4.44 MeV), and Z_{eff}. The existing data sets can be used as a starting point.
- Development of an integrated, automatic graphics system to notify an operator of cleared areas, indeterminate or suspect cargo, and the positive identification of high-Z material.

- Development of a system to insure cargo is scanned only to the extent necessary to determine with a specified level of confidence that cargo parameters.

20) Development of sophisticated algorithms.

Development of sophisticated algorithms other than simple ratios could be developed to maximally use the statistical information and thus reduce the necessary scan time and dose.

If additional information, such as attenuation of additional gamma lines, becomes available, simple ratios may still be used. However, a more elegant algorithm may allow more precise determination of the cargo characteristics (i.e. areal density, Z_{eff}). Research in this area should focus on development of predictive algorithm that uses all available information to determine the presence or absence of high-Z materials and provides better cargo characterization.

21) Exploration of the relationship between count rates and ratios.

Additional research should be undertaken to explore the relationship between count rates and ratios to inform development of the cargo scanning control system and minimize count time. Research in this area is closely related to those tasks listed previously under reduction to interrogation time.

During this thesis, experiments were conducted for significantly longer times than what is practical for a fielded cargo scanning system. This goal of this research should focus on determining if the relationships between count rates and ratios (specifically multiple ratios which consider multiple gamma lines) can inform the analysis seeking to determine the minimum amount of scan time required to interrogate a cargo.

22) Exploration of placing three columns of detectors to recover lost counts and improve statistics.

Placing three columns of detectors (one in the beam line and detector arrays on either side) and summing the signals may allow recovery of lost counts and improved statistics. This may allow a means of recovering escape peaks and bremsstrahlung from the 15.11 MeV line. The utility of this method can be explored using a GEANT 4 model and, if proven useful, validated using experiments with the present scanning system configuration.

Research in this area should include:

- Development of a simulation to determine how placement of the two additional detector arrays (and also considering coincidences in the detectors immediately below and above where the event occur) will impact counting statistics. While these adjacent arrays will not fall directly in the fan beam, consideration should also be given to determine how to best shield the detectors from scattered radiations that would interfere with the ability to sum counts.
- If the simulation indicates significant improvements to counting statistics (and therefore reductions to count times) are possible, conduct experiments to validate the simulation.

23) Study of gammas in the 6-9 MeV range.

Study of gamma lines in the 6-9 MeV range that appear in the spectra from unknown processes will allow determination of their origin and determine if these gamma lines can be used in the detection system.

Specific research should seek to determine the origin of the 6-7 and 8-9 MeV gammas present in the current data. Various methods could be used to determine the origin of these gammas. One method is to conduct a thorough search of (n,g) data to identify the range of possible sources. After elimination of sources that are not present in the current configuration, testing of the remaining target materials may allow identification of the source of these gammas. If the sources of the gammas can be determined and quantified, use of these gamma lines in the detection system (previously addressed in “possible use of additional gamma lines in the data”) should be considered. If not, an effort should be made to determine ways to suppress or eliminate the originating reactions.

24) Use of alternative accelerators.

Use of alternative accelerators for the production of monochromatic sources may allow development of a more effective scanning system with lower shielding requirements and lower dose.

A promising example of this would be a 16-18 MeV proton accelerator, which could be used to achieve the same gamma lines as described here, using the $^{12}C(p,p')^{12}C^{*}$ reaction. Research for this specific interaction should include determination of the 4.44 and 15.11 MeV gamma yields as a function of incident proton energy. Research for the use of alternative accelerators should consider systems that can be used to create promising low-threshold reactions to be identified in research suggested in the “consideration of alternative low-threshold nuclear interactions and reactions” section.

25) Utilization of fast neutrons.

Utilization of the fast neutrons produced in $^{11}B(d,n\gamma)^{12}C$ *for fast neutron radiography may allow improved reconstruction of areal densities and* Z_{eff} *of the cargo.* Further, fusion of neutron radiography and photon radiography data may lead to an improved reconstruction of densities and Z.

26) Use of delayed neutrons.

Use of delayed neutrons emanating from the cargo would allow confirmation of the presence of SNM.

These delayed neutrons can be created from neutron-induced fission from neutrons in the fan beam or from photo-fission from high-energy gammas. Specific research in this area should seek to quantify the number of delayed neutrons produced in a specific SNM mass (ideally related to the high-Z areal density detection threshold). A full GEANT 4 or MCNP6 model of the system should be developed to explore the difficulty of detecting these delayed neutrons.

Since the use of delayed neutrons may be an important aspect of confirmatory secondary screening, the model should be used to quantify the amount of delayed neutrons that must be produced (and hence the neutron and/or high energy gammas produced from the source) for a reasonable probability of identification. Consideration should also be given to simulating the delayed neutron detection problem if the cargo is surrounded by hydrogenous material, graphite, or a neutron absorber (e.g. Cd).

27) Variation of beam energy.

Variation of beam energy (e.g. by building a 2-piece target, one with ^{11}B*, one* ^{11}B *covered by a thin energy degrader) to allow for control over the 15.1 MeV line will allow use of non-spectroscopic detectors (e.g. CdWO2, or Cherenkov detectors) to reconstruct Z while operating in charge integrating mode.*

28) Compliance with ANSI N42.46 Standards.

Tests should be undertaken to ensure actual scanning of cargoes, reconstruction of cargo images, and tests of penetration comply with ANSI N42.46 standards.

Activities and standards that must be met include [**63**]:

- Mapping of isodose contour of 0.05 mrem/hr (time averaged) measured at 1 m above ground level.
- Measured cumulative radiation dose where crew/observers/control room personnel are located should not exceed 0.5 μSv in 1 hour (used as system performance comparison, not absolute limit)
- Quantification of the four imaging characteristics: penetration, spatial resolution, wire detection, and contrast sensitivity
    - Penetration using steel arrowhead standard carbon steel test object 30 cm long by 30 cm wide. Penetration is measured at a standard contrast of 20%.
    - Spatial resolution measures minimum separation between features of a test object (three slots or three rods) is defined as the smallest separation between the slots or rods for which all three are fully visible.
    - Wire detection seeks to determine the smallest diameter wire visible in the gamma-ray image.
    - Contrast sensitivity measures the minimum increase in steel thickness visible in the gamma-ray image using the same arrowhead shape as per penetration testing. Must be determined at 10%, 50%, and 80% of the maximum penetration thickness.

It should be noted that the proposed imaging system is a slightly different type of system than the imaging systems addressed in ANSI N42.46 so the spectrum of tests does not fully define the capabilities of the scanning system. Some of the important differences:

- The spatial resolution test seeks to "measure the minimum separation between features of a test object for which the individual features can be distinguished in an x-ray or gamma-ray image." In the proposed system, this is defined by detector size and distance from gamma source to the detector array.
- The penetration tests seeks "to measure the maximum thickness of steel through which the orientation of a specified test object can be determined in an x-ray or gamma-ray image." Again, if a carbon steel test object is used, this

only uses the information from the 4.44 MeV attenuation and system performance is defined by 4.44 MeV relative attenuation, detector selection and positioning, and is ultimately limited by the maximum areal density of the scanning method. However, this system is not designed to differentiate between carbon steel and Fe. It is designed to discriminate between medium- and high-Z materials, which is an entirely different capability.

- The wire test seeks "to determine the smallest diameter Cu wire that is visible in the x-ray or gamma-ray image. For the proposed scanning system, with the current gamma ray energies used, this is an impossible task since Cu is ratio neutral.
- Contrast sensitivity measures "the minimum increase in steel thickness visible in an x-ray or gamma-ray image." Again, this test only uses information gleaned from 4.44 MeV gamma attenuation. The ability to determine the orientation of the carbon steel test object will be defined by the detector size and placement, count time, and arbitrary thickness of the steel.

Based on the research conducted so far, while it is realistic to expect that the proposed system can do well for the spatial resolution, penetration, and contrast sensitivity tests, it will perform extremely poorly on the wire test. However, if additional detector arrays providing additional information are used in conjunction with the existing scanning configuration, it may be possible to create a system that also performs well on this test.

While ensuring compliance with ANSI N42.46 standards are important, additional tests should also be conducted to demonstrate the full capabilities of the system. These tests should specifically highlight the ability of the system to identify the presence of high-Z materials in cargo.

Specific work to support this area should include:

- Mapping of isodose contour of 0.05 mrem/hr (time averaged) measured at 1 m above ground level. This can easily be done with an MCNP6 simulation and validated with measurements on-site.
- Measured cumulative radiation dose where crew/observers/control room personnel are located should not exceed 0.5 μSv in 1 hour (used as system

performance comparison, not absolute limit). This can be accomplished using the isodose contour simulation.

- Eventual testing of the system to quantify performance of the four imaging characteristics: penetration, spatial resolution, wire detection, and contrast sensitivity.

An effort should be made to collaborate with government, regulatory bodies, and industry to develop a set of standards more relevant to SNM detection and identification.

29) Significant breakthroughs.

Uncoupling of the areal density and Z_{eff} *(equivalent to the effective mass attenuation coefficient of the cargo) or reliable determination of* Z_{eff} *or a small range of* Z_{eff} *for an unknown cargo would have a dramatic impact on the effectiveness of the proposed scanning system.*

It should be noted that there are two potential improvements that would mark breakthroughs and make the scanning technique significantly more successful. These may or may not come from further research on this system but their realization, whether through modification of this system or employment in parallel with another system, would significantly improve the system's capabilities:

- Decoupling of areal density and Z_{eff}.
- Reliable determination of Z_{eff} or a small range of Z_{eff} for an unknown cargo.

Achievement of one or both of these breakthroughs would yield a significantly more effective system. Research suggestions previously discussed that would improve areal density measurements are directly related to decoupling of areal density and Z_{eff} and would also lead to better estimation of Z_{eff} for an unknown cargo.

BIBLIOGRAPHY

[1] International Atomic Energy Agency. (2014) IAEA Incident and Trafficking Database: 2014 Fact Sheet. [Online]. http://www-ns.iaea.org/downloads/security/itdb-fact-sheet.pdf

[2] Nuclear Threat Initiative. (2013, February) NIS Nuclear Trafficking Collection. [Online]. http://www.nti.org/analysis/reports/nis-nuclear-trafficking-database/

[3] Alex. P & Spencer-Smith, Charlotte Schmid, "Perspectives on Terrorism: Illicit Radiological and Nuclear Trafficking, Smuggling, and Security Incidents in the Black Sea Region since the Fall of the Iron Curtain--an Open Soruce Inventory," *Perspectives on Terrorism*, vol. 6, no. 2, 2012. [Online]. http://www.terrorismanalysts.com/pt/index.php/pot/article/view/schmid-illicit-radiological/html

[4] Nuclear Threat Initiative. CNS Global Incidents and Trafficking Database. [Online]. http://www.nti.org/analysis/reports/cns-global-incidents-and-trafficking-database/

[5] Alan Cowell. (2014, July) The New York Times. [Online]. http://www.nytimes.com/2014/07/11/world/middleeast/iraq.html

[6] INTERPOL. (2014, December) INTERPOL. [Online]. http://www.interpol.int/News-and-media/News/2014/N2014-238

[7] Ban Ki-moon. (2007, June) United Nations. [Online]. http://www.un.org/press/en/2007/sgsm11040.doc.htm

[8] Barack Obama. (2009, April) The White House: Speeches & Remarks. [Online]. http://www.whitehouse.gov/the_press_office/Remarks-By-President-Barack-Obama-In-Prague-As-Delivered

[9] Marina Koren. (2013, February) Smithsonian.com. [Online]. http://www.smithsonianmag.com/science-nature/top-ten-cases-of-nuclear-thefts-gone-wrong-10854803/

[10] Matthew Bunn, "Securing the Bomb 2010: Securing All Nuclear Materials in Four Years," Project on Managing the Atom, Belfer Center for Science and International Affairs, Harvard Kennedy School, Harvard University, 2010.

[11] Roxane Cohen Silver, "An Introduction to "9/11: Ten Years Later"," *American Psychologist*, vol. 66, no. 6, pp. 427-428, 2011.

[12] Stephen Menesick, "Preventing the Unthinkable: An Overview of Threats, Risks, and US Policy Response to Nuclear Terrorism," *Global Security Studies*, vol. 2, no. 3, Summer 2011.

[13] United States. Defense Science Board. Task Force on Preventing and Defending Against Clandestine Nuclear Attack., "Report of the Defense

Science Board Task Force on Preventing and Defending Against Clandestine Nuclear Attack," Office of the Under Secretary of Defense for Acquisition, Technology, and Logistics, Washington, D.C., Report 2004.

[14] National Commission on Terrorist Attacks Upon the United States. (2004, July) The 9/11 Commission Report: Final Report of the National Commission on Terrorist Attacks Upon the United States (9/11 Report).

[15] Dick K Nanto, "9/11 Terrorism: Global Economic Costs," Congressional Research Service, CRS Report 2004.

[16] Organization for Economic Cooperation and Development. (2002) OECD: Economic Outlook, Analysis, and Forecasts. [Online]. http://www.oecd.org/eco/outlook/1935314.pdf

[17] Justin Bresolin. (2014, June) The Center for Arms Control and Non-Proliferation. [Online]. http://armscontrolcenter.org/publications/factsheets/fact_sheet_the_cooperative_threat_reduction_program/

[18] Global Initiative to Combat Nuclear Terrorism. The Global Initiative to Combat Nuclear Terrorism. [Online]. http://www.gicnt.org/

[19] Proliferation Security Initiative. Proliferation Security Initiative. [Online]. http://www.psi-online.info/Vertretung/psi/en/01-about-psi/0-about-us.html

[20] James Martin Center for Nonproliferation Studies. James Martin Center for Nonproliferation Studies: Combating the spread of weapons of mass destruction with training & analysis. [Online]. http://cns.miis.edu/inventory/organizations.htm

[21] Terrorism Research Initiative. Perspectives on Terrorism. [Online]. http://www.terrorismanalysts.com/pt/index.php/pot/article/view/jongman-internet-websites/html

[22] Angela & Terryn, Greg Canterbury. (2015) Nonproliferation. [Online]. http://armscontrolcenter.org/issues/nonproliferation/analysis_funding_reductions_nuclear_nonproliferation/

[23] Lina Grip. (2011, December) EU Non-Proliferation Consortium. [Online]. http://www.sipri.org/research/disarmament/eu-consortium/publications/publications/non-proliferation-paper-6

[24] Egle Murauskaite. (2013, September) European International Studies Organization. [Online]. http://www.eisa-net.org/be-bruga/eisa/files/events/warsaw2013/murauskaite_eunonproliferation.pdf

[25] International Atomic Energy Agency. The Agency's Programme and Budget 2014-2015. [Online]. http://www.iaea.org/safeguards/symposium/2014/images/pdfs/Programme_and_Budget_2014-2015.pdf

[26] U.S. Census Bureau. (2014, Feb) United States Census Bureau. [Online]. http://www.census.gov/foreign-trade/Press-Release/2013pr/12/ft900.pdf

[27] R. Kouzes, J. McDonald, D. Strachan, and S. Bowyer, *Radiation Detection and Interdiction at U.S. Borders*. New York: Oxford University Press, 2011, (Unpublished).

[28] CBP. (2014a, February) U.S. Customs and Border Protection. [Online]. http://www.cbp.gov/sites/default/files/documents/typical_day_fy12_2.pdf

[29] CBP. (2014c) CBP.gov. [Online]. http://www.cbp.gov/xp/cgov/border_security/border_patrol/recruiting_hiring/who_we_are.xml

[30] CBP. (2014b) CBP.gov. [Online]. http://www.cbp.gov/xp/cgov/border_security/border_patrol/

[31] Janice Cheryl Beaver, "US International Borders: Brief Facts," Congressional Research Service, 2006.

[32] Department of Homeland Security. Department of Homeland Security. [Online]. http://www.dhs.gov/cargo-screening

[33] U.S. Customs and Border Protection. U.S. Customs and Border Protection. [Online]. http://www.cbp.gov/border-security/air-sea/partners

[34] U.S. Customs and Border Protection. U.S. Customs and Border Protection. [Online]. http://www.cbp.gov/border-security/ports-entry/cargo-security/c-tpat-customs-trade-partnership-against-terrorism

[35] CBP. U.S. Customs and Border Protection. [Online]. http://www.cbp.gov/border-security/ports-entry/cargo-security/csi/csi-brief

[36] Richard C. Lanza, Radiation Portal Monitors, 2013, Presentation for a class given as part of the MIT, PSU, and Texas A&M Global Threat Reduction Initiative Nuclear Security Course.

[37] United States Nuclear Regulatory Commission, *Passive Nondestructive Assay of Nuclear Materials*, Doug Reilly, Norbert Ensslin, and Hastings and Smith, Eds. Washington D.C.: USNRC.

[38] ORTEC. ORTEC. [Online]. http://www.ortec-online.com/download/Why-High-Purity-Germanium-%28HPGe%29-Radiation-Detection-Technology-Superior-Other-Detector-Technologies-Isotope-Identification.pdf

[39] M.A., Manatt, D., & Slaughter, D. Descalle, "Analysis of Recent Manifests for Goods Imported through US Ports," Lawrence Livermore National Laboratory, 2006.

[40] Robert C. Runkle, David L. Chichester, and Scott J. Thompson, "Rattling Nucleons: New developments in active interrogation of special nuclear material," *Nuclear Instruments and Methods in Physics Research A*, pp.

75-95, 2011.

[41] CBP. U.S. Customs and Border Protection. [Online]. http://www.cbp.gov/sites/default/files/documents/technology_2.pdf

[42] Ludlum Measurements, Inc. Ludlum Measurements, Inc. [Online]. http://www.ludlums.com/images/stories/data_sheets/M4525-17500.pdf

[43] Rapiscan. Rapiscan Systems. [Online]. http://www.rapiscansystems.com/en/products/radiation_detection/tsa_vm250

[44] Presidio Systems, Inc. Presidio Systems, Inc. [Online]. http://www.presidiosystemsinc.com/PSI_RPM_SOQ.pdf

[45] Direct Industry. Direct Industry. [Online]. http://www.directindustry.com/industrial-manufacturer/radiation-detector-73877.html

[46] CSECO. CSECO Security Equipment Company. [Online]. http://www.cseco.com/Products/BusterK910B.aspx

[47] National Council on Radiation Protection, "NCRP Report No. 94: Exposure to the population in the United States and Canada from Natural Background Radiation," Bethesda, NCRP Report 1987.

[48] National Institute of Standards and Technology. (2014, October) Tables of X-Ray Mass Attenuation Coefficients and Mass Energy-Absorption Coefficients from 1 keV to 20 MeV for Elements Z = 1 to 92 and 48 Additional Substances of Dosimetric Interest*. [Online]. http://physics.nist.gov/PhysRefData/Xcom/html/xcom1.html

[49] DEQ Technical Sales, LLC. Shieldwerx SWX-201HD. [Online]. http://www.deqtech.com/Shieldwerx/Products/swx201hd.htm

[50] Kenneth S. Krane, *Introductory Nuclear Physics*. Canada: John Wiley & Sons, Inc., 1988.

[51] Eric S. Marshall, "New Considerations for Compact Cyclotrons.," Department of Nuclear Science and Engineering, Massachusetts Institute of Technology, Cambridge, 2012.

[52] Zach Hartwig, "DNDO / ARI Simulation Logbook Entry - Calculating

[53] Zach Hartwig, "21" B-HDPE strongly decreases fast neutron flux," Nuclear Science and Engineering, Massachusetts Institute of Technology, Cambridge, Internal Report 2014.

[54] Zach Hartwig. Accelerator-based In-situ Materials Surveillance / ADAQAcquisition. [Online]. https://github.com/zach-hartwig/ADAQAcquisition/blob/master/Readme.md

[55] Zach Hartwig. Accelerator-based In-situe Materials Surveillance / ADAQAnalysis. [Online]. https://github.com/zach-hartwig/ADAQAnalysis

[56] National Institute of Standards and Technology. (2013, January) NIST Center

for Neutron Research. [Online]. http://www.ncnr.nist.gov/resources/n-lengths/

[57] S Fetter et al., "Detecting Nuclear Warheads," *Science & Global Security*, pp. 225-302, 1990.

[58] Gary W Phillips, David J Nagel, and Timothy Coffey, *A Primer on the Detection of Nuclear and Radiological Weapons*. Washington DC: National Defense University Center for Technology and National Security Policy, 2005.

[59] Robert W. Hamm, SUBJECT: Test Report - Factor Acceptance Test, November 28, 2005.

[60] Marianne E. Hamm, Test Report - Factory Acceptance Tests, November 28, 2005, Report of factory acceptance tests from Marianna E. Hamm to Salvatore Gargiulo et al.

[61] TUNL Nuclear Data Evaluation Project. "Energy Level Diagram, 12C". [Online]. http://www.tunl.duke.edu/nucldata/figures/12figs/12_06_1990.pdf

[62] Z.S. Hartwig, Leigh Ann Kesler, and Brandon Sorbom. The MIT Vault Laboratory: Facilities and Equipment. [Online]. http://cstar.mit.edu/vault.php#

[63] American National Standards Institute, "ANSI N42.46-2008 American National Standard for Determination of the Imaging Performance of X-ray and Gamma-Ray Systems for Cargo and Vehicle Security Screening," Institute of Electrical and Electronics Engineers, New York, NY, Regulation 2008.

[64] GAO, *Combating Nuclear Smuggling. Lessons Learned from Cancelled Radiation Portal Monitor Program Could Help Future Acquisitions.* Washington D.C., 2013, United States Government Accountability Office. GAO-13-256.

[65] U.S. Department of Defense, "Nuclear Posture Review Report," Washington D.C., 2010.

[66] Glenn F. Knoll, *Radiation Detection and Measurement*, 3rd ed.: John Wiley & Sons, Inc., 2000.

[67] Robley D. Evans, *The Atomic Nucleus*. Malabar, Florida: Krieger Publishing Company, 1955.

[68] CBP. CBP.gov. [Online]. http://www.cbp.gov/xp/cgov/border_security/port_activities/cargo_exam/rad_portal1.xml

[69] Richard Lanza, Low Dose Inspection for Nuclear Threats using Monochromatic Gamma-Rays, February 20, 2014, Presentation at DNDO AIM Meeting.

[70] HPS, *ANSI/HPS N43.14-2011*. McLean, VA: Health Physics Society, 2011, Radiation Safety for Active Interrogation Systems for Security

Screening of Cargo, Energies up to 100 MeV.

[71] CBP. (2013) CBP.gov. [Online]. http://www.cbp.gov/xp/cgov/about/mission/guardians.xml

[72] Michael Silver, Email between Michael Silver (American Elements) and Buckley ODay, March 6, 2015, E-mail conversation indicated that while all Lanthanides can technically be shipped in bulk (hundreds of grams or more) only Ce, La, and Nd are.

[73] Bryan Bender. (2015, January) The Boston Globe. [Online]. http://www.bostonglobe.com/news/nation/2015/01/19/after-two-decades-russia-nuclear-security-cooperation-becomes-casualty-deteriorating-relations/5nh8NbtjitUE8UqVWFIooL/story.html

[74] International Chamber of Shipping. International Chamber of Shipping: Representing the Global Shipping Industry. [Online]. http://www.ics-shipping.org/shipping-facts/shipping-and-world-trade

[75] H. Yamanishi, "Design of a portable directional neutron source finder," *Nuclear Instruments and Methods in Physics Research Section A: Accelerators, Spectrometers, Detectors, and Associated Equipment*, vol. 544, no. 3, pp. 643-648, June 2005.

[76] N. Mascarenhas, J. Brenna, K. Krenz, and J. Lund, "Development of a Neutron Scatter Camera for Fission Neutrons," *Nuclear Science Symposium Conference Record, 2006.*, vol. 1, pp. 185-188, 2006.

[77] S. Ahlen, D. Dujmic, Peter Fisher, and A. Inglis, "A Background-Free Direction-Sensitive Neutron Detector," *Nuclear Science, IEEE Transactions*, vol. 57, no. 5, pp. 2740-2746, October 2010.

[78] GAO. (2011, September) US Government Accountability Office. [Online]. http://www.gao.gov/assets/590/585514.pdf

[79] James F. Ziegler, SRIM - The Stopping and Range of Ions in Matter, March 27, 2015, http://www.srim.org/ (SRIM version SRIM-2008.04).

[80] T.N. Taddeucci et al., "Neutron and gamma-ray production with low-energy beams," April 2007.

[81] Veronique Rebuffel and Jean-Marc Dinten. (2006) NDT.net. [Online]. http://www.ndt.net/article/ecndt2006/doc/Th.1.3.1.pdf